Active fibre-reinforced composites with embedded shape memory alloys

by

Federica Daghia

Relatore: Prof. Ing. Erasmo Viola
Correlatore: Prof. Ing. Francesco Ubertini
Dottorato di ricerca in Meccanica delle Strutture – XX ciclo
Coordinatore: Prof. Ing. Erasmo Viola

Keywords:
adaptive structures, fibre-reinforced composites, shape memory alloys

Settore scientifico disciplinare:
Area 08 – Ingegneria Civile e Architettura
ICAR/08 – Scienza delle Costruzioni

ALMA MATER STUDIORUM • Università di Bologna
Bologna, 23 marzo 2008

In theory, there is no difference
between theory and practice.
But, in practice, there is.

— JAN L. A. VAN DE SNEPSCHEUT

Contents

List of Figures

List of Tables

Compositi fibro-rinforzati attivi con leghe a memoria di forma

La tesi riguarda i compositi fibro-rinforzati contenenti fili a memoria di forma. L'applicazione strutturale dei materiali attivi permette lo sviluppo di strutture adattive, in grado di rispondere attivamente a cambiamenti dell'ambiente circostante. In particolare, attuatori a memoria di forma inseriti in un composito ne controllano la forma o la rigidezza, influenzando le proprietà statiche e dinamiche del composito stesso. Le applicazioni possibili sono molteplici ed includono la prevenzione dell'instabilità termica di pannelli esterni di aeromobili, il controllo della forma per il miglioramento aerodinamico e l'apertura e il posizionamento di strutture spaziali espandibili.

Lo studio dei compositi attivi è un argomento complesso e multidisciplinare, che richiede una profonda comprensione del comportamento accoppiato tipico dei materiali attivi, oltre che dell'interazione tra i diversi costituenti del composito. Sia i compositi fibro-rinforzati che le leghe a memoria di forma sono argomenti di ricerca molto attivi, che presentano una serie di problemi aperti di tipo sia sperimentale che di modellazione. Per questo, nonostante la tesi si concentri sui compositi attivi, alcuni risultati qui presentati possono essere utilizzati nel contesto dei compositi fibro-rinforzati tradizionali o di altre applicazioni delle leghe a memoria di forma.

Il corpo della tesi è suddiviso in quattro capitoli.

Nel primo capitolo sono introdotti i compositi attivi fibro-rinforzati, presentando una breve panoramica sulle principali tipologie di rinforzo, matrice e processo produttivo per i materiali compositi, insieme ad una introduzione e classificazione di alcuni materiali attivi.

Nel secondo capitolo sono esaminate alcune problematiche relative ai compositi fibro-rinforzati tradizionali. I principali modelli bidimensionali per piastre composite vengono derivati a partire da un solido tridimensionale soggetto a vincoli cinematici. Nel contesto della teoria al primo ordine, viene formulato un nuovo elemento finito semplice, accurato e computazionalmente efficiente, a partire da un approccio ibrido agli sforzi. La soluzione del problema bidimensionale è utilizzata per la ricostruzione delle tensioni lungo lo spessore del laminato e si sviluppa una procedura in due fasi che utilizza il Recovery by Compatibility in Patches, formulato recentemente e qui esteso al caso di pia-

stre laminate, per migliorare l'accuratezza della soluzione bidimensionale. La modellazione di elementi compositi anisotropi richiede di determinare un significativo numero di parametri elastici, che possono essere stimati tramite tecniche numerico-sperimentali. In questo contesto, vengono analizzati due diversi estimatori bayesiani, evidenziando analogie e differenze tra i due. Inoltre, viene proposta una procedura alternativa per migliorare la velocità di convergenza.

Nel terzo capitolo sono introdotte le leghe a memoria di forma, descrivendone proprietà e principali applicazioni. Diversi modelli costitutivi mono e triassiali di letteratura, basati su analogie con la plasticità, sono messi a confronto in maniera critica, evidenziandone potenzialità e limiti, legati principalmente alla definizione del diagramma di fase e alla scelta delle variabili interne. Successivamente, sono riportati alcuni risultati sperimentali sulla caratterizzazione di fili a memoria di forma. Tali risultati evidenziano fenomeni non rappresentati dalla corrente modellazione costitutiva; si propongono alcune idee per lo sviluppo di un modello alternativo.

Il quarto capitolo riguarda le piastre composite attive con fili a memoria di forma. Gli approcci di modellazione che possono essere impiegati per descrivere il comportamento di tali strutture sono numerosi e presentano differenti vantaggi e svantaggi, sia dal punto di vista della complessità che della versatilità. Un modello semplice, utile per descrivere le configurazioni di controllo della forma e della rigidezza in un contesto comune, è proposto e implementato. Successivamente, il modello è validato sperimentalmente, facendo riferimento alla configurazione di controllo della forma, la quale risulta essere la più sensibile alla scelta dei parametri del modello. Il lavoro sperimentale è suddiviso in due parti. Nella prima parte, un elemento composito attivo è realizzato incollando alcuni fili a memoria di forma predeformati su una striscia di laminato in fibra di carbonio. Si tratta di una struttura relativamente semplice da realizzare, ma utile a dimostrare sperimentalmente il concetto illustrato nella prima parte del capitolo. Nella seconda parte, si affrontano le problematiche relative alla realizzazione di un vero e proprio composito fibro-rinforzato con fili a memoria di forma integrati, considerando diverse scelte in termini di materiali e tecnologie impiegate. Anche se rimangono da affrontare diversi aspetti tecnologici, i risultati ottenuti dalla sperimentazione permettono di dimostrare il meccanismo di funzionamento dei compositi con fili a memoria di forma, risultando inoltre in ottimo accordo con le previsioni del modello proposto.

Introduction

This dissertation concerns active fibre-reinforced composites with embedded shape memory alloy wires. The structural application of active materials allows to develop adaptive structures which actively respond to changes in the environment, such as morphing structures, self-healing structures and power harvesting devices. In particular, shape memory alloy actuators integrated within a composite actively control the structural shape or stiffness, thus influencing the composite static and dynamic properties. Envisaged applications include, among others, the prevention of thermal buckling of the outer skin of air vehicles, shape changes in panels for improved aerodynamic characteristics and the deployment of large space structures.

The study and design of active composites is a complex and multidisciplinary topic, requiring in-depth understanding of both the coupled behaviour of active materials and the interaction between the different composite constituents. Both fibre-reinforced composites and shape memory alloys are extremely active research topics, whose modelling and experimental characterisation still present a number of open problems. Thus, while this dissertation focuses on active composites, some of the research results presented here can be usefully applied to traditional fibre-reinforced composites or other shape memory alloy applications.

The dissertation is composed of four chapters.

In the first chapter, active fibre-reinforced composites are introduced by giving an overview of the most common choices available for the reinforcement, matrix and production process, together with a brief introduction and classification of active materials.

The second chapter presents a number of original contributions regarding

the modelling of fibre-reinforced composites. Different two-dimensional laminate theories are derived from a parent three-dimensional theory, introducing a procedure for the a posteriori reconstruction of transverse stresses along the laminate thickness. Accurate through the thickness stresses are crucial for the composite modelling as they are responsible for some common failure mechanisms. A new finite element based on the First-order Shear Deformation Theory and a hybrid stress approach is proposed for the numerical solution of the two-dimensional laminate problem. The element is simple and computationally efficient. The transverse stresses through the laminate thickness are reconstructed starting from a general finite element solution. A two stages procedure is devised, based on Recovery by Compatibility in Patches and three-dimensional equilibrium. Finally, the determination of the elastic parameters of laminated structures via numerical-experimental Bayesian techniques is investigated. Two different estimators are analysed and compared, leading to the definition of an alternative procedure to improve convergence of the estimation process.

The third chapter focuses on shape memory alloys, describing their properties and applications. A number of constitutive models proposed in the literature, both one-dimensional and three-dimensional, are critically discussed and compared, underlining their potential and limitations, which are mainly related to the definition of the phase diagram and the choice of internal variables. Some new experimental results on shape memory alloy material characterisation are also presented. These experimental observations display some features of the shape memory alloy behaviour which are generally not included in the current models, thus some ideas are proposed for the development of a new constitutive model.

The fourth chapter, finally, focuses on active composite plates with embedded shape memory alloy wires. A number of different approaches can be used to predict the behaviour of such structures, each model presenting different advantages and drawbacks related to complexity and versatility. A simple model able to describe both shape and stiffness control configurations within the same context is proposed and implemented. The model is then validated considering the shape control configuration, which is the most sensitive to model parameters. The experimental work is divided in two parts. In the first part, an active composite is built by gluing prestrained shape memory alloy wires on a carbon fibre laminate strip. This structure is relatively simple to build, however it

is useful in order to experimentally demonstrate the feasibility of the concept proposed in the first part of the chapter. In the second part, the making of a fibre-reinforced composite with embedded shape memory alloy wires is investigated, considering different possible choices of materials and manufacturing processes. Although a number of technological issues still need to be faced, the experimental results allow to demonstrate the mechanism of shape control via embedded shape memory alloy wires, while showing a good agreement with the proposed model predictions.

Compositi fibro-rinforzati attivi

I materiali compositi sono formati da due o più costituenti diversi, ciascuno dei quali contribuisce a determinarne il comportamento complessivo. Più comunemente, il termine compositi si riferisce a materiali costituiti da una matrice la cui funzione è di unire e proteggere le fibre, che costituiscono il principale elemento resistente del composito. Anche limitandosi ai soli compositi fibro-rinforzati si riscontra un'enorme varietà di materiali diversi.

Tra i primi ad interessarsi di compositi fu negli anni '60 l'industria aerospaziale, in cerca di soluzioni per la realizzazione di componenti dal peso ridotto. Negli ultimi decenni, i compositi hanno cominciato ad essere utilizzati in altri settori, quali l'industria automobilistica, sportiva e delle costruzioni.

Il principale vantaggio nell'utilizzo dei materiali compositi è l'ottimo rapporto peso/resistenza, oltre alla possibilità di progettare il materiale a seconda delle necessità strutturali. Definendo la posizione delle fibre e il numero di strati è possibile progettare le proprietà del materiale in funzione della direzione di caricamento e dei requisiti locali di resistenza e rigidezza. Questa flessibilità implica però una notevole complessità associata alla progettazione di strutture composite rispetto alle strutture tradizionali, dato che il materiale e il processo di produzione devono essere definiti insieme alla struttura stessa.

Questi problemi, in aggiunta al costo ancora elevato dei materiali compositi, hanno finora ritardato l'utilizzo di tali materiali in applicazioni strutturali. Recentemente la tendenza si sta invertendo e cominciano a nascere nuove idee sulle possibili combinazioni di materiali diversi per ottenere un'infinita varietà di proprietà strutturali. Lo sviluppo di materiali attivi, quali i materiali piezoelettrici e le leghe a memoria di forma, ha aperto la strada alla realizzazione di compositi attivi. I materiali attivi mostrano un accoppiamento tra il campo meccanico e altri campi della fisica (termico, elettrico, magnetico, ecc.), che può essere sfruttato per realizzare sensori o attuatori. Inserendo un materiale attivo in un composito, questo svilupperà caratteristiche attive. La principale applicazione dei compositi attivi consiste nel controllo delle proprietà strutturali, che possono adattarsi a cambiamenti delle condizioni esterne.

Lo sviluppo dei compositi attivi presenta ulteriori difficoltà rispetto ai compositi fibro-rinforzati tradizionali. La modellazione di compositi attivi richiede la descrizione del campo meccanico e di quello accoppiato, coinvolgendo mecca-

nismi di accoppiamento che in alcuni casi non sono ancora pienamente compresi. Per materiali attivi di recente concezione, inoltre, non sono ancora disponibili informazioni sul comportamento a lungo termine. Tutte queste difficoltà rendono i compositi attivi un tema di ricerca molto complesso e promettente, che coinvolge numerose discipline (chimica, scienza dei materiali, ingegneria strutturale, etc.) per ottenere comportamenti strutturali che sarebbero impensabili con materiali tradizionali.

In questo capitolo, una breve descrizione di alcune tra le più comuni possibilità a disposizione per la definizione del rinforzo, della matrice e del processo produttivo per i compositi fibro-rinforzati tradizionali, insieme ad una panoramica su alcuni materiali attivi, permette di illustrare le enormi potenzialità dei compositi attivi.

Chapter 1

Active fibre-reinforced composites

Composites are materials made up of two or more constituents, each bestowing different characteristics on the overall material behaviour. A number of very different materials belong to this broad category, from traditional structural materials such as concrete and masonry all the way to newly devised polymers with embedded nanoparticles such as carbon nanotubes.

More commonly, the term composite refers to materials constituted by a matrix, whose function is to bind together and protect the fibres, which constitute the main load-bearing elements of the composite. Even within the narrower definition of fibre-reinforced composites, the variety of available materials is enormous. In particular, composites can be classified according to the type of matrix, reinforcement and technological process (Edwards, 1998).

Fibre-reinforced composites are becoming increasingly popular in a wide range of applications. Historically, among the first to take an interest in composites was the aerospace industry in the 1960s (Soutis, 2005). The main reason was the significant decrease in weight of composites as compared to traditional materials. In the last decades, however, composites have started to penetrate other industries, such as automotive, sporting goods and construction, where they are mainly used as reinforcement to repair and enhance the performance of existing structures (Bastianini et al., 2005; Stratford et al., 2004).

Among the advantages of composite materials are the high strength to weight ratio and the possibility to tailor the material to the structural needs. Indeed, by selecting the fibre placement and number of layers it is possible to design the material properties according to the direction of loading and the locally required strength and stiffness properties. This, however, implies a significant complexity in the design of composite structures as compared to traditional ones, since the material and the production process need to be designed together with the structure itself. Moreover, the material behaviour of composites in both elastic and inelastic range is rather complex to predict, as it involves mesoscale interaction of the different constituents.

The mentioned issues, together with the still high cost of composite materials as compared to traditional solutions, have delayed the massive use of composites in structural applications. In recent years, however, the interest in these kinds of materials has been ever increasing. A significant example of the advances in composite use is the new aircraft Boeing 787 Dreamliner, scheduled to enter into service in 2008: it is the first aircraft whose primary structure is made for as much as 50% of composites — including the fuselage and the wing. In this case, the use of composites greatly simplifies the structural elements: by manufacturing a one-piece fuselage section, the designers were able to eliminate 1,500 aluminium sheets and 40,000 - 50,000 fasteners (source: Boeing website[1]).

As fibre-reinforced composites become established, more ideas arise on how best to combine different materials to achieve a virtually infinite variety of structural properties. The development of active materials, such as piezoelectric materials and shape memory alloys, has paved the way to the creation of active composites. Active materials (also referred to as smart or intelligent materials) exhibit coupling between the mechanical field and some other physical field (thermal, electric, magnetic etc.), thus a stimulus in one of the fields provokes a response in the coupled field. This coupling can be exploited for sensing and/or actuation. In sensing, a stimulus in the mechanical field provokes a response in the coupled field which can be measured, while in actuation the coupled field is used to provoke a mechanical response. By embedding an active material in a composite, the composite itself can exhibit active properties.

Active composites can be used for many purposes, the main idea being to control and adapt the structural properties according to a change in external

[1] www.boeing.com

conditions (adaptive composites). Embedded sensing allows to monitor the structural conditions, while actuators can change the dynamic properties, stiffness or shape according to need. Even more, embedded systems can be designed with self-diagnosis and self-healing features.

The development of active composites poses even more challenges than traditional fibre-reinforced composites. Modelling active materials requires to take into account both the mechanical and the coupled field, thus increasing the size and complexity of the problem and, in many cases, introducing sources of non linearity. Moreover, in some cases the mechanisms underlying the coupled behaviour are still not fully understood, thus further investigation on the active material itself is required prior to considering the composite. Finally, for many active materials of recent conception not much information is available regarding the long term behaviour, such as fatigue life and stability of the response with increasing numbers of cycles. All the stated difficulties make active composites a very challenging yet promising topic for researchers, which involves many different disciplines (chemistry, material science, structural engineering etc.) working together to achieve structural performances which would have been unthinkable with traditional materials.

An overview of the most common choices available for the reinforcement, matrix and production process for traditional fibre-reinforced composites (Mazumdar, 2002), together with a brief introduction and classification of active materials, allow to get a glimpse of the enormous potential of active fibre-reinforced composites.

1.1 Reinforcement

Fibres are the main load-bearing element of the composite, thus it is mostly on the choice of the reinforcement that the composite mechanical properties depend. Choosing a reinforcement requires to define the type of fibres, their size and arrangement.

Fibres can be made of a wide variety of materials, both inorganic (e.g. metal, glass, carbon fibres) and organic (e.g. aramidic, natural fibres). Because of the small size of the cross-section (5 to 25 μm for the most common fibres) and the reduced amount of defects, fibres are generally stiffer and stronger than material in bulk form and tend to break in a fragile manner. In Figure 1.1, typical stress

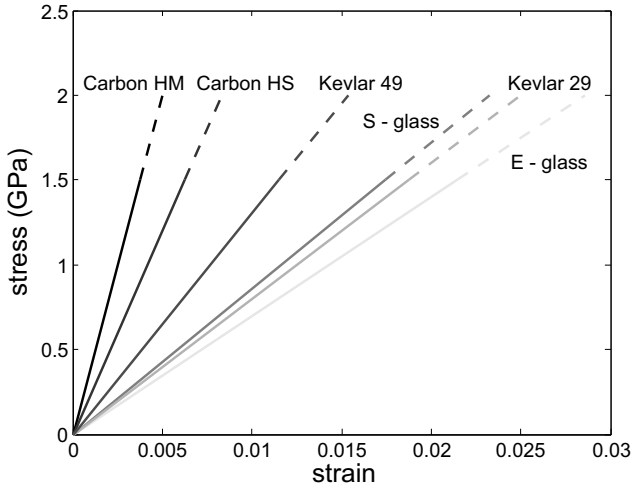

Figure 1.1: Typical stress-strain curves for various fibres

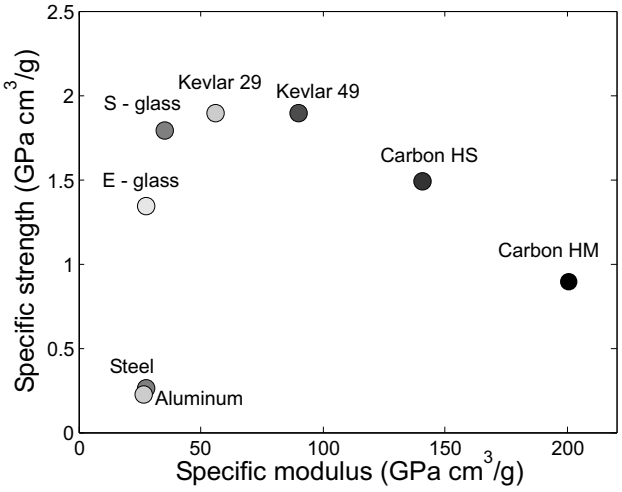

Figure 1.2: Specific properties of fibres and bulk materials

strain curves in uniaxial tension are shown for various types of fibres, whereas in Figure 1.2 the specific properties of various fibres are compared with those of bulk steel and aluminium.

Glass fibres are the cheapest among the reinforcements, thus they are the most common in applications. Their elastic modulus is comparatively low (slightly better for the S-glass type than the E-glass), thus they are used for both structural and non structural applications. Carbon fibres come in different varieties, classified as high strength and high modulus fibres. Their elastic modulus and specific elastic modulus are the highest, thus they are often favoured in low-weight structural applications. However, their cost is significantly higher than that of glass fibres. Aramidic fibres are synthetic organic fibres, also known with the commercial name of Kevlar. When drawn, aramidic fibres acquire anisotropic properties, thus their behaviour in compression is significantly worse than in tension. Because of their microstructure, aramidic fibres break in a more ductile way as compared to glass or carbon fibres; for this reason they are used in applications where energy dissipation is required, such as motorcycle helmets and bulletproof vests.

A variety of different reinforcements can be obtained from the same type of fibres, from thin two dimensional mats or fabrics to complex-shaped three-dimensional preforms. The properties of the resulting composite depend mainly on the fibre length (long versus short fibres) and orientation (random versus oriented). In general, the best material properties are obtained with long continuous fibres which are oriented in the loading direction. This situation allows to maximise the use of the material, but yields extremely anisotropic composites and may not be the best configuration, depending upon the application and manufacturing process. Nearly isotropic properties can be obtained with randomly oriented fibres, which can be held together with a resinous binder to form a mat. Depending upon the length of the fibres, this is called chopped fibres mat (short fibres, Figure 1.3(a)) or continuous mat (long fibres, Figure 1.3(b)).

Long continuous oriented fibres are arranged in bundles called rovings, which can be used to make woven or non woven fabric. Woven fabric is made of fibres woven together to form a single layer and it is classified according to the weave style. Some common weave styles are shown in Figure 1.3(d). The weave style defines the amount of fibres in each direction, thus it influences the degree of

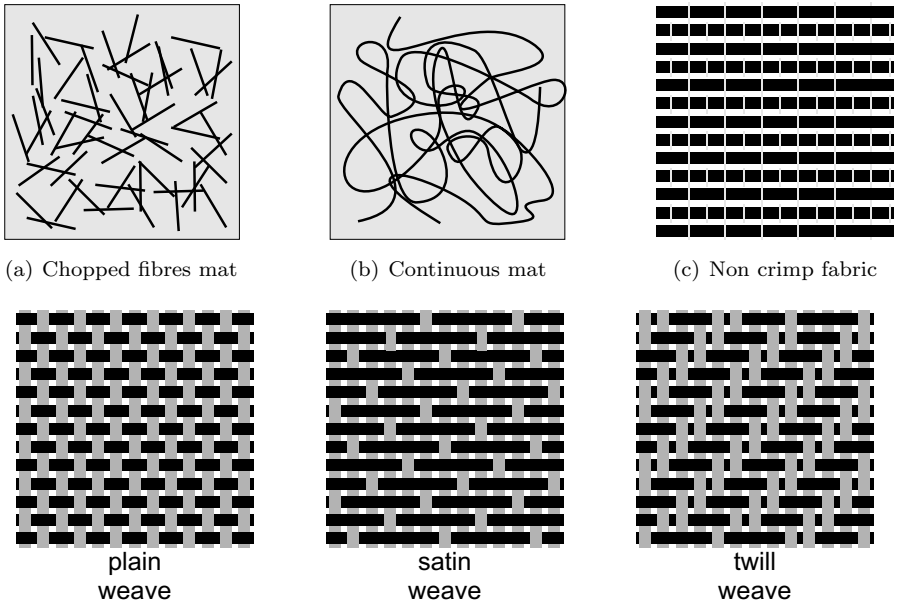

(a) Chopped fibres mat (b) Continuous mat (c) Non crimp fabric

(d) Some weave styles for woven fabric

Figure 1.3: Types of reinforcement

in-plane anisotropy of the composite. In plain weave, for example, the same amount of fibres are laid along two orthogonal directions, thus the composite properties along these two directions are the same. Non woven fabric, also called non crimp fabric, is made of fibres aligned parallel to each other and stitched together with polyester thread (Figure 1.3(c)). This allows the fibres to remain straight, thus increasing the strength of the composite with respect to woven fabric. Moreover, in non crimp fabric the fibres are aligned all along the same direction, resulting in the most anisotropic composite behaviour.

1.2 Matrix

The matrix has the role of binding and protecting the fibres in a composite. Many different materials can be used as matrix, such as metals, cement and polymers. Polymer matrices are by far the most common in composites applications and they are the only ones discussed here.

Polymers are subdivided into thermoplastic and thermoset resins. Because of differences in the microstructure, thermoplastic resins can repeatedly melt and harden when heated and cooled, whereas thermoset resins cannot be reformed once cured. Thermoplastics tend to have lower mechanical characteristics and higher viscosity than thermosets, thus they are often used for non structural applications and will not be dealt with in details here.

The selection of a polymer matrix is determined by a variety of factors, involving both the service life of the composite (maximum service temperature, fire and corrosion resistance, mechanical properties, etc.) and the manufacturing process (duration, temperature and pressure required in the cure cycle, viscosity, etc.). As regards the composite manufacturing, the resin can be given in liquid, semi-solid and solid form depending on the chosen process. To acquire its service characteristics, it undergoes a curing process, that is a chemical reaction which results in the formation of a three-dimensional cross-linked network. Depending upon the resin chemical composition and the properties which are to be achieved in the final composite, curing can be carried out in different conditions of pressure and temperature, with or without the presence of additives and catalysts.

Epoxy resins are the most widely used for structural applications because of their good mechanical properties. They are extremely versatile, as their properties and cure cycle can be tailored to meet various application needs. Their maximum service temperature goes from $90° - 120°$C all the way up to $200°$C[2]. Bismaleimide and polyimide resins provide higher service temperatures than epoxies (up to more than $350°$C), whereas lower cost resins include polyesters and phenolic resins, the last ones providing also flame resistance and low smoking properties.

[2] An indication of the maximum service temperature is given by the polymer's glass transition temperature T_g, which is a selection parameter in resin producers' data sheets.

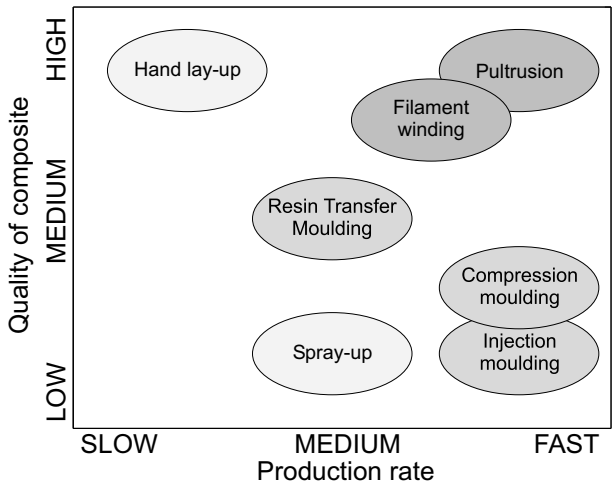

Figure 1.4: Production rate versus quality of the composite for some manufacturing processes

1.3 Manufacturing process

Many different composite manufacturing techniques are available, which differ in the quality of the final product, cost, production rate, achievable size and shape. Indeed, all these factors need to be taken into consideration when the process is selected. In particular, good quality of the resulting composite and high rate of production are usually contrasting needs, as the processes that yield the best results in terms of fibre quantity and placement are usually more time consuming. An exception is pultrusion, which is however suitable only for cylindrical shaped composites. The achievable quality and production rate of some manufacturing processes are reported in Figure 1.4.

Composite manufacturing consists of four phases: impregnation, lay-up, consolidation and solidification. In impregnation, fibres are thoroughly covered with matrix to ensure a good fibre-matrix interface. Naturally, in this phase matrix viscosity is a key factor. Depending upon the process, dry fibres or fibres already impregnated by the materials supplier (pre-pregs) are used. The lay-up

consists in positioning different layers of reinforcement one on top of the other to make a laminated composite. Each layer (lamina) can be made with a different reinforcement and the fibre orientation can vary from one layer to the other. Consolidation is a crucial phase which influences the quality of the final composite: a pressure is applied to remove voids and create the best possible contact between the laminae. Depending on the process, pressure can be applied by hand, with a vacuum pump, in autoclave or press. Finally, solidification fixes the composite shape: it is achieved by resin curing and can last from less than a minute to several hours.

The placement and orientation of the layers are conventionally defined by the laminate's stacking sequence, or lamination scheme. The laminae, or plies, are listed from the bottom to the top layer and defined by the fibre orientation with respect to an axis associated to the laminate (see Figure 1.5). If not otherwise specified, all laminae have the same thickness. An example of stacking sequence is $(0/45/90/-45/0)$. When ply stacking sequence, material and geometry are symmetric about the laminate midplane, the laminate is symmetric, and can be denoted by only the first half of the stacking sequence: $(0/45/90)_s = (0/45/90/90/45/0)$, or $(0/45/\bar{90})_s = (0/45/90/45/0)$ (the bar marks a single central layer). An antisymmetric laminate is a laminate whose stacking sequence is antisymmetric about the midplane, for example $(0/45/30/-30/-45/0)$. Cross-ply laminates are made up of layers with $0°$ and $90°$ orientation, angle ply laminates include also other stacking angles.

In the following, some composite manufacturing processes are described.

1.3.1 Hand lay-up

Hand lay-up is a very labour intensive technique, whose main advantage is to allow the production of good quality parts which can be large and complex-shaped. It consists in placing the layers on a lower mould by hand and then applying pressure and temperature by means of a vacuum bag or in autoclave to allow resin curing. Two main techniques are included in hand lay-up: pre-preg lay-up and wet lay-up. In the first case, fabrics which are already impregnated with the resin are used, in the second alternate layers of dry fibres and liquid resin are applied using a roller. The use of pre-pregs allows to control more effectively the amount of resin and fibres present in the final composite, thus

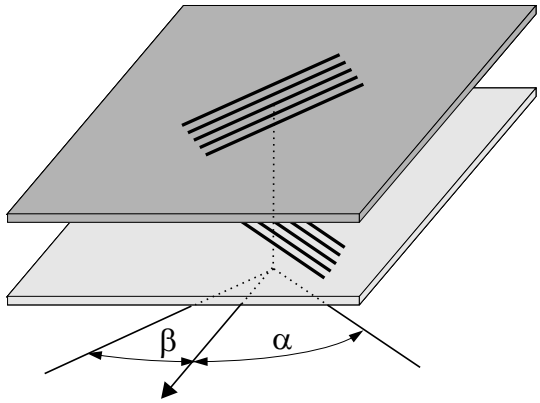

Figure 1.5: Laminae fibre orientation

obtaining a material with better properties. On the other hand, pre-pregs are more expensive than dry fibres and resin, require storage below room temperature and have a limited shelf life (usually six months to one year). In both cases, the final result strongly depends upon the skills of the laminator.

1.3.2 Spray-up

As hand lay-up, spray-up is an open mould process which allows to produce large and complex-shaped parts. It is a much faster technique, which however gives worse results in terms of composite properties. The fibres and matrix are sprayed on the mould by using a chopper gun, which chops and wets the fibres prior to depositing them on the mould. Once the material has been sprayed, rollers are used to remove entrapped air and the cure is usually done at room pressure and temperature.

1.3.3 Moulding

Moulding processes allow a high production rate as compared to the techniques described up to now. On the down side, their use is usually limited to non

structural parts because of the low properties obtained with moulding compounds. An exception is Resin Transfer Moulding (RTM), which is able to produce structural quality parts with a medium production rate. Also, most moulding techniques employ a lower and upper mould, as opposed to the single side mould used in hand lay-up and spray-up. Although the mould cost increases, closed-mould processes are advantageous because of the low volatile emissions and good surface finish on both sides.

Compression moulding and injection moulding make use of moulding compounds as raw materials. These are sheets (Sheet Moulding Compound, SMC) or bulks (Bulk Moulding Compound, BMC) of chopped glass fibres, resin and filler. These usually contain a low percentage of fibres (about 25%) and thus do not yield structural quality material. In compression moulding, a certain quantity of moulding compound (charge) is positioned in the bottom part of the mould, then the top part is closed with a certain velocity. The mould is usually pre-heated to facilitate the resin flow, after a few minutes of cure under heat and pressure the mould is opened and the composite is removed. In injection moulding, the moulding compound is heated and injected through a nozzle into the closed mould. Pressure and temperature are maintained during cure, then after a few minutes the mould is opened and the part removed.

Resin Transfer Moulding differs from the described procedures in that only the resin is injected. Dry fibre preforms are positioned between the top and bottom moulds, then low viscosity resin is injected inside the mould. This allows to control the amount and positioning of fibres and to obtain structural quality parts with a comparatively fast production rate. Naturally, the resin viscosity is a crucial issue in this process. In Vacuum Assisted RTM (VARTM), the resin infiltration and fibre wetting is helped by the presence of void. For very large parts, such as boat hulls, the top mould can be substituted by a vacuum bag. In this case, thickness of the resulting composite is less controllable but the cost of the mould is cut to half. This technique is also known with the name of resin infusion and is a good and cost-effective alternative to wet lay-up when it comes to the manufacturing of large and complex parts.

1.3.4 Pultrusion

Pultrusion is a low cost, high production rate, structural quality technique to produce cylindrical beam-like composites. Fibre rovings are impregnated by passing through a resin bath, then they are pulled through a heated die where they cure and achieve the desired shape. Curing occurs with high temperature and low pressure. The process is continuous, therefore composite beams of any length can be obtained. The disadvantages of this highly automated process are the limited shapes that can be achieved and the impossibility to choose the fibre orientation (unidirectional fibres along the beam axis or, at most, bidirectional fabrics can be used).

1.3.5 Filament winding

Filament winding is also a highly automated process, which yields good performance composites. Fibre rovings are passed through a resin bath and then wound over a rotating mandrel at a desired angle. Once the fibre winding is over, the composite is cured at room or high temperature, then the mandrel is extracted. The choice of fibre orientation is improved with respect to pultrusion, even though not every possible orientation can be achieved. As for pultrusion, the main disadvantage of filament winding is the limitation in the shapes that can be achieved (tubular, closed parts).

1.4 Active materials

Due to their coupled behaviour, active materials can be used for sensing and/or actuation purposes. The coupling can be related to intrinsic material characteristics, usually at the microstructural level, or to the 'intelligent' combination of different traditional materials. A variety of materials display active characteristics, thus different classifications are introduced to help identify the most appropriate for the sought application.

Some classification criteria are discussed here. One possibility, adopted in the following, is to distinguish active materials according to the coupled field (electrical, thermal, magnetic, chemical etc.). Other classifications include the type of material (metal, polymer, ceramic etc.) or the response obtained in terms of force and/or strain. The last classification is particularly useful when

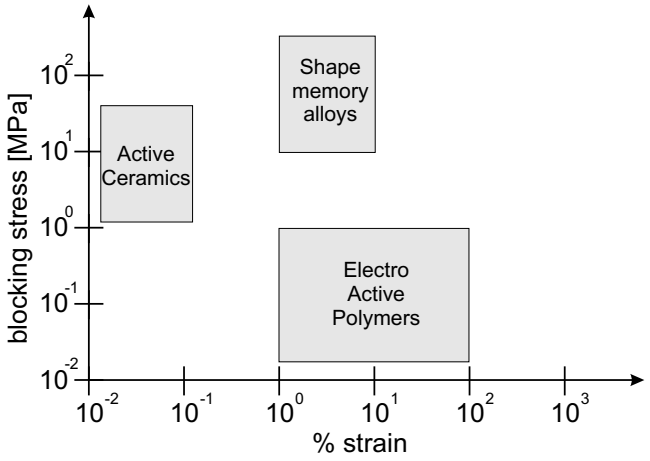

Figure 1.6: Classification of some active materials according to the stress-strain response

choosing a sensor or an actuator for a specific application. Indeed, the order of magnitude of the stress and strain which can be achieved from different active materials is extremely variable, as it can be seen in Figure 1.6. In particular, it is clear from the graph how shape memory alloys are significantly superior to active ceramics and electroactive polymers in both output stress and strain, thus making a good candidate for the creation of active composites.

An overview of some active materials and the principle lying at the basis of their coupled behaviour is given in the following.

1.4.1 Electrical coupling

The most common materials exhibiting electromechanical coupling are piezoelectric materials. The piezoelectric effect consists in an accumulation of electric charges as a consequence of applied stress (direct piezoelectric effect) or in a deformation generated by an applied electric field (inverse piezoelectric effect). The effect is related to the presence within the material of charged dipoles

whose orientation changes according to the applied electric field. Some crystals naturally display the piezoelectric effect, whose magnitude can be increased by the polarization process. Most piezoelectric materials used in applications are ceramics, but also some polymers are manufactured to display piezoelectric properties. Piezoceramic wafers can develop large forces, however the associated deformations are rather small (of the order of nanometers), therefore more complex configurations, such as stacks or bimorphs, are generally created to enhance the available deformation.

Among the polymers displaying electromechanical coupling, one should include dielectric elastomers. These are devices obtained by placing a layer of very compliant and nearly incompressible dielectric material between two thin compliant electrodes. By applying a current to the electrodes, these tend to get nearer to each other, thus squeezing the dielectric layer which elongates in the perpendicular direction due to the Poisson effect. Some issues related to the fabrication and use of dielectric elastomers are the choice of the dielecric material and the electrodes, which need to be extremely compliant in order not to break during the actuation, and the use of very high voltages, of the order of some kV.

1.4.2 Thermal coupling

All materials exhibit thermomechanical coupling, related mostly to the thermal expansion behaviour. However, in shape memory alloys this coupling is much stronger than in traditional materials and it is related to complex changes in the material microstructure. Shape memory alloys are the subject of Chapter 3 and they are not further discussed here.

1.4.3 Magnetic coupling

Materials exhibiting magnetomechanical coupling include magnetorheological fluids and magnetostrictive materials. Ferromagnetic shape memory alloys also belong to the latter group. Magnetorheological fluids are liquids whose viscosity greatly changes with an applied magnetic field, to the point of becoming viscous solids. Magnetostrictive materials can be deformed via an applied magnetic field, thanks to the orientation of the magnetisation axis. In ferromagnetic

shape memory alloys, different orientation of the martensitic microstructure with an applied magnetic field are responsible for the macroscopic deformation.

1.4.4 Chemical coupling

A new class of active materials whose coupled behaviour is related to chemical reactions are ionic polymers. The actuation mechanism is related to the change in volume of the polymer as it acquires or loses ions in oxidation-reduction reactions. Due to the type of material and the microstructural changes involved, very low forces but extremely large deformations can be achieved as compared to other active materials. The chemical reaction is usually triggered by electrical current, while the polymer is immersed in an electrolytic solution which provides the necessary ions. For this reason, ionic polymers are usually classified as wet, as opposed to piezoelectric polymers or dielectric elastomers, which can work in a dry environment. Recent research work, however, is aimed at devising new ways to provide ions for the chemical reaction, which would allow ionic polymers to operate in air.

Modellazione dei compositi fibro-rinforzati

Negli ultimi anni l'utilizzo dei materiali compositi in applicazioni ad elevata tecnologia è incrementato in maniera significativa. Lo sviluppo di nuove applicazioni, incluse quelle basate su materiali attivi integrati nella struttura, richiede la definizione di strumenti di modellazione semplici ed accurati in grado di descrivere il comportamento strutturale di elementi compositi. Per questo, gli strumenti analitici e numerici per la modellazione di tali materiali costituiscono un tema di ricerca molto attivo.

Sono state proposte numerose teorie strutturali per i laminati, molte delle quali descrivono il composito come un elemento di piastra o guscio bidimensionale. Le teorie bidimensionali sono in genere semplici e richiedono un numero limitato di parametri, per questo costituiscono una base ideale per lo sviluppo di strategie numeriche quale il metodo degli elementi finiti. D'altra parte, la riduzione di una struttura tridimensionale multistrato ad un singolo strato equivalente porta alla perdita di informazioni, in particolare relative alle tensioni lungo lo spessore, che potrebbero rivelarsi cruciali per l'accurata valutazione del comportamento del composito e dei suoi meccanismi di danneggiamento. La formulazione di un modello bidimensionale a partire dalla teoria tridimensionale rimuove in parte tale inconveniente, permettendo di ricostruire a posteriori le tensioni lungo lo spessore. Nella sezione 2.1 vengono derivati alcuni modelli bidimensionali secondo questa logica e viene discussa la procedura analitica per la ricostruzione delle quantità tridimensionali.

Una volta scelto un modello analitico, è necessario definire procedure numeriche accurate e computazionalmente efficienti. Nella sezione 2.2 si propone un nuovo elemento finito basato sulla teoria al primo ordine, definita nella sezione 2.1. Una formulazione ibrida agli sforzi ed un'accurata selezione delle approssimazioni per sforzi e spostamenti permettono di costruire un elemento semplice, stabile e computazionalmente efficiente, preparando la strada per la ricostruzione delle quantità tridimensionali.

La procedura analitica di ricostruzione, descritta nella sezione 2.1, non è automaticamente applicabile a partire da una soluzione bidimensionale approssimata. Nascono infatti alcuni problemi riguardanti la convergenza delle quantità ricostruite ed il soddisfacimento delle condizioni al contorno del problema tridimensionale. Nella sezione 2.3 si definisce una strategia generale per la rico-

struzione delle tensioni lungo lo spessore a partire da soluzioni bidimensionali agli elementi finiti.

La modellazione dei materiali compositi richiede la conoscenza delle proprietà elastiche del laminato, difficili da determinare con i metodi sperimentali tradizionali. Le tecniche numerico-sperimentali basate sulla misura delle frequenze naturali del composito rappresentano una valida alternativa ai metodi statici tradizionali. Nella sezione 2.4 sono messe a confronto alcune tecniche operanti in un contesto bayesiano, concentrandosi in particolare sull'influenza dei valori iniziali sul risultato dell'operazione di stima.

Chapter 2

Modelling of fibre-reinforced composites

Recently, the use of fibre-reinforced composites in high technology applications has dramatically increased. The development of new composite applications, including those based on embedded active materials, has engendered the need for simple and accurate modelling tools to describe their structural behaviour. In particular, both analytical and numerical tools for composite modelling are the subject of ongoing research.

Many laminate theories have been proposed, a number of them describing the composite as a two-dimensional plate or shell structure (see, for example, Carrera, 2002; Carvelli and Savoia, 1997; Ghugal and Shimpi, 2002; Reddy, 1997). Two-dimensional theories are generally simple and require a limited number of parameters, thus they are an ideal basis for the development of numerical solution strategies like the finite element method. On the other hand, reducing a three-dimensional multilayered composite structure to an equivalent single layer leads to a loss of information which might be crucial for the accurate evaluation of the composite behaviour and failure modes. For this reason, it is convenient to formulate the two-dimensional model as descending from a parent three-dimensional theory. This allows to reconstruct some of the three-dimensional quantities by post processing the two-dimensional solution. In Section 2.1, the outlined derivation is carried out for various two-dimensional

theories and the post processing allowing to reconstruct the three-dimensional quantities is discussed.

Once the analytical model has been established, accurate and computationally efficient numerical solution procedures need to be defined. Focusing on the finite element method, in Section 2.2 a new finite element is proposed, based on the First-order Shear Deformation Theory established in Section 2.1. A hybrid stress formulation and a careful selection of the displacement and stress approximations leads to a simple, stable and computationally efficient element and paves the way for the numerical post processing of the two-dimensional finite element solution.

Reconstruction of three-dimensional quantities starting from approximate two-dimensional solutions, such as those obtained via finite elements, is not straightforward. Indeed, problems arise concerning the convergence of the reconstructed quantities and the satisfaction of three-dimensional boundary conditions. A general strategy for the reconstruction of three-dimensional quantities starting from a two-dimensional finite element solution is defined in Section 2.3.

Composites modelling requires the knowledge of the laminate material properties, which are not easily determined via traditional testing methods. For this reason, Section 2.4 deals with the analysis and comparison of numerical-experimental techniques for the estimation of the laminate material properties from natural frequency data.

2.1 Analytical modelling of laminated plates

The modelling of complex and multi-phase materials such as composites can be approached from a variety of points of view. In particular, it is possible to distinguish between micromechanical and macromechanical approaches. In the first case, the different constituents (fibres and matrix) are modelled separately and their interaction is taken into consideration, while in the second some homogenisation technique is employed to reduce the overall composite behaviour to that of a homogeneous equivalent continuum.

The two approaches are fundamentally different in complexity and capability to model the behaviour of composite materials. Micromechanical approaches, though complex, are able to reproduce phenomena, such as fibre slipping, matrix cracking and other mechanisms involving the different constituents, which

cannot be observed in the context of macromechanical models. These, on the other hand, are simple and require the introduction of a limited number of variables, thus they are suitable to model large scale structures with a reasonable computational effort.

A bridge between the two strategies is constituted by the so called multiscale techniques. These strategies allow to jump back and forth between the micro and macromechanical approaches, passing information between the two worlds and observing each phenomenon at the appropriate scale. For the use of multiscale techniques in the analysis of laminated composites, see Ladevèze et al. (2006). In the following, only macroscale models are taken into consideration.

Macromechanical approaches, as already pointed out, model each lamina as a homogeneous material with non isotropic material properties. Low symmetry material models include monoclinic materials, having a single plane of material symmetry, and orthotropic materials, which present three orthogonal planes of material symmetry. Because of the presence of fibres aligned along one or two orthogonal directions, unidirectional and woven fabric laminates are usually modelled as orthotropic materials.

Once the lamina has been established as a homogeneous anisotropic continuum, there still remain various choices on the modelling of the laminated composite. One can distinguish between Equivalent Single Layer (ESL) and layerwise theories. ESL theories are discussed in detail in the following section, a brief account on the idea behind layerwise theories is given here.

As the name suggests, layerwise theories model each lamina, or layer, as a plate (or shell) structural element, then impose interlaminar continuity conditions on the displacements and transverse stresses, thus joining the laminae together. In particular, displacements are assumed to be $\mathcal{C}^0$-continuous in the thickness, with discontinuous derivatives between the laminae, allowing for the presence of discontinuous strains. On the other hand, transverse stresses are set to be continuous between the laminae: this is possible because of the change in constitutive properties, due to the change in material or in the lamina fibre orientation. Partial layerwise theories account for continuous transverse shear stresses across laminae, while full layerwise theories include also the continuity of transverse normal stress. Depending on the assumptions, each layerwise theory yields a different approximation of a full three-dimensional theory, always satisfying interlaminar continuity conditions and thus allowing to properly ac-

count for transverse shear and transverse normal effects. These are necessary to accurately model the behaviour of thick laminates and to predict phenomena occurring at the lamina level, such as delamination.

2.1.1 Equivalent Single Layer theories

Equivalent Single Layer theories model laminated plates as an equivalent single lamina with complex constitutive properties. They are fully two-dimensional models, which are derived by generalising the theories already developed for single layer plates. As such, many ESL theories are present, each originated from a different single layer plate theory and so making different choices as regards the admissible displacement field.

Common to all ESL theories is the loss of interlaminar continuity of transverse stresses. Indeed, in these models the displacement field typical of a single layer plate is postulated for a laminate, which is non homogeneous in the thickness direction. This discrepancy with respect to the three-dimensional description is a drawback of ESL theories with respect to layerwise models, however it can be partially overcome by considering the ESL theory as descending from a parent three-dimensional theory. Indeed, if a structural theory is postulated directly, all information which is not contained in the assumed description is lost. On the other hand, if the theory is established as descending from a parent three-dimensional theory some of this information can be reconstructed in the post processing of the structural theory results.

Plate theories can be derived by considering a three-dimensional body with special shape and partitionability (plate-like body) and setting some restrictions on the admissible deformations. Via the theory of constrained continua, the three-dimensional compatibility, constitutive and equilibrium equations are written based on the defined kinematic ansatz, then the equations for the two-dimensional flat body (plate) can be derived in different ways (DiCarlo et al., 2001; Teresi and Tiero, 1997). Later, once the two-dimensional problem is solved, post processing considerations allow to reconstruct some of the quantities that have been lost in the three-dimensional to two-dimensional mapping.

In particular, crucial to the soundness of the procedure is the concept of reactive stresses (Lembo and Podio-Guidugli, 2007). If the ansatz on the admissible displacements is regarded as internal constraints to the plate-like body,

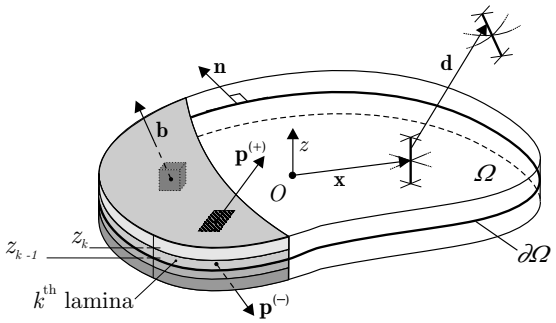

Figure 2.1: Plate-like body

the three-dimensional stress field $\boldsymbol{\sigma}$ decomposes into an active and a reactive part:

$$\boldsymbol{\sigma} = \boldsymbol{\sigma}^{\mathrm{A}} + \boldsymbol{\sigma}^{\mathrm{R}}. \tag{2.1}$$

The active part $\boldsymbol{\sigma}^{\mathrm{A}}$ is related to the deformation via constitutive equations; the reactive part $\boldsymbol{\sigma}^{\mathrm{R}}$ is given the role of maintaining the constraints, while doing no work for each admissible deformation. Thus, reactive stresses can be regarded as reactions to the constraints. The null-working condition can be stipulated pointwise or partwise, with resulting integral conditions corresponding to the peculiar partitionability in plate-like subdomains. It can be easily realised that, when the three-dimensional plate-like body is mapped into the two-dimensional plate model, only active stresses come into play. Thus, $\boldsymbol{\sigma}^{\mathrm{A}}$ is constitutively determined by the solution of the plate problem, while $\boldsymbol{\sigma}^{\mathrm{R}}$ can be selected a posteriori by enforcing the three-dimensional equilibrium equations, in order to improve the approximation the three-dimensional stress field $\boldsymbol{\sigma}$.

In the following, the outlined derivation is briefly carried out for some of the most common plate theories, introducing a common notation. They include the Classical Laminated Plate Theory (CLPT), which is the laminated plate equivalent of Kirchhoff-Love single layer plate theory; the First-order Shear Deformation Theory (FSDT), based on Reissner-Mindlin assumptions; a general higher-order theory and the third-order theory proposed by Reddy (1984).

A plate-like body is a three-dimensional body whose reference shape is a right cylinder of modest height h (Figure 2.1). Let $(x_1, x_2, z) = (\mathbf{x}, z)$ denote the

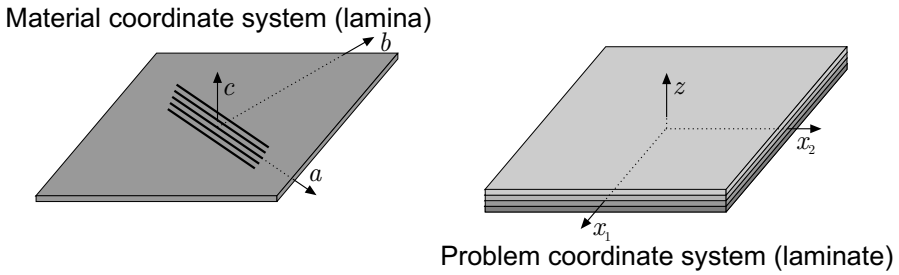

Figure 2.2: Material and problem coordinate systems

coordinates of a point with respect to a Cartesian system with the z-axis parallel to the generators of the cylinder. Notice that the problem coordinate system (x_1, x_2, z) is in general different from the material coordinate system (a, b, c) associated to each lamina. The latter is related to the material symmetry, as depicted in Figure 2.2. The cylinder cross section at $z = 0$ is denoted by Ω, with boundary $\partial\Omega$, while the top and bottom surfaces at $z = \pm h/2$ are denoted by $\Omega^{(+)}$ and $\Omega^{(-)}$, respectively. The typical material fibre is denoted by $\mathcal{F}$ and its undeformed configuration is defined by $(\mathbf{x} = \text{const.}, -h/2 \leq z \leq h/2)$. Body forces $(\mathbf{b}_x, b_z)$ and surface loads $\left(\mathbf{p}_x^{(+)}, p_z^{(+)}\right)$, $\left(\mathbf{p}_x^{(-)}, p_z^{(-)}\right)$ are prescribed inside the body and on the top and bottom surfaces, respectively.

Classical Laminated Plate Theory

In the Classical Laminated Plate Theory, the following kinematic ansatz is made on the admissible displacement field $\mathbf{d}$:

$$\nabla_z^2 \mathbf{d} = \mathbf{0}, \tag{2.2}$$

$$\nabla_z \mathbf{d} \cdot \mathbf{k} = 0, \tag{2.3}$$

$$\nabla_x d_z = -\nabla_z \mathbf{d}_x, \tag{2.4}$$

with $\mathbf{k}$ being the unit vector normal to Ω and ∇_z and ∇_x the derivatives with respect to z and $(x_1,\ x_2)$ respectively. Condition (2.2) states that material fibres $\mathcal{F}$ remain straight after the deformation, while (2.3) precludes fibre extension. Finally, condition (2.4) imposes the orthogonality of the fibres to the deformed middle surface of the plate.

Due to the constraints, $\mathbf{d}$ assumes the form:

$$\mathbf{d} = \begin{bmatrix} \mathbf{u}(\mathbf{x}) - z\nabla_x w(\mathbf{x}) \\ w(\mathbf{x}) \end{bmatrix}, \tag{2.5}$$

where $\mathbf{u}(\mathbf{x})$ and $w(\mathbf{x})$ are the in-plane and transverse displacements of a point belonging to the Ω. Note that the three-dimensional displacement field of the plate-like body is fully defined once $\mathbf{u}$ and w are known. These quantities, called the generalised displacements, are function only of the position of the fibre $\mathcal{F}$, thus the fibre is the minimum unit for the two-dimensional model. The same is true in the other plate theories presented in the following.

The three-dimensional strain tensor $\boldsymbol{\varepsilon}$ can be derived from the compatibility equations:

$$\boldsymbol{\varepsilon} = \begin{bmatrix} \mathbf{e} & \frac{1}{2}\boldsymbol{\gamma} \\ \frac{1}{2}\boldsymbol{\gamma}^{\mathrm{T}} & \varepsilon_z \end{bmatrix}, \quad \boldsymbol{\varepsilon} = \nabla^{(s)}\mathbf{d}, \tag{2.6}$$

where $\nabla^{(s)}$ = sym grad is the compatibility operator, $\mathbf{e}$ is the in-plane strain tensor, $\boldsymbol{\gamma}$ the transverse shear strain vector and ε_z the transverse normal strain. These quantities can be expressed by introducing the generalised strains, which are once again function only of the fibre position $\mathbf{x}$. Introducing the expression for the displacement field, Equation (2.5), into Equation (2.6) we obtain

$$\mathbf{e} = \nabla_x^{(s)}\mathbf{u} - z\nabla_x^{(s)}(\nabla_x w) = \boldsymbol{\mu} + z\boldsymbol{\chi}, \tag{2.7}$$

$$\boldsymbol{\gamma} = \nabla_x w - \nabla_x w = \mathbf{0}, \tag{2.8}$$

$$\varepsilon_z = \nabla_z w = 0, \tag{2.9}$$

where $\boldsymbol{\mu}(\mathbf{x})$ and $\boldsymbol{\chi}(\mathbf{x})$ are the membranal strains and the curvatures, respectively. The physical meaning of the generalised strains is clarified by Figure 2.3, which shows the deformation of a small element under the effect of each generalised strain component.

Note that the transverse normal strain ε_z is null as required by condition (2.3). Also, due to condition (2.4), transverse shear strains $\boldsymbol{\gamma}$ are null in the CLPT. This is a major drawback of this theory, since shearing effects are negligible only for thin plates. The problem is emphasised when modelling laminated composite plates, whose anisotropy renders shear effects even more significant than in single layer isotropic plates.

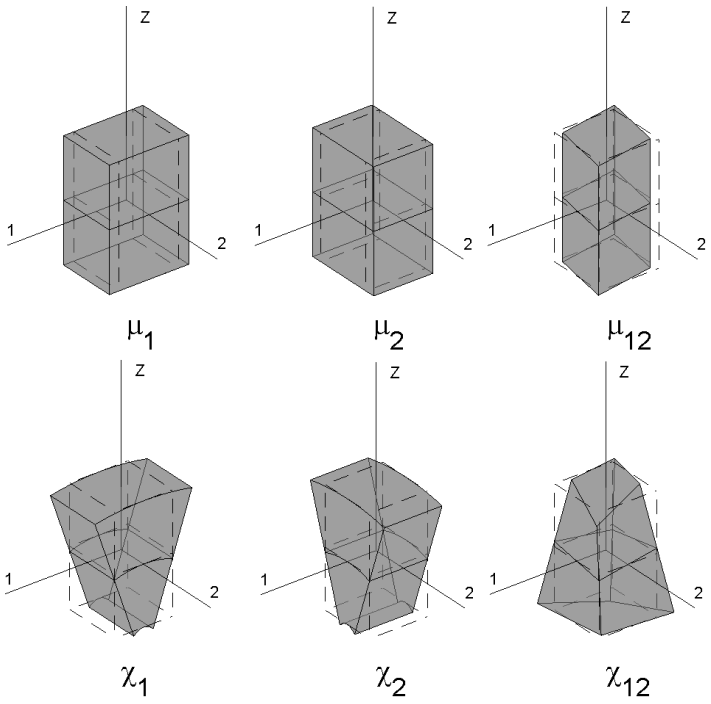

Figure 2.3: Generalised strains for the CLPT

Analogously to the strain tensor, the three-dimensional stress tensor $\boldsymbol{\sigma}$ can be separated into the in-plane stresses $\mathbf{s}$, the transverse shear stresses $\boldsymbol{\tau}$ and the out of plane normal stress σ_z:

$$\boldsymbol{\sigma} = \begin{bmatrix} \mathbf{s} & \boldsymbol{\tau} \\ \boldsymbol{\tau}^{\mathrm{T}} & \sigma_z \end{bmatrix}. \tag{2.10}$$

The three-dimensional equilibrium equations are not influenced by the kinematic ansatz, thus they are common to the derivation of all theories. They do not enter the derivation of the two-dimensional theory but they are crucial in the definition of the reactive stress field. As such, they are not reported here but recalled later in this section, where the post processing of the two-dimensional solution is discussed.

The three-dimensional constitutive relations, relating the active stress to the strain of the constrained plate-like body, are defined for each lamina, which is assumed to be formed by a linearly elastic material having a general monoclinic symmetry, with symmetry plane parallel to Ω. The active transverse stresses are null:

$$\boldsymbol{\tau}^{\mathrm{A}} = \mathbf{0}, \quad \sigma_z^{\mathrm{A}} = 0 \tag{2.11}$$

and the constitutive equations for the k-th lamina are written as:

$$\mathbf{s}^{\mathrm{A}} = \tilde{\mathbf{C}}_m^{(k)} \mathbf{e}, \tag{2.12}$$

where $\tilde{\mathbf{C}}_m^{(k)}$ collects the elastic coefficients of the constrained material, that are, in principle, different from those of the unconstrained material. Using standard arguments of the theory of constrained continua, the constrained elasticity tensor can be put in the common form:

$$\tilde{\mathbf{C}}_m^{(k)} = \mathbf{C}_m^{(k)}, \tag{2.13}$$

where $\mathbf{C}_m^{(k)}$ are the reduced in-plane elastic tensors of the (unconstrained) material of the k-th lamina. The use of the reduced in-plane elastic constants is justified by deriving the constitutive equations via mixed variational methods (Teresi and Tiero, 1997); this derivation allows to reconcile the contrasting assumptions of null strain and null stress in the thickness direction, which is a typical inconsistency of plate theories. Note that only in-plane constitutive equations are reported, as in CLPT transverse strains are null, thus $\boldsymbol{\tau} = \boldsymbol{\tau}^{\mathrm{R}}$ and

$\sigma_z = \sigma_z^{\mathrm{R}}$ and transverse stresses need to be reconstructed via three-dimensional equilibrium in the post processing.

Once the three-dimensional equations for the constrained plate-like body have been established, the three-dimensional body is mapped into the two-dimensional plate by considering the fibre $\mathcal{F}$ as the minimum unit.

The fibre kinematics is described by the generalised displacements and strains, as defined in Equations (2.5) and (2.7).

The two-dimensional equilibrium equations can be obtained by applying the virtual work principle for all admissible displacements consistent with the kinematic assumptions. Then integration by parts and localisation yields the plate balance equations at both internal points

$$\nabla_x \cdot \mathbf{N} + \mathbf{q}_x = \mathbf{0}, \quad \nabla_x \cdot (\nabla_x \cdot \mathbf{M}) + \nabla_x \cdot \mathbf{c} + q_z = 0, \tag{2.14}$$

and boundary points of the flat region Ω, together with the definition of the two-dimensional stress measures and the two-dimensional load descriptors:

$$\mathbf{N} = \int_{\mathcal{F}} \mathbf{s} \mathrm{d}z, \quad \mathbf{M} = \int_{\mathcal{F}} z\mathbf{s} \mathrm{d}z, \tag{2.15}$$

$$\mathbf{q}_x = \int_{\mathcal{F}} \mathbf{b}_x \mathrm{d}z + \left(\mathbf{p}_x^{(+)} + \mathbf{p}_x^{(-)}\right), \ \mathbf{c} = \int_{\mathcal{F}} z\mathbf{b}_x \mathrm{d}z + \frac{h}{2}\left(\mathbf{p}_x^{(+)} - \mathbf{p}_x^{(-)}\right), \tag{2.16}$$

$$q_z = \int_{\mathcal{F}} b_z \mathrm{d}z + p_z^{(+)} + p_z^{(-)}. \tag{2.17}$$

The plate constitutive equations can be determined by substituting the constitutive relations for the constrained material in the form of Equation (2.12) into the definition of the stress resultants:

$$\mathbf{N} = \mathbf{C}_m \boldsymbol{\mu} + \mathbf{C}_{mb} \boldsymbol{\chi}, \tag{2.18}$$

$$\mathbf{M} = \mathbf{C}_{mb} \boldsymbol{\mu} + \mathbf{C}_b \boldsymbol{\chi}, \tag{2.19}$$

where the laminate stiffness matrices are given by

$$\mathbf{C}_m = \sum_k^{n.layers} (z_k - z_{k-1})\, \mathbf{C}_m^{(k)}, \tag{2.20}$$

$$\mathbf{C}_{mb} = \frac{1}{2} \sum_k^{n.layers} \left(z_k^2 - z_{k-1}^2\right) \mathbf{C}_m^{(k)}, \tag{2.21}$$

$$\mathbf{C}_b = \frac{1}{3} \sum_k^{n.layers} \left(z_k^3 - z_{k-1}^3\right) \mathbf{C}_m^{(k)}. \tag{2.22}$$

Notice that the constitutive matrices $\mathbf{C}_m^{(k)}$ for the k-th lamina need to be written in the problem coordinates, thus they are different for laminae made of the same material but with different orientation of the reinforcement. This feature causes the typical coupling of the bending and membrane behaviour via the term $\mathbf{C}_{mb}$, which is zero only if the laminate stacking sequence is symmetric.

As underlined earlier, once the plate problem is solved the active part of the stress is constitutively determined. Then, three-dimensional equilibrium equations can be used to evaluate the reactive part, as discussed later in this section.

First-order Shear Deformation Theory

The First-order shear deformation theory partially overcomes the drawbacks of the Classical Laminated Plate Theory by removing the condition of orthogonality of the fibre with respect to the plate middle surface. Thus, the kinematic ansatz is the following:

$$\nabla_z^2 \mathbf{d} = \mathbf{0}, \tag{2.23}$$

$$\nabla_z \mathbf{d} \cdot \mathbf{k} = 0. \tag{2.24}$$

Since it includes transverse shear deformation, FSDT is more suitable to model moderately thick plates, but yields layerwise constant transverse shear stresses which violate interlaminar equilibrium and may not be acceptable when accurate information on such quantities is required. As in the CLPT, the transverse stresses approximation can be improved by introducing the reactive stress field, as it will be discussed further in this section. Unlike in the Classical Theory,

however, the reconstructed transverse shear stresses can be used to improve iteratively the solution of the two-dimensional problem.

For these reasons, the FSDT constitutes an ideal basis for the development of numerical strategies for the structural analysis of laminated composite plates. Within this context, a new finite element based on a hybrid stress approach is formulated and tested in Section 2.2, while a numerical procedure for the reconstruction of the transverse stresses is presented in Section 2.3.

The FSDT three-dimensional displacement field is the following:

$$\mathbf{d} = \begin{bmatrix} \mathbf{u}(\mathbf{x}) + z\boldsymbol{\theta}(\mathbf{x}) \\ w(\mathbf{x}) \end{bmatrix}. \tag{2.25}$$

Observe that, with respect to the CLPT, the new generalised displacements $\boldsymbol{\theta}$ are introduced: they are the rotations of the fibre with respect to the undeformed configuration.

Three-dimensional strains are expressed as follows:

$$\mathbf{e} = \nabla_x^{(s)}\mathbf{u} + z\nabla_x^{(s)}\boldsymbol{\theta} = \boldsymbol{\mu} + z\boldsymbol{\chi}, \tag{2.26}$$

$$\boldsymbol{\gamma} = \nabla_x w + \boldsymbol{\theta}, \tag{2.27}$$

$$\varepsilon_z = 0. \tag{2.28}$$

Note that, as anticipated, the transverse shear strains are not zero, but they are constant along the fibre. Thus, the generalised strains are $\boldsymbol{\mu}$, $\boldsymbol{\chi}$ and $\boldsymbol{\gamma}$. Moreover, the curvature $\boldsymbol{\chi}$, though having the same role in the definition of the in-plane strain tensor $\mathbf{e}$, assumes a different expression with respect to the CLPT. Figure 2.4 shows the deformation of a small element under the effect of each generalised strain component of the FSDT.

The constitutive relations for each lamina include, besides the in-plane part reported in Equation (2.12), also the transverse shear part:

$$\boldsymbol{\tau}^{\mathrm{A}} = \boldsymbol{\kappa} \odot \mathbf{C}_s^{(k)}\boldsymbol{\gamma}, \tag{2.29}$$

where symbol $\odot$ denotes the product component by component and $\boldsymbol{\kappa}$ contains the so called shear correction factors:

$$\boldsymbol{\kappa} = \begin{bmatrix} \kappa_{11} & \kappa_{12} \\ \kappa_{12} & \kappa_{22} \end{bmatrix}. \tag{2.30}$$

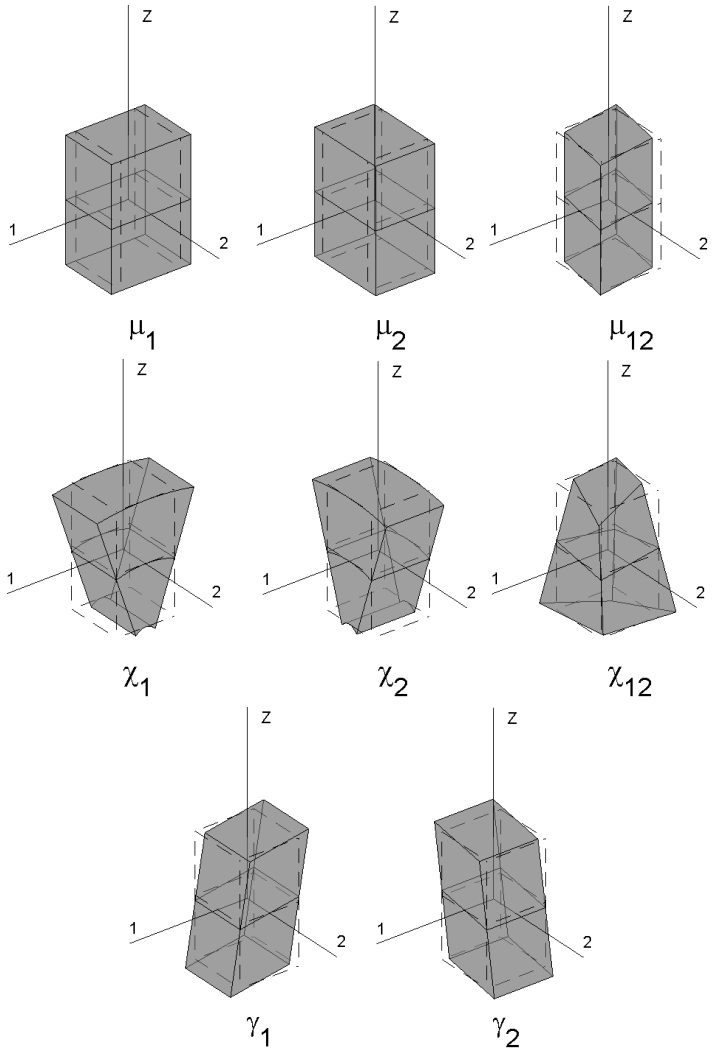

Figure 2.4: Generalised strains for the FSDT

The matrix $\boldsymbol{\kappa}$ naturally arises from the derivation of the constitutive equations via mixed variational methods (Teresi and Tiero, 1997), accounting for the difference between the transverse shear stresses as seen by the three-dimensional and two-dimensional models. Here, $\boldsymbol{\kappa}$ is assumed to be constant along the plate thickness. It should be remarked that the shear correction factors are not known a priori and the usual values $\kappa_{11} = \kappa_{22} = 5/6$ and $\kappa_{12} = 0$ are correct only for homogeneous plates. The shear correction factors are the key of the iterative strategy which can be used in the FSDT to improve the two-dimensional solution. For a laminated plate, they depend upon the stacking sequence and the solution of the problem itself. Once a tentative two-dimensional solution is available, reconstruction of three-dimensional transverse shear stresses allows to update $\boldsymbol{\kappa}$ and the new shear correction factors can be used to solve the two-dimensional problem once again (Auricchio and Sacco, 1999a; Noor et al., 1990). A procedure to evaluate the shear correction factors based on a mixed variational method is discussed later in this section.

Three-dimensional to two-dimensional mapping occurs as in the CLPT. The kinematics is described by the generalised displacements $\mathbf{u}$, w and $\boldsymbol{\theta}$ and the generalised strains $\boldsymbol{\mu}$, $\boldsymbol{\chi}$ and $\boldsymbol{\gamma}$ as defined for the FSDT.

The field two-dimensional equilibrium equations take the following form:

$$\nabla_x \cdot \mathbf{N} + \mathbf{q}_x = \mathbf{0}, \quad \nabla_x \cdot \mathbf{M} - \mathbf{S} + \mathbf{c} = 0, \quad \nabla_x \cdot \mathbf{S} + q_z = 0, \tag{2.31}$$

where symbols are as defined in Equations (2.15) to (2.17) and the transverse shear stress resultant $\mathbf{S}$ is defined as

$$\mathbf{S} = \int_{\mathcal{F}} \boldsymbol{\tau} \mathrm{d}z. \tag{2.32}$$

The in-plane and bending constitutive equations for the FSDT plate are the same as those introduced in CLPT (Equations (2.18) and (2.19)), while the transverse shear constitutive equation is given here:

$$\mathbf{S} \;=\; \mathbf{C}_s \boldsymbol{\gamma}, \tag{2.33}$$

where

$$\mathbf{C}_s \;=\; \boldsymbol{\kappa} \odot \sum_{k}^{n.layers} (z_k - z_{k-1})\, \mathbf{C}_s^{(k)}. \tag{2.34}$$

For further convenience, the inverse relations are also introduced:

$$\boldsymbol{\mu} = \mathbf{F}_m\mathbf{N} + \mathbf{F}_{mb}\mathbf{M}, \tag{2.35}$$

$$\boldsymbol{\chi} = \mathbf{F}_{mb}\mathbf{N} + \mathbf{F}_b\mathbf{M}, \tag{2.36}$$

$$\boldsymbol{\gamma} = \mathbf{F}_s\mathbf{S}. \tag{2.37}$$

As already anticipated, post processing of the two-dimensional solution and evaluation of the reactive stresses assumes a particular significance in the FSDT, as it allows to iteratively update the shear correction factors, thus improving the two-dimensional plate solution. The post processing is discussed later in this section.

Higher-order theories and Reddy's third-order theory

A way to improve the transverse shear stresses obtained in the FSDT model is to loosen the constraint on the in-plane part of the displacement. Thus, the kinematic ansatz of the FSDT is replaced with the following:

$$\nabla_z^n\mathbf{d} = \mathbf{0},\ n > 2, \tag{2.38}$$

$$\nabla_z\mathbf{d}\cdot\mathbf{k} = 0. \tag{2.39}$$

In this case, the fibres do not remain straight but deform according to a polynomial of order $(n-1)$. For this reason, such theories are known as higher-order theories.

A well-known higher-order theory is the third-order theory proposed by Reddy (1984), often referred to with the acronym HSDT (Higher-order Shear Deformation Theory). It is derived from a general third-order theory ($n = 4$ in condition (2.38)) by introducing a further condition on the transverse shear stresses, which are taken to be null at the top and bottom surfaces of the plate. The development of a general higher-order theory and of the HSDT in particular is shown in the following.

The displacement field $\mathbf{d}$ for a general higher-order theory is the following:

$$\mathbf{d} = \begin{bmatrix} \mathbf{u}(\mathbf{x}) + \sum_{m=1}^{n-1} z^m\boldsymbol{\theta}^{(m)}(\mathbf{x}) \\ w(\mathbf{x}) \end{bmatrix}, \tag{2.40}$$

while for Reddy's HSDT it becomes

$$\mathbf{d} = \begin{bmatrix} \mathbf{u}(\mathbf{x}) + z\boldsymbol{\theta}(\mathbf{x}) + cz^3\left[\boldsymbol{\theta}(\mathbf{x}) + \nabla_x w(\mathbf{x})\right] \\ w(\mathbf{x}) \end{bmatrix}. \tag{2.41}$$

Here, $\boldsymbol{\theta}^{(m)}$ are higher-order kinematic parameters, with $\boldsymbol{\theta}^{(1)}$ coinciding with the rotations $\boldsymbol{\theta}$ as defined in the FSDT, $c = -4/\left(3h^2\right)$, where h is the laminate thickness. For a general higher-order theory, the loosened kinematic ansatz increases the range of admissible displacements, thus more generalised displacement parameters are required to describe it. On the other hand, the conditions on the transverse shear stresses imposed by Reddy's HSDT allows to eliminate some of these parameters, leaving only those already present in the FSDT. This is obviously an advantage from the point of view of model complexity, however the extra constraints have significant consequences on the independence of the generalised strains, as discussed in the following.

For higher-order theories, higher-order curvatures $\boldsymbol{\chi}^{(m)}$ and generalised transverse shear strains $\boldsymbol{\gamma}^{(m)}$ are introduced:

$$\mathbf{e} = \nabla_x^{(s)}\mathbf{u} + \sum_{m=1}^{n-1} z^m \nabla_x^{(s)}\boldsymbol{\theta}^{(m)} = \boldsymbol{\mu} + \sum_{m=1}^{n-1} z^m \boldsymbol{\chi}^{(m)}, \tag{2.42}$$

$$\boldsymbol{\gamma} = \nabla_x w + \sum_{m=1}^{n-1} m z^{m-1}\boldsymbol{\theta}^{(m)} = \sum_{m=1}^{n-1} z^{m-1}\boldsymbol{\gamma}^{(m)}. \tag{2.43}$$

Note that $\boldsymbol{\gamma}^{(1)}$ and $\boldsymbol{\chi}^{(1)}$ coincide with the classical transverse shear strains and curvatures, $\boldsymbol{\gamma}$ and $\boldsymbol{\chi}$, as defined in the FSDT. For Reddy's HSDT, on the other hand, we have:

$$\begin{aligned} \mathbf{e} &= \nabla_x^{(s)}\mathbf{u} + z\nabla_x^{(s)}\boldsymbol{\theta} + cz^3\left[\nabla_x^{(s)}\boldsymbol{\theta} + \nabla_x^{(s)}\left(\nabla_x w\right)\right] = \\ &= \boldsymbol{\mu} + z\boldsymbol{\chi}^{(1)} + z^3\boldsymbol{\chi}^{(3)}, \end{aligned} \tag{2.44}$$

$$\boldsymbol{\gamma} = \nabla_x w + \boldsymbol{\theta} + 3cz^2\left(\boldsymbol{\theta} + \nabla_x w\right) = \boldsymbol{\gamma}^{(1)} + z^2\boldsymbol{\gamma}^{(3)}. \tag{2.45}$$

With respect to the FSDT, the third-order curvatures $\boldsymbol{\chi}^{(3)}$ and generalised transverse shear strains $\boldsymbol{\gamma}^{(3)}$ are introduced. However, taking a closer look to the expressions above one realises that $\boldsymbol{\gamma}^{(1)}$ and $\boldsymbol{\gamma}^{(3)}$ are linearly dependent, since they differ only because of the multiplicative constant $3c$. Thus, transverse

shear strains are not made up of a linear and a higher order part, but the fibre $\mathcal{F}$ is constrained to deform according to a third-order polynomial orthogonal to the top and bottom surfaces (because of the condition on null transverse shear stresses on the two surfaces, which reflects on the dual strain components). Also, the higher-order curvatures $\boldsymbol{\chi}^{(3)}$ are linearly dependent on the derivatives of $\boldsymbol{\gamma}^{(1)}$ (as happens also in general higher-order theories). Thus, those introduced are not new and independent parameters (as can be expected, since no new generalised displacement was introduced with respect to the FSDT), but they are deeply intertwined.

For simplicity, the number of generalised strains can be reduced by bringing the constant c out of the definition of the generalised strains. The expressions become:

$$\mathbf{e} = \boldsymbol{\mu} + z\boldsymbol{\chi} + cz^3\boldsymbol{\chi}^{(h)}, \tag{2.46}$$

$$\boldsymbol{\gamma} = \left(1 + 3cz^2\right)\boldsymbol{\gamma}, \tag{2.47}$$

where $\boldsymbol{\mu}$, $\boldsymbol{\chi}$ and $\boldsymbol{\gamma}$ are the same as those defined in the FSDT, and higher-order curvatures $\boldsymbol{\chi}^{(h)}$ are introduced. Figure 2.5 shows the deformation of a small element due to each generalised strain component for Reddy's HSDT. Note that, for what said before, in the elements depicting constant higher order curvatures, linear transverse shear strains are also present.

Differently from the FSDT, the higher-order theories yield transverse shear stresses which are not layerwise constant, thus it is generally thought that such theories do not require shear correction factors. However, as pointed out by Huang (1994), this is not the case for multilayered laminates. Indeed, as already pointed out, interlaminar continuity of transverse shear stresses is not satisfied by any ESL theory, thus shear correction factors involving the difference between constitutively determined and post processed shear stresses can always be defined. These considerations, though included for completeness, are beyond the scope of this work, therefore higher-order theories are here presented without the use of shear correction factors. Thus, the k-th lamina equations become:

$$\mathbf{s}^{\mathrm{A}} = \mathbf{C}_m^{(k)}\mathbf{e}, \quad \boldsymbol{\tau}^{\mathrm{A}} = \mathbf{C}_s^{(k)}\boldsymbol{\gamma}. \tag{2.48}$$

The two-dimensional kinematics is described by the generalised displacements and strains previously introduced. As already mentioned, for Reddy's

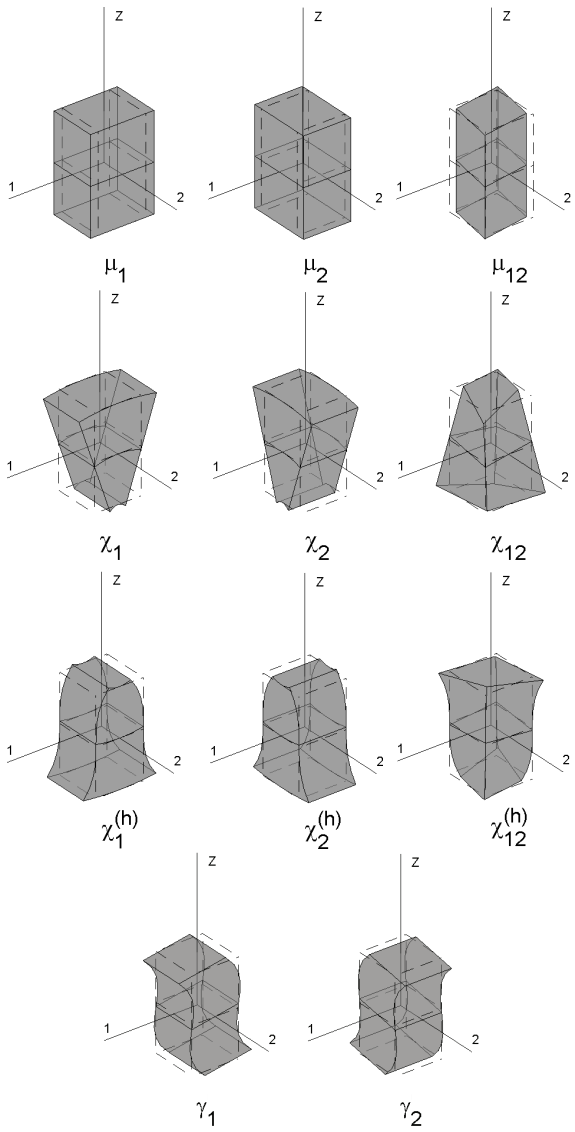

Figure 2.5: Generalised strains for the HSDT

HSDT they are the same ones as for the FSDT, even though the resulting three-dimensional displacement field is different. For higher-order theories, more parameters are introduced.

Two-dimensional field equilibrium equations are as follows for a general higher-order theory:

$$\nabla_x \cdot \mathbf{N} + \mathbf{q}_x = \mathbf{0}, \;\; \nabla_x \cdot \mathbf{S}^{(1)} + q_z = 0, \tag{2.49}$$

$$\nabla_x \cdot \mathbf{M}^{(m)} - \mathbf{S}^{(m)} + \mathbf{c}^{(m)} = 0 \text{ with } 1 \leq m < n, \tag{2.50}$$

where higher-order generalised stresses and load descriptors are introduced as the dual quantities of higher order generalised strains:

$$\mathbf{M}^{(m)} = \int_{\mathcal{F}} z^m \mathbf{s} \mathrm{d}z, \;\; \mathbf{S}^{(m)} = \int_{\mathcal{F}} z^{m-1} \boldsymbol{\tau} \mathrm{d}z, \tag{2.51}$$

$$\mathbf{c}^{(m)} = \int_{\mathcal{F}} z^m \mathbf{b}_x \mathrm{d}z + \left(\frac{h}{2}\right)^m \left[\mathbf{p}_x^{(+)} + (-1)^m \mathbf{p}_x^{(-)}\right]. \tag{2.52}$$

For Reddy's HSDT:

$$\nabla_x \cdot \mathbf{N} + \mathbf{q}_x = \mathbf{0}, \;\; \nabla_x \cdot \mathbf{M} + \nabla_x \cdot \mathbf{M}^{(h)} - \mathbf{S} + \mathbf{c} + \mathbf{c}^{(h)} = \mathbf{0}, \tag{2.53}$$

$$-\nabla_x \cdot \left(\nabla_x \cdot \mathbf{M}^{(h)}\right) + \nabla_x \cdot \mathbf{S} + \nabla_x \cdot \mathbf{c}^{(h)} + q_z = 0, \tag{2.54}$$

where

$$\mathbf{M}^{(h)} = \int_{\mathcal{F}} c z^3 \mathbf{s} \mathrm{d}z, \;\; \mathbf{S} = \int_{\mathcal{F}} \left(1 + 3cz^2\right) \boldsymbol{\tau} \mathrm{d}z, \tag{2.55}$$

$$\mathbf{c}^{(h)} = \int_{\mathcal{F}} c z^3 \mathbf{b}_x \mathrm{d}z + c \left(\frac{h}{2}\right)^3 \left(\mathbf{p}_x^{(+)} - \mathbf{p}_x^{(-)}\right). \tag{2.56}$$

In the same way, two-dimensional constitutive equations contain higher-order terms, whose membrane and bending parts are still coupled:

$$\mathbf{N} = \mathbf{C}_m \boldsymbol{\mu} + \sum_{m=1}^{n-1} \mathbf{C}_{mb}^{(m)} \boldsymbol{\chi}^{(m)}, \tag{2.57}$$

$$\mathbf{M}^{(p)} = \mathbf{C}_{mb}^{(p)} \boldsymbol{\mu} + \sum_{m=1}^{n-1} \mathbf{C}_b^{(p,m)} \boldsymbol{\chi}^{(m)}, \tag{2.58}$$

$$\mathbf{S}^{(p)} = \sum_{m=1}^{n-1} \mathbf{C}_s^{(p,m)} \boldsymbol{\gamma}^{(m)}, \tag{2.59}$$

where the laminate stiffness matrices are given by

$$\mathbf{C}_{mb}^{(m)} = \sum_{k}^{n.layers} \int_{z_{k-1}}^{z_k} z^m \mathbf{C}_m^{(k)}, \tag{2.60}$$

$$\mathbf{C}_{b}^{(p,m)} = \sum_{k}^{n.layers} \int_{z_{k-1}}^{z_k} z^{m+p} \mathbf{C}_m^{(k)}, \tag{2.61}$$

$$\mathbf{C}_{s}^{(p,m)} = \sum_{k}^{n.layers} \int_{z_{k-1}}^{z_k} z^{m+p-2} \mathbf{C}_s^{(k)}. \tag{2.62}$$

For Reddy's HSDT:

$$\mathbf{N} = \mathbf{C}_m \boldsymbol{\mu} + \mathbf{C}_{mb} \boldsymbol{\chi} + \mathbf{C}_{mb}^{(h)} \boldsymbol{\chi}^{(h)}, \tag{2.63}$$

$$\mathbf{M} = \mathbf{C}_{mb} \boldsymbol{\mu} + \mathbf{C}_b \boldsymbol{\chi} + \mathbf{C}_{bb}^{(h)} \boldsymbol{\chi}^{(h)}, \tag{2.64}$$

$$\mathbf{M}^{(h)} = \mathbf{C}_{mb}^{(h)} \boldsymbol{\mu} + \mathbf{C}_{bb}^{(h)} \boldsymbol{\chi} + \mathbf{C}_b^{(h)} \boldsymbol{\chi}^{(h)}, \tag{2.65}$$

$$\mathbf{S} = \mathbf{C}_s^{(h)} \boldsymbol{\gamma}, \tag{2.66}$$

where

$$\mathbf{C}_{mb}^{(h)} = \sum_{k}^{n.layers} \int_{z_{k-1}}^{z_k} c z^3 \mathbf{C}_m^{(k)}, \tag{2.67}$$

$$\mathbf{C}_{bb}^{(h)} = \sum_{k}^{n.layers} \int_{z_{k-1}}^{z_k} c z^4 \mathbf{C}_m^{(k)}, \tag{2.68}$$

$$\mathbf{C}_{b}^{(h)} = \sum_{k}^{n.layers} \int_{z_{k-1}}^{z_k} c^2 z^6 \mathbf{C}_m^{(k)}, \tag{2.69}$$

$$\mathbf{C}_{s}^{(h)} = \sum_{k}^{n.layers} \int_{z_{k-1}}^{z_k} \left(1 + 3cz^2\right)^2 \mathbf{C}_s^{(k)}. \tag{2.70}$$

As in the previous cases, post processing allows to reconstruct reactive stresses from three-dimensional equilibrium. In particular, for a n-th order theory, n-th order in-plane stresses yield $(n+1)$-th order transverse shear stresses.

Transverse refinement

The higher-order theories described in the previous paragraph introduce a polynomial refinement of the in-plane displacement in order to enrich the FSDT

kinematic hypothesis. A different possibility is to improve the transverse displacement by relaxing the kinematic ansatz on the fibre extension, that is to say

$$\nabla_z \mathbf{d} \cdot \mathbf{k} \neq 0. \tag{2.71}$$

The in-plane part of the displacement field $\mathbf{d}$ can be chosen according to the FSDT or any of the higher-order theories previously described, while the transverse part becomes

$$d_z = w(\mathbf{x}) + \sum_{m=1}^{n} z^m w^{(m)}(\mathbf{x}). \tag{2.72}$$

The full derivation of the two-dimensional theory proceeds as usual and it is not reported here. Instead, a few comments are given on the consequences of introducing a transverse refinement.

Differently from in-plane refinement, indeed, transverse refinement leads to non zero transverse normal strain:

$$\varepsilon_z = \sum_{m=1}^{n} m z^{m-1} w^{(m)} = \sum_{m=1}^{n} z^{m-1} \varepsilon_z^{(m)}. \tag{2.73}$$

As a consequence, constitutive equations for the transverse normal stress and strain components need to be introduced. Moreover, work-conjugate stress resultants involving the transverse normal stress σ_z arise, defined as

$$S_z^{(m)} = \int_{\mathcal{F}} z^{m-1} \sigma_z \mathrm{d}z. \tag{2.74}$$

From the previous equation, it is clear that this type of refinement allows the transverse normal stress σ_z to play an active role in the two-dimensional plate model. Thus, differently from all the models discussed previously, we have $\sigma_z^{\mathrm{A}} \neq 0$. Still, the two-dimensional stress representation could be improved in the post processing by introducing the reactive stresses.

Reconstruction of the transverse stresses

The decomposition of the three-dimensional stress field $\boldsymbol{\sigma}$ into an active and a reactive part can be used to improve the approximation of the stress field, once the solution of the two-dimensional problem has been obtained. Indeed, while

the active stresses $\boldsymbol{\sigma}^{\mathrm{A}}$ are constitutively determined by the two-dimensional solution, the reactive stresses $\boldsymbol{\sigma}^{\mathrm{R}}$ can be selected by enforcing the three-dimensional equilibrium equations. This reconstruction procedure can be carried out for every ESL theory, however it gains a particular significance in the FSDT theory, as the reconstructed stresses can be used to iteratively evaluate the shear correction factors.

The local three-dimensional equilibrium conditions are given by

$$\mathrm{div}\boldsymbol{\sigma} + \mathbf{b} = \mathbf{0}, \tag{2.75}$$

or by the following extended form:

$$\nabla_x \cdot \mathbf{s} + \nabla_z \boldsymbol{\tau} + \mathbf{b}_x = \mathbf{0}, \tag{2.76}$$

$$\nabla_x \cdot \boldsymbol{\tau} + \nabla_z \sigma_z + b_z = 0. \tag{2.77}$$

By assuming the in-plane stresses $\mathbf{s}$ as completely constitutively determined ($\mathbf{s} = \mathbf{s}^{\mathrm{A}}$, $\mathbf{s}^{\mathrm{R}} = \mathbf{0}$), Equation (2.76) can be used to determine the transverse shear stresses:

$$\boldsymbol{\tau}(z) = -\mathbf{p}_x^{(-)} - \int_{-\frac{h}{2}}^{z} (\nabla_x \cdot \mathbf{s} + \mathbf{b}_x)\,\mathrm{d}z, \tag{2.78}$$

then Equation (2.77) allows to evaluate the transverse normal stress:

$$\sigma_z(z) = -p_z^{(-)} - \int_{-\frac{h}{2}}^{z} (\nabla_x \cdot \boldsymbol{\tau} + b_z)\,\mathrm{d}z. \tag{2.79}$$

Notice that the above solutions have been given directly in terms of total stresses (sum of active and reactive parts), as is usual for the technical literature.

As it was already anticipated, the outlined reconstruction procedure can be applied to any ESL theory. In CLPT, transverse deformations are null due to the kinematic hypothesis introduced, thus the transverse stresses consist of the sole reactive part:

$$\boldsymbol{\tau}^{\mathrm{CLPT}} = \boldsymbol{\tau}^{\mathrm{R}}, \quad \sigma_z^{\mathrm{CLPT}} = \sigma_z^{\mathrm{R}}. \tag{2.80}$$

In this case, the reconstruction procedure can be used to obtain a better approximation of the three-dimensional stress field but it does not influence the two-dimensional plate solution. In FSDT, on the other hand, the transverse shear term appears in the two-dimensional equations, thus

$$\boldsymbol{\tau}^{\mathrm{FSDT}} = \boldsymbol{\tau}^{\mathrm{A}} + \boldsymbol{\tau}^{\mathrm{R}}, \quad \sigma_z^{\mathrm{FSDT}} = \sigma_z^{\mathrm{R}}. \tag{2.81}$$

The reconstructed transverse shear stress profiles can be used to iteratively evaluate the shear correction factors (2.30), allowing to improve the two-dimensional plate solution.

In order to ensure consistency with both the three-dimensional and two-dimensional models, the reconstructed transverse stresses should satisfy the boundary conditions on the top and bottom surfaces of the plate-like body:

$$\boldsymbol{\tau}\left(-\frac{h}{2}\right) = -\mathbf{p}_x^{(-)},\ \boldsymbol{\tau}\left(\frac{h}{2}\right) = \mathbf{p}_x^{(+)}, \tag{2.82}$$

$$\sigma_z\left(-\frac{h}{2}\right) = -p_z^{(-)},\ \sigma_z\left(\frac{h}{2}\right) = p_z^{(+)}. \tag{2.83}$$

Moreover, in FSDT, the reconstructed transverse shear stresses should satisfy the static equivalence condition, Equation (2.32). It is proven in the following that, if the stress resultants $\mathbf{N}$, $\mathbf{M}$ and $\mathbf{S}$ satisfy the plate equilibrium equations, Equation (2.31), then the transverse stresses as determined by Equations (2.78) and (2.79) meet all the aforementioned conditions.

Proof. The first of conditions (2.82) is trivially met. To verify the second, one can simply evaluate $\boldsymbol{\tau}$ at the top surface:

$$\begin{aligned}\boldsymbol{\tau}\left(\frac{h}{2}\right) &= -\mathbf{p}_x^{(-)} - \int_{-\frac{h}{2}}^{\frac{h}{2}} (\nabla_x \cdot \mathbf{s} + \mathbf{b}_x)\,\mathrm{d}z = \\ &= -\mathbf{p}_x^{(-)} - \nabla_x \cdot \int_{\mathcal{F}} \mathbf{s}\mathrm{d}z - \int_{\mathcal{F}} \mathbf{b}_x \mathrm{d}z.\end{aligned} \tag{2.84}$$

Using Equations (2.15) and (2.16) yields

$$\boldsymbol{\tau}\left(\frac{h}{2}\right) = -\nabla_x \cdot \mathbf{N} - \mathbf{q}_x + \mathbf{p}_x^{(+)}. \tag{2.85}$$

Thus, if membrane forces satisfy pointwise the plate equilibrium conditions (2.31), the second of conditions (2.82) is met.

To prove the static equivalence condition (2.32), we can multiply the three-dimensional equilibrium condition (2.76) by z and integrate it along the thickness:

$$\int_{\mathcal{F}} z\nabla_x \cdot \mathbf{s}\mathrm{d}z + \int_{\mathcal{F}} z\nabla_z \boldsymbol{\tau}\mathrm{d}z + \int_{\mathcal{F}} z\mathbf{b}_x \mathrm{d}z = 0. \tag{2.86}$$

Integrating by parts the second term and recalling Equations (2.15) and (2.16) lead to

$$\nabla_x \cdot \mathbf{M} - \int_{\mathcal{F}} \boldsymbol{\tau} \mathrm{d}z + \frac{h}{2}\left[\boldsymbol{\tau}\left(\frac{h}{2}\right) + \boldsymbol{\tau}\left(-\frac{h}{2}\right)\right] + \mathbf{c} - \frac{h}{2}\left(\mathbf{p}_x^{(+)} - \mathbf{p}_x^{(-)}\right) = 0. \quad (2.87)$$

Therefore, since $\boldsymbol{\tau}$ satisfies the equilibrium conditions on the top and bottom surfaces, if the internal moments $\mathbf{M}$ satisfy the plate equilibrium conditions (2.31), then it follows

$$\mathbf{S} - \int_{\mathcal{F}} \boldsymbol{\tau} \mathrm{d}z = \mathbf{0}. \quad (2.88)$$

As regards the boundary conditions for σ_z, while the first of conditions (2.83) is again trivial, the second can be verified by evaluating σ_z at the top laminate surface:

$$\begin{aligned} \sigma_z\left(\frac{h}{2}\right) &= -p_z^{(-)} - \int_{-\frac{h}{2}}^{\frac{h}{2}} \left(\nabla_x \cdot \boldsymbol{\tau} + b_z\right) \mathrm{d}z = \\ &= -p_z^{(-)} - \nabla_x \cdot \int_{\mathcal{F}} \boldsymbol{\tau} \mathrm{d}z - \int_{\mathcal{F}} b_z \mathrm{d}z. \end{aligned} \quad (2.89)$$

Using Equations (2.32) and (2.17) yields

$$\sigma_z\left(\frac{h}{2}\right) = -\nabla_x \cdot \mathbf{S} - q_z + p_z^{(+)}. \quad (2.90)$$

Thus, if the third of Equations (2.31) is pointwise satisfied, the boundary condition for σ_z on the top laminate surface is met. □

Once the transverse shear stress profiles are known, shear correction factors can be determined by enforcing the stationarity of the Hellinger-Reissner functional with respect to $\mathbf{N}$, $\mathbf{M}$ and $\mathbf{S}$ (Teresi and Tiero, 1997). Focusing the attention on the transverse shear term per unit area, we have:

$$\int_{\mathcal{F}} \left(\mathbf{F}_s^{(k)} \boldsymbol{\tau} - \boldsymbol{\gamma}\right) \delta\boldsymbol{\tau} \mathrm{d}z, \quad (2.91)$$

where $\boldsymbol{\tau}$ is to be intended as the total three-dimensional transverse shear stress. This stress term can be represented in the general form

$$\boldsymbol{\tau} = \mathbf{g}_h\left(z\right) \odot \mathbf{S}\left(\mathbf{x}\right) + \mathbf{g}_p\left(z, \mathbf{x}\right), \quad (2.92)$$

where $\mathbf{g}_h$ collects piecewise shape functions defining the shear stress profiles in the thickness and vanishing on the upper and lower faces and $\mathbf{g}_p$ collects null average functions on the thickness, accounting for the actual equilibrium conditions on the two faces.

Substituting Equation (2.92) into Equation (2.91) and making it stationary with respect to $\mathbf{S}$ yields

$$\mathbf{F}_s\mathbf{S} - \boldsymbol{\gamma} + \boldsymbol{\gamma}_0 = \mathbf{0}, \tag{2.93}$$

which defines the transverse shear flexibility response of the laminate, where

$$\mathbf{F}_s = \mathbf{C}_s^{-1} = \int_{\mathcal{F}} (\mathbf{g}_h \otimes \mathbf{g}_h) \odot \mathbf{F}_s^{(k)} \mathrm{d}z, \tag{2.94}$$

$$\boldsymbol{\gamma}_0 = \int_{\mathcal{F}} \left(\mathbf{F}_s^{(k)}\mathbf{g}_p\right) \odot \mathbf{g}_h \mathrm{d}z, \tag{2.95}$$

being $\otimes$ the dyadic product. Notice that, as observed by Teresi and Tiero (1997), the resulting configuration of the plate is not natural, since $\boldsymbol{\gamma}_0$ is in general different from zero, although the parent plate-like body has been supposed in a natural configuration. However, in practice, this term is generally not considered, since $\mathbf{g}_p$ in Equation (2.92) is set to zero according to the classical FSDT stress hypothesis, stating that transverse shear stress components vanish on the upper and lower faces. This is simply a different manner to mimic the three-dimensional behaviour, which does not imply any variational crime since the above procedure is of mixed type and Equation (2.92) is not required to necessarily satisfy all the equilibrium conditions. A discussion on the influence of non homogeneous conditions can be found in the paper by Carrera (2007).

Considering Equations (2.29) and (2.94) permits to compute the shear correction factors, once $\boldsymbol{\tau}$ has been reconstructed starting from the plate solution. Unfortunately, as already noted, the solution itself depends on the shear factors, so that their computation results in a non linear problem. A successful strategy to tackle this problem is to select some tentative values for the shear factors, for example those for homogeneous plates, and use them to start an iterative predictor-corrector procedure, as suggested by Auricchio and Sacco (1999a) and Noor et al. (1990).

2.2 A hybrid-stress finite element for laminated plates

The Equivalent Single Layer theories described in the previous section are the most common tool for the analysis of laminated composite plates. In particular, the FSDT is often favoured as a simple yet accurate description of the three-dimensional plate-like body behaviour, especially when used in conjunction with the transverse stresses reconstruction and iterative evaluation of the shear correction factors. For these reasons, the FSDT is an ideal basis for the development of numerical solution strategies, such as the finite element method.

Several laminated plate finite elements were developed in the last decades (see among others Alfano et al. (2001); Auricchio et al. (2001); Auricchio and Sacco (1999a, 2003); Auricchio et al. (1999, 2006); Cazzani et al. (2005); Cen et al. (2002); Kim and Cho (2007)) based on FSDT. The basic features of a competitive element are: simplicity, computational efficiency and accuracy. In particular, the element should not suffer from shear locking or other pathologies, such as spurious kinematic modes or parasitic shear stresses. Moreover, it should be accompanied by an effective procedure to reconstruct the three-dimensional transverse stresses through the laminate thickness. Based on these desirable features and starting from the element earlier formulated by Auricchio and Taylor (1994) for single layer isotropic plates, Auricchio and Sacco (1999a) developed a four node mixed-enhanced laminated plate finite element, recently extended to treat monoclinic laminae (Auricchio et al., 2006). Alfano et al. (2001), on the other hand, generalised the well known MITC finite element (Bathe, 1996) to laminated composite plates. Both the approaches were proposed in conjunction with a procedure to update the shear correction factors and to reconstruct the transverse stress profiles, based on three-dimensional equilibrium. In the following, a new finite element for laminated plates is proposed based on a hybrid stress approach, while a numerical strategy for the post processing of the finite element solution is discussed in Section 2.3.

A new quadrilateral four node finite element for laminated plates with general monoclinic laminae is developed in this section, based on the FSDT as derived in Section 2.1.1 (Daghia et al., 2008). A hybrid stress formulation is adopted by generalising the one presented by de Miranda and Ubertini (2006) for single layer isotropic plates. In particular, the formulation is rewritten to

include the membrane-bending coupling typical of laminated plates. The new element is designed to be simple, free of locking and readily implementable into existing finite element codes. To this purpose, the transverse displacement approximation is enhanced via the so called linked interpolation, which includes nodal rotation parameters through higher-order interpolation functions. Moreover, an approximation which is a priori equilibrated within each element is assumed for both membrane and bending-shear stress resultants. It is ruled by the minimum number of parameters for element stability, which are eliminated at the element level. The resulting element has four nodes, five degrees of freedom per node and involves only compatible displacement functions. It is locking-free, passes all the patch tests and exhibits little sensitivity to geometric distortions. It should be noted that the equilibrated stress assumption, besides being a key point of the element formulation, acquires a special importance in view of the reconstruction of the transverse stress profiles, as discussed in Section 2.3.

Note that, in the following, tensorial notation is abandoned and matrix notation is used instead, as is common for finite element derivation.

2.2.1 Hybrid stress formulation

The mixed variational formulation of the FSDT stems from the stationarity condition for the Hellinger-Reissner functional:

$$\begin{aligned}\Pi_{HR}= -\frac{1}{2}\int_\Omega \left[\mathbf{N}^{\mathrm{T}}\left(\mathbf{F}_m\mathbf{N}+\mathbf{F}_{mb}\mathbf{M}\right)+\mathbf{M}^{\mathrm{T}}\left(\mathbf{F}_{mb}\mathbf{N}+\mathbf{F}_b\mathbf{M}\right)+\mathbf{S}^{\mathrm{T}}\mathbf{F}_s\mathbf{S}\right]\mathrm{d}\Omega+\\ +\int_\Omega\left[\mathbf{N}^{\mathrm{T}}\mathbf{D}_m\mathbf{u}+\mathbf{M}^{\mathrm{T}}\mathbf{D}_m\boldsymbol{\theta}+\mathbf{S}^{\mathrm{T}}\left(\mathbf{D}_s w+\boldsymbol{\theta}\right)\right]\mathrm{d}\Omega-\Pi_{ext},\end{aligned} \tag{2.96}$$

where Π_{ext} is the work done by external loads, $\mathbf{D}_m$ and $\mathbf{D}_s$ are differential operators. Assuming that $\mathbf{N}$, $\mathbf{M}$ and $\mathbf{S}$ satisfy a priori the plate equilibrium equations, the mixed functional Π_{HR} reduces to the following hybrid stress functional:

$$\begin{aligned}\Pi_{HY}= -\frac{1}{2}\int_\Omega \left[\mathbf{N}^{\mathrm{T}}\left(\mathbf{F}_m\mathbf{N}+\mathbf{F}_{mb}\mathbf{M}\right)+\mathbf{M}^{\mathrm{T}}\left(\mathbf{F}_{mb}\mathbf{N}+\mathbf{F}_b\mathbf{M}\right)+\mathbf{S}^{\mathrm{T}}\mathbf{F}_s\mathbf{S}\right]\mathrm{d}\Omega+\\ +\int_{\partial\Omega}\left(\mathbf{u}^{\mathrm{T}}\mathbf{n}_m^{\mathrm{T}}\mathbf{N}+\boldsymbol{\theta}^{\mathrm{T}}\mathbf{n}_m^{\mathrm{T}}\mathbf{M}+w\mathbf{n}_s^{\mathrm{T}}\mathbf{S}\right)\mathrm{d}\left(\partial\Omega\right)-\hat{\Pi}_{ext},\end{aligned} \tag{2.97}$$

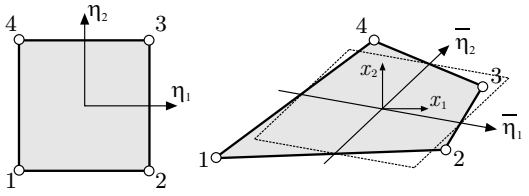

Figure 2.6: Coordinate systems for the plate element

where $\hat{\Pi}_{ext}$ is the work done by external boundary loads, $\mathbf{n}_m$ and $\mathbf{n}_s$ contain the components of the outward normal to the boundary $\partial\Omega$:

$$\mathbf{n}_m = \begin{bmatrix} n_1 & 0 \\ 0 & n_2 \\ n_2 & n_1 \end{bmatrix}, \quad \mathbf{n}_s = \begin{bmatrix} n_1 \\ n_2 \end{bmatrix}. \tag{2.98}$$

The hybrid stress functional Π_{HY}, involving both stress resultants and generalised displacements as independent variables, is the variational support for the subsequent development of the finite element scheme. Notice that in the discretised version of functional (2.97): (i) stress resultants are required to satisfy the plate equilibrium equations within each element Ω_e and can be discontinuous across element boundaries $\partial\Omega_e$, (ii) generalised displacements are active only on the element boundaries $\partial\Omega_e$ and are required to be continuous across them.

2.2.2 Finite element assumptions

Geometry description

The element geometry is represented based on a four node scheme. The transformation between the local Cartesian coordinates (x_1, x_2) and the natural coordinates (η_1, η_2) (see Figure 2.6) is given by

$$x_i = a_{1i}\eta_1 + a_{2i}\eta_1\eta_2 + a_{3i}\eta_2, \tag{2.99}$$

where

$$\begin{bmatrix} a_{1i} \\ a_{2i} \\ a_{3i} \end{bmatrix} = \frac{1}{4} \begin{bmatrix} -1 & 1 & 1 & -1 \\ 1 & -1 & 1 & -1 \\ -1 & -1 & 1 & 1 \end{bmatrix} \begin{bmatrix} x_{i1} \\ x_{i2} \\ x_{i3} \\ x_{i4} \end{bmatrix}, \tag{2.100}$$

being x_{ij} the local coordinates of the jth corner.

For later convenience, a skew coordinate system $(\bar{\eta}_1, \bar{\eta}_2)$ is introduced as follows:

$$\bar{\eta}_1 = \eta_1 + \frac{j_2}{j_0}\eta_1\eta_2, \;\; \bar{\eta}_2 = \eta_2 + \frac{j_1}{j_0}\eta_1\eta_2, \tag{2.101}$$

where

$$j_0 = a_{11}a_{32} - a_{12}a_{31}, \;\; j_1 = a_{11}a_{22} - a_{12}a_{21}, \;\; j_2 = a_{21}a_{32} - a_{22}a_{31}. \tag{2.102}$$

Assumed generalised displacements

In order to avoid locking, the displacement interpolation for w needs to be enriched with respect to that used for $\boldsymbol{\theta}$. For this reason, the interpolation for $\mathbf{u}$ and $\boldsymbol{\theta}$ is simply bilinear, ruled by the standard nodal degrees of freedom $\mathbf{q}_u$ and $\mathbf{q}_\theta$, while the interpolation for w, bilinear in the transverse nodal displacements $\mathbf{q}_w$, is enriched with higher order functions ruled by the nodal rotations $\mathbf{q}_\theta$ (linked interpolation):

$$\mathbf{u} = \mathbf{U}_u\mathbf{q}_u, \;\; \boldsymbol{\theta} = \mathbf{U}_\theta\mathbf{q}_\theta, \;\; w = \mathbf{U}_w\mathbf{q}_w + \mathbf{L}\mathbf{q}_\theta. \tag{2.103}$$

This allows to improve the interpolation for w without introducing additional kinematic degrees of freedom.

Matrices $\mathbf{U}_\bullet$ collect the standard four node shape functions:

$$U_i = \frac{1}{4}\left(1 + \eta_{1i}\eta_1\right)\left(1 + \eta_{2i}\eta_2\right), \tag{2.104}$$

being η_{1i} and η_{2i} the natural coordinates at node i.

The higher order part is defined as follows:

$$\mathbf{L}\mathbf{q}_\theta = -\sum_{i=1}^{4} \hat{L}_i l_i \left(\theta^2_{ni} - \theta^1_{ni}\right), \tag{2.105}$$

where l_i is the length of side i, θ^1_{ni} and θ^2_{ni} are the components of the rotation in the direction normal to side i at its two ends, respectively, and $\hat{L}_i$ are edge bubble functions defined as

$$\hat{L}_i = \frac{1}{16}\left[1+(1-\delta_{i4})\,\eta_1\right]\left[1-(1-\delta_{i2})\,\eta_1\right]\left[1+(1-\delta_{i1})\,\eta_2\right]\left[1-(1-\delta_{i3})\,\eta_2\right], \tag{2.106}$$

where δ_{ij} is the Kronecker delta.

Note that the above interpolation leads to constant transverse shear strains along each side of the element. However, this is generally not sufficient to remove locking due to interior inconsistency and shear strains need to be accommodated in the element interior using, for example, internal bubble functions (Auricchio and Sacco, 1999a; Auricchio et al., 2006). In the present formulation these additional degrees of freedom are not necessary since the displacements actually play their role only on the element boundary.

Assumed stress resultants

The stress resultants are approximated independently on each element and such to satisfy the plate equilibrium equations pointwise within the element. Using the skew coordinates $\bar{\eta}_1$, $\bar{\eta}_2$, the resultant moments $\mathbf{M}$ and shear forces $\mathbf{S}$ are assumed as suggested by de Miranda and Ubertini (2006) for the 9βQ4 element:

$$\begin{bmatrix} \mathbf{M} \\ \mathbf{S} \end{bmatrix} = \left[\begin{array}{ccccc|cccc} 1 & 0 & 0 & a_{11}^2\bar{\eta}_2 & a_{31}^2\bar{\eta}_1 & a_{11}\bar{\eta}_1 a_{31}\bar{\eta}_2 & 0 & a_{11}^2\bar{\eta}_1\bar{\eta}_2 & a_{31}^2\bar{\eta}_1\bar{\eta}_2 \\ 0 & 1 & 0 & a_{12}^2\bar{\eta}_2 & a_{32}^2\bar{\eta}_1 & 0 & a_{12}\bar{\eta}_1 a_{32}\bar{\eta}_2 & a_{12}^2\bar{\eta}_1\bar{\eta}_2 & a_{32}^2\bar{\eta}_1\bar{\eta}_2 \\ 0 & 0 & 1 & a_{11}a_{12}\bar{\eta}_2 & a_{31}a_{32}\bar{\eta}_1 & 0 & 0 & a_{11}a_{12}\bar{\eta}_1\bar{\eta}_2 & a_{31}a_{32}\bar{\eta}_1\bar{\eta}_2 \\ \hline 0 & 0 & 0 & 0 & 0 & 1 & 0 & a_{11}\bar{\eta}_2 & a_{31}\bar{\eta}_1 \\ 0 & 0 & 0 & 0 & 0 & 0 & 1 & a_{12}\bar{\eta}_2 & a_{32}\bar{\eta}_1 \end{array}\right] \begin{bmatrix} \boldsymbol{\beta}_b \\ \boldsymbol{\beta}_s \end{bmatrix}, \tag{2.107}$$

and the membrane forces $\mathbf{N}$ as suggested by Yuan et al. (1993):

$$\mathbf{N} = \begin{bmatrix} 1 & 0 & 0 & a_{11}^2\bar{\eta}_2 & a_{31}^2\bar{\eta}_1 \\ 0 & 1 & 0 & a_{12}^2\bar{\eta}_2 & a_{32}^2\bar{\eta}_1 \\ 0 & 0 & 1 & a_{11}a_{12}\bar{\eta}_2 & a_{31}a_{32}\bar{\eta}_1 \end{bmatrix} \boldsymbol{\beta}_m, \tag{2.108}$$

where parameters $\boldsymbol{\beta}_m$, $\boldsymbol{\beta}_b$ and $\boldsymbol{\beta}_s$ are local to each element. The above approximations are proved to satisfy pointwise the plate equilibrium equations in the homogeneous form. According to de Miranda and Ubertini (2006), the presence of field loads can be taken into account by a particular solution $(\mathbf{N}_p, \mathbf{M}_p, \mathbf{S}_p,)$ of the plate equilibrium equations. Therefore, the final approximation can be written in compact form as

$$\mathbf{N} = \mathbf{P}_m\boldsymbol{\beta}_m + \mathbf{N}_p, \quad \mathbf{M} = \mathbf{P}_b\boldsymbol{\beta}_b + \mathbf{P}_{bs}\boldsymbol{\beta}_s + \mathbf{M}_p, \quad \mathbf{S} = \mathbf{P}_s\boldsymbol{\beta}_s + \mathbf{S}_p. \tag{2.109}$$

In the case of general loading ($\mathbf{q}_x^{\mathrm{T}} = [q_1,\, q_2]$, $\mathbf{c}^{\mathrm{T}} = [c_1,\, c_2]$, q_z), the particular solution ($\mathbf{N}_p$, $\mathbf{M}_p$, $\mathbf{S}_p$) can be chosen as

$$\mathbf{N}_p = \begin{bmatrix} -\displaystyle\int_0^{x_1} q_1 \mathrm{d}x_1 \\ -\displaystyle\int_0^{x_2} q_2 \mathrm{d}x_2 \\ 0 \end{bmatrix}, \tag{2.110}$$

$$\mathbf{M}_p = \begin{bmatrix} \displaystyle\int_0^{x_1} (S_{1p} - c_1)\,\mathrm{d}x_1 \\ \displaystyle\int_0^{x_2} (S_{2p} - c_2)\,\mathrm{d}x_2 \\ 0 \end{bmatrix}, \; \mathbf{S}_p = -\frac{1}{2}\begin{bmatrix} \displaystyle\int_0^{x_1} q_z \mathrm{d}x_1 \\ \displaystyle\int_0^{x_2} q_z \mathrm{d}x_2 \end{bmatrix}. \tag{2.111}$$

This expression has been adopted for the numerical tests.

It should be emphasised that the chosen approximation is optimal in the sense that it involves the minimum number of $\boldsymbol{\beta}$ parameters while providing element stability, i.e. without introducing any zero energy mode.

2.2.3 Finite element equations

Introducing the above assumptions in the hybrid stress functional (2.97) referred to the single element and making it stationary yield the following discrete ele-

ment equations:

$$\left[\begin{array}{c:c} \mathbf{H} & \mathbf{G} \\ \hdashline \mathbf{G}^{\mathrm{T}} & \mathbf{0} \end{array}\right] \left[\begin{array}{c} \boldsymbol{\beta} \\ \hdashline \mathbf{q} \end{array}\right] = \left[\begin{array}{c} \mathbf{g} \\ \hdashline \mathbf{h} \end{array}\right], \tag{2.112}$$

where

$$\mathbf{H} = \begin{bmatrix} \mathbf{H}_m^m & \mathbf{H}_{sm}^{mb} & \mathbf{H}_{bm}^{mb} \\ \left(\mathbf{H}_{sm}^{mb}\right)^{\mathrm{T}} & \mathbf{H}_s^b + \mathbf{H}_s^s & \mathbf{H}_{bs}^b \\ \left(\mathbf{H}_{bm}^{mb}\right)^{\mathrm{T}} & \left(\mathbf{H}_{bs}^b\right)^{\mathrm{T}} & \mathbf{H}_b^b \end{bmatrix}, \quad \mathbf{G} = \begin{bmatrix} \mathbf{G}_m^u & \mathbf{0} & \mathbf{0} \\ \mathbf{0} & \mathbf{G}_s^w & \mathbf{G}_{bs}^\theta + \mathbf{G}_s^{w\theta} \\ \mathbf{0} & \mathbf{0} & \mathbf{G}_b^\theta \end{bmatrix}, \tag{2.113}$$

$$\boldsymbol{\beta} = \begin{bmatrix} \boldsymbol{\beta}_m \\ \boldsymbol{\beta}_s \\ \boldsymbol{\beta}_b \end{bmatrix}, \quad \mathbf{q} = \begin{bmatrix} \mathbf{q}_u \\ \mathbf{q}_w \\ \mathbf{q}_\theta \end{bmatrix}, \quad \mathbf{g} = \begin{bmatrix} \mathbf{g}_m \\ \mathbf{g}_s \\ \mathbf{g}_b \end{bmatrix}, \quad \mathbf{h} = \begin{bmatrix} \mathbf{h}_u \\ \mathbf{h}_w \\ \mathbf{h}_\theta \end{bmatrix}. \tag{2.114}$$

Here, $\mathbf{g}$ are the terms due to the prescribed loads and $\mathbf{h}$ are the element nodal generalised forces. Observe that the equations are strongly coupled due to the coupling in the stress resultants approximation, the linking on the displacement interpolation and the membrane-bending coupled behaviour of laminated plates. The matrices involved are defined as follows:

$$\mathbf{H}_m^m = \int_\Omega \mathbf{P}_m^{\mathrm{T}} \mathbf{F}_m \mathbf{P}_m \mathrm{d}\Omega, \qquad \mathbf{H}_{sm}^{mb} = \int_\Omega \mathbf{P}_m^{\mathrm{T}} \mathbf{F}_{mb} \mathbf{P}_{bs} \mathrm{d}\Omega, \tag{2.115}$$

$$\mathbf{H}_{bm}^{mb} = \int_\Omega \mathbf{P}_m^{\mathrm{T}} \mathbf{F}_{mb} \mathbf{P}_b \mathrm{d}\Omega, \qquad \mathbf{H}_s^s = \int_\Omega \mathbf{P}_s^{\mathrm{T}} \mathbf{F}_s \mathbf{P}_s \mathrm{d}\Omega, \tag{2.116}$$

$$\mathbf{H}_s^b = \int_\Omega \mathbf{P}_{bs}^{\mathrm{T}} \mathbf{F}_b \mathbf{P}_{bs} \mathrm{d}\Omega, \qquad \mathbf{H}_{bs}^b = \int_\Omega \mathbf{P}_{bs}^{\mathrm{T}} \mathbf{F}_b \mathbf{P}_b \mathrm{d}\Omega, \tag{2.117}$$

$$\mathbf{H}_b^b = \int_\Omega \mathbf{P}_b^{\mathrm{T}} \mathbf{F}_b \mathbf{P}_b \mathrm{d}\Omega, \qquad \left(\mathbf{G}_m^u\right)^{\mathrm{T}} = \int_{\partial\Omega} \mathbf{U}_u^{\mathrm{T}} \mathbf{n}_m^{\mathrm{T}} \mathbf{P}_m \mathrm{d}\left(\partial\Omega\right), \tag{2.118}$$

$$\left(\mathbf{G}_s^w\right)^{\mathrm{T}} = \int_{\partial\Omega} \mathbf{U}_w^{\mathrm{T}} \mathbf{n}_s^{\mathrm{T}} \mathbf{P}_s \mathrm{d}\left(\partial\Omega\right), \qquad \left(\mathbf{G}_{bs}^\theta\right)^{\mathrm{T}} = \int_{\partial\Omega} \mathbf{U}_\theta^{\mathrm{T}} \mathbf{n}_m^{\mathrm{T}} \mathbf{P}_{bs} \mathrm{d}\left(\partial\Omega\right), \tag{2.119}$$

$$\left(\mathbf{G}_s^{w\theta}\right)^{\mathrm{T}} = \int_{\partial\Omega} \mathbf{L}^{\mathrm{T}} \mathbf{n}_s^{\mathrm{T}} \mathbf{P}_s \mathrm{d}\left(\partial\Omega\right), \qquad \left(\mathbf{G}_b^\theta\right)^{\mathrm{T}} = \int_{\partial\Omega} \mathbf{U}_\theta^{\mathrm{T}} \mathbf{n}_m^{\mathrm{T}} \mathbf{P}_b \mathrm{d}\left(\partial\Omega\right). \tag{2.120}$$

The inner parameters $\boldsymbol{\beta}$ can be condensed out at the element level and the elemental equations take the standard form involving only nodal displacements:

$$\begin{bmatrix} \mathbf{h}_u \\ \mathbf{h}_w \\ \mathbf{h}_\theta \end{bmatrix} = \begin{bmatrix} \mathbf{K}_{uu} & \mathbf{K}_{uw} & \mathbf{K}_{u\theta} \\ \mathbf{K}_{uw}^{\mathrm{T}} & \mathbf{K}_{ww} & \mathbf{K}_{w\theta} \\ \mathbf{K}_{u\theta}^{\mathrm{T}} & \mathbf{K}_{w\theta}^{\mathrm{T}} & \mathbf{K}_{\theta\theta} \end{bmatrix} \begin{bmatrix} \mathbf{q}_u \\ \mathbf{q}_w \\ \mathbf{q}_\theta \end{bmatrix} - \begin{bmatrix} \mathbf{f}_u \\ \mathbf{f}_w \\ \mathbf{f}_\theta \end{bmatrix}. \tag{2.121}$$

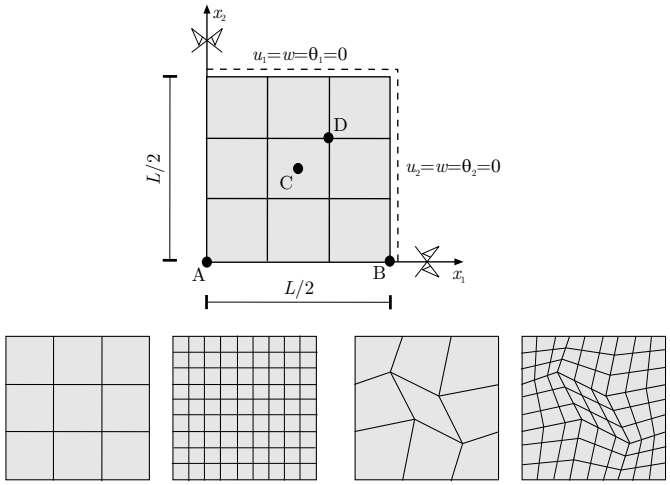

Figure 2.7: Simply supported square plate, regular and distorted mesh patterns

As it can be immediately realised, this relation can be easily implemented into existing finite element codes. Notice that, with respect to the mixed-enhanced finite element proposed by Auricchio and Sacco (1999a) and Auricchio et al. (2006) and based on linked interpolation for the transverse displacement, the present element does not require internal bubble functions and enhanced incompatible modes, whose number depends on the material response ($5+8\times3$ for monoclinic layers). The greater simplicity reflects also on a higher computational efficiency since only 14 inner parameters should be eliminated at the element level.

2.2.4 Numerical testing of the finite element performance

In this section, some numerical tests are carried out in order to investigate the performance of the proposed laminate finite element (HQ4). The same test case is later used in Section 2.3 to test the transverse shear stress reconstruction procedure.

A simply supported square plate of side L (Figure 2.7) is considered under both uniform and sinusoidal load, with maximum intensity q. The side to

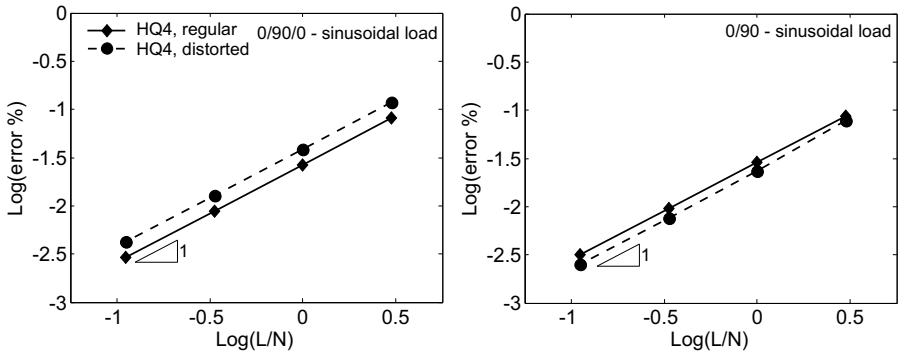

Figure 2.8: Convergence in energy norm for sinusoidal load and both the stacking sequences

thickness ratio of the laminate is $L/h = 10$. Two different stacking sequences are analysed: a symmetric (0/90/0) laminate and an antisymmetric (0/90) one. Due to the in-plane double symmetry, only one quarter of the plate is studied. The regular and distorted mesh patterns used in the analyses are shown in Figure 2.7.

The lamina mechanical properties in the material coordinates are the following:

$$E_a = 25\,E_b, \quad \nu_{ab} = 0.25, \quad G_{ac} = G_{ab} = 0.5\,E_b, \quad G_{bc} = 0.2\,E_b. \tag{2.122}$$

The shear correction factors are computed by assuming cylindrical bending (Laitinen et al., 1995) and are considered as constant (that is they are not updated using the recovered shear stress profiles): $\kappa_{11} = 235445/404004$, $\kappa_{22} = 289/360$, $\kappa_{12} = 0$ for the (0/90/0) laminate, $\kappa_{11} = 297680/362481$, $\kappa_{22} = \kappa_{11}$ and $\kappa_{12} = 0$ for the (0/90) laminate.

The reference solution are computed according to Reddy (1997).

Global and local convergence properties are discussed for both the load cases and both the stacking sequences, using regular and distorted meshes. In the uniform load case, the results are compared with those predicted by the MITC laminated plate element, implemented in the commercial software ADINA.

Figure 2.8 shows the convergence in energy norm in the case of sinusoidal load

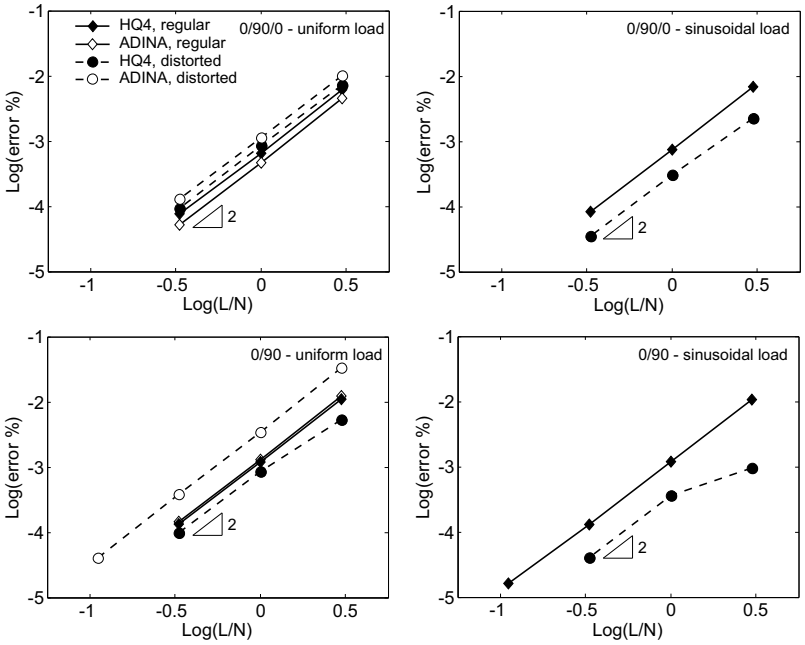

Figure 2.9: Convergence of the transverse displacement at point A for different loads and stacking sequences

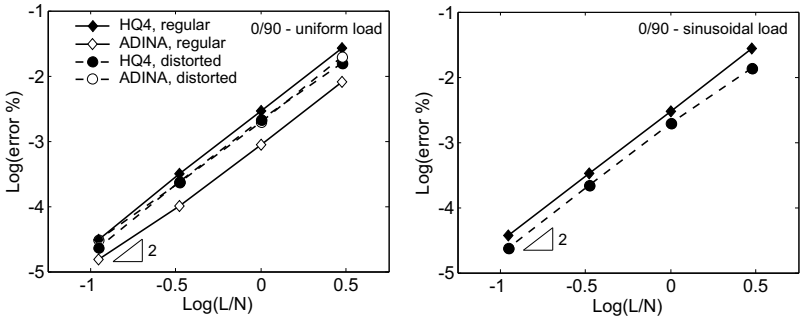

Figure 2.10: Convergence of the in-plane displacement at point B for the (0/90) stacking sequence and both uniform and sinusoidal load

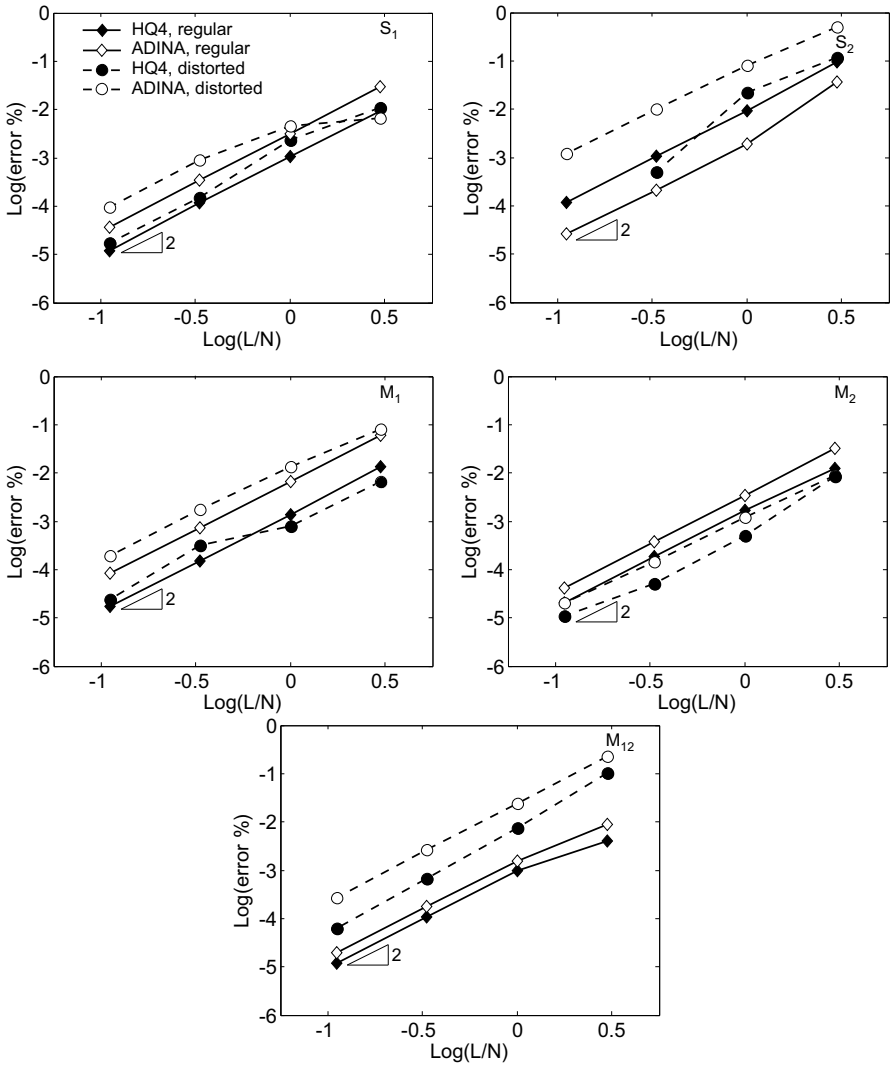

Figure 2.11: Convergence of the stress resultants at point C for the (0/90/0) stacking sequence and uniform load

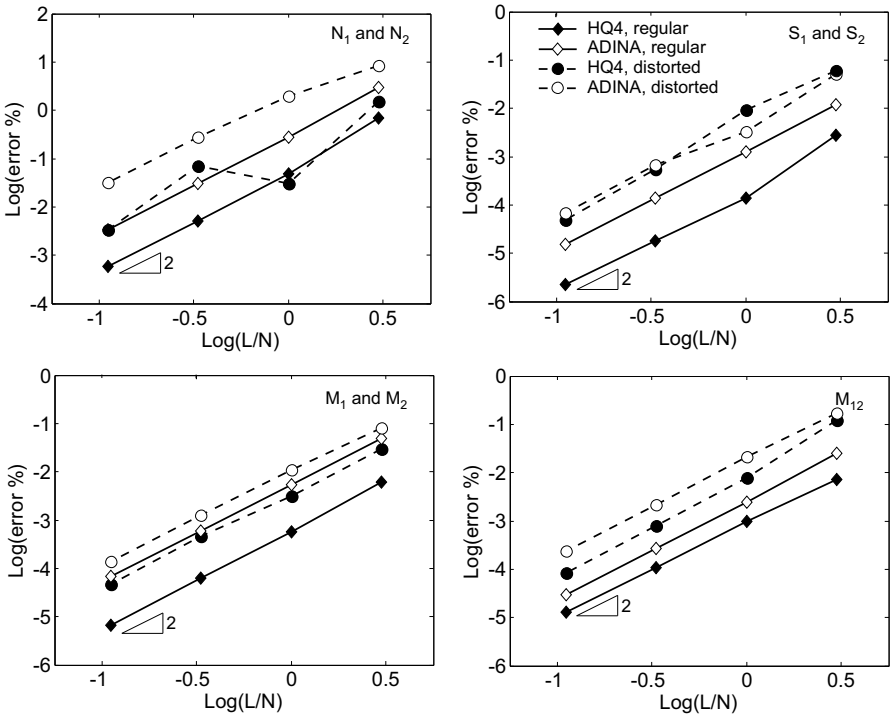

Figure 2.12: Convergence of the stress resultants at point C for the (0/90) stacking sequence and uniform load

Table 2.1: Transverse displacement $\bar{w}$ at point A for simply supported (0/90/0) laminate subjected to uniform load

Ref. sol. (Reddy, 1997)		1.16754	
mesh	3×3	9×9	27×27
HQ4, regular	1.17482	1.16831	1.16763
HQ4, distorted	1.17610	1.16853	1.16765
ADINA, regular	1.17282	1.16808	1.16760
ADINA, distorted	1.15553	1.16620	1.16739

Table 2.2: Transverse displacement $\bar{w}$ at point A and in-plane displacement $\bar{u}_1$ at point B for simply supported (0/90) laminate subjected to uniform load

		$\bar{w}$			$\bar{u}_1$	
Ref. sol. (Reddy, 1997)		1.95058			0.12940	
mesh	3×3	9×9	27×27	3×3	9×9	27×27
HQ4, regular	1.97191	1.95293	1.95084	0.13285	0.12978	0.12944
HQ4, distorted	1.96109	1.95227	1.95077	0.13147	0.12968	0.12943
ADINA, regular	1.92668	1.94807	1.95030	0.12836	0.12929	0.12939
ADINA, distorted	1.88549	1.94390	1.94983	0.12683	0.12915	0.12937

Table 2.3: Stress resultants at point C for simply supported (0/90/0) laminate subjected to uniform load

		$\bar{S}_1$			$\bar{S}_2$	
Ref. sol. (Reddy, 1997)		-18.9515			-1.12587	
mesh	3×3	9×9	27×27	3×3	9×9	27×27
HQ4, regular	-18.7782	-18.9311	-18.9492	-1.23522	-1.13633	-1.12704
HQ4, distorted	-18.7426	-18.9063	-18.9486	-0.99111	-1.10086	-1.12529
ADINA, regular	-18.3930	-18.8925	-18.9450	-1.16665	-1.12802	-1.12610
ADINA, distorted	-19.0768	-18.8650	-18.9346	-1.68125	-1.21503	-1.13727
		$\bar{M}_1$			$\bar{M}_2$	
Ref. sol. (Reddy, 1997)		7.01608			1.14959	
mesh	3×3	9×9	27×27	3×3	9×9	27×27
HQ4, regular	6.92084	7.00641	7.01501	1.16411	1.15150	1.14981
HQ4, distorted	6.96898	7.01050	7.01388	1.13975	1.14901	1.14953
ADINA, regular	6.59260	6.96909	7.01086	1.11246	1.14565	1.14916
ADINA, distorted	6.44039	6.92332	7.00380	1.15971	1.15100	1.14976

		$\bar{M}_{12}$	
Ref. sol. (Reddy, 1997)		-0.31692	
	3×3	9×9	27×27
HQ4, regular	-0.31562	-0.31661	-0.31689
HQ4, distorted	-0.28380	-0.31456	-0.31671
ADINA, regular	-0.31968	-0.31742	-0.31698
ADINA, distorted	-0.24488	-0.30914	-0.31610

Table 2.4: Stress resultants at point C for simply supported (0/90) laminate subjected to uniform load

		$\bar{N}_1 = \bar{N}_2$			$\bar{S}_1 = \bar{S}_2$	
Ref. sol. (Reddy, 1997)		-0.01910			-9.71082	
mesh	3×3	9×9	27×27	3×3	9×9	27×27
HQ4, regular	-.03235	-.02001	-.01920	-9.73822	-9.70950	-9.71064
HQ4, distorted	.01035	-.01967	-.01774	-9.13132	-9.62003	-9.70547
ADINA, regular	-.07579	-.02437	-.01968	-9.59597	-9.69853	-9.70948
ADINA, distorted	-.17646	-.05685	-.02435	-10.20210	-9.67910	-9.70421
		$\bar{M}_1 = \bar{M}_2$			$\bar{M}_{12}$	
Ref. sol. (Reddy, 1997)		3.67599			-0.66318	
mesh	3×3	9×9	27×27	3×3	9×9	27×27
HQ4, regular	3.65353	3.67387	3.67575	-0.65847	-0.66253	-0.66311
HQ4, distorted	3.56463	3.66430	3.67427	-0.58042	-0.65794	-0.66264
ADINA, regular	3.49680	3.65598	3.67377	-0.64660	-0.66156	-0.66300
ADINA, distorted	3.38096	3.63580	3.67138	-0.54975	-0.64927	-0.66174

for the two different stacking sequences, with N denoting the number of elements per side. As it can be observed an optimal behaviour is experienced with a very low sensitivity to geometry distortions. Pointwise convergence results are reported in Figures 2.9 and 2.10, showing the transverse displacement w in the plate centre (point A in Figure 2.7) and the in-plane displacement u_1 at point B, respectively. Note that the in-plane displacements are different from zero in the (0/90) antisymmetric laminate because of the membrane-bending coupling. In addition, Figures 2.11 and 2.12 show the convergence of the generalised stresses at point C under uniform load for the symmetric and the antisymmetric case, respectively. Finally, Tables 2.1-2.4 report some results predicted by the present element and ADINA. The quantities are rendered dimensionless as follows:

$$\bar{w} = w\frac{100E_b}{qh\left(L/h\right)^4}, \quad \bar{u}_1 = u_1\frac{100E_b}{qh\left(L/h\right)^4}, \tag{2.123}$$

$$\bar{\mathbf{N}} = \mathbf{N}\frac{100}{qh\left(L/h\right)^2}, \quad \bar{\mathbf{M}} = \mathbf{M}\frac{100}{qh^2\left(L/h\right)^2}, \quad \bar{\mathbf{S}} = \mathbf{S}\frac{100}{qh\left(L/h\right)}. \tag{2.124}$$

As it can be noted, a superconvergent behaviour is observed for the stress resultants at point C, using either HQ4 or ADINA. Indeed, the convergence rate obtained elsewhere is one, as expected (see for example Figures 2.15 and 2.16 in Section 2.3 for convergence at point D).

All these results show that the performance of the HQ4 element is comparable with that of the MITC element from both the point of view of accuracy and convergence rate. However, the proposed element tends to be less sensitive to mesh distortions and more accurate in terms of stress resultants.

2.3 Reconstruction of the transverse stresses

Once the solution of the plate problem is available, the transverse stresses can be reconstructed through Equations (2.78) and (2.79) introducing the constitutively determined in-plane stresses (Daghia et al., 2008). A satisfactory approximation of the transverse shear stresses is particularly important in order to iteratively update the shear correction factors, as outlined in Section 2.1.1. The passage from the analytical strategy to the numerical implementation, however, requires a few careful considerations.

First of all, the need for pointwise equilibrated stress resultants as pointed out in Section 2.1.1 is not necessarily met by approximate numerical solutions. Indeed, if pointwise two-dimensional equilibrium is lacking, automatic satisfaction of the boundary conditions and static equivalence of the reconstructed transverse stresses is lost. For this reason, the two-dimensional stresses obtained via a hybrid stress approach, such as the one proposed in Section 2.2, are ideal candidates for a post processing based on local three-dimensional equilibrium. On the other hand, the reconstruction procedures associated to other finite elements, such as those by Alfano et al. (2001), Auricchio and Sacco (1999a) and Auricchio et al. (2006), need to be corrected to properly account for the boundary equilibrium conditions and the static equivalence. The same equilibrium defect affects also the procedures proposed by Noor et al. (1994) and Park and Kim (2003), both based on a superconvergent recovery of the in-plane stresses in the different layers.

The second issue to be taken into consideration concerns the convergence of the numerically reconstructed transverse stresses to the theoretical (FSDT) plate solution. Indeed, accuracy of the reconstructed shear stresses depends on the accuracy of the first derivatives of the finite element stress resultants, as they are used to determine the in-plane active stress. This is a crucial point of all the procedures based on local equilibrium, especially for low order plate finite elements like the one presented in Section 2.2 or those proposed by Alfano

et al. (2001), Auricchio and Sacco (1999a), Auricchio et al. (2006) and Cen et al. (2002), and generally leads to non convergent results. Here, a two stages reconstruction strategy is proposed to overcome this difficulty. First, a patch-based superconvergent procedure is applied to recover the stress resultants by locally post processing the finite element solution, then the recovered values are used to reconstruct the transverse shear stresses, following the idea early proposed by Noor et al. (1994). In this paper, the recovery is carried out by the procedure called Recovery by Compatibility in Patches (RCP) (Benedetti et al., 2006; Ubertini, 2004), which has been recently extended to homogeneous plate structures (Castellazzi et al., 2006) and is here established for laminates. Besides being simple, stable, robust and very efficient from the computational point of view, it has been proved to be superconvergent in certain circumstances and, using patches centred on an element instead of a node, yields recovered stress resultants which satisfy the plate equilibrium equations. This is a key feature in this context since, as already mentioned, the reconstruction procedure can be applied without any correction due to non equilibrated terms. Once accurate transverse shear stresses are reconstructed, the third local equilibrium condition can be used to compute the transverse normal stress profile. Indeed, the accuracy of this second reconstruction step depends on the accuracy of the first derivatives of the transverse shear stresses. Some possible strategies to further improve the quality of the resultant transverse normal stress are outlined in the following.

It should be emphasised that the whole procedure based on RCP recovery and shear stresses reconstruction is quite general and can be successfully applied to different laminate finite elements, without any modification or adjustment. The outlined strategy differs from the one proposed by Noor et al. (1994) for the assumed recovery technique and patch configuration, which guarantees local equilibrium. On the other hand, it is similar to the one proposed by Cen et al. (2002), based on a hybrid enhanced elementwise post processing procedure. However, the present recovery works on patches instead of simple elements and this is the key feature which actually guarantees robustness and superconvergence. A comparative analysis of various models and techniques to evaluate out of plane stresses a priori or a posteriori was carried out by Carrera (2000), who also proposed a similar reconstruction procedure based on a partial mixed formulation, called weak form of Hooke's law and operating on single elements

instead of patches. Other strategies to evaluate laminate transverse stresses proposed in the literature include the simplified reconstruction procedure proposed by Rolfes and Rohwer (1997), based on assuming two cylindrical bending modes and neglecting the influence of membrane forces, and, more recently, the enhanced first-order theory allowing for through the thickness recovery of displacements and stresses developed by Kim and Cho (2007).

2.3.1 Recovery by Compatibility in Patches

Recovery by Compatibility in Patches (RCP) is a stress recovery procedure based on the minimisation of the complementary energy associated to a patch of elements, considered as a separate system, among an assumed set of equilibrated fields. Hence, it substantially attempts to enhance equilibrium while relaxing compatibility. Here, it is applied in the version based on the element patch configuration (Benedetti et al., 2006), that is with patches defined by an element (central element) and the union of elements surrounding it, as shown in Figure 2.13. The same patch configuration was early adopted by Mohite and Upadhyay (2002) as the support for a strain recovery procedure. The new solution computed over the patch is taken directly as the recovered solution for the central element, with no need of any additional averaging process. In this way, the recovered stress resultants on each element are simply obtained by forming the associated patch and applying the RCP procedure over it. Notice that the recovered solution is discontinuous across the elements but satisfies pointwise the plate equilibrium equations within each element, as required to be used for the subsequent reconstruction procedure of transverse stresses.

To apply the recovery procedure, a new approximation for stress resultants over the patch is introduced:

$$\begin{bmatrix} \mathbf{N}^r \\ \mathbf{M}^r \\ \mathbf{S}^r \end{bmatrix} = \mathbf{P}^r \boldsymbol{\alpha} + \begin{bmatrix} \mathbf{N}_p \\ \mathbf{M}_p \\ \mathbf{S}_p \end{bmatrix}, \tag{2.125}$$

where the superscript r denotes the recovered solution, $\mathbf{P}^r$ is a matrix of self-equilibrated modes, $\boldsymbol{\alpha}$ is a vector of unknown parameters and the last term is a particular solution of the plate equilibrium equations, which is taken as equal to the one selected for the plate finite element formulation (see Section 2.2.2).

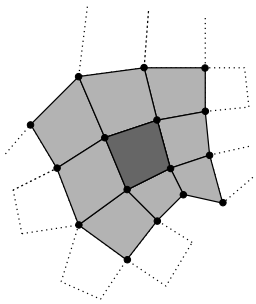

Figure 2.13: Element patch for the RCP

In particular, an approximation ruled by 14 α-parameters is selected based on linear polynomial expansions in terms of local coordinates (x_1, x_2) centred on the patch:

$$\begin{bmatrix} \mathbf{N}^r \\ \mathbf{M}^r \\ \mathbf{S}^r \end{bmatrix} = \begin{bmatrix} 1 & 0 & 0 & x_2 & 0 & 0 & 0 & 0 & 0 & 0 & 0 & 0 & 0 & 0 \\ 0 & 1 & 0 & 0 & x_1 & 0 & 0 & 0 & 0 & 0 & 0 & 0 & 0 & 0 \\ 0 & 0 & 1 & 0 & 0 & 0 & 0 & 0 & 0 & 0 & 0 & 0 & 0 & 0 \\ 0 & 0 & 0 & 0 & 0 & 1 & x_1 & x_2 & 0 & 0 & 0 & 0 & 0 & 0 \\ 0 & 0 & 0 & 0 & 0 & 0 & 0 & 0 & 1 & x_1 & x_2 & 0 & 0 & 0 \\ 0 & 0 & 0 & 0 & 0 & 0 & 0 & 0 & 0 & 0 & 0 & 1 & x_1 & x_2 \\ 0 & 0 & 0 & 0 & 0 & 0 & 1 & 0 & 0 & 0 & 0 & 0 & 0 & 1 \\ 0 & 0 & 0 & 0 & 0 & 0 & 0 & 0 & 0 & 0 & 1 & 0 & 1 & 0 \end{bmatrix} \boldsymbol{\alpha}. \tag{2.126}$$

Then, the RCP minimisation yields the following compatibility condition over each patch Ω_p:

$$\int_{\Omega_p} \left[\delta\mathbf{N}^{r\mathrm{T}} \left(\boldsymbol{\mu}^r - \boldsymbol{\mu}^h\right) + \delta\mathbf{M}^{r\mathrm{T}} \left(\boldsymbol{\chi}^r - \boldsymbol{\chi}^h\right) + \delta\mathbf{S}^{r\mathrm{T}} \left(\boldsymbol{\gamma}^r - \boldsymbol{\gamma}^h\right)\right] \mathrm{d}\Omega_p = 0 \qquad \forall \ \left(\delta\mathbf{N}^r,\ \delta\mathbf{M}^r,\ \delta\mathbf{S}^r\right), \tag{2.127}$$

where $(\boldsymbol{\mu}^r, \boldsymbol{\chi}^r, \boldsymbol{\gamma}^r)$ are the strain components obtained from the recovered stress resultants via the plate constitutive equations and $\left(\boldsymbol{\mu}^h, \boldsymbol{\chi}^h, \boldsymbol{\gamma}^h\right)$ are the strain components resulting from the finite element solution. They could be computed from either the assumed finite element displacements, via the plate compatibility

equations, or the assumed finite element stress resultants, via the plate constitutive equations. These two possibilities offered by mixed finite elements have been explored by Castellazzi et al. (2006). Here, the first alternative based on the finite element kinematics is adopted.

Substituting Equation (2.125) into Equation (2.127) leads to a system of 14 linear algebraic equations, whose solution permits to determine the α-parameters and, hence, the recovered stress resultants over the central element of the patch:

$$\mathbf{H}\boldsymbol{\alpha} = \mathbf{g}, \tag{2.128}$$

where

$$\mathbf{H} = \sum_{j-1}^{nep} \int_{\Omega_j} \mathbf{P}^{r\mathrm{T}} \begin{bmatrix} \mathbf{F}_m & \mathbf{F}_{mb} & \mathbf{0} \\ & \mathbf{F}_b & \mathbf{0} \\ \mathrm{sym} & & \mathbf{F}_s \end{bmatrix} \mathbf{P}^r \mathrm{d}\Omega, \tag{2.129}$$

$$\mathbf{g} = \sum_{j=1}^{nep} \int_{\Omega_j} \mathbf{P}^{r\mathrm{T}} \begin{bmatrix} \mathbf{D}_m\mathbf{U}_u\mathbf{q}_u - \mathbf{F}_m\mathbf{N}_p - \mathbf{F}_{mb}\mathbf{M}_p \\ \mathbf{D}_m\mathbf{U}_\theta\mathbf{q}_\theta - \mathbf{F}_{mb}\mathbf{N}_p - \mathbf{F}_b\mathbf{M}_p \\ \mathbf{D}_s\mathbf{U}_w\mathbf{q}_w + (\mathbf{D}_s\mathbf{L} + \mathbf{U}_\theta)\,\mathbf{q}_\theta - \mathbf{F}_s\mathbf{S}_p \end{bmatrix} \mathrm{d}\Omega, \tag{2.130}$$

where

$$\mathbf{D}_m = \begin{bmatrix} \partial/\partial x_1 & 0 \\ 0 & \partial/\partial x_2 \\ \partial/\partial x_2 & \partial/\partial x_1 \end{bmatrix}, \qquad \mathbf{D}_s = \begin{bmatrix} \partial/\partial x_1 \\ \partial/\partial x_2 \end{bmatrix}, \tag{2.131}$$

nep is the number of elements in the patch and Ω_j the domain of the general element of the patch.

It should be remarked that the outlined procedure is very simple, easily implementable into existing codes, unconditionally stable and computationally efficient. In particular, differently from the procedure proposed by Alfano et al. (2001) for MITC elements, which is an L^2 projection over the entire domain, it is a minimum condition over small patches of elements with an extremely low computational cost. Moreover, the RCP procedure has been proved to be truly superconvergent on certain regular mesh patterns but, anyway, extremely robust on general mesh patterns (Benedetti et al., 2006), with an almost optimal rate of convergence. In the present case, the rate of convergence expected for the recovered stress resultants is about two in energy norm (one order higher than the finite element stress resultants).

2.3.2 Reconstruction of the transverse shear stresses

The higher convergence rate of the recovered stress resultants is expected to ensure convergence of their first derivatives in the element interior and, as a consequence, convergence of the subsequent reconstruction procedure of transverse shear stresses:

$$\begin{aligned}\boldsymbol{\tau}(z) &= -\mathbf{p}_x^{(-)} + \int_{-\frac{h}{2}}^{z} \Big\{ \mathbf{D}_m^* \mathbf{C}_m^{(k)} \\ &\quad [(\mathbf{F}_m \mathbf{N}^r + \mathbf{F}_{mb} \mathbf{M}^r) + z\,(\mathbf{F}_{mb} \mathbf{N}^r + \mathbf{F}_b \mathbf{M}^r)] - \mathbf{b}_x \Big\}\, \mathrm{d}z, \quad (2.132)\end{aligned}$$

where the in-plane stresses are computed using the recovered stress resultants and the symbol $*$ denotes the adjoint operator.

2.3.3 Reconstruction of the transverse normal stress

Once accurate transverse shear stress profiles have been obtained, they can be used in Equation (2.79) to evaluate the transverse normal stress. As already mentioned, the whole procedure is statically admissible, so that the resultant transverse normal stress automatically satisfies both the boundary equilibrium conditions. It should be remarked, however, that the reconstruction accuracy depends on the first derivatives of the transverse shear stresses with respect to the in-plane coordinates, as they enter Equation (2.79), and consequently on the second derivatives of the stress resultants. For this reason, the RCP recovery should be carried out using at least a quadratic stress approximation. With this consideration, the quality of the predicted profiles is generally satisfactory at the centre of the elements, but tends to deteriorate for thick laminates while moving towards the element boundaries. Indeed, even with a quadratic stress approximation, the proposed recovery procedure, as well as most of the available superconvergent recovery procedures, is not designed to guarantee a priori convergence of second derivatives everywhere within the element. For this reason, accurate transverse normal stresses are not a priori guaranteed everywhere within the element by using the recovered shear stresses computed according to the previous section. However, the resultant profiles are accurate enough for a preliminary evaluation of thick laminate response. Note that, differently from the transverse shear stresses which are needed also to evaluate the shear correction factors, the transverse normal stress does not influence at all the plate

solution.

Two different strategies can be devised to further enhance accuracy of the transverse normal stress and guarantee its convergence in any case (see the paper by Vallet et al. (2007) for some details on Hessian recovery techniques). The first strategy is to apply a second superconvergent recovery procedure, inspired by the RCP procedure, to improve transverse shear stresses before reconstructing the transverse normal stress using three-dimensional equilibrium. Differently from the second regularisation proposed by Alfano et al. (2001), the procedure should be patch-based and should preserve equilibrium. Similarly to the first RCP recovery previously described, compatibility is relaxed by enforcing the following condition on each patch:

$$\int_{\Omega_p \times \mathcal{F}} \left[\delta \mathbf{s}^{\bar{r}\mathrm{T}} \left(\mathbf{e}^{\bar{r}} - \mathbf{e}^{r} \right) + \delta \boldsymbol{\tau}^{\bar{r}\mathrm{T}} \left(\boldsymbol{\gamma}^{\bar{r}} - \boldsymbol{\gamma}^{r} \right) \right] \mathrm{d}V = 0 \ \ \forall \ \left(\delta \mathbf{s}^{\bar{r}}, \ \delta \boldsymbol{\tau}^{\bar{r}} \right), \qquad (2.133)$$

where the superscript r denotes the quantities related to the first RCP recovery, while the superscript $\bar{r}$ denotes the newly recovered quantities. The assumptions for $\mathbf{s}^{\bar{r}}$ and $\boldsymbol{\tau}^{\bar{r}}$ should satisfy the three-dimensional equilibrium and the interlaminar continuity conditions, in particular the in-plane stresses should be piecewise linear along the thickness direction while the transverse shear stresses should contain at least piecewise parabolic terms. The second strategy is to properly modify the outlined recovery procedure of the stress resultants by using larger node centred patches and separately interpolate the stress resultants and their first and second derivatives, so to ensure the required convergence. Both the strategies are promising but they are still under investigation. Thus, only the numerical results on transverse shear stresses are discussed in the next section.

2.3.4 Numerical testing of the reconstruction procedure

In this section, a numerical investigation of the procedure proposed to reconstruct transverse shear stresses from recovery and three-dimensional equilibrium is carried out. The test case considered is the same as in Section 2.2.4. The two-dimensional problem finite element solution is obtained using the HQ4 element presented in the previous section.

The first set of graphs highlights the key role of the RCP procedure in this context. Figure 2.14 shows the convergence in energy norm of the shear stress

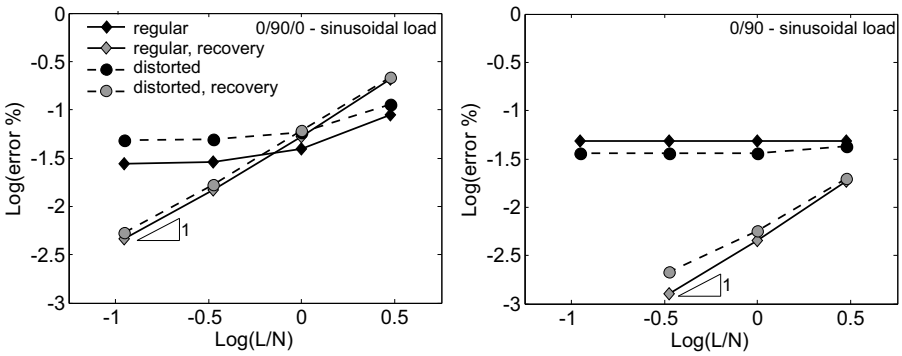

Figure 2.14: Convergence in energy norm of the shear stress profiles for sinusoidal load and both the stacking sequences, using HQ4 with or without RCP recovery

profiles reconstructed using directly the finite element in-plane stresses or those recovered by RCP:

$$error = \int_{\Omega\times\mathcal{F}} \left(\boldsymbol{\tau} - \boldsymbol{\tau}_{ref}\right)^{\mathrm{T}} \mathbf{F}_s^{(k)} \left(\boldsymbol{\tau} - \boldsymbol{\tau}_{ref}\right) \mathrm{d}V. \tag{2.134}$$

The sinusoidal load case is considered with both the stacking sequences. The reference solution for the shear stress profiles is that obtained from the continuum FSDT, using the same shear correction factors.

The plots of Figure 2.14 reveal that the reconstruction procedure used directly with the finite element results does not converge globally, although it may converge at some special points. Indeed, this is always the case if the procedure is applied to two-dimensional solutions obtained using four node finite elements. On the contrary, using the RCP recovery the reconstructed shear stress profiles globally converge at an optimal rate. This anomalous behaviour is due to the low convergence rate of the finite element stress resultants, that is generally one as shown by Figures 2.15 and 2.16, exception done for some special points, such as the centre of the element, where occasionally it may be two, as shown by Figures 2.11 and 2.12 in Section 2.2. Figures 2.15 and 2.16, indeed, depict the convergence of the moments at point D, before and after RCP recovery. It should be noted that point D coincides with a node in all the

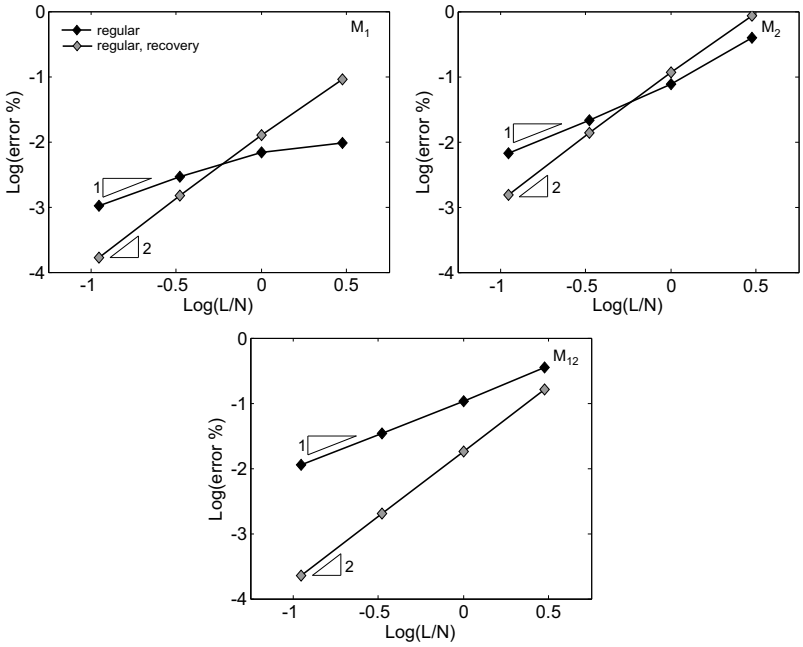

Figure 2.15: Convergence of the moments at point D by HQ4 with or without RCP recovery, for the (0/90/0) stacking sequence and sinusoidal load

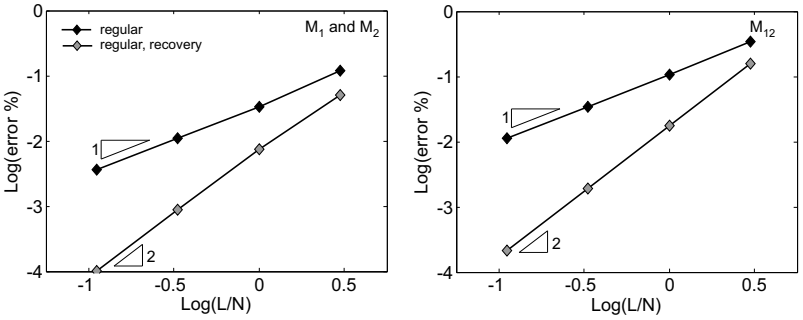

Figure 2.16: Convergence of the moments at point D by HQ4 with or without RCP recovery, for the (0/90) stacking sequence and sinusoidal load

sequence of refined meshes (see Figure 2.7). Since both finite element and recovered stress resultants are discontinuous across elements, the values reported have been computed for the element having D as the top right-hand node. It should be remarked that point D is a severe point for recovery procedures, since the error tends to concentrate on the element boundaries. Nevertheless, RCP recovery significantly improves the solution.

To sum up, the above results demonstrate that RCP procedure can be successfully applied also to laminated plates and confirm the superconvergence properties. In fact the recovered stress resultants, besides being generally more accurate, exhibit a convergence rate of almost two everywhere and not only at the element centre. As a consequence, the RCP-based reconstructed shear stress profiles globally converge, as shown by Figure 2.14.

To complete the experimental evaluation, Figures 2.17-2.20 show the dimensionless transverse shear stress profiles at point C for the two different stacking sequences and the sinusoidal load. The shear stress is rendered dimensionless as follows:

$$\bar{\tau}_{zs} = \tau_{zs} \frac{100}{q\,(L/h)}. \tag{2.135}$$

In the first two figures, the profiles reconstructed by making use of RCP recovery are shown for three mesh refinements. As it can be observed, the profiles quickly converge to the reference solution. In Figures 2.19 and 2.20, on the other hand, the profiles predicted with or without recovery are illustrated for 9×9 meshes of regular and distorted elements. Observing for example the results in terms of $\bar{\tau}_{z2}$ for the (0/90/0) laminate with the distorted mesh (black dots in Figure 2.19), it is evident that the shape of the profile is very different from the reference solution, although the shear force (represented by the area beneath the graph) is similar. This confirms that, while the value of the shear force is close to the exact one, the quality of the shear stress profiles may be very poor unless the RCP recovery is employed. In this case, the shear stress profiles are accurately captured even on coarse meshes.

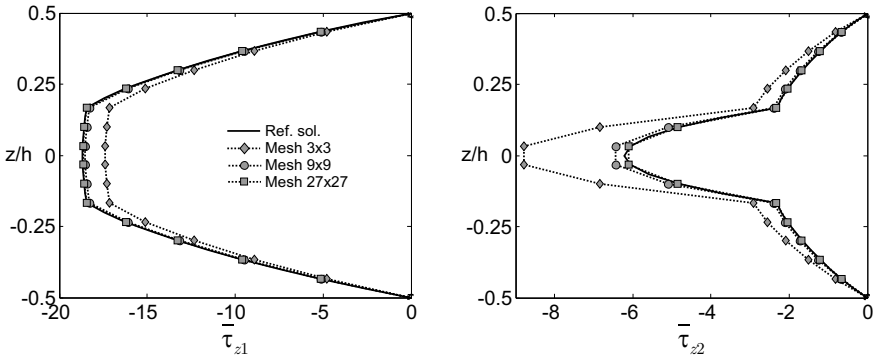

Figure 2.17: Shear stress profiles at point C using RCP recovery on various regular meshes, for the stacking sequence (0/90/0) and sinusoidal load

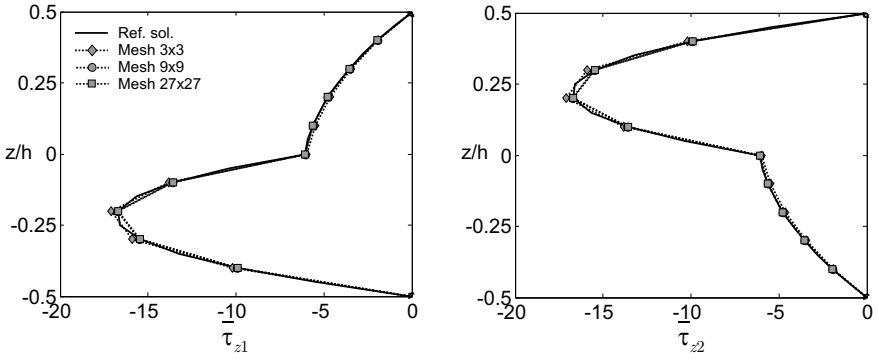

Figure 2.18: Shear stress profiles at point C using RCP recovery on various regular meshes, for the stacking sequence (0/90) and sinusoidal load

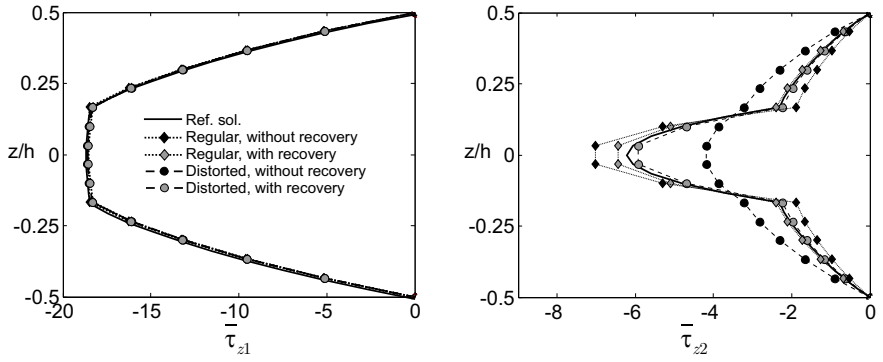

Figure 2.19: Shear stress profiles at point C with and without RCP recovery on 9×9 meshes for the stacking sequence (0/90/0) and sinusoidal load

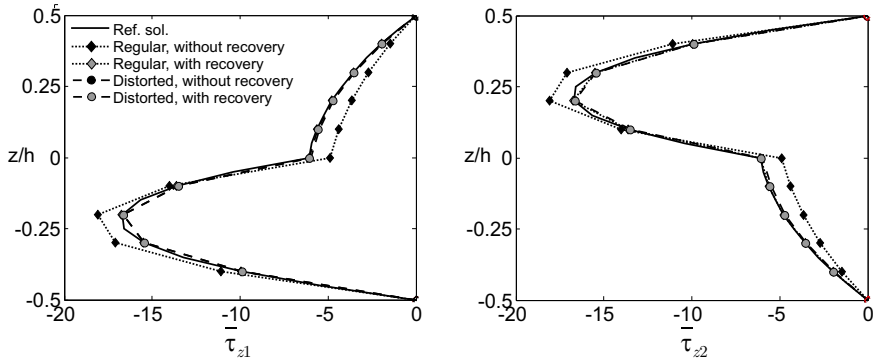

Figure 2.20: Shear stress profiles at point C with and without RCP recovery on 9×9 meshes for the stacking sequence (0/90) and sinusoidal load

2.4 Bayesian estimation of laminates' elastic constants

Equivalent Single Layer and layerwise laminate theories model laminae as orthotropic continua, thus they require the definition of the lamina constitutive properties in the material reference system. Even if the properties in the transverse direction are neglected, the independent material constants are significantly more than in the isotropic case, and generally more difficult to determine. Indeed, traditional static tests on laminates with a general stacking sequence are not able to identify the separate material properties because of the coupled behaviour described in the previous sessions. The typical solution is to test ad hoc specimens, whose laminae contain fibres oriented all in the same direction. Thus, results obtained for a $(0)_n$ laminate are generalised to a single lamina, regardless of the scale effects which might influence this passage. Moreover, even on a fully unidirectional laminate some material properties, such as the in-plane and transverse shear moduli, are not easily determined.

An alternative approach to determine material properties for a laminate with a general stacking sequence is represented by the so called numerical-experimental techniques. These are estimation methods which attempt to minimise in some sense the difference between measured data and the response predicted by an assumed model. Structural applications include identification of the characteristics of damaged and undamaged structures via dynamic and static experiments (see, for example, Di Paola and Bilello, 2004). Non destructive techniques based on the use of vibration data to identify structural characteristics date back to the 1970s. Statistical analysis of vibrating structural systems was early carried out by Collins and Thomson (1969) and Hasselman and Hart (1972). A probabilistic method to identify the elastic constants of simple structures starting from natural frequency data was proposed by Collins et al. (1974). Since the 1990s, the same approach has been applied to laminated composite plates (see for example Viola et al. (2003) and the references therein).

Here, only natural frequency measurements are supposed to be available for the identification process, since they can be evaluated experimentally through a simple modal test and, in most approaches present in the literature, they are generally found to be sufficient to estimate satisfactorily the elastic constants. Anyway, the estimation process could be improved by adding more information

on the structural response, such as that coming from mode shapes.

Many approaches have been proposed which differ in the choice of the theoretical and numerical model and the procedure used to estimate the elastic constants. In particular, these procedures aim at minimising a non linear objective function, which involves the difference between measured and numerical frequencies, and differ in the objective function and the algorithm used to solve the non linear minimisation problem.

The simplest objective functions are ordinary least squares or weighted least squares (Frederiksen, 1997). These functions take into account only the information coming from the experiment, and require no a priori knowledge on the possible parameter values. Although general, this approach needs robust and advanced search algorithms to obtain reliable results. Optimum design techniques were employed by Hwang and Chang (2000), experimental design techniques together with the response surface method were employed by Bledzki et al. (1999) and Rikards et al. (2001) and a feasible directions non linear interior point algorithm was employed by Araujo et al. (2002, 2000).

Alternatively, more complex objective functions can be adopted by taking into account the a priori information on the elastic constants (Bayesian framework). This is the approach used, among others, by Lai and Ip (1996) for thin plates and later extended to thick plates by Bartoli et al. (2003). A different choice to take into account the a priori knowledge on initial values can be found in the work by Hongxing et al. (2000) and Sol et al. (1997). A comparison between different methods for the identification of in-plane elastic constants of steel orthotropic plates was carried out by Lauwagie et al. (2003). In all these cases, the minimum of the objective function can be easily computed through a simple iterative algorithm, provided that the initial guesses of the elastic constants are not too far from the target values. Indeed, this is often the case for laminated composites, since a reasonable set of initial estimates can be found through the rule of mixtures, given the geometric properties of the laminae (fibre and matrix volume fraction) and an initial guess on the components' material properties (fibre and matrix elastic constants).

In this section, two well known estimators which make use of a priori information are considered for the identification of elastic constants of thick plates based on measured natural frequencies (Daghia et al., 2007a). The first estimator stems from Bayes theorem and can be strictly termed as Bayesian. The

second estimator is the minimum variance estimator. In the following, they are shortly referred to as B and MVE. The two estimators are compared by focusing on the role played by the a priori information. Although the two formulations are very different, a detailed analysis reveals a certain resemblance between the two, which helps to understand their behaviour and suggests an improved solution procedure (referred to as MVE-mod in the following). To complete the estimation process, four nodes finite elements based on Reddy's HSDT are used to model the plate. A higher-order theory is used since it is expected to accurately capture the first natural modes, which are usually measured for estimation purposes.

2.4.1 Bayesian estimators comparison

In a physical problem, the relationship between the problem data (input) and the outcome of the experiment (output) can be generally represented by

$$\mathbf{Y} = \boldsymbol{\eta}(\boldsymbol{\beta}) + \boldsymbol{\varepsilon}, \tag{2.136}$$

where $\mathbf{Y}$ is the vector containing the output values, $\boldsymbol{\eta}$ is a function representing the model used to describe the phenomenon, $\boldsymbol{\beta}$ is the vector of the input parameters and $\boldsymbol{\varepsilon}$ is the error, which includes both modelling and measurement errors. In structural engineering, $\boldsymbol{\beta}$ are the geometrical and mechanical properties of the structure and $\mathbf{Y}$ represents the structural response, for example in terms of natural frequencies.

While Equation (2.136) describes the direct problem, that is predicting the experiment outcome given the problem data, a number of different objective functions can be defined in order to estimate the input parameters from a set of measured experimental data. In particular, focusing on Bayesian estimators, the data required by the estimation procedure includes a set of initial parameter estimates $\boldsymbol{\mu}$.

Bayesian estimator (B)

The Bayesian estimator (Beck and Arnold, 1977) is obtained by applying Bayes theorem of conditional probabilities, that states:

$$f(\boldsymbol{\beta}|\mathbf{Y}) = \frac{f(\mathbf{Y}|\boldsymbol{\beta})f(\boldsymbol{\beta})}{f(\mathbf{Y})}, \tag{2.137}$$

where $f(a)$ is the probability density function of the variable a and $f(a|b)$ stands for the probability of the event a given that the event b has occurred. In the B estimator, the aim is to maximise the function (2.137). The probability densities $f(\mathbf{Y}|\boldsymbol{\beta})$ and $f(\boldsymbol{\beta})$ are given by the following functions:

$$f(\mathbf{Y}|\boldsymbol{\beta}) = \sqrt{\frac{|\mathbf{V}_Y|^{-1}}{(2\pi)^m}} exp\left(-\frac{(\mathbf{Y}-\boldsymbol{\eta})^{\mathrm{T}}\mathbf{V}_Y^{-1}(\mathbf{Y}-\boldsymbol{\eta})}{2}\right), \tag{2.138}$$

$$f(\boldsymbol{\beta}) = \sqrt{\frac{|\mathbf{V}_\beta|^{-1}}{(2\pi)^p}} exp\left(-\frac{(\boldsymbol{\beta}-\boldsymbol{\mu})^{\mathrm{T}}\mathbf{V}_\beta^{-1}(\boldsymbol{\beta}-\boldsymbol{\mu})}{2}\right), \tag{2.139}$$

where $\mathbf{V}_Y$ and $\mathbf{V}_\beta$ are the covariance matrices of the experimental error and initial estimates, respectively, m is the number of experimental observations and p is the number of parameters. Equation (2.138) represents the information deduced from the experiment, while Equation (2.139) represents the a priori information on the parameters to be estimated. The matrices $\mathbf{V}_Y$ and $\mathbf{V}_\beta$ have to be specified by the analyst.

Using Equations (2.138) and (2.139), the natural logarithm of equation (2.137) takes the form:

$$\ln(f(\boldsymbol{\beta}|\mathbf{Y})) = -\frac{1}{2}\left[(m+p)\ln(2\pi) + \ln|\mathbf{V}_Y| + \ln|\mathbf{V}_\beta| + S_B\right] - \ln\left(f(\mathbf{Y})\right), \tag{2.140}$$

where the only term dependent on the parameters is

$$S_B = (\mathbf{Y}-\boldsymbol{\eta})^{\mathrm{T}}\mathbf{V}_Y^{-1}(\mathbf{Y}-\boldsymbol{\eta}) + (\boldsymbol{\beta}-\boldsymbol{\mu})^{\mathrm{T}}\mathbf{V}_\beta^{-1}(\boldsymbol{\beta}-\boldsymbol{\mu}), \tag{2.141}$$

thus the B estimator is obtained by minimising S_B. Calculating the derivatives with respect to $\boldsymbol{\beta}$ and setting them equal to zero, one obtains:

$$\bigtriangledown_\beta S_B = 2\left[-\mathbf{S}^{\mathrm{T}}(\boldsymbol{\beta})\mathbf{V}_Y^{-1}(\mathbf{Y}-\boldsymbol{\eta}(\boldsymbol{\beta})) - \mathbf{V}_\beta^{-1}(\boldsymbol{\mu}-\boldsymbol{\beta})\right] = \mathbf{0}, \tag{2.142}$$

where

$$\mathbf{S}(\boldsymbol{\beta}) = \bigtriangledown_\beta \boldsymbol{\eta}(\boldsymbol{\beta}) \tag{2.143}$$

is the sensitivity matrix. Notice that in Equation (2.142) the parameters $\boldsymbol{\beta}$ appear both explicitly and implicitly.

In order to minimise S_B, an iterative procedure is established. Let $\mathbf{b}$ be a vector of initial parameter values. The term $\boldsymbol{\eta}(\boldsymbol{\beta})$ is approximated by a truncated Taylor series expansion in the neighbourhood of $\mathbf{b}$:

$$\boldsymbol{\eta}(\boldsymbol{\beta}) \approx \boldsymbol{\eta}(\mathbf{b}) + \mathbf{S}(\mathbf{b})(\boldsymbol{\beta} - \mathbf{b}), \qquad \mathbf{S}\left(\boldsymbol{\beta}\right) \approx \mathbf{S}\left(\mathbf{b}\right). \tag{2.144}$$

Hence, Equation (2.142) takes the form

$$\mathbf{S}^{\mathrm{T}}(\mathbf{b})\mathbf{V}_Y^{-1}\left[\mathbf{Y} - \boldsymbol{\eta}(\mathbf{b}) - \mathbf{S}(\mathbf{b})(\boldsymbol{\beta} - \mathbf{b})\right] + \mathbf{V}_\beta^{-1}\left(\boldsymbol{\mu} - \boldsymbol{\beta}\right) \approx \mathbf{0} \tag{2.145}$$

and a recurrence relation can be established:

$$\left(\mathbf{S}^k\right)^{\mathrm{T}}\mathbf{V}_Y^{-1}\left[\mathbf{Y} - \boldsymbol{\eta}^k - \mathbf{S}^k\left(\mathbf{b}^{k+1} - \boldsymbol{\mu}\right) - \mathbf{S}^k\left(\boldsymbol{\mu} - \mathbf{b}^k\right)\right] - \mathbf{V}_\beta^{-1}\left(\mathbf{b}^{k+1} - \boldsymbol{\mu}\right) = 0, \tag{2.146}$$

where the superscript k denotes the quantity calculated at the k-th iteration, $\mathbf{b}^k$ are the prior set of estimates and $\mathbf{b}^{k+1}$ are the parameter estimates at the end of the current iteration.

Solving for $\mathbf{b}^{k+1}$ yields:

$$\mathbf{b}^{k+1} = \boldsymbol{\mu} + \left[\left(\mathbf{S}^k\right)^{\mathrm{T}}\mathbf{V}_Y^{-1}\mathbf{S}^k + \mathbf{V}_\beta^{-1}\right]^{-1}\left(\mathbf{S}^k\right)^{\mathrm{T}}\mathbf{V}_Y^{-1}\left[\mathbf{Y} - \boldsymbol{\eta}^k - \mathbf{S}^k\left(\boldsymbol{\mu} - \mathbf{b}^k\right)\right]. \tag{2.147}$$

Minimum variance estimator (MVE)

The estimator presented in the work of Collins et al. (1974) is obtained by minimising the variance associated with the estimator.

The function $\boldsymbol{\eta}(\boldsymbol{\beta})$ is expanded in Taylor series as in (2.144). The relation (2.136) between the experimental measurements and the parameters becomes:

$$\mathbf{Y} \quad \approx \quad \boldsymbol{\eta}(\mathbf{b}) + \mathbf{S}(\mathbf{b})(\boldsymbol{\beta} - \mathbf{b}) + \boldsymbol{\varepsilon}. \tag{2.148}$$

Then, introducing the following quantities

$$\bar{\boldsymbol{\beta}} = (\boldsymbol{\beta} - \mathbf{b}), \qquad \bar{\mathbf{Y}} = \mathbf{Y} - \boldsymbol{\eta}(\mathbf{b}),$$

Equation (2.148) can be written as

$$\bar{\mathbf{Y}} = \mathbf{S}\bar{\boldsymbol{\beta}} + \boldsymbol{\varepsilon}. \tag{2.149}$$

The variables $\bar{\boldsymbol{\beta}}$ are normally distributed with zero mean and covariance matrix $\mathbf{V}_{\bar{\beta}} = \mathbf{V}_{\beta}$. The experimental errors $\boldsymbol{\varepsilon}$ are assumed to be normally distributed, with zero mean and covariance $\mathbf{V}_Y$, and uncorrelated with $\bar{\boldsymbol{\beta}}$. Thus, the mean of $\bar{\mathbf{Y}}$ is null, the covariance of $\bar{\mathbf{Y}}$ and the covariance of $\bar{\mathbf{Y}}$ and $\bar{\boldsymbol{\beta}}$ are given by

$$\mathbf{V}_{\bar{Y}} = \mathbf{S}\mathbf{V}_{\beta}\mathbf{S}^{\mathrm{T}} + \mathbf{V}_Y, \qquad \mathbf{V}_{\bar{Y}\bar{\boldsymbol{\beta}}} = \mathbf{S}\mathbf{V}_{\beta}. \tag{2.150}$$

The following inverse relation holds:

$$\bar{\boldsymbol{\beta}}^* = \mathbf{G}\bar{\mathbf{Y}}, \tag{2.151}$$

where $\bar{\boldsymbol{\beta}}^*$ is the vector of the estimates of $\bar{\boldsymbol{\beta}}$.

The aim is to find the estimator $\mathbf{G}$ that minimises the variance associated with the estimator itself:

$$E[(\bar{\boldsymbol{\beta}}^* - \bar{\boldsymbol{\beta}})(\bar{\boldsymbol{\beta}}^* - \bar{\boldsymbol{\beta}})^{\mathrm{T}}] = \mathbf{G}\mathbf{V}_{\bar{Y}}\mathbf{G}^{\mathrm{T}} - \mathbf{V}_{\bar{Y}\bar{\beta}}^{\mathrm{T}}\mathbf{G}^{\mathrm{T}} - \mathbf{G}\mathbf{V}_{\bar{Y}\bar{\beta}} + \mathbf{V}_Y. \tag{2.152}$$

This yields:

$$\mathbf{G} = \mathbf{V}_{\bar{Y}\bar{\beta}}^{\mathrm{T}}\mathbf{V}_{\bar{Y}}^{-1} \tag{2.153}$$

and, with some algebra, the estimator can be put in the form

$$\boldsymbol{\beta} = \mathbf{b} + \mathbf{V}_{\beta}\mathbf{S}^{\mathrm{T}}(\mathbf{S}\mathbf{V}_{\beta}\mathbf{S}^{\mathrm{T}} + \mathbf{V}_Y)^{-1}(\mathbf{Y} - \boldsymbol{\eta}(\mathbf{b})). \tag{2.154}$$

By setting $\boldsymbol{\beta} = \mathbf{b}^{k+1}$ and $\mathbf{b} = \mathbf{b}^k$, the following iteration scheme can be established:

$$\mathbf{b}^{k+1} = \mathbf{b}^k + \mathbf{V}_{\beta}(\mathbf{S}^k)^{\mathrm{T}}\left[\mathbf{S}^k\mathbf{V}_{\beta}(\mathbf{S}^k)^{\mathrm{T}} + \mathbf{V}_Y\right]^{-1}(\mathbf{Y} - \boldsymbol{\eta}^k). \tag{2.155}$$

At the end of each iteration it is possible to evaluate the new covariance matrix of the parameters $\mathbf{V}_{\beta}^{k+1}$ by

$$\begin{aligned} \mathbf{V}_{\beta}^{k+1} &= \mathbf{V}_{\beta} - \mathbf{V}_{\bar{Y}\bar{\beta}}^{\mathrm{T}}\mathbf{V}_{\bar{Y}}^{-1}\mathbf{V}_{\bar{Y}\bar{\beta}} = \\ &= \mathbf{V}_{\beta} - \mathbf{V}_{\beta}(\mathbf{S}^k)^{\mathrm{T}}\left[\mathbf{S}^k\mathbf{V}_{\beta}(\mathbf{S}^k)^{\mathrm{T}} + \mathbf{V}_Y\right]^{-1}\mathbf{S}^k\mathbf{V}_{\beta}. \end{aligned} \tag{2.156}$$

Remarks on the equivalence of the estimators

The two iteration schemes (2.147) and (2.155) coalesce if posing $\mu = \mathbf{b}^k$. In other words, the MVE estimator can be interpreted as a B estimator with initial parameters not kept fixed, but updated at each iteration. A proof of this statement can be obtained through the inversion lemma of matrices.

Proof. The following matrix identity holds:

$$(\mathbf{I}_P + \mathbf{AB})^{-1}\mathbf{A} = \mathbf{A}(\mathbf{I}_N + \mathbf{BA})^{-1}, \tag{2.157}$$

where $\mathbf{A}_{P\times N}$ and $\mathbf{B}_{N\times P}$ are general matrices, $\mathbf{I}_P$ and $\mathbf{I}_N$ are the identity matrices of dimensions P and N. By posing $\mathbf{A} = \mathbf{V}_\beta \mathbf{S}^{\mathrm{T}} \mathbf{V}_Y^{-1}$ and $\mathbf{B} = \mathbf{S}$, Equation (2.157) becomes:

$$(\mathbf{V}_\beta^{-1} + \mathbf{S}^{\mathrm{T}}\mathbf{V}_Y^{-1}\mathbf{S})^{-1}\mathbf{S}^{\mathrm{T}}\mathbf{V}_Y^{-1} \quad = \quad \mathbf{V}_\beta \mathbf{S}^{\mathrm{T}}(\mathbf{V}_Y + \mathbf{S}\mathbf{V}_\beta \mathbf{S}^{\mathrm{T}})^{-1}, \tag{2.158}$$

which shows the equivalence between Equations (2.147) and (2.155) under the hypothesis $\boldsymbol{\mu} = \mathbf{b}^k$. □

To sum up, the two estimators coincide in the linear case, but the iterative corrections needed for non linear problems may lead to very different results. In the B estimator, the a priori information enters the objective function and somehow conditions the final estimates, besides driving the estimation process. In the MVE estimator, on the other hand, the a priori information provides starting values to the solution algorithm and its influence gradually decreases as the iterations proceed, so that only the experimental information is retained at the end.

Convergence criterion

The iteration schemes presented in (2.147) and (2.155) require the definition of a convergence criterion. Here, a criterion based on the parameter estimates is adopted: the iterations stop when the updated parameters $\mathbf{b}^{k+1}$ fall within a certain interval from the previous set of estimates $\mathbf{b}^k$. This can be written as

$$\left| \frac{b_i^{k+1} - b_i^k}{b_i^k} \right| \leq \mathrm{TOL} \qquad \forall i, \tag{2.159}$$

where TOL is the prescribed tolerance.

Estimator components for the dynamic identification of laminated composite plates

So far, the estimators have been presented in general terms, while in the following the meaning of the quantities introduced is specified for the dynamic identification of laminated plates.

The experimental data is composed of a set of undamped natural frequencies f_{exp} of the free edge plate. The output of both model and experiment is represented in terms of the plate eigenvalues, obtained as the solution of the classical eigenvalue problem

$$(\mathbf{K} - \lambda \mathbf{M})\,\mathbf{a} = \mathbf{0}, \tag{2.160}$$

which are related to the undamped natural frequencies by the following relation:

$$\lambda = (2\pi f)^2 . \tag{2.161}$$

A simple displacement based finite element formulated for Reddy's HSDT was used to determine the stiffness and mass matrices $\mathbf{K}$ and $\mathbf{M}$. Anyway, the same procedure can obviously be applied using any model, provided it can accurately capture the natural frequencies which are involved in the estimation process.

The deviation associated to the experimental eigenvalues can be evaluated as

$$\delta\lambda_{exp} = \left(\frac{\partial \lambda_{exp}}{\partial f_{exp}}\right)\delta_f = 8\pi^2 f_{exp}\delta_f, \tag{2.162}$$

where δ_f is the deviation of f_{exp}.

The parameters to be estimated are the reduced stiffness coefficients of the laminae in the material coordinates, $\bar{C}_{ij}^{(k)}$, from which the laminae elastic constants can be obtained. In particular, in order to model both the in-plane and through the thickness plate behaviour, the constants to be estimated are E_a, E_b, ν_{ab}, G_{ab}, G_{ac} and G_{bc}, where the material coordinate system (a, b, c) is defined in Figure 2.2. The deviation associated to the stiffness parameters is obtained from the deviation associated to the elastic constants.

The quantities which appear in the estimator formulae (2.147) and (2.155) are

$$\begin{aligned}
\mathbf{Y}^{\mathrm{T}} &= \left[\ \lambda_{exp,1} \quad \lambda_{exp,2} \quad \cdots \quad \lambda_{exp,m}\ \right], \\
\boldsymbol{\eta}^{\mathrm{T}} &= \left[\ \lambda_1 \quad \lambda_2 \quad \cdots \quad \lambda_m\ \right], \\
\mathbf{b} &= \left[\ \bar{C}_{ij}^{(k)}\ \right], \\
\mathbf{V}_Y &= diag(\delta\lambda_{exp,i}), \\
\mathbf{V}_\beta &= diag(\delta\bar{C}_{ij}^{(k)}),
\end{aligned}$$

where m is the number of experimental frequencies considered and λ_i are the numerical eigenvalues corresponding to the current value of the stiffness coefficients $\mathbf{b}$.

The typical component of the sensitivity matrix $\mathbf{S}$ is:

$$S_{ij} = \frac{\partial \lambda_i}{\partial b_j}, \tag{2.163}$$

where b_j denotes the j-th component of $\mathbf{b}$. It can be evaluated, as early proposed by Collins and Thomson (1969) and Fox and Kapoor (1968), by

$$\frac{\partial \lambda_i}{\partial b_j} = \frac{1}{\mathbf{a}_i^{\mathrm{T}} \mathbf{M} \mathbf{a}_i} \mathbf{a}_i^{\mathrm{T}} \frac{\partial \mathbf{K}}{\partial b_j} \mathbf{a}_i. \tag{2.164}$$

Notice that the sensitivity coefficients (2.163) can be normalised as follows (Ayorinde and Yu, 2005):

$$s_{ij} = \frac{\partial \lambda_i}{\partial b_j} \frac{b_j}{\lambda_i}. \tag{2.165}$$

In this way the sensitivity of each mode to different parameters can be evaluated and compared.

Analysis and comparison

In this section the behaviour of the B and MVE estimators is analysed and compared through some numerical tests, devised ad hoc to highlight similarities and differences. Two different single-layer orthotropic rectangular plates, whose geometric characteristics are reported in Table 2.5, are modelled through Reddy's third order theory for a given set of elastic constants (target). The two plates are discretised by uniform meshes of 8×4 and 8×8 elements, respectively. Supposing to operate in ideal conditions, the experimental frequencies are taken as equal to the numerical ones for the estimation process. This eliminates all the sources of error (such as modelling and measurement errors, see Equation (2.136)) and the estimators are expected to yield the target elastic constants, starting from a set of guessed initial values. On the other hand, only the first 14 natural frequencies are considered in the estimation (see Table 2.6) since it is well known that in real experimental conditions it is difficult to measure frequencies associated to higher modes. Moreover, capturing higher modes may require more accurate plate models.

Table 2.5: Characteristics of Plate 1 and Plate 2

	length L	width W	mean thickness h	density ρ	stacking sequence
Plate 1	200 mm	100 mm	6.6 mm	1000 kg/m^3	[0]
Plate 2	100 mm	100 mm	10 mm	1500 kg/m^3	[0]

Table 2.6: Input frequencies of Plate 1 and Plate 2

Plate 1				Plate 2			
mode no.	f_{exp}	mode no.	f_{exp}	mode no.	f_{exp}	mode no.	f_{exp}
1	611.23	8	5406.2	1	2555.5	8	13985
2	2002.7	9	6121.1	2	3591.6	9	15744
3	2171.2	10	6389.0	3	6069.2	10	16334
4	2338.5	11	6520.0	4	9146.4	11	16440
5	2478.2	12	7357.6	5	10677	12	18067
6	3810.3	13	8343.2	6	11305	13	18156
7	5165.3	14	8809.4	7	11512	14	18371

Various numerical tests have been carried out for different initial guesses and parameter covariance. The final estimates and number of iterations performed by the estimation procedures are reported in Tables 2.7-2.12. To check convergence, the tolerance has been set to TOL $= 10^{-3}$. The deviation of the experimental data was assumed to be $\delta_f = 0.01 \cdot f_{exp}$. In order to establish a common ground for comparison, the deviation associated to each elastic constant is taken proportional to the constant itself by a factor d. The symbol - indicates that the procedure does not converge. Since the two plates considered are single-layer, the superscript (k) referring to the k-th lamina is dropped in the following.

Since both the algorithms are based on the sensitivity matrix, a sensitivity analysis is useful to understand the behaviour of the two estimators. The absolute values of the normalised sensitivity coefficients (2.165) are plotted in Figures 2.21 and 2.22 for Plate 1 and Plate 2, respectively.

Both diagrams show that the first natural frequencies are more sensitive to $\bar{C}_{11}$, $\bar{C}_{22}$ and $\bar{C}_{66}$, that is the stiffness coefficients associated to the two elastic

Table 2.7: Test 1 on Plate 1: final estimates and iterations

	dev. d	E_a (GPa)	E_b (GPa)	ν_{ab}	G_{ab} (GPa)	G_{ac} (GPa)	G_{bc} (GPa)	n. iter.
Initial		100	7	0.33	4	4	1	
B	1/3	-	-	-	-	-	-	-
B	1/6	145.0	10.41	0.2087	3.008	3.554	1.404	15
B	1/10	142.0	10.47	0.2149	3.019	3.924	1.277	7
MVE	1/3	-	-	-	-	-	-	-
MVE	1/6	150.1	9.996	0.2539	3.000	2.995	2.004	87
MVE	1/10	149.8	10.01	0.2389	3.000	3.015	1.989	85
Target		150	10	0.25	3	3	2	

Table 2.8: Test 2 on Plate 1: final estimates and iterations

	dev. d	E_a (GPa)	E_b (GPa)	ν_{ab}	G_{ab} (GPa)	G_{ac} (GPa)	G_{bc} (GPa)	n. iter.
Initial		180	12	0.20	2	2	4	
B	1/3	152.4	9.870	0.2787	2.997	2.791	2.261	10
B	1/6	156.7	9.663	0.2726	2.981	2.397	3.442	9
B	1/10	159.2	9.630	0.2639	2.962	2.272	3.801	7
MVE	1/3	150.0	10.00	0.2493	3.000	3.001	1.999	34
MVE	1/6	150.0	10.00	0.2466	3.000	3.005	1.998	41
MVE	1/10	150.3	9.987	0.2626	3.000	2.977	2.013	18
Target		150	10	0.25	3	3	2	

Table 2.9: Test 3 on Plate 1: final estimates and iterations

	dev. d	E_a (GPa)	E_b (GPa)	ν_{ab}	G_{ab} (GPa)	G_{ac} (GPa)	G_{bc} (GPa)	n. iter.
Initial		130	11	0.20	3.5	3.5	1.5	
B	1/3	148.9	10.12	0.2122	3.002	3.113	1.832	6
B	1/6	147.7	10.21	0.2099	3.004	3.234	1.695	6
B	1/10	146.5	10.28	0.2104	3.007	3.366	1.602	5
MVE	1/3	150.0	9.999	0.2509	3.000	2.999	2.001	20
MVE	1/6	149.9	10.00	0.2458	3.000	3.006	1.997	19
MVE	1/10	149.8	10.01	0.2382	3.000	3.015	1.991	56
Target		150	10	0.25	3	3	2	

Table 2.10: Test 1 on Plate 2: final estimates and iterations

	dev. d	E_a (GPa)	E_b (GPa)	ν_{ab}	G_{ab} (GPa)	G_{ac} (GPa)	G_{bc} (GPa)	n. iter.
Initial		280	28	0.19	15	15	8	
B	1/3	205.7	19.98	0.2626	9.914	10.21	4.090	5
B	1/6	198.1	19.68	0.2656	9.8723	11.88	4.298	5
B	1/10	195.64	19.62	0.2660	9.845	12.67	4.408	7
MVE	1/3	210.2	19.97	0.2393	9.932	9.497	4.159	4
MVE	1/6	201.8	19.82	0.5290	9.910	10.24	4.086	139
MVE	1/10	207.6	19.99	0.3296	9.925	9.751	4.075	197
Target		207	20	0.25	10	10	4	

Table 2.11: Test 2 on Plate 2: final estimates and iterations

	dev. d	E_a (GPa)	E_b (GPa)	ν_{ab}	G_{ab} (GPa)	G_{ac} (GPa)	G_{bc} (GPa)	n. iter.
Initial		160	26	0.31	7	7	6	
B	1/3	275.6	20.38	0.5312	11.13	2.988	9.804	11
B	1/6	296.3	23.82	0.3084	11.09	2.362	9.393	12
B	1/10	197.2	20.48	0.4001	9.861	4.627	7.426	8
MVE	1/3	-	-	-	-	-	-	-
MVE	1/6	-	-	-	-	-	-	-
MVE	1/10	229.5	19.93	0.2837	9.968	3.869	13.11	82
Target		207	20	0.25	10	10	4	

Table 2.12: Test 3 on Plate 2: final estimates and iterations

	dev. d	E_a (GPa)	E_b (GPa)	ν_{ab}	G_{ab} (GPa)	G_{ac} (GPa)	G_{bc} (GPa)	n. iter.
Initial		160	14	0.31	7	7	6	
B	1/3	210.8	19.95	0.2260	10.01	9.418	4.077	6
B	1/6	215.7	19.82	0.2211	9.927	8.651	4.368	6
B	1/10	216.1	19.41	0.2235	9.862	8.316	4.896	5
MVE	1/3	206.9	20.00	0.2364	10.00	10.05	4.002	66
MVE	1/6	206.8	20.00	0.2235	10.00	10.08	4.005	13
MVE	1/10	210.2	19.97	0.2216	9.933	9.517	4.164	18
Target		207	20	0.25	10	10	4	

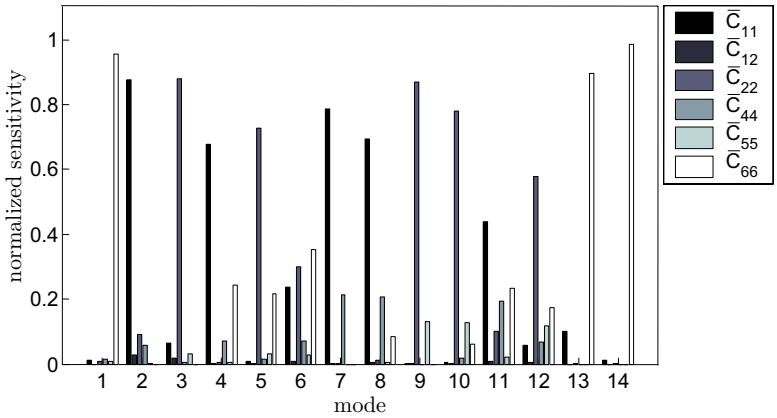

Figure 2.21: Forward sensitivity analysis for Plate 1

moduli E_a and E_b and the in-plane shear modulus G_{ab}. This means that the experimental data contain more information on $\bar{C}_{11}$, $\bar{C}_{22}$ and $\bar{C}_{66}$ rather than on $\bar{C}_{44}$, $\bar{C}_{55}$ and $\bar{C}_{12}$. As a consequence, the transverse shear moduli G_{bc} and G_{ac} and Poisson's ratio ν_{ab} are expected to be more difficult to estimate with respect to the in-plane elastic constants.

The sensitivities are also influenced by the plate aspect ratio. Plate 1 ($L/W = 2$) is more sensitive to $\bar{C}_{12}$, which accounts for directional effects. On the other hand, Plate 2 ($L/W = 1$) is less sensitive to $\bar{C}_{11}$, since the modulus E_b is much lower than E_a and, consequently, most low frequency modes involve the b direction. Therefore the geometry of Plate 1 is preferable as it allows a more effective overall identification of the elastic constants. This should be taken into consideration when setting up the experiment. More details on optimal experiment design can be found in the work by Frederiksen (1998).

Some of the quantities which enter the estimation process should be defined by the analyst. These are the initial parameter estimates $\boldsymbol{\mu}$ and the covariance matrices $\mathbf{V}_\beta$ and $\mathbf{V}_Y$. Obviously, convergence of the iterative procedures (2.147) and (2.155) strongly depends upon these choices. The covariance matrices influ-

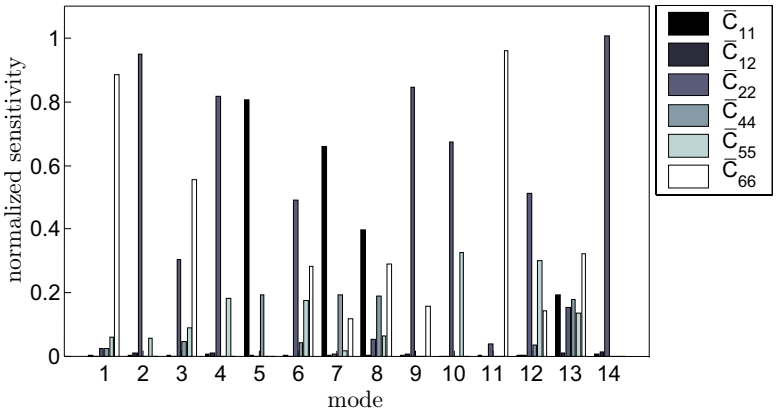

Figure 2.22: Forward sensitivity analysis for Plate 2

ence the amount of parameter correction at each iteration. High confidence on the initial estimates (that is, small entries in $\mathbf{V}_\beta$) results in small corrections, while low confidence on the initial estimates may lead to large corrections, especially in the first step. On the other hand, the smaller the covariance $\mathbf{V}_Y$ associated with the experimental values, the larger is the parameter correction. Thus, for convergence reasons, $\mathbf{V}_\beta$ should not be too large and $\mathbf{V}_Y$ not too small.

Another important choice is the combined definition of the initial estimates for E_a and E_b. In particular, for initial value sets with E_a overestimated and E_b underestimated, or viceversa, the estimation procedures tend to fail. An explanation can be given by considering the sensitivity coefficients in Equation (2.165). Both s_{i1} and s_{i3} are positive for every mode. As a consequence, initial values for $\bar{C}_{22}$ higher than the real ones result in model frequencies higher than the real ones. Analogously, initial values for $\bar{C}_{11}$ lower than the real ones result in model frequencies lower than the real ones. These two opposite effects are both strong, because the sensitivity coefficients are high, and may engender an oscillatory behaviour of the stepwise corrected parameters with loss of

convergence.

As already pointed out, the difference between the two estimators, from the analytical point of view, lies on the role of the initial estimates. In the B estimator, the initial values are fixed, while in the MVE they serve as starting values of the iterative scheme, which are updated at each iteration. As a consequence, the dependence of the final estimates upon the initial guesses is very different in the two estimators (see Tables 2.7-2.12).

If the algorithm converges to the global minimum, the MVE estimates depend only upon the information available in the experimental data: high sensitivity to the parameters implies that the target values are obtained. In this case, any difference between final estimates and target values is due to the stop criterion. On the contrary, different initial values or different deviations yield significantly different estimates using the B algorithm. The bias is stronger as the deviation becomes smaller and the parameters are forced to remain close to the initial guesses. A clear example of this behaviour can be seen by observing Tables 2.8 and 2.9: the E_a estimates are included in the interval between the initial and target values and move closer to the initial guesses as the deviation d becomes smaller. On the other hand, the B estimator is much more efficient than the MVE estimator, as clearly revealed by the number of iterations performed.

2.4.2 A modified procedure

Here, a two stages solution strategy is presented aiming at improving convergence of the MVE estimator. The modified MVE estimator is denoted by MVE-mod. The idea stems from the observation that there are two sets of parameters with very different influence on the natural frequencies. In fact, as noticed in the previous section, the eigenvalues are very sensitive to $\bar{C}_{11}$, $\bar{C}_{22}$ and $\bar{C}_{66}$ and much less to $\bar{C}_{12}$, $\bar{C}_{44}$ and $\bar{C}_{55}$ (see Figures 2.21 and 2.22). For this reason, the correction of the last three stiffness coefficients is much slower. This suggests to split the MVE estimation procedure into two stages as follows.

- In the first stage, the estimation procedure is carried out using small values for the parameter deviations, in order to avoid the risk of non convergence. The tolerance is set to a value larger than the prescribed one: $\mathrm{TOL} = 10^{-2}$. This stage is designed for the parameters most sensitive to

Table 2.13: Test 1 on Plate 1: MVE-mod final estimates and iterations

	dev. d	E_a (GPa)	E_b (GPa)	ν_{ab}	G_{ab} (GPa)	G_{ac} (GPa)	G_{bc} (GPa)	n. iter.
Initial		100	7	0.33	4	4	1	
stage 1	1/6	151.2	9.868	0.3129	2.998	2.892	2.196	41
stage 2	1/3	150.0	10.00	0.2507	3.000	2.999	2.001	16
stage 1	1/10	149.2	10.13	0.2080	3.002	3.083	1.815	9
stage 2	1/3	150.0	10.00	0.2492	3.000	3.001	1.999	17
Target		150	10	0.25	3	3	2	

Table 2.14: Test 2 on Plate 1: MVE-mod final estimates and iterations

	dev. d	E_a (GPa)	E_b (GPa)	ν_{ab}	G_{ab} (GPa)	G_{ac} (GPa)	G_{bc} (GPa)	n. iter.
Initial		180	12	0.20	2	2	4	
stage 1	1/3	149.9	10.01	0.2416	3.000	3.011	1.994	24
stage 2	1/2	150.0	10.00	0.2498	3.000	3.000	2.000	7
stage 1	1/6	149.7	10.02	0.2234	3.001	3.024	1.987	9
stage 2	1/3	150.0	10.00	0.2492	3.000	3.001	1.999	15
stage 1	1/10	150.4	9.978	0.2635	2.999	2.958	2.030	14
stage 2	1/3	150.0	10.00	0.2506	3.000	2.999	2.000	11
Target		150	10	0.25	3	3	2	

the frequency data (typically E_a, E_b and G_{ab}), which quickly converge.

- In the second stage, the initial values are taken as the final estimates of the first stage, but the deviations associated to the parameters are increased. This is expected to accelerate convergence of the remaining parameters, without interfering with the estimation of the parameters which have already reached convergence during the first stage. The tolerance is set to the prescribed value: $\text{TOL} = 10^{-3}$.

To show the advantages of the MVE-mod procedure, the same numerical tests discussed in the previous section are considered. The results are shown in Tables 2.13-2.18. As it can be seen from the last column, the final estimates are very similar to the ones predicted by the classical MVE procedure, but convergence is faster.

Table 2.15: Test 3 on Plate 1: MVE-mod final estimates and iterations

	dev. d	E_a (GPa)	E_b (GPa)	ν_{ab}	G_{ab} (GPa)	G_{ac} (GPa)	G_{bc} (GPa)	n. iter.
Initial		130	11	0.20	3.5	3.5	1.5	
stage 1	1/3	150.1	9.990	0.2598	3.000	2.987	2.008	9
stage 2	1/2	150.0	10.00	0.2503	3.000	3.000	2.000	7
stage 1	1/6	150.0	10.00	0.2407	3.000	3.004	1.996	5
stage 2	1/3	150.0	10.00	0.2491	3.000	3.001	1.999	10
stage 1	1/10	149.5	10.08	0.2214	3.001	3.054	1.893	7
stage 2	1/3	150.0	10.00	0.2491	3.000	3.001	1.999	17
Target		150	10	0.25	3	3	2	

Table 2.16: Test 1 on Plate 2: MVE-mod final estimates and iterations

	dev. d	E_a (GPa)	E_b (GPa)	ν_{ab}	G_{ab} (GPa)	G_{ac} (GPa)	G_{bc} (GPa)	n. iter.
Initial		280	28	0.19	15	15	8	
stage 1	1/3	210.1	19.97	0.2394	9.932	9.500	1.459	3
stage2	1/2	210.2	19.97	0.2392	9.932	9.497	4.159	1
stage 1	1/6	201.7	19.81	0.3299	9.905	10.87	4.148	24
stage 2	1/3	201.7	19.82	0.5467	9.911	10.19	4.080	30
stage 1	1/10	206.7	19.99	0.2569	9.920	10.06	4.083	8
stage 2	1/3	208.0	19.99	0.4095	9.927	9.523	4.056	61
Target		207	20	0.25	10	10	4	

Table 2.17: Test 2 on Plate 2: MVE-mod final estimates and iterations

	dev. d	E_a (GPa)	E_b (GPa)	ν_{ab}	G_{ab} (GPa)	G_{ac} (GPa)	G_{bc} (GPa)	n. iter.
Initial		160	26	0.31	7	7	6	
stage 1	1/10	227.7	20.16	0.3298	9.994	3.897	10.74	24
stage 2	1/3	230.0	19.93	0.2795	9.968	3.869	13.15	12
Target		207	20	0.25	10	10	4	

Table 2.18: Test 3 on Plate 2: MVE-mod final estimates and iterations

	dev. d	E_a (GPa)	E_b (GPa)	ν_{ab}	G_{ab} (GPa)	G_{ac} (GPa)	G_{bc} (GPa)	n. iter.
Initial		160	14	0.31	7	7	6	
stage 1	1/3	206.5	20.00	0.2140	9.998	10.15	4.003	5
stage 2	1/2	207.0	20.00	0.2452	10.00	10.02	4.001	44
stage 1	1/6	207.4	20.00	0.2223	10.00	9.981	4.011	8
stage 2	1/3	206.9	20.00	0.2393	10.00	10.04	4.002	44
stage 1	1/10	212.1	19.96	0.2199	9.944	9.254	4.184	8
stage 2	1/3	210.0	19.97	0.2227	9.931	9.547	4.161	4
Target		207	20	0.25	10	10	4	

2.4.3 Testing of the estimator procedures

Various case studies are solved using the B, MVE and MVE-mod procedures. Two cross-ply laminates, having the same material properties and stacking sequence but different aspect ratio, are considered in the first case study. Initially, the estimation is carried out using the natural frequencies obtained numerically, then a real experiment is simulated by using pseudo-experimental input frequencies. In the second case study, a cross-ply and an angle-ply laminates are taken into consideration to investigate the effect of the stacking sequence; in this example, the input frequencies are again assumed as equal to the numerical frequencies, so to disregard any sources of error. Finally, the third case study deals with a single-layer carbon-epoxy plate studied by Frederiksen (1997). In this case, the input frequencies are real experimental measurements, so that both modelling and measurement errors are present.

In stage 2 of the MVE-mod procedure, the deviations are twice those in the first stage.

Cross-ply symmetric laminate

Two cross-ply symmetric laminates with stacking sequence (0/90/90/0) and different geometry were considered. Plate 1c is square, while Plate 2c is rectangular with sides ratio 1 : 2. The plates were discretised using 20×20 and 20×10 finite elements, respectively, their characteristics are reported in Table 2.19. Figure 2.23 represents the natural modes associated to the considered frequencies for the rectangular plate. The input frequencies are reported in Table 2.20 and the

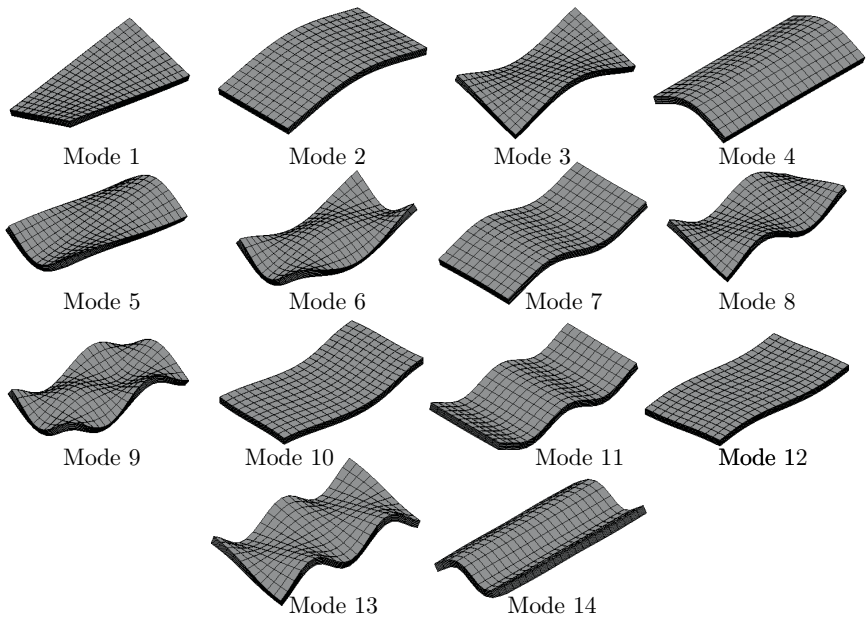

Figure 2.23: Natural modes corresponding to the frequencies considered in the analysis (Plate 2c)

results for Plates 1c and 2c are reported in Table 2.21.

In Plate 1c, only the elastic constants E_a and G_{ab} were evaluated within less than 10% of the target values, while the other parameters were not estimated correctly. On the other hand, in Plate 2c much better results were obtained, especially using the MVE and MVE-mod estimators. These results show once again the importance of the choice of the experiment, as already pointed out in the examples concerning single layer orthotropic plates. As regards the behaviour of the different algorithms, in Plate 2c the MVE and MVE-mod algorithms yield the target values, while the B estimator still shows a bias which is higher for the parameter for which information is less. Also, it can be seen that the MVE-mod requires less iterations than the original MVE.

The elastic constants for Plate 2c are estimated using pseudo-experimental

Table 2.19: Characteristics of Plate 1c and Plate 2c

	length L	width W	mean thickness h	density ρ	stacking sequence
Plate 1	100 mm	100 mm	4 mm	1500 kg/m^3	[0/90/90/0]
Plate 2	100 mm	50 mm	4 mm	1500 kg/m^3	[0/90/90/0]

Table 2.20: Input frequencies of Plates 1c and 2c

Plate 1					Plate 2				
mode	f_{num}	mode	f_{num}	mode	f_{num}	f_{pseudo}	mode	f_{num}	f_{pseudo}
1	546.46	8	4245.4	1	1074.4	1089.6	8	8095.6	8192.0
2	1482.1	9	5878.9	2	3268.5	3234.0	9	10717	10788
3	1832.9	10	7428.7	3	3820.8	3830.7	10	11476	11624
4	3269.4	11	7651.2	4	5704.8	5613.3	11	12677	12767
5	3416.4	12	7698.1	5	6037.4	6027.9	12	12710	12814
6	3961.3	13	7792.5	6	7544.4	7542.9	13	12994	13084
7	4105.3	14	8242.7	7	7688.2	7595.8	14	14145	14089

Table 2.21: Final estimates and iterations for Plates 1c and 2c

Plate 1c		E_a (GPa)	E_b (GPa)	ν_{ab}	G_{ab} (GPa)	G_{ac} (GPa)	G_{bc} (GPa)	n. iter.
Initial		150	8	0.3	5	5	3	
deviation		18	3	0.1	0.5	0.5	0.5	
B		124.4	4.459	0.5441	2.512	4.263	0.4114	5
MVE		125.5	4.153	0.7757	2.489	4.195	0.3602	20
MVE-mod	1	125.6	4.167	0.7479	2.489	4.176	0.3662	12
	2	125.5	4.152	0.7757	2.489	4.200	0.3591	5
Target		125	5	0.25	2.5	2.5	1	

Plate 2c		E_a (GPa)	E_b (GPa)	ν_{ab}	G_{ab} (GPa)	G_{ac} (GPa)	G_{bc} (GPa)	n. iter.
Initial		150	8	0.3	5	5	3	
deviation		18	3	0.1	0.5	0.5	0.5	
B		123.6	4.079	0.5353	2.507	3.564	0.7374	9
MVE		125.0	5.000	0.2535	2.500	2.500	0.9999	64
MVE-mod	1	125.0	4.993	0.2718	2.500	2.500	0.9995	38
	2	125.0	5.000	0.2508	2.500	2.500	1.000	13
Target		125	5	0.25	2.5	2.5	1	

Table 2.22: Final estimates and iterations for Plate 2c - pseudoexperimental frequencies

		E_a (GPa)	E_b (GPa)	ν_{ab}	G_{ab} (GPa)	G_{ac} (GPa)	G_{bc} (GPa)	n. iter.
Initial		150	8	0.3	5	5	3	
deviation		18	3	0.1	0.5	0.5	0.5	
B		119.8	4.100	0.5469	2.581	3.739	0.7843	7
MVE		120.8	4.830	0.4371	2.572	2.668	1.041	48
MVE-mod	1	121.1	4.582	0.6817	2.612	2.673	0.9658	17
	2	120.8	4.830	0.4395	2.572	2.668	1.041	11
Target		125	5	0.25	2.5	2.5	1	

frequencies to simulate a real experimental set of data. Pseudo-experimental input data are generated by introducing some error on the natural frequencies obtained numerically. Each numerical frequency f_{num} is substituted by a random value f_{pseudo} extracted from a Gaussian probability distribution with mean f_{num} and deviation δf. As already stated, the deviation δf for each frequency is taken proportional to the frequency itself. This represents the fact that higher natural frequencies are usually affected by more experimental error that lower frequencies. The results are reported in Table 2.22.

Comparing the final estimates in Tables 2.21 and 2.22, it can be seen that the error introduced in the input frequencies reflects on the results obtained by all procedures, affecting particularly the parameters for which little information is available, such as ν_{ab}. Besides that, the MVE and MVE-mod estimators yield analogous results, while the B estimator shows the bias already noticed in the tests carried out using the numerically generated frequencies.

Cross-ply versus angle-ply non symmetric laminate

A cross-ply and an angle-ply laminate, having the same geometrical and mechanical characteristics, are considered in this case study. The specimens characteristics are reported in Table 2.23 and the input natural frequencies computed by a uniform mesh of 20×20 elements are reported in Table 2.24. Table 2.25 collects the results for the three procedures. The more complicated stacking sequence of the angle-ply laminate increases the difficulties in the identification of the in-plane elastic constant. In the B estimator, this is reflected in final

Table 2.23: Characteristics of cross-ply and angle-ply plates

length L	width W	thickness h	density ρ	stacking sequence
100 mm	50 mm	3.3 mm	1500 kg/m^3	$[(0/90)_8 0(90/0)_8]$
100 mm	50 mm	3.3 mm	1500 kg/m^3	$[(0/45/90/-45)_4 0(45/90/-45/0)_4]$

Table 2.24: Input frequencies for cross-ply and angle-ply plates

Cross-ply				Angle-ply			
mode no.	f_{exp}	mode no.	f_{exp}	mode no.	f_{exp}	mode no.	f_{exp}
1	1369.7	8	10103	1	2074.4	8	10657
2	2335.6	9	11779	2	2250.7	9	11641
3	3598.6	10	12755	3	4956.8	10	13459
4	6255.1	11	12872	4	5602.9	11	15491
5	7390.8	12	16071	5	7456.6	12	17182
6	8372.0	13	17280	6	8609.7	13	19113
7	8755.9	14	18504	7	8613.2	14	19121

Table 2.25: Final estimates and iterations for cross-ply and angle-ply plates

Cross-ply		E_a (GPa)	E_b (GPa)	ν_{ab}	G_{ab} (GPa)	G_{ac} (GPa)	G_{bc} (GPa)	n. iter.
Initial		150	17	0.25	8	8	5	
deviation		17.5	4	0.05	1.5	1.5	1.5	
B		120.1	13.69	0.2812	5.989	6.206	3.206	3
MVE		125.0	9.458	0.3058	6.000	5.996	3.000	39
MVE-mod	1	124.9	9.449	0.3306	5.999	5.983	2.985	10
	2	125.0	9.491	0.3013	6.000	5.999	3.000	13
Target		125	9.5	0.30	6	6	3	

Angle-ply		E_a (GPa)	E_b (GPa)	ν_{ab}	G_{ab} (GPa)	G_{ac} (GPa)	G_{bc} (GPa)	n. iter.
Initial		150	17	0.25	8	8	5	
deviation		17.5	4	0.05	1.5	1.5	1.5	
B		119.0	12.84	0.3231	6.943	6.178	3.179	3
MVE		124.9	9.306	0.3233	6.103	5.998	2.996	94
MVE-mod	1	124.3	8.653	0.4175	6.504	5.983	2.986	9
	2	125.0	9.469	0.3036	6.017	6.000	2.999	34
Target		125	9.5	0.30	6	6	3	

estimates that are more influenced by the initial values. In the MVE and MVE-mod procedures, the number of iterations required increases, but the accuracy of the final estimates is not significantly modified.

Single-layer carbon-epoxy plate

A single-layer unidirectional carbon-epoxy (T300 carbon fibre) composite plate is considered. The elastic constants were estimated by Frederiksen (1997) using a two step approach. Firstly, a thin specimen was considered for the estimation of the four in-plane elastic constants. Subsequently, a second thicker specimen was taken in order to estimate the two transverse shear moduli. In this work, only the second specimen is taken into consideration in order to simultaneously estimate all the six elastic constants. The known specimen characteristics are reported in Table 2.26 and the measured natural frequencies are reported in Table 2.27.

The initial set of estimates needed for the estimation process are obtained through the rule of mixtures, with a fibre volume fraction v_f of 60%. Producers' technical sheets provide the following data:

$$\begin{array}{rl} \text{carbon fibre T300} & E_f = 230 - 240 \text{ GPa} \\ & \nu_f = 0.27 \\ \text{epoxy resin} & E_m = 7 \text{ GPa} \\ & \nu_m = 0.36 \end{array}$$

where the subscripts f and m stand for fibre and matrix elastic constants. The values of E and ν allow to evaluate G_f and G_m, then the rule of mixtures can be applied:

$$\begin{aligned} E_a &= E_f v_f + E_m v_m = 144 \text{ GPa} \\ E_b &= \frac{E_f E_m}{E_f v_m + E_m v_f} = 16.5 \text{ GPa} \\ \nu_{ab} &= \nu_f v_f + \nu_m v_m = 0.30 \\ G_{ab} = G_{ac} &= \frac{G_f G_m}{G_f v_m + G_m v_f} = 6 \text{ GPa} \end{aligned}$$

where v_m is the matrix volume fraction. The initial value for G_{bc} is taken as 4 GPa. The plate is analysed by a 50×50 element mesh, which has been verified to satisfactorily resolve the first 14 natural modes.

The results of the estimation process are collected in Table 2.28, together with the assumed deviations. As it can be observed, they are in good agreement with the values found by Frederiksen (1997).

Comparing the estimators, one notices once again that the B estimator exhibits some bias in the identification of the constants ν_{ab}, G_{ac} and G_{bc}, because of the less sensitivity of the natural frequencies. On the contrary, this is not observed in the MVE estimator, which yields quite good estimates.

Table 2.26: Characteristics of carbon-epoxy plate

length L	width W	mean thickness h	density ρ	stacking sequence	fibre volume fraction
100.1 mm	53.0 mm	3.36 mm	1537 kg/m^3	[0]	60%

Table 2.27: Measured frequencies for carbon-epoxy plate

mode no.	f_{exp}	mode no.	f_{exp}
1	1121.4	8	7671.4
2	2795.4	9	8073.0
3	2971.5	10	8431.8
4	3590.6	11	10212
5	3633.1	12	10281
6	5947.5	13	14007
7	7655.1	14	14048

Table 2.28: Estimates for carbon-epoxy plate

	E_a (GPa)	E_b (GPa)	ν_{ab}	G_{ab} (GPa)	G_{ac} (GPa)	G_{bc} (GPa)
Initial	144	16.5	0.30	6	6	4
deviation	15	3.5	0.05	1.5	1.5	1.5
B	113.5	8.47	0.361	4.44	4.31	3.39
MVE	113.3	8.52	0.323	4.45	4.42	2.91
Frederiksen (1997)	113.0	8.50	0.323	4.45	4.43	2.97

Le leghe a memoria di forma

Le leghe a memoria di forma sono materiali in grado di recuperare la forma originale in seguito a grandi deformazioni, secondo due diverse modalità:

- *se il materiale è deformato a bassa temperatura, il recupero avviene in seguito al riscaldamento sopra una temperatura critica. Questa proprietà è nota con il nome di effetto a memoria di forma;*
- *se il materiale è deformato ad alta temperatura, il recupero avviene in seguito alla semplice rimozione del carico applicato. Questa proprietà è nota con il nome di superelasticità.*

L'effetto a memoria di forma fu osservato per la prima volta negli anni '30 su leghe di oro e cadmio. L'interesse in questi materiali si diffuse soprattutto a partire dagli anni '60, quando le proprietà di recupero della forma furono osservate in una lega di nichel e titanio, ribattezzata Nitinol dal nome del laboratorio dove la scoperta fu effettuata (Nichel Titanium Naval Ordnance Laboratory). Nonostante la presenza di proprietà a memoria di forma in altre leghe, il Nitinol è ancora oggi la lega a memoria di forma più diffusa commercialmente.

Le proprietà macroscopiche dei materiali a memoria di forma sono legate a cambiamenti microstrutturali che avvengono all'interno del materiale. La struttura e l'organizzazione dei cristalli all'interno del materiale sono infatti influenzate dalla temperatura e dallo sforzo applicato, dando origine ad un significativo accoppiamento termomeccanico. Le proprietà e le caratteristiche microstrutturali dei materiali a memoria di forma sono discusse nella sezione 3.1.

I materiali a memoria di forma mostrano il comportamento accoppiato tipico dei materiali attivi. In particolare, l'effetto a memoria di forma associato al riscaldamento può essere utilizzato per realizzare attuatori, mentre sono stati portati avanti alcuni tentativi di realizzare sensori basati sulle proprietà associate alle diverse microstrutture. D'altra parte, il recupero superelastico della forma non richiede alcun intervento esterno; per questo la superelasticità è spesso sfruttata in applicazioni passive. Nella sezione 3.2 sono discusse alcune applicazioni delle leghe a memoria di forma.

La modellazione dei materiali attivi, in particolare delle leghe a memoria di forma, costituisce un problema ancora aperto. In letteratura sono stati proposti

numerosi modelli costitutivi, ognuno dei quali descrive solo alcuni degli aspetti del complesso comportamento termomeccanico dei materiali a memoria di forma. Inoltre, non tutti gli aspetti del comportamento delle leghe a memoria di forma sono, ad oggi, stati chiariti. Nella sezione 3.3 si propone una discussione critica di diversi modelli costitutivi monoassiali e triassiali per le leghe a memoria di forma, mentre nella sezione 3.4 sono riportati e discussi alcuni risultati sperimentali che mostrano comportamenti non descritti dai modelli costitutivi correnti.

Chapter 3

Shape memory alloys

Shape memory alloys (SMA) are metal alloys able to recover their original shape after large deformations (Otsuka and Wayman, 1999). Depending upon the alloy material properties and the external conditions, shape recovery can occur in two ways:

- if the material is deformed at low temperature, its original shape can be recovered by heating it above a characteristic temperature. This property is known as the shape memory effect (SME);

- if the material is deformed at high temperature, its original shape can be recovered by simply removing the applied load. This property is known as superelasticity or pseudoelasticity (SE).

The shape memory effect was first observed in gold-cadmium alloys (Chang, 1951; Ölander, 1932). Widespread interest on shape memory materials, however, had to wait until the 1960s, when shape memory properties were observed in a nickel-titanium alloy (Buehler et al., 1963). From the name of the laboratory where these effect were observed, the Ni-Ti alloy became known as Nitinol (Nickel Titanium Naval Ordnance Laboratory) and it is still the most common commercially available shape memory alloy. Various other materials are known to display shape memory properties, such as ternary nickel-titanium alloys (Ni-Ti-Cu, Ni-Ti-Fe, etc.) and copper based alloys (Cu-Zn, Cu-Al-Ni, etc.).

The macroscopic properties of shape memory alloys are related to changes in the material microstructure. Indeed, the crystal structure and arrangement within these materials are influenced by both temperature and applied stress, resulting in a strong thermomechanical coupling. The shape memory alloy properties and microstructure are discussed in Section 3.1.

Shape memory alloys exhibit the coupled behaviour typical of active materials. In particular, the shape recovery associated to heating typical of the shape memory effect can be used for actuation, while some attempts have been carried out to use the property changes associated to the different microstructures for sensing. On the other hand, superelastic shape recovery involves no temperature change, therefore superelasticity is generally used in passive applications. Some applications of shape memory alloys are discussed in Section 3.2.

The modelling of active materials, and in particular of shape memory alloys, is still an open problem. Indeed, a number of constitutive models have been proposed in the literature, each describing different characteristics of the complex shape memory alloy behaviour. Moreover, some features of the shape memory alloy material behaviour are not fully understood to this day. A critical discussion of various one and three-dimensional shape memory alloys constitutive models is carried out in Section 3.3, while in Section 3.4 some experimental observation are presented and discussed regarding phenomena which are not included in the current constitutive modelling.

3.1 Shape memory alloy properties

Shape memory alloys exhibit two peculiar properties, known as the shape memory effect and superelasticity. If the material is deformed at low temperature, upon unloading it retains an apparently plastic deformation, which can be recovered by heating it above a characteristic temperature (thermal recovery, known as the shape memory effect). At high temperature, on the other hand, large deformations can be recovered by simply removing the applied load (mechanical recovery, known as superelasticity).

The shape memory effect is depicted in Figure 3.1 in the stress-strain-temperature space. The material starts from the reference configuration 1 at a given temperature and zero stress. If the stress is increased, the material behaviour is at first linearly elastic (slope 1–2), then apparently plastic deformations

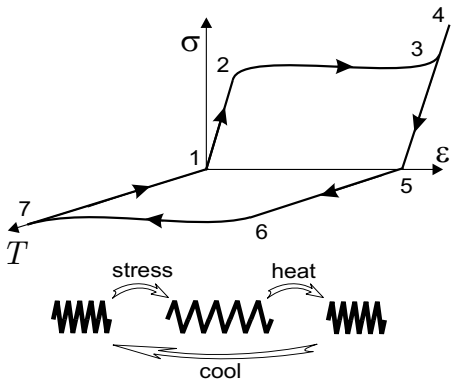

Figure 3.1: Shape memory effect

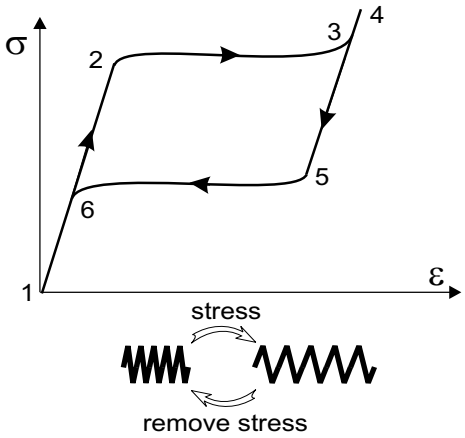

Figure 3.2: Superelasticity

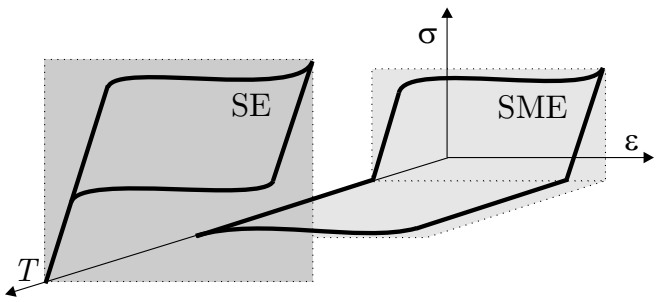

Figure 3.3: Shape memory effect and superelasticity

start to develop at nearly constant stress (plateau 2–3). Unlike the plastic deformation, however, the shape memory alloy deformation reaches saturation and further increase of the load leads to a new linear elastic branch (slope 3–4). Upon unloading, a residual deformation is present (point 5), which can be recovered by heating the material to a characteristic temperature under no load (points 6–7). Finally, if the material is cooled down to the initial temperature, the initial material state 1 is completely recovered.

Superelasticity is depicted in the stress-strain space in Figure 3.2. The loading branch is similar to the one described for the shape memory effect (points 1–4), whereas a stress plateau is present upon unloading (points 5–6), leading to no residual deformation at zero stress. Due to the presence of a small hysteresis loop between the loading and unloading plateau, this property is often referred to as pseudoelasticity.

These apparently unrelated properties can be observed in the same material if it is tested at different temperatures (Figure 3.3). Indeed, the characteristic temperature that separates the shape memory alloy and superelasticity temperature ranges depends upon the alloy type and chemical composition, thus it is possible to find alloys which show either of the effects at room temperature.

The thermal shape recovery associated to shape memory effect can be used for actuation purposes. Indeed, if shape recovery occurs under an applied load, mechanical work is developed. Figure 3.4 depicts a very simple experiment: a

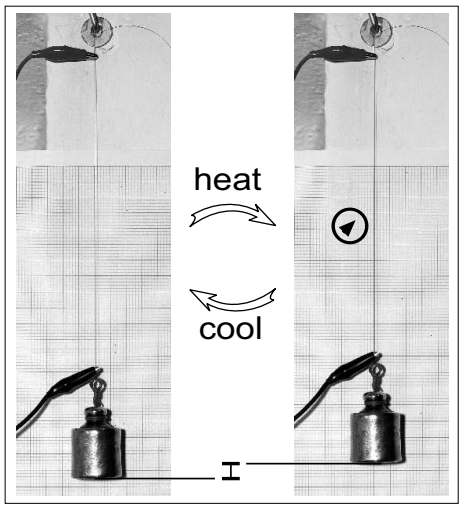

Figure 3.4: Shape recovery under applied load

Flexinol® wire 0.15 mm in diameter was able to lift a mass of 200 g by 10 mm when electrically heated. On the other hand, if the shape memory alloy is completely constrained and prevented from recovering its original shape, upon heating it develops high recovery stresses which depend upon the temperature and initial deformation. This phenomenon is usually referred to as constrained recovery and it is very important in applications such as shape memory alloy hybrid composites (discussed in Chapter 4), as in that case the composite constitutes a constraint to the shape memory alloy wires.

The described shape memory effect is also known as one-way shape memory effect, as only the high-temperature shape is memorised by the material. Indeed, no change in shape occurs upon cooling under no applied load (Figure 3.1, points 7–1). The two-way memory effect, on the other hand, is related to the ability of the material to remember two different shapes in the cold and hot configuration. This property allows to move between the two shapes by simply changing the temperature, with no need of applied load. The two-way shape memory effect is schematically represented in Figure 3.5(b). It should be noted that, while the one-way shape memory effect is an intrinsic characteristic of shape memory

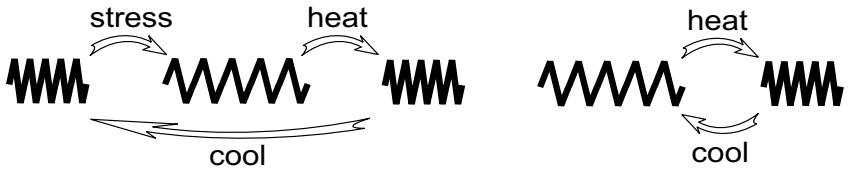

(a) One-way shape memory effect (b) Two-way shape memory effect

Figure 3.5: One-way and two-way shape memory effect

alloys, two-way memory needs to be induced by particular treatments, such as training. Training, that is repeatedly cycling the material in different ways, is also useful to stabilise the shape memory alloys properties.

3.1.1 Martensitic phase transitions

The shape memory alloys macroscopic behaviour depends upon the presence within the material of two solid phases with different degrees of symmetry, which can transform one into the other due to a change in temperature and stress conditions.

The parent phase, austenite, has a high symmetry crystal structure (typically body centred cubic) and it is stable at high temperature and low levels of stress. Martensite, on the other hand, has lower symmetry (typically rhombohedral or monoclinic), thus it can appear in a number of cristallographically equivalent variants, which differ in their orientation with respect to the material axes. The different martensitic variants formed in a single grain of polycrystalline shape memory alloy can be observed in Figure 3.6. The phase transition between the two crystal structures is displacive, thus it requires only small movements of the atoms within the crystal lattice and its evolution is time-independent[1].

Figure 3.7 depicts the different crystal structures and arrangements in the appropriate zones of the uniaxial stress-temperature plane. The forward austenite to martensite phase transition is exothermic and can be triggered by a de-

[1]Diffusive phase transitions, on the other hand, require breaking of the crystal lattice and long distance atom movements, thus their evolution depends upon the time of reaction.

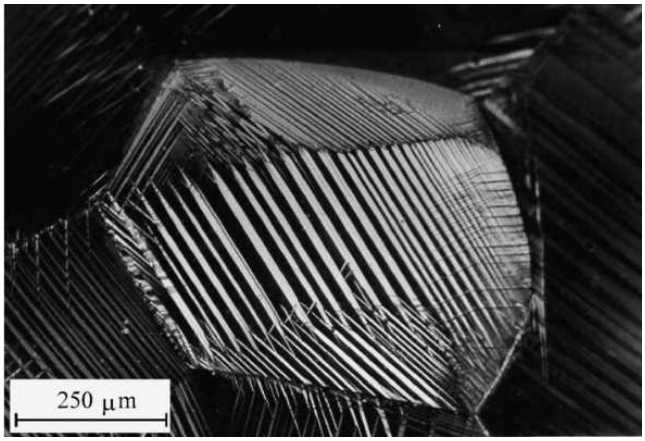

Figure 3.6: Formation of different martensitic variants in a single grain of polycrystalline CuZnAl alloy during uniaxial tensile loading (Patoor et al., 2006)

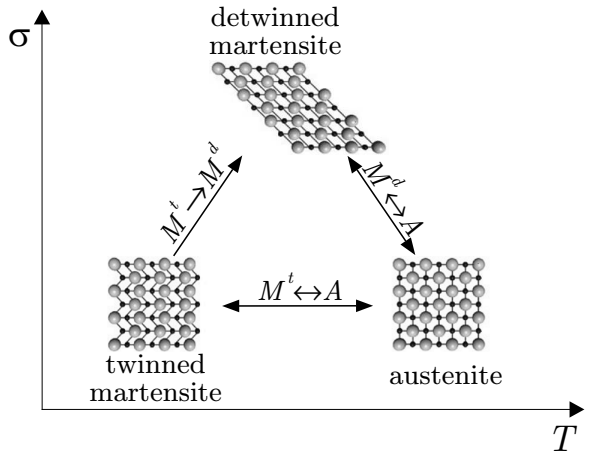

Figure 3.7: Crystal structures and arrangements in the stress-temperature plane

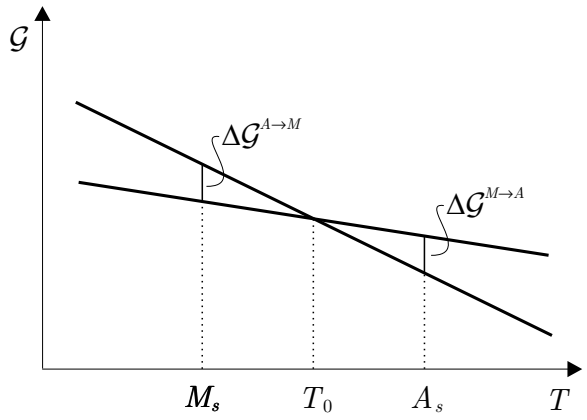

Figure 3.8: Free energy of austenite and martensite as a function of temperature

crease in temperature or by an applied load. If the transformation is purely temperature-induced (Figure 3.7, $M^t \leftrightarrow A$), the martensite variants rearrange themselves to accommodate the macroscopic austenitic shape (twinned martensite). In the presence of an applied load (Figure 3.7, $M^d \leftrightarrow A$), the growth of some martensite variants is favoured and a macroscopic deformation is associated to the phase transition (detwinned martensite). An applied load can also cause martensite reorientation, resulting in detwinning of twinned martensite (Figure 3.7, $M^t \rightarrow M^d$) or change in the orientation of detwinned martensite with a change in the direction of the applied load. It should be clear from this description that the low symmetry martensite crystals can be arranged in different ways, depending upon the material stress and temperature history. The microscopic martensite crystal arrangements may correspond to a macroscopic change with respect to the austenitic shape. In the reverse phase transition, on the other hand, all martensite variants transform into the only possible austenite crystal structure, thus recovering the original memorised shape.

The forward and reverse phase transitions do not occur in the same stress and temperature conditions. Indeed, a hysteresis is present, leaving a range of stresses and temperatures in which the two phases can coexist. Figure 3.8

shows a schematic representation of the Gibbs free energy of the two phases as a function of temperature. Here, T_0 denotes the equilibrium temperature, that is the temperature at which the energy of both phases is the same. The energy change in a system related to a martensitic transformation, $\Delta\mathcal{G}$, is composed of a chemical term, related to the change in crystal structure, and a non chemical term, related to the elastic and surface energies. For phase transition to occur, the driving force for the transformation needs to overcome the non chemical energy change. For this reason, forward transformation starts at a temperature M_s, below T_0, and its driving force is denoted with $\Delta\mathcal{G}^{A\rightarrow M}$ in Figure 3.8, while reverse transformation starts at a temperature A_s, above T_0, and its driving force is denoted with $\Delta\mathcal{G}^{M\rightarrow A}$ in Figure 3.8.

For materials displaying the shape memory effect, the energy barrier to be overcome for phase transition is quite small. This kind of martensitic transformations are usually defined as thermoelastic, as opposed to non thermoelastic martensitic transformations occurring, for example, in steel. In that case, the energy barrier for phase transition is much higher, thus the reverse martensite to austenite phase transition cannot occur and an essential condition for the display of shape memory properties is removed.

Some Ni-Ti alloys display a two step phase transition. Upon cooling, austenite transforms first into a trigonal structure known as the R-phase, which in turn changes into martensite as the temperature continues to decrease. The austenite to R-phase transition has a very small hysteresis, it is associated to a limited recoverable shape change (about 1% elongation versus the 10% elongation associated to martensite) and a significant change in electrical resistivity.

3.1.2 Micromechanical interpretation of shape memory alloy properties

The shape memory alloy behaviour can be interpreted in light of the described phase transitions and reorientation of martensite variants. The loading paths associated to the shape memory effect and superelasticity are depicted in Figures 3.9 and 3.10, respectively, while the numbers in the text refer to those reported in Figures 3.1 and 3.2.

As the shape memory effect occurs at low temperatures, the material microstructure is initially composed of twinned martensite. Upon loading, the ap-

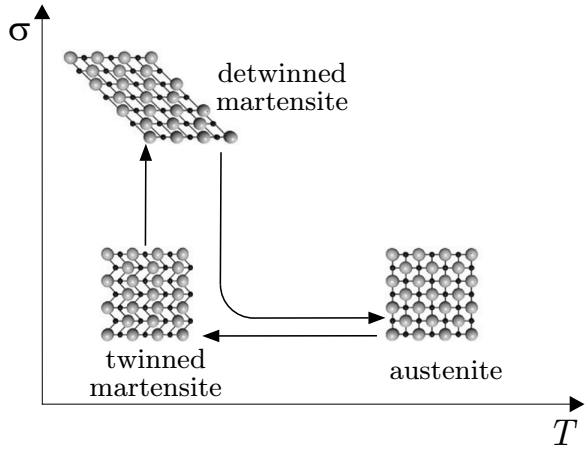

Figure 3.9: Loading path and phase transitions for the shape memory effect

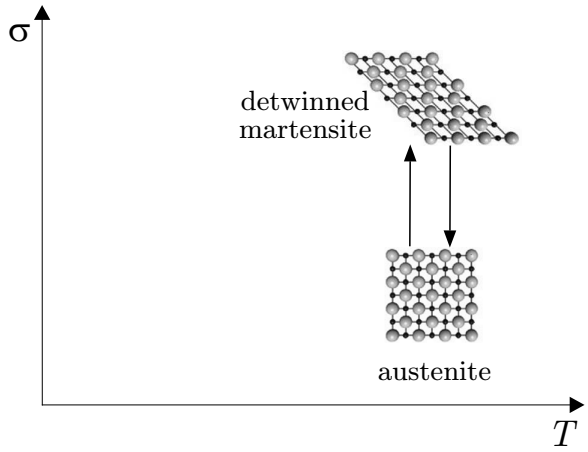

Figure 3.10: Loading path and phase transitions for superelasticity

plied stress reaches the critical value for detwinning (point 2) and the martensite reorientation starts, associated to a macroscopic deformation (plateau 2–3). At the end of the plateau, the martensite is completely detwinned and further loading only causes elastic deformation of the new microstructure (slope 3–4). Upon unloading, the macroscopic deformation is retained as all variants of martensite are equally stable (point 5). When the material is heated above a critical temperature, the martensite to austenite phase transition starts, allowing to recover the macroscopic deformation (points 6–7). During cooling, the austenite to martensite transition occurs under no load, thus no macroscopic change can be observed (points 7–1).

In superelasticity, the material microstructure is initially austenitic. During loading, the critical stress for phase transition is reached (point 2) and the material transforms directly into detwinned martensite (plateau 2–3). As described in the previous paragraph, once the phase transition is complete further loading only causes elastic deformation of the detwinned martensite (slope 3–4). Austenite is the only stable phase at high temperature and no stress, therefore during unloading the critical stress for the reverse phase transition is reached and the macroscopic deformation is recovered (plateau 5–6).

3.2 Shape memory alloy applications

Due to their good structural characteristics, typical of metals, and their unique functional properties, shape memory alloys can be successfully employed in a variety of applications. While biomedical devices based on both the shape memory effect and superelasticity are rather common nowadays, issues related to cost and difficulties in modelling are still an obstacle to a widespread use of these materials in other engineering fields. In the following, some shape memory alloy applications are presented and briefly discussed. Applications involving shape memory alloy elements embedded in a structure, on the other hand, are discussed in Chapter 4 and not dealt with here. For a review on shape memory alloy applications, see Van Humbeeck (2001).

3.2.1 Couplings and fasteners

The stress developed by shape memory alloys when shape recovery is prevented (constrained recovery) can be used to build couplings and fasteners. Indeed, the first large scale applications of the shape memory effect was a hydraulic coupling used to join titanium tubing in the Grumman F-14 aircraft in 1971[2] (Otsuka and Wayman, 1999). The simplest fastener is a metal ring supplied in the expanded martensitic condition. When heated, the ring shrinks and applies a uniform radial pressure to the elements to be fastened. The main advantages of such devices are the reliability, simplicity of assembly (allowing their use in difficult to access areas) and the possibility of joining different materials together. On the other hand, they are generally more expensive than other alternative solutions and their operation temperature range is limited by the onset of the martensitic phase transition.

Another device exploiting recovery stress is the static rock breaker: compressed shape memory alloy elements are placed into boreholes and heated to develop stresses of the order of hundreds of megapascals. The resulting procedure is safer, silent and produces no vibration or dust, moreover it can be used in difficult environments such as water or other liquids.

3.2.2 Actuators

Thermal shape recovery can be used for actuation purposes[3], as anticipated in the previous section. Shape memory alloy actuators are simple and lightweight with respect to traditional actuators, such as motors, and offer a high power to weight ratio. They can be designed without friction and vibrating parts, avoiding the production of dust particles and sparks, thus they are extremely silent and apt to work in harsh environments. On the other hand, their efficiency is quite low and their operating bandwidth is significantly limited by the time required for cooling. Indeed, heating can be achieved quickly and easily, for example through Joule heating, but cooling is hardly controllable and may require a long time, depending upon the size of the components. Two-way memory can

[2]Nowadays, shape memory alloy fasteners are produced by various companies, such as Intrinsic Devices Inc. (www.intrinsicdevices.com).

[3]In Italy, shape memory actuators for industrial applications are produced by Saes Getters S.p.A. (www.saesgetters.com).

be used for actuation; alternatively, a bias element needs to be introduced to restore the deformed position upon cooling.

The limited size and simplicity of actuation make shape memory alloy especially suitable for robotics applications. Cooling time is considerably shortened in micro-actuators, improving the actuator bandwidth. High precision manipulation of micro-objects can be obtained with shape memory alloy microgrippers (Krevet and Kohl, 2003). Compact and lightweight actuators whose movement mimics biological tendons' behaviour are an ideal candidate for the development of prosthetic robot hands (Price et al., 2007).

Space applications, requiring a tight control of the weight of the apparatus to be launched in orbit, benefit from the high power to weight ratio of shape memory alloy actuators. Moreover, shape memory alloy actuators allow to achieve highly controllable and smooth movements, significantly reducing acceleration and preventing unwanted movements in a zero gravity environment. Envisaged applications include release mechanisms (Fragnito and Vetrella, 2002) and deployment of large lightweight structures (Pollard and Jenkins, 2005). A pioneering shape memory alloy space application was the actuation of a rotating arm placed on the Mars Pathfinder, launched by NASA on December 4, 1996 (Jenkins and Landis, 1995).

Recently, the use of shape memory alloy actuators has started to penetrate the automotive industry. In Italy, the Fiat research centre (CRF)[4] is investigating a number of different actuator applications, including air conditioning, locks release, rear-view mirrors positioning and anti-dazzle devices.

The applications described up to now require external heating of the shape memory alloy element to trigger the actuation. A different concept employs the temperature of the surrounding environment as the actuation mechanism. In this case, shape memory alloys act as both sensors and actuators, for example actuating a fire suppression system once the room temperature has reached a critical level (Zhuiykov, 2008).

3.2.3 Biomedical devices

Biomedical devices based both on the shape memory effect and superelasticity are the most common and commercially available applications of shape memory

[4] www.crf.it

alloys[5]. Indeed, biomedical applications are less affected by the cost limitations which are still preventing a wider diffusion of shape memory alloys in other engineering fields. The high biocompatibility of Nitinol allows to use it as implant material. Moreover, the extremely stable body temperature can either ensure a controllable behaviour of superelastic devices or be used as the mechanism to trigger shape recovery.

Superelastic eyeglass frames are rather common nowadays. An important feature of superelasticity is the unloading shape recovery, occurring at nearly constant stress (Figure 3.2). Orthodontic wires providing a steady force regardless of large teeth movements are based on this principle, as well as orthopaedic devices such as bone anchors and staples. Superelastic guidewires and surgical instruments for microinvasive surgery allow miniaturisation, simplicity of design and ease of sterilisation.

The best known biomedical application of shape memory alloys are stents. These are small tubular shaped devices inserted to prevent occlusion of arteries. During implant, the stent is collapsed to a small diameter and put over a catheter. Once it reaches the required position, it is expanded and acts as a scaffolding, keeping the artery open and facilitating the blood flow. Stainless steel stents are expanded using a balloon catheter, whereas shape memory alloy stents can exploit superelasticity or the shape memory effect to self-expand in the operating shape.

3.2.4 Civil engineering applications

Shape memory alloy applications in civil engineering are still significantly limited by the high cost and small size of shape memory alloy components. However, a number of applications are being proposed in the literature (Janke et al., 2005), mostly exploiting the shape memory alloy damping capacity for energy dissipation. The more recent idea to use shape memory alloy bars as concrete reinforcement falls within the topic of shape memory alloy composites, thus it is not discussed here.

Shape memory alloys have a significant damping capacity, related to the hysteresis present in both superelastic and shape memory stress-strain curves.

[5]Some shape memory alloy companies, such as Memry Corp. (www.memry.com), are specialised in biomedical devices.

This feature can be used in earthquake engineering to develop passive control devices which reduce the response of a structural system during dynamic excitation (Casciati et al., 1998). The cost issue can be partially overcome by using copper based shape memory alloys (Casciati and Faravelli, 2004). Seismic protection devices can be included in new buildings or added as a retrofit to existing and historical structures. The development of shape memory alloy passive devices for new buildings and historical constructions have been the subjects of two European research projects.

The MANSIDE (1999) project (Memory Alloys for New Seismic Isolation and Energy Dissipation Devices) involved researchers from Italy, Belgium, Sweden and Greece on the seismic protection of new buildings via shape memory alloy isolators and dissipation devices. The complete shape recovery at zero load in superelastic devices was used to develop recentring units, which allow to recover the large displacements in isolators at the end of the seismic action. Dissipation devices were developed using both superelastic and martensitic elements. Hybrid solutions were also proposed involving the use of traditional steel dissipation devices together with shape memory alloy recentering units. Guidelines for shape memory alloy-based seismic devices were published at the end of the project (Dolce and Nicoletti, 1999).

The ISTECH (2000) project (Innovative Stability Techniques for the European Cultural Heritage) led to two pioneering shape memory alloy applications in Italian historical buildings. The idea is to use shape memory alloy devices to prevent two classical damage mechanisms of masonry buildings: out of plane collapse and diagonal cracks. The first mechanism is the most dangerous and can be prevented by improving the connections between the walls placed in different directions. This is usually done with steel connections, whose linear elastic behaviour might end up exerting excessive forces and damaging historical masonry. Superelastic devices, on the other hand, can limit the forces applied on the masonry by tuning the upper and lower transformation plateau. This concept was applied in the restoration of Assisi Upper Basilica, whose pediment had been damaged during the earthquake which hit central Italy on the 26th and 27th September 1997. The second damage mechanism can be prevented by pre-compressing the masonry walls. With respect to traditional steel devices, superelastic elements exert only a limited pre-compression force and dissipate part of the seismic action due to their damping capacity. This concept was

applied in the seismic retrofitting of the San Giorgio in Trignano bell tower in San Martino in Rio (Reggio Emilia), damaged by an earthquake on the 15th October 1996.

Most civil engineering applications involve superelastic passive devices, which are deemed to be more reliable as they require no external energy input. A recent application, named the Spider project, makes use of the shape memory effect to create a self erecting structure.

3.3 Modelling of shape memory alloys

Shape memory alloys display a strong thermomechanical coupling related to the presence of martensitic phase transitions. Investigating these materials at the macroscopic level requires the definition of new constitutive laws[6] which are able to represent the coupling. Generally, two different approaches are possible to define the constitutive laws, namely a micromechanical and a phenomenological approach. In the first case, the material behaviour at the microscopic level is described, then the macroscopic constitutive laws are obtained by averaging the investigated phenomena over a Reference Volume Element (RVE). In the phenomenological approach, on the other hand, only the macroscopic behaviour is taken into consideration and the material state is assumed known if some variables (state variables) are known. The state variables describe the macroscopic phenomena and may or may not be related to the actual microscopic material characteristics. A classical example is that of plasticity in metals: using a micromechanical approach, one would describe the phenomenon by investigating the movement of defects and dislocations inside the material, while within a phenomenological approach a new variable, the plastic strain, is introduced to macroscopically describe the material behaviour. A review of various micromechanical and phenomenological constitutive models for shape memory alloys was recently published by Lagoudas et al. (2006) and Patoor et al. (2006).

The modelling of shape memory alloys has been a topic of interest ever since the discovery of the shape memory effect. The approaches outlined in the previous paragraph have been exploited by researchers to propose many models, both one-dimensional and three-dimensional. However, the modelling of shape

[6] "Constitutive equations [...] describe the macroscopic behaviour resulting from the internal constitution of the material" (Malvern, 1969).

memory alloys is still an open problem, given the many recent literature articles on the topic. The reason for the active interest, besides the many cutting edge applications of shape memory alloys, resides in the utter complexity of the phenomena to be described. Thus, no models have been formulated that are able to describe thoroughly the shape memory alloy behaviour, but a wide variety of models exists among which one can choose in order to to describe a given set of phenomena. Some features of the shape memory alloy material behaviour have not yet been fully explained and, to the author's knowledge, are not included in any published constitutive model, as it will be shown later in this chapter.

In this section, a number of one-dimensional and three-dimensional phenomenological constitutive models for shape memory alloys are considered and compared, concentrating in particular on plasticity-like models. Indeed, due to the presence of a stress plateau similar to the one observed in plasticity, many shape memory alloy models are based on a plasticity-like formalism. Other approaches, however, can be followed. Within the phenomenological approach, another possibility is to consider Ginzburg-Landau models, such as the one proposed by Fabrizio et al. (2008). A successful phenomenological model is required to be thermodynamically consistent, therefore in the following paragraph a short outline of continuum thermodynamics and plasticity theories is presented, mostly inspired from the book by Lemaitre and Chaboche (1994).

3.3.1 Outline of phenomenological thermodynamics

In phenomenological thermodynamics, the thermodynamic state of a material at a given point and instant is completely described by a set of state variables at that instant, that depend only upon the point considered. Different material behaviours can thus be described by choosing the appropriate set of state variables, whose evolution in time constitutes a thermodynamic process. Indeed, thermodynamically admissible processes must satisfy the second principle of thermodynamics, thus the entropy inequality constitutes a constraint to the admissible constitutive laws for real materials (Coleman and Noll, 1963).

State variables can be divided into observable variables (typically the total strain $\boldsymbol{\varepsilon}$ and the temperature T), which are the only ones involved in non dissipative phenomena, and internal variables. Internal variables are introduced

to keep track of the history of the material, which in dissipative phenomena influences the material current behaviour. Their choice is largely subjective and influences the kind of phenomena which a given model is able to represent. Some examples of internal variables often introduced in shape memory alloy constitutive models are the martensite volume fraction and the total transformation strain. The different choices of internal variables in shape memory alloy models is discussed further into this chapter, while in this paragraph they will be generally denoted by $(V_1, \ldots, V_k)$.

Once the state variables have been chosen, they are used to postulate the existence of a thermodynamic potential, or free energy. Various free energies can be defined whose difference consists in the choice of the independent variables. For example, Helmholtz free energy is a function of the strain, temperature and internal variables:

$$\Psi = \Psi\left(\boldsymbol{\varepsilon}, T, V_1, \ldots, V_k\right), \tag{3.1}$$

while Gibbs free energy can be obtained from Helmholtz free energy via a Legendre transform, making stress the independent variable:

$$\mathcal{G} = \mathcal{G}\left(\boldsymbol{\sigma}, T, V_1, \ldots, V_k\right). \tag{3.2}$$

Knowledge of the thermodynamic potential yields the constitutive equations by satisfying the second principle of thermodynamics. The following derivation is carried out with reference to Helmholtz free energy, but one can proceed equivalently with different potentials.

The second principle of thermodynamics in local form can be expressed as follows:

$$\rho\dot{s} + \nabla \cdot \frac{\mathbf{q}}{T} - \frac{r}{T} \geq 0, \tag{3.3}$$

where ρ is the density, s is the specific entropy, $\mathbf{q}$ is the heat flux and r the external heat source. Equation (3.3) does not explicitly contain all the state variables, but can be reformulated by taking into account the first principle of thermodynamics (conservation of energy) and the principle of virtual power, obtaining:

$$\boldsymbol{\sigma} \cdot \dot{\boldsymbol{\varepsilon}} + \rho\left(T\dot{s} - \dot{e}\right) - \mathbf{q} \cdot \frac{\nabla T}{T} \geq 0, \tag{3.4}$$

where e is the internal energy of the material.

Helmholtz free energy is defined as

$$\Psi = \Psi\left(\boldsymbol{\varepsilon}, T, V_1, \ldots, V_k\right) = e - Ts, \tag{3.5}$$

thus the term $\dot{e}$ in Equation (3.4) can be substituted, yielding

$$\boldsymbol{\sigma} \cdot \dot{\boldsymbol{\varepsilon}} + \rho\left(-s\dot{T} - \dot{\Psi}\right) - \mathbf{q} \cdot \frac{\nabla T}{T} \geq 0, \tag{3.6}$$

The rate of change of the free energy $\dot{\Psi}$ can be expressed in terms of partial derivatives with respect to the state variables, substitution in the previous equation yields

$$\left(\boldsymbol{\sigma} - \rho\frac{\partial \Psi}{\partial \boldsymbol{\varepsilon}}\right) \cdot \dot{\varepsilon} - \rho\left(s + \frac{\partial \Psi}{\partial T}\right)\dot{T} - \rho\frac{\partial \Psi}{\partial V_1}\dot{V}_1 - \ldots - \rho\frac{\partial \Psi}{\partial V_k}\dot{V}_k - \frac{\mathbf{q}}{T} \cdot \nabla T \geq 0. \tag{3.7}$$

As this inequality must be satisfied by every admissible thermodynamic process, by considering an elastic deformation at constant temperature which does not involve an evolution of the internal variables one obtains

$$\boldsymbol{\sigma} = \rho\frac{\partial \Psi}{\partial \boldsymbol{\varepsilon}}, \tag{3.8}$$

which is the constitutive equation for the stress. Analogously, for entropy one can obtain

$$s = -\frac{\partial \Psi}{\partial T}. \tag{3.9}$$

As for the internal variables, it is possible to define the associated thermodynamic driving forces:

$$A_k = \rho\frac{\partial \Psi}{\partial V_k}. \tag{3.10}$$

Equation (3.7) can thus be written as

$$-A_1\dot{V}_1 - \ldots - A_k\dot{V}_k - \frac{\mathbf{q}}{T} \cdot \nabla T \geq 0. \tag{3.11}$$

This is the dissipation inequality, stating that the total dissipation must be greater than zero for real materials. The total dissipation is obtained as the sum of mechanical dissipation, associated with the evolution of the internal variables, and thermal dissipation.

Defining constitutive laws via a thermodynamic potential automatically yields the thermomechanical coupling. Indeed, while temperature terms are introduced in the mechanical problem via the stress constitutive law, the entropy constitutive law allows to introduce mechanical dissipation effects in the heat equation. Indeed, taking into account the first principle of thermodynamics, Fourier's law and the entropy constitutive equation, one can write

$$\rho c\dot{T} - k\nabla \cdot (\nabla T) = b, \tag{3.12}$$

where c is the specific heat capacity, k is the thermal conductivity and b represents the heat source:

$$b = r + \rho T \left(\frac{\partial^2 \Psi}{\partial T \partial \boldsymbol{\varepsilon}} \cdot \dot{\boldsymbol{\varepsilon}} + \frac{\partial^2 \Psi}{\partial T \partial V_k} \dot{V}_k \right) - \frac{\partial \Psi}{\partial V_k} \dot{V}_k. \tag{3.13}$$

Here, the external heat source r was previously defined, the parenthesis contains terms related to thermomechanical coupling and the last term introduces mechanical dissipation caused by the evolution of the internal variables.

The constitutive equations introduced so far do not give any information as to the evolution of the internal variables. It is therefore necessary to introduce kinetic laws, which must again be in accord with the dissipation inequality. A way to define the kinetic laws is via the introduction of a dissipation potential, which needs to satisfy some properties in order to ensure the positiveness of the mechanical dissipation. Some details on the definition of kinetic laws for plasticity models, which are formally similar to those used in many shape memory alloy models, are given in the following.

3.3.2 Outline of plasticity theories

In plasticity models, the strain is usually divided into elastic and inelastic parts: $\boldsymbol{\varepsilon} = \boldsymbol{\varepsilon}_e + \boldsymbol{\varepsilon}_{in}$. The inelastic strain can be further decomposed into thermal and plastic strain: $\boldsymbol{\varepsilon}_{in} = \boldsymbol{\varepsilon}_{th} + \boldsymbol{\varepsilon}_p$, which constitutes an internal variable of the plasticity model. In shape memory alloy modelling, the transformation strain $\boldsymbol{\varepsilon}_{tr}$ associated to detwinned martensite is generally used in place of the plastic strain.

The kinetic laws require the definition of a yield surface f and a plastic potential F, which are written in terms of the thermodynamic driving forces.

The yield surface f, often called transformation surface in shape memory alloy models, governs the onset of plastic deformations, while the plastic potential F defines the direction of plastic flow. In associated plasticity, $f \equiv F$, but a more general case of non associated plasticity is considered in the following presentation.

The kinetic laws, or flow rules, are written in terms of the plastic potential F as:

$$\dot{\boldsymbol{\varepsilon}}_p = \dot{\zeta}\frac{\partial F}{\partial \boldsymbol{\sigma}}, \quad -\dot{V}_k = \dot{\zeta}\frac{\partial F}{\partial A_k} \tag{3.14}$$

Here, the derivative of the plastic potential with respect to the dual variables defines the direction of increment of the internal variables, while $\dot{\zeta}$ is the plastic multiplier.

The yield surface defines the limit of the elastic domain. Inside the surface, that is when $f < 0$, the internal variables do not vary, therefore the plastic multiplier $\dot{\zeta} = 0$. On the surface ($f = 0$), the internal variables change and the plastic multiplier is non zero, while points outside the surface are not admissible. The described cases can be summarised in the Kuhn-Tucker condition:

$$\dot{\zeta} \geq 0, \quad f \leq 0, \quad \dot{\zeta} f = 0 \tag{3.15}$$

The fulfilment of this condition, also known as consistency condition, allows to evaluate the plastic multiplier and, therefore, the change in the internal variables via Equation (3.14). Note that the transformation surface may change as the internal variables evolve, thus generating a hardening behaviour.

In associated plasticity, if the limit function is convex and the normality rule is fulfilled, the satisfaction of the dissipation inequality (3.11) is automatically guaranteed.

In the following sections, various one-dimensional and three-dimensional models for shape memory alloys are introduced and discussed within the approach of phenomenological thermodynamics. It should be underlined that, in order to facilitate comparison between the different models, a common notation has been defined and is used consistently throughout the models description.

3.3.3 One-dimensional models

One-dimensional models are still the most widely used constitutive relations for shape memory alloys. Indeed, three-dimensional model are quite complex to

handle and in some cases not strictly necessary, as many applications involve the use of shape memory wires or ribbons. Moreover, not much experimental data is available to validate a full three-dimensional shape memory alloy behaviour. For all these reasons, this paragraph is devoted to the presentation and discussion of some of the most common shape memory alloy one-dimensional constitutive models.

As already pointed out previously, the models discussed in this section are defined within the context of phenomenological thermodynamics and plasticity theory. Considering only one-dimensional behaviour, however, greatly simplifies the mathematical treatment of the problem. In particular, the yield surface degenerates into a line. Thus, the presentation of the one-dimensional models is somewhat simplified with respect to the three-dimensional models which are discussed later.

Two groups of one-dimensional models are discussed in some details in the following. The first group contains the models proposed in the works by Tanaka (1986), Liang and Rogers (1990) and Brinson (1993), the second is a group of models proposed by Auricchio and Sacco (1997, 1999b, 2001) and Auricchio et al. (2003). This is by no means an exhaustive discussion, however the choice was dictated by different reasons, which are detailed in the following.

The models by Tanaka (1986), Liang and Rogers (1990) and Brinson (1993) were among the first to be proposed in the literature. They are very simple constitutive laws in which the martensite volume fraction is taken as internal variable. These models are still very popular because of their simplicity and ability to represent both shape memory effect and superelasticity. The interest they still raise is proven by the several recent works concerned with their comparative evaluation. In particular, the works of Epps and Chopra (1997) and Prahlad and Chopra (2001) investigate the correspondence of the three material models with experimental data, while Żak et al. (2003) comparatively evaluate the behaviour of various models for use with active composites. A correction to an inconsistency present in Brinson's model was recently proposed by Buravalla and Khandelwal (2007). A modified Brinson's model able to account for the experimental behaviour in constrained recovery is presented later in this chapter (Daghia et al., 2006).

The models by Auricchio and Sacco were proposed more recently in the context of generalised plasticity (Lubliner and Auricchio, 1996). They are a

family of models having a similar structure, in which different choices of the internal variables allow to represent different features of the shape memory alloy behaviour, such as superelasticity, shape memory effect, two-way shape memory effect and training. The possibility to describe different properties by simply including new internal variables within an existing modelling framework is particularly attractive, as this allows to tune the model complexity according to the investigated problem.

Models proposed by Tanaka, Liang and Rogers, Brinson

The models proposed by Tanaka (1986), Liang and Rogers (1990) and Brinson (1993) are based on the Helmholtz free energy, even though its functional form is not explicitly given. The internal variable considered by Tanaka and Liang and Rogers is the martensite volume fraction, while in Brinson's model the twinned and detwinned martensite fractions are introduced as separate variables, thus allowing to model the shape memory effect at low temperatures. In the notation adopted here, the detwinned and twinned fractions are denoted by ξ^d and ξ^t respectively, while in models where only one martensite fraction is involved it is denoted by ξ^d. As all models are one-dimensional, the transformation strain is simply defined as $\varepsilon_{tr} = \varepsilon_L \xi^d$, where ε_L is a material parameter denoting the maximum strain associated to the phase transformation.

The constitutive law for stress is the following:

$$\dot{\sigma} = E\dot{\varepsilon} + \Theta\dot{T} + \Omega\dot{\xi^d} \tag{3.16}$$

where E, Θ and Ω are material moduli, which in Brinson's model are considered to vary as a function of the total martensite fraction $\left(\xi^d + \xi^t\right)$.

The onset of phase transformation is defined with the help of experimental phase diagrams, reported in Figure 3.11. The zero stress transformation temperatures, M_f, M_s, A_s and A_f, the slopes of the transformation lines in the stress-temperature plane, C_M and C_A, and the critical stresses for detwinning, σ_s and σ_f, are all material parameters which need to be determined experimentally. Note that, even though the parameters are apparently the same, they need to be chosen differently depending upon the model in order to predict a similar material behaviour.

Phase transformation occurs within the zones of the phase diagram marked in grey, as long as the loading path follows the direction of the arrows. Outside

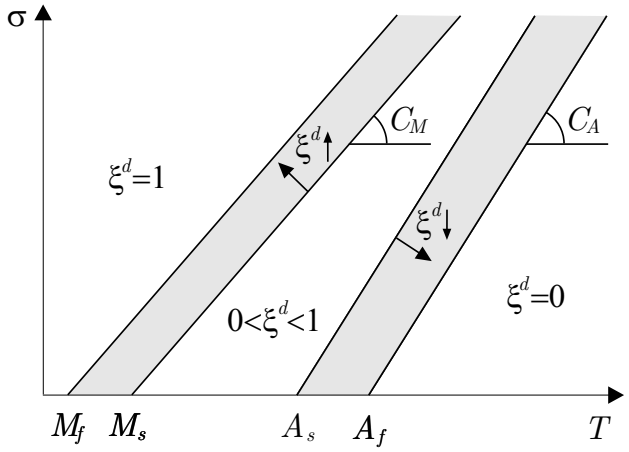

(a) Tanaka (1986) and Liang and Rogers (1990)

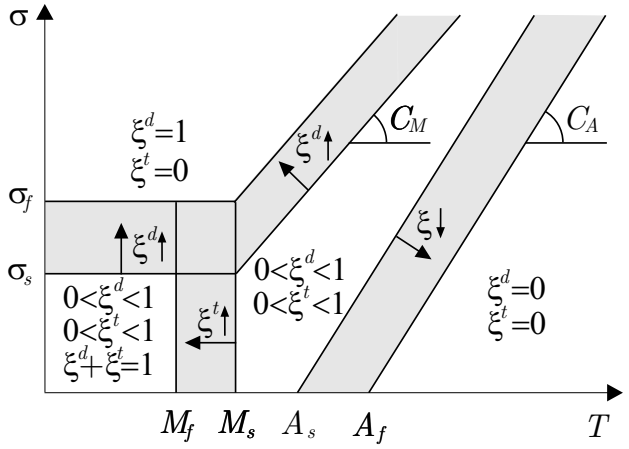

(b) Brinson (1993)

Figure 3.11: Phase diagrams for Tanaka (1986), Liang and Rogers (1990) and Brinson (1993) models

the phase transformation zones, the volume fractions of the different phases are constant, their values depending upon the previous loading history of the material. The possible values assumed by the different volume fractions in each area of the phase diagram are marked in Figure 3.11.

Within the phase transformation zones, the kinetic laws are given as follows:

- Tanaka:
  - forward $A \rightarrow M$ transformation:
$$\xi^d = 1 - \exp\left[A_M \left(T - M_s\right) + B_M \sigma\right], \tag{3.17}$$
  - reverse $M \rightarrow A$ transformation:
$$\xi^d = \exp\left[A_A \left(T - A_s\right) + B_A \sigma\right], \tag{3.18}$$

  where A_M, A_A, B_M and B_A are material constants in terms of the transition temperatures;

- Liang and Rogers:
  - forward $A \rightarrow M$ transformation:
$$\xi^d = \frac{1 - \xi_0^d}{2} \cos\left[\frac{\pi}{M_s - M_f}\left(T - M_f - \frac{\sigma}{C_M}\right)\right] + \frac{1 + \xi_0^d}{2}, \tag{3.19}$$
  - reverse $M \rightarrow A$ transformation:
$$\xi^d = \frac{\xi_0^d}{2} \cos\left[\frac{\pi}{A_f - A_s}\left(T - A_s - \frac{\sigma}{C_A}\right)\right] + \frac{\xi_0^d}{2}, \tag{3.20}$$

  where ξ_0^d is the martensite fraction prior to entering the phase transformation zone;

- Brinson:
  - forward $(A, M^t) \rightarrow M^d$ transformation $(T > M_s)$:
$$\xi^d = \frac{1 - \xi_0^d}{2} \cos\left\{\frac{\pi}{\sigma_s - \sigma_f}\left[\sigma - \sigma_f - C_M\left(T - M_s\right)\right]\right\} + \frac{1 + \xi_0^d}{2}, \tag{3.21}$$
$$\xi^t = \xi_0^t - \frac{\xi_0^t}{1 - \xi_0^d}\left(\xi^d - \xi_0^d\right), \tag{3.22}$$

– forward $(A, M^t) \rightarrow M^d$ transformation ($T < M_s$):

$$\xi^d = \frac{1-\xi_0^d}{2}\cos\left[\frac{\pi}{\sigma_s-\sigma_f}\left(\sigma-\sigma_f\right)\right]+\frac{1+\xi_0^d}{2}, \tag{3.23}$$

$$\xi^t = \xi_0^t - \frac{\xi_0^t}{1-\xi_0^d}\left(\xi^d-\xi_0^d\right), \tag{3.24}$$

– forward $A \rightarrow M^t$ transformation:

$$\xi^t = \frac{1-\xi_0^d-\xi_0^t}{2}\left\{\cos\left[\frac{\pi}{M_s-M_f}\left(T-M_f\right)\right]+1\right\}+\xi_0^t, \tag{3.25}$$

– reverse $\left(M^t, M^d\right) \rightarrow A$ transformation:

$$\xi^d = \frac{\xi_0^d}{2}\left\{\cos\left[\frac{\pi}{A_f-A_s}\left(T-A_s-\frac{\sigma}{C_A}\right)\right]+1\right\}, \tag{3.26}$$

$$\xi^t = \frac{\xi_0^t}{2}\left\{\cos\left[\frac{\pi}{A_f-A_s}\left(T-A_s-\frac{\sigma}{C_A}\right)\right]+1\right\}, \tag{3.27}$$

where ξ_0^d and ξ_0^t are the detwinned and twinned martensite fractions prior to entering the phase transformation zone.

Later, in Lagoudas et al. (2006), the same kinetic laws were shown to derive from a particular choice of the hardening functions within the definition of the free energy.

Models proposed by Auricchio and Sacco

The models proposed in various works by Auricchio and Sacco are derived within the framework of generalised plasticity (Lubliner and Auricchio, 1996). In each model, an appropriate choice of the internal variables allows to represent different features of the shape memory alloy behaviour. This way, depending upon the problem considered, the complexity of the model can be tailored by including only the required variables and equations.

Starting from a simple model for superelasticity at constant temperature (model AS1, Auricchio and Sacco, 1997), the following models are improved by including the shape memory effect (model AS2, Auricchio and Sacco, 1999b), the coupling with the heat equation (model AS3, Auricchio and Sacco, 2001)

Table 3.1: Comparison between the different models proposed by Auricchio and Sacco

MODEL	obser. variables	int. variables	non-constant parameters	coupling	modelling capabilities
AS1	ε	ξ^d	yes	no	SE at $T = \text{const.}$
AS2	ε, T	ξ^d, ξ^t, β	yes	no	SE, SME
AS3	ε, T	ξ^d	no	yes	SE at different loading rates
AS4	ε, T	ξ^d, β, γ_M, γ_A	yes	no	SE, SME at $T > M_s$, TWME, training

and finally the two-way memory effect and training (model AS4, Auricchio et al., 2003). The different choices operated in each model, together with the phenomena they are able to represent, are summarised in Table 3.1 and detailed in the following.

Apart from AS1, all models are strain and temperature driven, that is the conditions for the onset of phase transition are given in terms of strain and temperature (rather than the usual stress and temperature). This choice is aimed at simplifying numerical implementation of the constitutive models into displacement-based finite element codes. Indeed, model AS2 is actually implemented in the commercial finite element code ADINA (ADINA, 2006). For the same reason, all models are given in both the time-continuous and time-discrete frame and a predictor-corrector integration algorithm is suggested. Only the time-continuous model formulation is discussed here, for further details refer to the cited articles.

The volume fractions of the different constituents are introduced as internal variables. A single martensite fraction ξ^d is used in models AS1, AS3 and AS4, which deal exclusively with phenomena occurring at temperatures higher than martensite start ($T > M_s$), while the twinned and detwinned fractions, ξ^t and ξ^d, are defined separately in model AS2 to take into account the shape memory effect occurring at low temperatures. This last choice is similar to the one operated in Brinson's model. Models AS2 and AS4 introduce the internal variable β to describe the reorientation of detwinned martensite. In AS4, the two-way memory effect and training are modelled by introducing the irre-

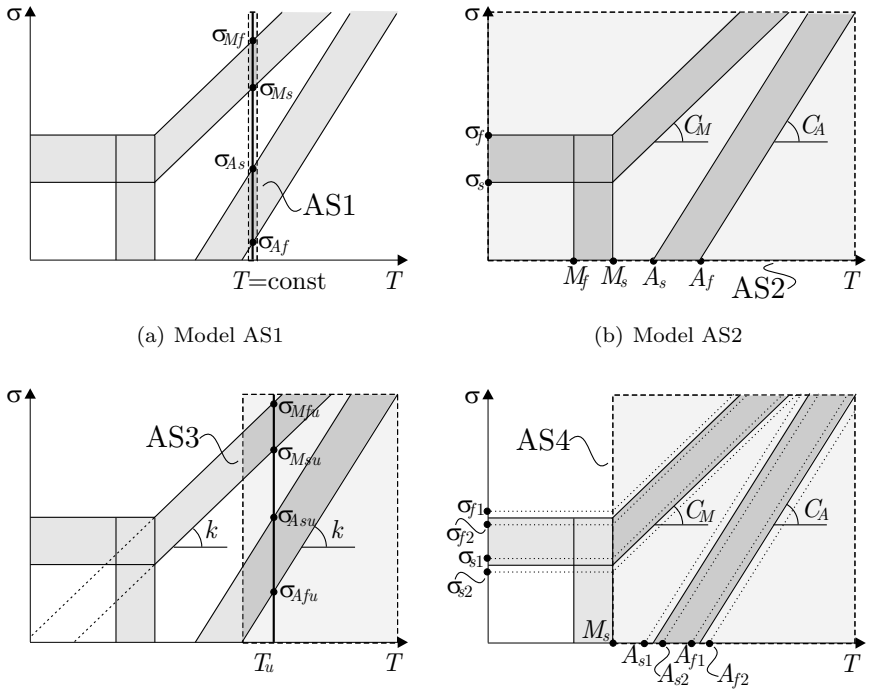

(a) Model AS1

(b) Model AS2

(c) Model AS3

(d) Model AS4

Figure 3.12: Phase diagrams for Auricchio and Sacco's models

versible martensite fraction ξ_R, that is the fraction of martensite which is not able to transform back into austenite during reverse transformation. The total martensite fraction ξ^d is thus divided into a reversible and an irreversible part: $\xi^d = \xi + \xi_R$. The evolution of the irreversible martensite fraction and the change in the transformation zones introduced in model AS4 are related to the total amount of forward and reverse transformation accumulated throughout the cycles. In order to keep track of these quantities, the internal variables γ_M and γ_A are introduced in model AS4.

In the spirit of plasticity models, strain is additively separated into the elastic and inelastic parts. The inelastic strain is a function of the temperature (thermal

strain, $\boldsymbol{\varepsilon}_{th}$) and the detwinned martensite fraction (transformation strain, $\boldsymbol{\varepsilon}_{tr}$):

- AS1: $\varepsilon = \varepsilon_e + \varepsilon_L \xi^d \mathrm{sgn}\,(\sigma)$;
- AS2: $\varepsilon = \varepsilon_e + \xi^d \beta + \alpha\,(T - T_0)$;
- AS3: $\varepsilon = \varepsilon_e + \varepsilon_L \xi^d \mathrm{sgn}\,(\sigma) + \alpha\,(T - T_0)$;
- AS4: $\varepsilon = \varepsilon_e + \left(\xi^d - \xi_R\right)\beta + \xi_R \kappa + \alpha\,(T - T_0)$.

Here, the term $\mathrm{sgn}\,(\sigma)$ is introduced to take into account the different directions of detwinning (tension and compression). Note that the behaviour in tension and compression of shape memory alloys is generally different, thus different material parameters need to be defined. For example, ε_L specialises into ε_L^+ and ε_L^-, in tension and compression respectively. The parameter κ, introduced in AS4 to model training, is set to ε_L^+ if training is in tension, $-\varepsilon_L^-$ if training is in compression, respectively. The term β, describing martensite reorientation, is defined as

$$\dot{\beta} = \mathcal{H}^{ss} \gamma \left[\varepsilon_L \mathrm{sgn}\,(\sigma) - \beta\right] \left(|\sigma| - \sigma^{ss}\right), \tag{3.28}$$

with

$$\mathcal{H}^{ss} = \begin{cases} 1 & \text{when } |\sigma| > \sigma^{ss} \\ 0 & \text{otherwise} \end{cases} \tag{3.29}$$

Here, σ^{ss} is a limit stress that activates the reorientation process, while γ is a material parameter measuring the velocity of reorientation. Note that β is introduced only in AS2 and AS4, which are designed to model the shape memory effect and thus require a description of the change of martensite orientation from tension to compression and viceversa. On the other hand, no reorientation is possible in AS1 and AS3, focused on superelasticity. In principle, model AS3 would be able to describe the shape memory effect occurring at temperatures above M_s, since both temperature and detwinned martensite fraction are model variables. However, the absence of the reorientation term β reduces the model to superelasticity description only.

The constitutive equation for the stress is expressed as

$$\sigma = E \varepsilon_e \tag{3.30}$$

where the elastic modulus E is either constant (model AS3) or given as s function of the total martensite fraction. Different homogenisation possibilities are

explored in model AS1, while the choice retained in the following models is derived from the Reuss scheme:

$$E\left(\xi^d + \xi^t\right) = \frac{E_A E_M}{E_M + \left(\xi^d + \xi^t\right)\left(E_A - E_M\right)}. \tag{3.31}$$

All kinetic laws defining the evolution of the different phase fractions have a similar structure, given by:

$$\dot{\xi} = a\xi_0 \mathcal{H} \frac{\dot{F}}{\left(F - F_f\right)^b}. \tag{3.32}$$

Here, a and b are material parameters which can be different for the various phase transformations. If they are set to one, the kinetic laws become linear (models AS1, AS2 and AS3). Similarly to $\mathcal{H}^{ss}$ in (3.29), $\mathcal{H}$ is an indicator function which is 1 within the corresponding transformation zone, 0 otherwise. This term allows to define which transformations are active at a given moment. It should be noted that, because of the general framework in which the model is developed, the transformation zones may or may not be disjoint.

In the following, the terms appearing in Equation (3.32) are defined for each model and phase transition:

- AS1:
  - forward $A \rightarrow M$ transformation:

$$\begin{aligned}
F &= |\sigma|, && (3.33)\\
F_s &= \sigma_{Ms}, && (3.34)\\
F_f &= \sigma_{Mf}, && (3.35)\\
\mathcal{H} &= \begin{cases} 1 \text{ if } (\dot{F} > 0) \wedge (F_s < F < F_f) \\ 0 \text{ otherwise,} \end{cases} && (3.36)\\
\xi &= \xi^d, && (3.37)\\
\xi_0 &= -\left(1 - \xi^d\right), && (3.38)
\end{aligned}$$

– reverse $M \to A$ transformation:

$$
\begin{aligned}
F &= |\sigma|\,, && (3.39)\\
F_s &= \sigma_{As}, && (3.40)\\
F_f &= \sigma_{Af}, && (3.41)\\
\mathcal{H} &= \begin{cases} 1 \text{ if } (\dot{F} < 0) \wedge (F_f < F < F_s) \\ 0 \text{ otherwise,} \end{cases} && (3.42)\\
\xi &= \xi^d, && (3.43)\\
\xi_0 &= \xi^d, && (3.44)
\end{aligned}
$$

where σ_{Ms}, σ_{Mf}, σ_{As} and σ_{Af} are the stresses at the beginning and end of the forward and reverse transformation at a fixed temperature T. This corresponds to considering a section of the phase diagram, as shown in Figure 3.12(a);

- AS2:

  – forward $(A, M^t) \to M^d$ transformation $(T > M_s)$:

$$
\begin{aligned}
F &= |\varepsilon| - \frac{C_M T}{E}, && (3.45)\\
F_s &= \varepsilon_L \xi^d + \frac{\sigma_s - C_M M_s}{E}, && (3.46)\\
F_f &= \varepsilon_L + \frac{\sigma_f - C_M M_s}{E_M}, && (3.47)\\
\mathcal{H} &= \begin{cases} 1 \text{ if } (\dot{F} > 0) \wedge (F_s \le F \le F_f) \wedge (T \ge M_s) \\ 0 \text{ otherwise,} \end{cases} && (3.48)
\end{aligned}
$$

  * detwinned martensite evolution:

$$
\begin{aligned}
\xi &= \xi^d, && (3.49)\\
\xi_0 &= -\left(1 - \xi^d\right), && (3.50)
\end{aligned}
$$

  * twinned martensite evolution:

$$
\begin{aligned}
\xi &= \xi^t, && (3.51)\\
\xi_0 &= \xi^t, && (3.52)
\end{aligned}
$$

– forward $(A, M^t) \rightarrow M^d$ transformation $(T < M_s)$:

$$F = |\varepsilon|, \tag{3.53}$$

$$F_s = \varepsilon_L \xi^d + \frac{\sigma_s}{E}, \tag{3.54}$$

$$F_f = \varepsilon_L + \frac{\sigma_f}{E_M}, \tag{3.55}$$

$$\mathcal{H} = \begin{cases} 1 \text{ if } (\dot{F} > 0) \wedge (F_s \leq F \leq F_f) \wedge (T \leq M_s) \\ 0 \text{ otherwise,} \end{cases} \tag{3.56}$$

∗ detwinned martensite evolution:

$$\xi = \xi^d, \tag{3.57}$$

$$\xi_0 = -\left(1 - \xi^d\right), \tag{3.58}$$

∗ twinned martensite evolution:

$$\xi = \xi^t, \tag{3.59}$$

$$\xi_0 = \xi^t, \tag{3.60}$$

– forward $A \rightarrow M^t$ transformation:

$$F = T, \tag{3.61}$$

$$F_s = M_s, \tag{3.62}$$

$$F_f = M_f, \tag{3.63}$$

$$\mathcal{H} = \begin{cases} 1 \text{ if } (\dot{F} < 0) \wedge (F_f < F < F_s) \\ 0 \text{ otherwise,} \end{cases} \tag{3.64}$$

$$\xi = \xi^t, \tag{3.65}$$

$$\xi_0 = -\left(1 - \xi^d - \xi^t\right), \tag{3.66}$$

– reverse $\left(M^t, M^d\right) \rightarrow A$ transformation:

$$F = |\varepsilon| - \frac{C_A T}{E}, \tag{3.67}$$

$$F_s = \varepsilon_L \xi^d - \frac{C_A A_s}{E}, \tag{3.68}$$

$$F_f = -\frac{C_A A_f}{E_A}, \tag{3.69}$$

$$\mathcal{H} = \begin{cases} 1 \text{ if } (\dot{F} < 0) \wedge (F_f < F < F_s) \\ 0 \text{ otherwise,} \end{cases} \tag{3.70}$$

∗ detwinned martensite evolution:

$$\xi = \xi^d, \tag{3.71}$$
$$\xi_0 = \xi^d, \tag{3.72}$$

∗ twinned martensite evolution:

$$\xi = \xi^t, \tag{3.73}$$
$$\xi_0 = \xi^t. \tag{3.74}$$

Note that the whole phase diagram is described by model AS2 (see Figure 3.12(b));

- AS3:
  - forward $A \to M$ transformation:

$$F = |\varepsilon| - \frac{k}{E}\left(T - T_u\right), \tag{3.75}$$
$$F_s = \varepsilon_L \xi^d + \frac{\sigma_{Msu}}{E}, \tag{3.76}$$
$$F_f = \varepsilon_L + \frac{\sigma_{Mfu}}{E}, \tag{3.77}$$
$$\mathcal{H} = \begin{cases} 1 \text{ if } (\dot{F} > 0) \wedge (F_s < F < F_f) \\ 0 \text{ otherwise,} \end{cases} \tag{3.78}$$
$$\xi = \xi^d, \tag{3.79}$$
$$\xi_0 = -\left(1 - \xi^d\right), \tag{3.80}$$

  - reverse $M \to A$ transformation:

$$F = |\varepsilon| - \frac{k}{E}\left(T - T_u\right), \tag{3.81}$$
$$F_s = \varepsilon_L \xi^d + \frac{\sigma_{Asu}}{E}, \tag{3.82}$$
$$F_f = \frac{\sigma_{Afu}}{E}, \tag{3.83}$$
$$\mathcal{H} = \begin{cases} 1 \text{ if } (\dot{F} < 0) \wedge (F_f < F < F_s) \\ 0 \text{ otherwise,} \end{cases} \tag{3.84}$$
$$\xi = \xi^d, \tag{3.85}$$
$$\xi_0 = \xi^d. \tag{3.86}$$

Here, T_u is an upper bound temperature and the stresses at which the forward and reverse transformations begin and end at temperature T_u are denoted by σ_{Msu}, σ_{Mfu}, σ_{Asu} and σ_{Afu}, respectively. This is just a different way of characterising the phase diagram (see Figure 3.12(c)). Moreover, as in model AS3 the functional form of the free energy is explicitly given, the slope of the phase transformation lines in the stress-temperature space is derived from the definition of the thermodynamic driving force, resulting

$$C_M = C_A = k = -\frac{\Delta s}{\varepsilon_L}. \tag{3.87}$$

Thus, the onset of phase transition is related to the change in entropy between the two phases Δs and to the maximum transformation strain. This is similar to what observed in the three-dimensional model by Popov and Lagoudas (2007), discussed further on in this chapter;

- AS4:

  – forward $A \rightarrow M$ transformation:

$$\begin{aligned}
F &= \varepsilon \mathrm{sgn}(\sigma) - \frac{C_M T}{E}, && (3.88)\\
F_s &= \left[\left(\xi^d - \xi_R\right)\beta + \xi_R \kappa\right] \mathrm{sgn}(\sigma) + \frac{\sigma_s - C_M M_s}{E}, && (3.89)\\
F_f &= \left[\left(1 - \xi_R\right)\beta + \xi_R \kappa\right] \mathrm{sgn}(\sigma) + \frac{\sigma_f - C_M M_s}{E_M}, && (3.90)\\
\mathcal{H} &= \begin{cases} 1 \text{ if } (\dot{F} > 0) \wedge (F_s < F < F_f) \\ 0 \text{ otherwise,} \end{cases} && (3.91)\\
\xi &= \xi^d, && (3.92)\\
\xi_0 &= -\left(1 - \xi^d\right) && (3.93)
\end{aligned}$$

– reverse $M \rightarrow A$ transformation:

$$F = \varepsilon \mathrm{sgn}(\sigma) - \frac{C_A T}{E}, \tag{3.94}$$

$$F_s = \left[\left(\xi^d - \xi_R\right)\beta + \xi_R \kappa\right] \mathrm{sgn}(\sigma) - \frac{C_A A_s}{E}, \tag{3.95}$$

$$F_f = \xi_R \kappa \mathrm{sgn}(\sigma) - \frac{C_A A_f}{E_A}, \tag{3.96}$$

$$\mathcal{H} = \begin{cases} 1 \text{ if } (\dot{F} < 0) \wedge (F_f < F < F_s) \\ 0 \text{ otherwise,} \end{cases} \tag{3.97}$$

$$\xi = \xi^d, \tag{3.98}$$

$$\xi_0 = \xi^d - \xi_R. \tag{3.99}$$

Note that the material parameters σ_s, σ_f, A_s and A_f are not constant in this model, but evolve from the virgin to the trained material (see Figure 3.12(d)). Their evolution, as well as the evolution of the irreversible martensite fraction ξ_R, is given in the following.

All terms described up to now are common to all four models. In addition, models AS3 and AS4 have special features detailed here.

In model AS3, complete thermomechanical coupling is defined by explicitating the functional form of the Helmholtz free energy. Then the heat equation is derived as described in Section 3.3.1 and automatically contains the coupling terms. The free energy is

$$\begin{aligned} \Psi =& \left[\left(e_A - T s_A\right) + \xi^d \left(\Delta e - T \Delta s\right)\right] + C\left[\left(T - T_0\right) - T \ln \frac{T}{T_0}\right] + \\ &+ \frac{1}{2} E \left[\varepsilon - \varepsilon_L \xi^d \mathrm{sgn}(\sigma)\right]^2 - \left(T - T_0\right)\left[\varepsilon - \varepsilon_L \xi^d \mathrm{sgn}(\sigma)\right] E\alpha, \end{aligned} \tag{3.100}$$

where the subscript A denotes quantities referred to the austenite phase, Δe and Δs are the differences in internal energy and entropy between martensite and austenite, T_0 denotes the temperature of the reference state.

The constitutive equation for the stress has already been introduced, while the constitutive equation for the entropy, necessary to write the coupled heat equation, is here recalled:

$$s = -\frac{\partial \Psi}{\partial T} = s_A + \xi^d \Delta s + C \ln \frac{T}{T_0} + \left[\varepsilon - \varepsilon_L \xi^d \mathrm{sgn}(\sigma)\right] E\alpha. \tag{3.101}$$

Assuming that the external contribution is null, the heat source is given by the sum of the thermomechanical coupling terms and the mechanical dissipation (see Equation (3.13)):

$$\begin{aligned} b &= T\left\{-E\alpha\dot{\varepsilon} + \left[\varepsilon_L \mathrm{sgn}(\sigma) E\alpha - \Delta s\right]\dot{\xi}^d\right\} + \\ &\quad + \left(\varepsilon_L\left|\sigma\right| + T\Delta s - \Delta e\right)\dot{\xi}^d. \end{aligned} \tag{3.102}$$

The heat equation is then given by Equation (3.12). Note that the term in the last bracket is the thermodynamic driving force associated to the internal variable ξ^d, which is used to define the kinetic equations for the variable itself.

By simultaneously solving the thermal and mechanical problems, model AS3 allows to study the effect of the loading rate on the shape memory alloy response. If the loading is fast and the heat generated by the phase transformation is not given time to dissipate, the phase transition zone of the stress-strain diagram changes significantly: in particular, the slope of the plateau zone is higher the fastest the loading rate. This result is similar to that described in Motahari and Ghassemieh (2007), where a simple model considering isothermal and adiabatic response (that is the two limit cases) is proposed. The influence of the loading rate on the shape memory alloy behaviour is particularly significant in seismic applications, where fast loads are involved and an accurate prediction of the dissipation is important.

In model AS4, new internal variables and relations are introduced in order to predict the training and the two-way memory effect. These effects are related to the total amount of forward and reverse transformation accumulated throughout the loading cycles. In order to keep track of these quantities, two new internal variables are introduced, γ_M and γ_A. Their evolution is the following:

$$\dot{\gamma}_M = \left|\dot{\xi}^d_{AM}\right|, \quad \dot{\gamma}_A = \left|\dot{\xi}^d_{MA}\right| \tag{3.103}$$

where ξ^d_{AM} and ξ^d_{MA} represent the martensite fraction during the forward ($A \rightarrow M$) and reverse ($M \rightarrow A$) transformation, respectively. Note that due to the presence of the modulus, γ_M and γ_A are always increasing and represent, in some sense, the amount of training that the material received.

According to the physical interpretation adopted in the paper, as the material is loaded and unloaded a fraction of the formed martensite is not able

to transform back to austenite. The irreversible martensite fraction ξ_R is thus introduced:

$$\xi_R = \xi_L \left[1 - \exp\left(-b_r \gamma_M\right)\right], \tag{3.104}$$

where ξ_L is the maximum irreversible martensite fraction which can be formed and b_r is a material parameter measuring the ability of the material to be trained.

Moreover, experimental observations show that the shape memory alloy behaviour is not initially stable, but stabilised after a certain number of loading cycles. In particular, the transformation zones shift to the right-bottom part of the phase diagram (see Figure 3.12(d)). In order to model this, the material parameters defining the transformation zones evolve according to exponential equations:

$$\sigma_s = \sigma_{s1} - (\sigma_{s1} - \sigma_{s2}) \left[1 - \exp\left(-b_{sM} \gamma_A\right)\right], \tag{3.105}$$

$$\sigma_f = \sigma_{f1} - (\sigma_{f1} - \sigma_{f2}) \left[1 - \exp\left(-b_{fM} \gamma_A\right)\right], \tag{3.106}$$

$$A_s = A_{s1} - (A_{s1} - A_{s2}) \left[1 - \exp\left(-b_{sA} \gamma_M\right)\right], \tag{3.107}$$

$$A_f = A_{f1} - (A_{f1} - A_{f2}) \left[1 - \exp\left(-b_{fA} \gamma_M\right)\right], \tag{3.108}$$

where the subscripts 1 and 2 indicate the transformation parameters for virgin and trained material, respectively, b_{sM}, b_{fM}, b_{sA} and b_{fA} are material parameters. Note that the transformation zone for the forward $A \rightarrow M$ transformation evolves as a function of γ_A, which represents the total amount of reverse transformation and viceversa.

3.3.4 Three-dimensional models

Most shape memory alloy applications involve the use of devices displaying one-dimensional behaviour, such as wires and ribbons. On the other hand, a three-dimensional description of the material behaviour may be required in order to model complex devices, such as stents or composite elements with embedded shape memory alloys. Even within phenomenological models, however, the extension of one-dimensional shape memory alloy models to a full three-dimensional description is not straightforward and some choices must be made which significantly influence the model predictive capabilities. In particular, the use of scalar or tensorial quantities as the main internal variables can drastically change the way some microscopic phenomena are portrayed.

When describing the three-dimensional shape memory alloy behaviour, all possible orientations of the martensite variants need to be accounted for. In single crystals, only a finite number N of martensite variants can appear depending upon the crystal symmetry (e.g., in the cubic to tetragonal transformation 3 martensite variants are possible, while in the cubic to monoclinic transformation 24 variants can appear, see Boyd and Lagoudas, 1996a), thus a way to represent all possible material configurations is to introduce N martensite fraction internal variables. Polycrystalline shape memory alloys, on the other hand, are made up of single crystal grains with different orientations. As the martensite variants are defined with respect to the crystallographic axes, whose orientation changes in the different grains, in polycrystalline shape memory alloys N internal variables are not sufficient to thoroughly describe the material microstructure.

Due to the presence of differently oriented martensite variants, the proportional relation between the transformation strain and the detwinned martensite fraction introduced in most one-dimensional shape memory alloy models is not obviously extended to three dimensions. In three-dimensional models, the amount of phase transformation can still be described in terms of scalar internal variables representing the volume fractions of the different constituents (as in Popov and Lagoudas, 2007) or directly in terms of the tensorial transformation strain (as in Auricchio and Petrini, 2004a). These different approaches deeply influence the model structure, their advantages and drawbacks are outlined in the following and detailed in the remainder of this section. In the first case, the transformation strain evolves together with the corresponding scalar variable, thus other (tensorial) internal variables need to be introduced in order to depict martensite reorientation. In the second case, a single tensorial variable depicts phase transformation, detwinning and martensite reorientation, but the model is not able to distinguish among different phases if no macroscopic deformation is associated to them. The discussion suggests to adopt an alternative approach, based on the introduction of two independent internal variables to define the crystal structure and arrangement: a scalar variable could be used to keep track of the martensite fraction, while its orientation could be described by an independent tensorial variable denoting the mean martensite strain. The roles played by the two different variables are similar, though not identical, to those of the detwinned martensite volume fraction ξ^d and the reorientation

parameter β in the models by Auricchio and Sacco, described in the previous section. A similar approach was recently adopted in the model proposed by Peultier et al. (2007).

Another issue to be dealt with in three-dimensional plasticity-like shape memory alloy models is the definition of the transformation surface. Provided some mathematical properties, such as convexity, are satisfied, different surfaces can be defined within a given model without altering its structure (see, for example, Qidway and Lagoudas, 2000). Symmetric transformation surfaces are usually defined in terms of the second deviatoric stress invariant (Auricchio and Petrini, 2002; Popov and Lagoudas, 2007), while the third invariant can be introduced to account for tension-compression asymmetry (Auricchio and Petrini, 2004a; Qidway and Lagoudas, 2000). Indeed, the different behaviour in tension and compression is widely accounted for both by experimental observations and model predictions (Lexcellent and Schlömerkemper, 2007).

Popov and Lagoudas model

The model recently proposed by Popov and Lagoudas (2007) belongs to a family of models developed by Lagoudas and coworkers starting from the mid 1990s (Bo and Lagoudas, 1999a,b,c; Bo et al., 1999; Boyd and Lagoudas, 1996a,b; Lagoudas and Bo, 1999; Lagoudas et al., 1996; Popov and Lagoudas, 2007; Qidway and Lagoudas, 2000). In these works, micromechanical considerations and an averaging process over the Reference Volume Element (Bo and Lagoudas, 1999a; Boyd and Lagoudas, 1996a) constitute the rational basis for the development of phenomenological models. As in the works by Auricchio and Sacco, all models developed by Lagoudas and coworkers have the same structure, while the introduction or removal of the appropriate internal variables allow to predict different phenomena. In the following, the most recent version of the model (Popov and Lagoudas, 2007) is discussed in details, while some comments are given on the choices operated in the previous works.

In all models, internal variables are introduced to describe the microstructure in terms of mass fractions of the different phases (as the phase transformation is mostly volume-preserving, the mass and the volume fractions are considered equivalent). As discussed earlier for one-dimensional models, a single internal variable ξ^d may be chosen to define the whole martensite fraction (Bo and Lagoudas, 1999a; Boyd and Lagoudas, 1996a; Qidway and Lagoudas,

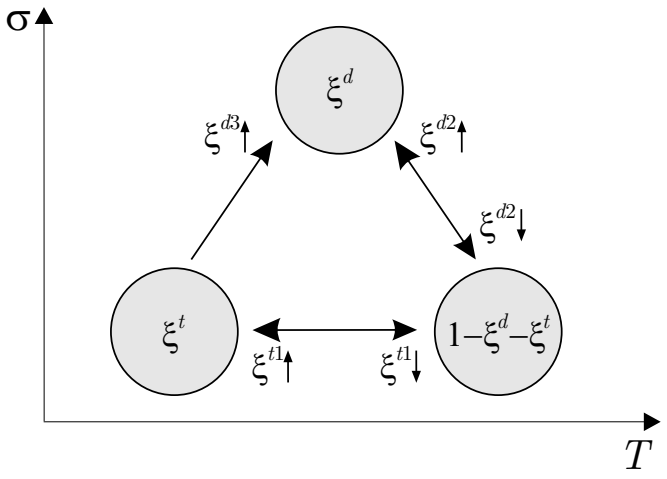

Figure 3.13: Internal variables for Popov and Lagoudas (2007) model

2000), alternatively two variables ξ^d and ξ^t may be introduced for detwinned and twinned martensite, respectively (Boyd and Lagoudas, 1996a). In Popov and Lagoudas (2007), the phase volume fractions are distinguished according to their origin (see Figure 3.13). Three internal variables are thus introduced: ξ^{t1} is the twinned martensite fraction, generated via phase transformation from austenite, ξ^{d2} and ξ^{d3} are the detwinned martensite fractions generated via phase transformation from austenite and via detwinning from twinned martensite, respectively. Thus, the total twinned and detwinned martensite fractions are

$$\xi^t = \xi^t_0 + \xi^{t1} - \xi^{d3}, \;\; \xi^d = \xi^d_0 + \xi^{d2} + \xi^{d3}. \tag{3.109}$$

This choice allows to keep track of detwinning and phase transformation as separate phenomena.

Different effects contribute to the overall inelastic strain: thermal expansion, phase transformation, detwinning of twinned martensite, reorientation of detwinned martensite and plastic strain. Each model includes different terms

from this set.

Having introduced the phase volume fractions as internal variables, the transformation strain $\boldsymbol{\varepsilon}_{tr}$ is directly related to ξ^d via an evolution equation of the type $\dot{\boldsymbol{\varepsilon}}_{tr} = \boldsymbol{\Lambda}\dot{\xi}^d$, where the tensor $\boldsymbol{\Lambda}$ is a function of the applied stress during the forward transformation and of the current transformation strain during the reverse transformation. This ensures complete disappearance of the transformation strain when $\xi^d = 0$. This relation is obtained through micromechanical considerations in Boyd and Lagoudas (1996a) and Bo and Lagoudas (1999a) and derived as a consequence of the principle of maximum transformation dissipation in Qidway and Lagoudas (2000). In the model by Popov and Lagoudas (2007), detwinning and transformation strain are defined by two flow rules and may be regulated by different tensors:

$$\dot{\boldsymbol{\varepsilon}}_d = \boldsymbol{\Lambda}_d \dot{\xi}^{d3}, \quad \dot{\boldsymbol{\varepsilon}}_{tr} = \boldsymbol{\Lambda}_{tr} \dot{\xi}^{d2}. \tag{3.110}$$

Tensors $\boldsymbol{\Lambda}_d$ and $\boldsymbol{\Lambda}_{tr}$ are specified as

$$\boldsymbol{\Lambda}_d = \sqrt{\frac{3}{2}} \varepsilon_{L,d} \frac{\operatorname{dev}(\boldsymbol{\sigma})}{\|\operatorname{dev}(\boldsymbol{\sigma})\|}, \tag{3.111}$$

$$\boldsymbol{\Lambda}_{tr} = \begin{cases} \sqrt{\frac{3}{2}} \varepsilon_{L,tr} \frac{\operatorname{dev}(\boldsymbol{\sigma})}{\|\operatorname{dev}(\boldsymbol{\sigma})\|} & \text{for } \dot{\xi}^{t2} > 0 \\ \sqrt{\frac{3}{2}} \varepsilon_{L,tr} \frac{\operatorname{dev}(\boldsymbol{\varepsilon}_{tr} + \boldsymbol{\varepsilon}_d)}{\|\operatorname{dev}(\boldsymbol{\varepsilon}_{tr} + \boldsymbol{\varepsilon}_d)\|} & \text{for } \dot{\xi}^{t2} < 0 \end{cases}, \tag{3.112}$$

where $\operatorname{dev}(\cdot)$ denotes the deviatoric part of a tensor, $\varepsilon_{L,d}$ and $\varepsilon_{L,tr}$ are material parameters defining the maximum uniaxial strain in detwinning and transformation, respectively.

As the transformation and detwinning strain evolve together with the corresponding martensite fractions and no other strain variable related to the material microstructure is introduced, the model by Popov and Lagoudas (2007) does not allow for reorientation of detwinned martensite. This constitutes a significant limitation, as it is not possible to model tension-compression loading cycles below the austenite finish temperature or loading paths in which the load direction changes over time. This limitation could be overcome by introducing new internal variables, such as the detwinned martensite reorientation strain $\boldsymbol{\varepsilon}_r$. This way, three different tensors would be used to represent the transformation, detwinning and reorientation strains, namely $\boldsymbol{\varepsilon}_{tr}$, $\boldsymbol{\varepsilon}_d$ and $\boldsymbol{\varepsilon}_r$.

The idea outlined to model detwinned martensite reorientation is, obviously, not the only possible approach. Detwinning and reorientation are, in fact, the same phenomenon. In both cases, indeed, the martensite crystals change their orientation because of a change in the applied load: in the first case, twinned martensite becomes detwinned, while in the second case the change is between different detwinned martensite variants. As the twinned and detwinned martensite are described with different internal variables in Popov and Lagoudas (2007), detwinning and reorientation must be described separately. On the other hand, a single martensite volume fraction internal variable ξ^d would lead to a single reorientation tensor $\boldsymbol{\varepsilon}_r$ to model reorientation of both twinned and detwinned martensite (see Boyd and Lagoudas, 1996a).

Finally, plastic deformations are introduced in Bo and Lagoudas (1999a,b,c) and Lagoudas and Bo (1999) to account for the irreversible phenomena related to two-way memory and training. This choice implies a different microstructural interpretation with respect to the one adopted by Auricchio et al. (2003), who depicted the same phenomena by introducing the accumulation of irreversible martensite.

In order to obtain the constitutive equations, a functional form of the free energy is explicitly defined in every model. Gibbs free energy is considered as most experimental tests are carried out in stress control. From micromechanical considerations, the free energy is made up of two parts:

$$\mathcal{G} = \mathcal{G}_{pure} + \mathcal{G}_{mix}, \tag{3.113}$$

where $\mathcal{G}_{pure}$ is the thermoelastic energy of the pure phases, while $\mathcal{G}_{mix}$ represents the energy of mixing, responsible for the transformation behaviour. Indeed, it has been shown by Lagoudas et al. (1996, 2006) that many earlier models can be interpreted within the same context with an appropriate choice of the term $\mathcal{G}_{mix}$. In Popov and Lagoudas (2007), the thermoelastic energy of a general phase $\alpha = \{A, M\}$ is given as follows:

$$\begin{aligned} \mathcal{G}_\alpha &= -\frac{1}{2\rho}\boldsymbol{\sigma}\cdot\mathbf{F}_\alpha\boldsymbol{\sigma} - \frac{1}{\rho}\boldsymbol{\sigma}\cdot\boldsymbol{\alpha}_\alpha\left(T-T_0\right) - \frac{1}{\rho}\boldsymbol{\sigma}\cdot\left(\boldsymbol{\varepsilon}_{tr}+\boldsymbol{\varepsilon}_d\right) + \\ &\quad + c_\alpha\left[\left(T-T_0\right) - T\ln\frac{T}{T_0}\right] - s_{0\alpha}\left(T-T_0\right) + e_{0\alpha}, \end{aligned} \tag{3.114}$$

where $\mathbf{F}$ is the flexibility tensor, $\boldsymbol{\alpha}$ is the thermal expansion coefficients tensor, c is the specific heat capacity, s_0 and e_0 the entropy and internal energy at the

reference state and the subscript α refers to the general phase α. The energy $\mathcal{G}_{pure}$ is therefore obtained as

$$\begin{aligned}\mathcal{G}_{pure} &= \mathcal{G}_A + \left(\xi^t + \xi^d\right)\left(\mathcal{G}_M - \mathcal{G}_A\right) = \\ &= -\frac{1}{2\rho}\boldsymbol{\sigma}\cdot\mathbf{F}\boldsymbol{\sigma} - \frac{1}{\rho}\boldsymbol{\sigma}\cdot\boldsymbol{\alpha}\left(T - T_0\right) - \frac{1}{\rho}\boldsymbol{\sigma}\cdot\left(\boldsymbol{\varepsilon}_{tr} + \boldsymbol{\varepsilon}_d\right) + \\ &\quad + c\left[\left(T - T_0\right) - T\ln\frac{T}{T_0}\right] - s_0\left(T - T_0\right) + e_0, \end{aligned} \tag{3.115}$$

where the material parameters are a function of the martensite fraction:

$$\mathbf{F} = \mathbf{F}\left(\xi^t + \xi^d\right) = \mathbf{F}_A + \left(\xi^t + \xi^d\right)\Delta\mathbf{F}, \tag{3.116}$$

$$\boldsymbol{\alpha} = \boldsymbol{\alpha}\left(\xi^t + \xi^d\right) = \boldsymbol{\alpha}_A + \left(\xi^t + \xi^d\right)\Delta\boldsymbol{\alpha}, \tag{3.117}$$

$$c = c\left(\xi^t + \xi^d\right) = c_A + \left(\xi^t + \xi^d\right)\Delta c, \tag{3.118}$$

$$s_0 = s_0\left(\xi^t + \xi^d\right) = s_{0A} + \left(\xi^t + \xi^d\right)\Delta s_0, \tag{3.119}$$

$$e_0 = e_0\left(\xi^t + \xi^d\right) = e_{0A} + \left(\xi^t + \xi^d\right)\Delta e_0. \tag{3.120}$$

The free energy of mixing is the following:

$$\mathcal{G}_{mix} = \frac{1}{\rho}\int_0^t \left[f_1\dot{\xi}^{t1}(\tau) + f_2\dot{\xi}^{d2}(\tau) + f_3\dot{\xi}^{d3}(\tau)\right]\mathrm{d}\tau, \tag{3.121}$$

where

$$f_1 = f_1\left(\xi^{t1}, \xi^{d2}, \xi^{d3}, \operatorname{sgn}\left(\dot{\xi}^{t1}\right)\right), \tag{3.122}$$

$$f_2 = f_2\left(\xi^{t1}, \xi^{d2}, \xi^{d3}, \operatorname{sgn}\left(\dot{\xi}^{d2}\right)\right), \tag{3.123}$$

$$f_3 = f_3\left(\xi^{t1}, \xi^{d2}, \xi^{d3}\right) \tag{3.124}$$

are general hardening functions which may be different for the forward and reverse transformation. The choice of the hardening functions depends upon the material considered and should be part of material characterisation. In Popov and Lagoudas (2007) they are simply chosen as a linear function of the martensite fractions:

$$f_1 = \begin{cases} \Delta_1^+\xi^t \text{ for } \dot{\xi}^{t1} > 0 \\ \Delta_1^-\xi^t \text{ for } \dot{\xi}^{t1} < 0 \end{cases}, \tag{3.125}$$

$$f_2 = \begin{cases} \Delta_2^+\xi^d \text{ for } \dot{\xi}^{d2} > 0 \\ \Delta_2^-\xi^d \text{ for } \dot{\xi}^{d2} < 0 \end{cases}, \tag{3.126}$$

$$f_2 = \Delta_3\xi^d \text{ for } \dot{\xi}^{d3} > 0, \tag{3.127}$$

where $\Delta_1^{\pm}$, $\Delta_2^{\pm}$ and Δ_3 are material parameters which serve as scaling factors so that $f_i(0) = 0$ and $f_i(1) = 1$. Note that the superscripts $+$ and $-$ denote the forward and reverse transformations, respectively.

The constitutive equations are chosen to satisfy the second principle of thermodynamics. They are

$$\boldsymbol{\sigma} = \mathbf{F}^{(-1)}\left[\boldsymbol{\varepsilon} - \boldsymbol{\alpha}(T - T_0) - \boldsymbol{\varepsilon}_{tr} - \boldsymbol{\varepsilon}_d\right], \tag{3.128}$$

$$s = \frac{1}{\rho}\boldsymbol{\sigma}\cdot\boldsymbol{\alpha} + c\ln\frac{T}{T_0} + s_0. \tag{3.129}$$

The thermodynamic driving forces associated to the internal variables ξ^{t1}, ξ^{d2} and ξ^{d3} are the following

$$\pi_{t1} = \tilde{\pi} - f_1, \quad \pi_{d2} = \tilde{\pi} + \boldsymbol{\sigma}\cdot\boldsymbol{\Lambda}_{tr} - f_2, \quad \pi_{d3} = \boldsymbol{\sigma}\cdot\boldsymbol{\Lambda}_d - f_3, \tag{3.130}$$

where

$$\begin{aligned}\tilde{\pi} =& \frac{1}{2}\boldsymbol{\sigma}\cdot\Delta\mathbf{F}\boldsymbol{\sigma} + \boldsymbol{\sigma}\cdot\Delta\boldsymbol{\alpha}(T - T_0) + \rho\Delta s_0 T + \\ &- \rho\Delta c\left[(T - T_0) - \ln\frac{T}{T_0}\right] - \rho\Delta e_0.\end{aligned} \tag{3.131}$$

The transformation and detwinning surfaces are defined as follows:

$$F_1^+ = \pi_{t1} - Y_1^+ = 0, \qquad F_1^- = -\pi_{t1} - Y_1^- = 0, \tag{3.132}$$

$$F_2^+ = \pi_{d2} - Y_2^+ = 0, \qquad F_2^- = -\pi_{d2} - Y_2^- = 0, \tag{3.133}$$

$$F_3 = \pi_{d3} - Y_3 = 0, \tag{3.134}$$

where $Y_1^{\pm}$, $Y_2^{\pm}$ and Y_3 are material parameters. The corresponding consistency conditions are defined directly in terms of the internal variables evolution:

$$\dot{\xi}^{t1} \geq 0,\ F_1^+ \leq 0,\ F_1^+\dot{\xi}^{t1} = 0, \tag{3.135}$$

$$\dot{\xi}^{t1} \leq 0,\ F_1^- \leq 0,\ F_1^-\dot{\xi}^{t1} = 0, \tag{3.136}$$

$$\dot{\xi}^{d2} \geq 0,\ F_2^+ \leq 0,\ F_2^+\dot{\xi}^{d2} = 0, \tag{3.137}$$

$$\dot{\xi}^{d2} \leq 0,\ F_2^- \leq 0,\ F_2^-\dot{\xi}^{d2} = 0, \tag{3.138}$$

$$\dot{\xi}^{d3} \geq 0,\ F_3 \leq 0,\ F_3\dot{\xi}^{d3} = 0, \tag{3.139}$$

thus $\dot{\xi}^{t1}$, $\dot{\xi}^{d2}$ and $\dot{\xi}^{d3}$ are the consistency parameters for the model. The evolution of the internal variables can thus be obtained directly by enforcing the

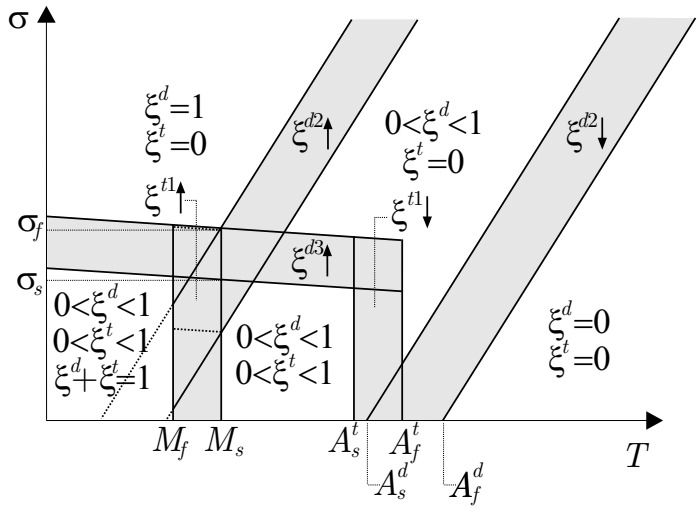

Figure 3.14: Phase diagram for Popov and Lagoudas (2007) model

consistency conditions, then the corresponding inelastic strain evolution can be evaluated from the flow rules (3.110). Note that the martensite fractions must satisfy the following constraints:

$$0 \leq \xi^t \leq 1, \tag{3.140}$$

$$0 \leq \xi^d \leq 1, \tag{3.141}$$

$$0 \leq \left(\xi^d + \xi^t\right) \leq 1, \tag{3.142}$$

thus the consistency condition for a given transformation holds only until the corresponding transformation is complete.

The model described up to now requires the definition of a number of parameters. In particular, the parameters defining the transformation and hardening behaviour, namely ($\Delta_i^{\pm}$, Δ_3, $Y_i^{\pm}$, Y_3, $f_i^{\pm}$, f_3) where $i = \{1, 2\}$, are related to the uniaxial phase diagram in the stress-temperature space (see Figure 3.14). Note that the phase diagram depicted in Figure 3.14 is different from those assumed in the models discussed up to now. Indeed, as different internal variables

are defined for phase transformations and detwinning, five independent strips are depicted in the phase diagram, each associated to one of the transformation surfaces (3.132), (3.133) and (3.134). Even though the relative position of the transformation strips is restricted by thermodynamic considerations, this approach allows a certain freedom to define the transformation behaviour. In particular, a novelty introduced in this model is the difference between the reverse transformation temperatures for twinned and detwinned martensite (A_s^d and A_f^d versus A_s^t and A_f^t). This distinction is motivated by calorimetric observations and it is further discussed in Section 3.4. Moreover, the detwinning strip does not end at the martensite start temperature but extends all the way to the reverse transformation. This prevents the existence of twinned martensite at high stress levels, which was possible for certain loading paths in the previous phase diagrams. Other differences with respect to previously proposed phase diagrams are the presence of a vertical twinned martensite to austenite transformation strip and the possibility to either extend to zero stress or limit at a critical stress value the detwinned martensite forward transformation, according to the level of training of the material. Once the phase diagram is experimentally defined, the transformation and hardening parameters can be determined by simulating various simple loading paths. The calculations are straightforward and they are not reported.

The remaining model parameters include the characteristics of the single phases and the maximum uniaxial transformation and detwinning strain: ($\mathbf{F}_\alpha$, $\boldsymbol{\alpha}_\alpha$, c_α, $s_{0\alpha}$, $e_{0\alpha}$, $\varepsilon_{L,d}$, $\varepsilon_{L,tr}$), where $\alpha = \{A, M\}$. These parameters have a direct physical interpretation and can be determined via mechanic and calorimetric tests.

The compliances and thermal expansion coefficients of the two phases can be determined by standard tests. The maximum transformation and detwinning strain are easily evaluated via uniaxial tests with complete transformation or detwinning.

The specific heat capacity of the two phases can be determined from calorimetric measurements. In particular, it is often safe to assume the same specific heat for austenite and martensite, thus in the following calculations we set $\Delta c = 0$.

The difference in internal energy and entropy between the two phases, Δe_0 and Δs_0 respectively, can be determined via differential scanning calorimeter

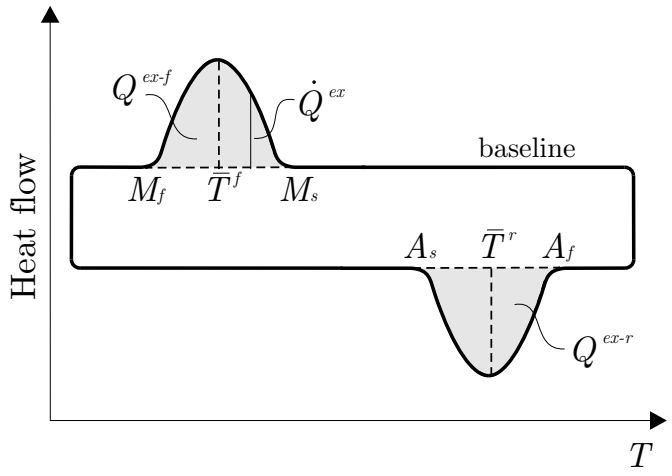

Figure 3.15: Schematic representation of a DSC measurement for shape memory alloys

measurements (Bo et al., 1999; Lagoudas and Bo, 1999). The differential scanning calorimeter (DSC) allows to measure the heat flow through a sample of material when the material is heated or cooled at zero stress. A schematic representation of a DSC measurement is reported in Figure 3.15. The baseline represents the heat flow in the absence of phase transformation, while the peaks and troughs occurring during phase transformation are related to the latent heat. In particular, the rate of the excess heat is given by $\dot{Q}^{ex} = \dot{Q} - c\dot{T}$ and it is represented by the distance between the curve and the baseline. Integrating over the temperature yields the total latent heat Q^{ex} for the forward or reverse transformation, represented by the shaded areas in Figure 3.15. Notice that the DSC curves can be used to determine the zero stress transformation temperatures M_s, M_f, A_s and A_f.

The difference in internal energy between austenite and martensite, Δe_0, is related to the entropy difference Δs_0 and it can be determined by defining the equilibrium temperature T^{eq}. The equilibrium temperature is the temperature

at which the driving force at zero stress is null (Raniecki and Lexcellent, 1994), thus:

$$\rho\Delta s_0 T^{eq} - \rho\Delta e_0 = 0. \tag{3.143}$$

Assuming that the equilibrium temperature is given by $T^{eq} = \left(M_s + A_f^t\right)/2$, one obtains

$$\rho\Delta e_0 = \rho\Delta s_0 \frac{M_s + A_f^t}{2}. \tag{3.144}$$

The entropy difference is related to the total latent heat Q^{ex}. As already pointed out, Q^{ex} can be measured experimentally via DSC. Its analytical value is obtained in the following starting from the heat equation, Equation (3.12). The heat source, Equation (3.13), can be rewritten in terms of the Gibbs free energy as

$$b = r + \rho T\left(\frac{\partial^2 \mathcal{G}}{\partial T \partial \boldsymbol{\sigma}} \cdot \dot{\boldsymbol{\sigma}} + \frac{\partial^2 \mathcal{G}}{\partial T \partial V_k}\dot{V}_k\right) - \frac{\partial \mathcal{G}}{\partial V_k}\dot{V}_k. \tag{3.145}$$

Then, considering Equation (3.12) and the rate of specific heat change $\rho\dot{Q} = r - \nabla \cdot \mathbf{q}$ it is possible to evaluate the rate of the excess heat:

$$\rho\dot{Q}^{ex} = -\rho T\left(\frac{\partial^2 \mathcal{G}}{\partial T \partial \boldsymbol{\sigma}} \cdot \dot{\boldsymbol{\sigma}} + \frac{\partial^2 \mathcal{G}}{\partial T \partial V_k}\dot{V}_k\right) + A_k \dot{V}_k. \tag{3.146}$$

During a DSC test on a sample containing no detwinned martensite, the stress is null and the only evolving internal variable is ξ^{t1}. The rate of excess heat thus becomes

$$\rho\dot{Q}^{ex} = \left(-\rho T \frac{\partial^2 \mathcal{G}}{\partial T \partial \xi^{t1}} + \pi_{t1}\right)\dot{\xi}^{t1}. \tag{3.147}$$

During forward transformation, the first consistency condition (3.135) becomes

$$\pi_{t1} = Y_1^+, \quad F_{1,T}^+ \dot{T} + F_{1,\xi^{t1}}^+ \dot{\xi}^{t1} = 0, \tag{3.148}$$

thus combining the previous expressions yields

$$\rho\dot{Q}^{ex} = -\left(-\rho T \frac{\partial^2 \mathcal{G}}{\partial T \partial \xi^{t1}} + Y_1^+\right)\frac{F_{1,T}^+}{F_{1,\xi^{t1}}^+}\dot{T}. \tag{3.149}$$

The functional form of the free energy previously introduced enables us to write

$$\rho\dot{Q}^{ex} = -\left(\rho T \Delta s_0 + Y_1^+\right)\frac{F_{1,T}^+}{F_{1,\xi^{t1}}^+}\dot{T}. \tag{3.150}$$

Integrating yields the total latent heat for the forward transformation

$$Q^{ex-f} = \rho \Delta s_0 \bar{T}^f - Y_1^+, \tag{3.151}$$

where the temperature $\bar{T}^f$ is an average temperature for the forward phase transformation, defined as

$$\bar{T}^f = -\int_{\infty}^{-\infty} T \frac{F_{1,T}^+}{F_{1,\xi^{t1}}^+} \dot{T} = \int_{-\infty}^{\infty} T \frac{F_{1,T}^+}{F_{1,\xi^{t1}}^+} \dot{T}. \tag{3.152}$$

An approximation of $\bar{T}^f$ can be determined by considering a temperature which divides the area representing the latent heat in two equal parts. Notice that

$$\int_{\infty}^{-\infty} \frac{F_{1,T}^+}{F_{1,\xi^{t1}}^+} \dot{T} = \int_{\infty}^{-\infty} \dot{\xi}^{t1} = 1, \tag{3.153}$$

as the twinned martensite fraction goes from zero to one during the complete forward transformation. In an analogous way, for the reverse transformation it is possible to obtain

$$Q^{ex-r} = -\rho \Delta s_0 \bar{T}^r - Y_1^-, \tag{3.154}$$

where

$$\bar{T}^r = \int_{-\infty}^{\infty} T \frac{F_{1,T}^-}{F_{1,\xi^{t1}}^-} \dot{T}. \tag{3.155}$$

Neglecting irreversible phenomena, the total latent heat released during forward transformation should be equal to the one absorbed during reverse transformation, that is $\left|Q^{ex-f}\right| = |Q^{ex-r}|$. This yields

$$Q^{ex-f} - Q^{ex-r} = 2Q^{ex-f} = \rho \Delta s_0 \left(\bar{T}^f + \bar{T}^r\right) - Y_1^+ + Y_1^-. \tag{3.156}$$

From the expressions for $Y_1^{\pm}$ reported in Popov and Lagoudas (2007) and Equation (3.144) we obtain $Y_1^+ - Y_1^- = 0$, thus Δs_0 can be evaluated as follows

$$\rho \Delta s_0 = \frac{2Q^{ex-f}}{\bar{T}^f + \bar{T}^r}. \tag{3.157}$$

It is interesting to notice that, as already anticipated in the discussion of the models proposed by Auricchio and Sacco earlier in this chapter, the entropy difference is also related to the slope of the $A \rightarrow M^d$ transformation lines in

the uniaxial phase diagram. Indeed, neglecting the difference in elastic moduli and thermal expansion coefficients between the two phases, the uniaxial transformation lines become

$$\rho\Delta s_0 T - \rho\Delta e_0 + \sigma\varepsilon_{L,tr} - f_2 \pm Y_2^{\mp} = 0, \tag{3.158}$$

thus, in the stress-temperature plane, the slope is

$$k = -\frac{\rho\Delta s_0}{\varepsilon_{L,tr}}. \tag{3.159}$$

Indeed, due to the different properties between the two phases, the transformation curves are not exactly linear, but this effect is evident mostly at high stress levels.

Auricchio and Petrini model

The model proposed by Auricchio and Petrini (2004a) was developed starting from the work of Souza et al. (1998). First, some improvements to the time-continuous model and the integration algorithms were proposed (Auricchio and Petrini, 2002), then complete thermomechanical coupling was introduced (Auricchio and Petrini, 2004a,b). More recently, a modified model introducing the effect of permanent deformations was proposed (Auricchio et al., 2007). Here, the 2004 version of the model is discussed in details and some comments are included concerning the other works.

This model is cast in the framework of generalised standard materials. This framework, along with the choice of convex potentials, allows to demonstrate the well-posedness of the model (which automatically satisfies the second principle of thermodynamics) and thus to have a robust time-continuous model to be used for subsequent numerical developments.

The transformation strain tensor $\boldsymbol{\varepsilon}_{tr}$ is chosen as internal variable. Experimental evidence suggests that martensitic transformations preserve the volume, thus the transformation strain is a purely deviatoric tensor. The choice of a tensorial internal variable makes the model by Auricchio and Petrini dramatically different from the models proposed by Lagoudas and coworkers, previously discussed. Indeed, the martensite volume fraction is not defined here and the phase transformation is viewed only through its effect on the transformation

strain. For this reason, the model can only distinguish between an undeformed parent phase (which could be either austenite or twinned martensite) and a product phase which shows some degree of detwinning. This feature may be viewed as a limitation of the model, as it does not allow to account for the different material properties of austenite and martensite and to model purely temperature-induced phase transformation (such as the one occurring during a DSC test). On the other hand, the transformation strain evolution law does not need to be related to the evolution of a scalar parameter, thus phase transformation, detwinning of twinned martensite and reorientation between different detwinned martensite variants can be described within the same evolution law. Another internal variable is introduced in the modified model (Auricchio et al., 2007) in order to keep track of the permanent inelastic strain.

A convex free energy function is postulated. As the time-discrete version of the model is going to be used for finite element simulations, a strain-driven problem is formulated by using Helmholtz free energy:

$$\begin{aligned}\Psi &= \frac{1}{2}K\left[\mathrm{tr}\left(\boldsymbol{\varepsilon}\right)\right]^2 + G\left\|\mathrm{dev}\left(\boldsymbol{\varepsilon}\right) - \boldsymbol{\varepsilon}_{tr}\right\|^2 - 3\alpha K\,\mathrm{tr}\left(\boldsymbol{\varepsilon}\right)\left(T - T_0\right) + \\ &\quad + c\left[\left(T - T_0\right) - T\ln\frac{T}{T_0}\right] - s_0 T + e_0 + \\ &\quad + k\left\langle T - M_f\right\rangle\left\|\boldsymbol{\varepsilon}_{tr}\right\| + \frac{1}{2}h\left\|\boldsymbol{\varepsilon}_{tr}\right\|^2 + \mathscr{I}_{\varepsilon_L}\left(\boldsymbol{\varepsilon}_{tr}\right), \end{aligned} \tag{3.160}$$

where $\mathrm{tr}\left(\cdot\right)$ denotes the trace of a tensor, K and G are the bulk and shear moduli, α is the thermal expansion coefficient, k and h are material parameters and $\langle\cdot\rangle$ denotes the positive part of the argument. Here, the first line contains the thermoelastic volumetric and deviatoric terms; the second line contains the energy related to temperature change; finally, the third line contains the terms related to phase transformation and hardening. In particular, the last term is an indicator function used to limit the norm of the transformation strain:

$$\mathscr{I}_{\varepsilon_L}\left(\boldsymbol{\varepsilon}_{tr}\right) = \begin{cases} 0 & \text{if } \left\|\boldsymbol{\varepsilon}_{tr}\right\| \leq \varepsilon_L \\ +\infty & \text{if } \left\|\boldsymbol{\varepsilon}_{tr}\right\| > \varepsilon_L \end{cases}. \tag{3.161}$$

The constitutive equations are derived using standard arguments:

$$\begin{aligned} \mathrm{tr}\,(\boldsymbol{\sigma}) &= 3K\left[\mathrm{tr}\,(\boldsymbol{\varepsilon}) - 3\alpha\,(T - T_0)\right], && (3.162)\\ \mathrm{dev}\,(\boldsymbol{\sigma}) &= 2G\left(\mathrm{dev}\,(\boldsymbol{\varepsilon}) - \boldsymbol{\varepsilon}_{tr}\right), && (3.163)\\ s &= 3\alpha K \mathrm{tr}\,(\boldsymbol{\varepsilon}) + c\ln\frac{T}{T_0} + s_0 - k\left\|\boldsymbol{\varepsilon}_{tr}\right\|\frac{\langle T - M_f\rangle}{\|T - M_f\|}. && (3.164)\end{aligned}$$

The thermodynamic driving force of the transformation is

$$\mathbf{X} = \mathrm{dev}\,(\boldsymbol{\sigma}) - \left[k\,\langle T - M_f\rangle + h\left\|\boldsymbol{\varepsilon}_{tr}\right\| + \gamma\right]\frac{\partial\left\|\boldsymbol{\varepsilon}_{tr}\right\|}{\partial\boldsymbol{\varepsilon}_{tr}}, \tag{3.165}$$

where

$$\begin{aligned} &\gamma = 0 \quad \text{if } \left\|\boldsymbol{\varepsilon}_{tr}\right\| < \varepsilon_L,\\ &\gamma \geq 0 \quad \text{if } \left\|\boldsymbol{\varepsilon}_{tr}\right\| = \varepsilon_L. \end{aligned} \tag{3.166}$$

Note that the bracketed term in Equation (3.165) has a role similar to that of the back-stress in classical plasticity, defining the position of the centre of the elastic domain. As the derivative of the transformation strain norm is not defined for $\left\|\boldsymbol{\varepsilon}_{tr}\right\| = 0$, in the time-discrete version of the model the Euclidean norm is substituted with a regularised norm:

$$\left\|\boldsymbol{\varepsilon}_{tr}\right\|_{reg} = \left\|\boldsymbol{\varepsilon}_{tr}\right\| - \frac{\delta^{(\delta+1)/\delta}}{\delta - 1}\left(\left\|\boldsymbol{\varepsilon}_{tr}\right\| + \delta\right)^{(\delta-1)/\delta}, \tag{3.167}$$

where δ is a regularisation parameter.

A transformation function which accounts for tension-compression asymmetry is defined:

$$F\,(\mathbf{X}) = \sqrt{2J_2} + m\frac{J_3}{J_2} - R, \tag{3.168}$$

where J_2 and J_3 are the second and third invariant of the tensor $\mathbf{X}$, m and R are material parameters related to the critical detwinning stresses in tension and compression, σ_t and σ_c:

$$m = \sqrt{\frac{27}{2}}\frac{\sigma_c - \sigma_t}{\sigma_c + \sigma_t}, \quad R = 2\sqrt{\frac{2}{3}}\frac{\sigma_c\sigma_t}{\sigma_c + \sigma_t}. \tag{3.169}$$

It should be $m \leq 0.46$ in order to ensure convexity of the transformation function. Notice that, in previous versions of the model, a symmetric transformation function was defined

$$F\,(\mathbf{X}) = \|\mathbf{X}\| - R, \tag{3.170}$$

and R was defined in terms of the forward and reverse transformation temperatures:

$$R = k\left(A_f - M_f\right). \tag{3.171}$$

As in associated plasticity, the transformation function and the plastic potentials coincide and the flow rule for the transformation strain is the following:

$$\dot{\varepsilon}_{tr} = \dot{\zeta}\frac{\partial F\left(\mathbf{X}\right)}{\partial \boldsymbol{\sigma}}, \tag{3.172}$$

along with the Kuhn-Tucker condition

$$\dot{\zeta} \geq 0, \;\; F \leq 0, \;\; \dot{\zeta}F = 0. \tag{3.173}$$

The role of the material parameters introduced in the Auricchio and Petrini (2004a) model is discussed here. As the model does not distinguish between austenite and twinned martensite, a single set of elastic and thermal properties is considered: $(K, G, \alpha, c, s_0, e_0)$. In particular, the entropy difference Δs_0 between the two phases, which in the model by Popov and Lagoudas (2007) was seen to be responsible for the slope of the transformation lines in the uniaxial phase diagram (see Equation (3.159)), is not portrayed in this model. Its role is played by the parameter k: for temperatures above M_f, indeed, the centre of the elastic domain linearly depends on the temperature. For temperatures below M_f, on the other hand, the position of the elastic domain is independent of temperature, thus representing the horizontal martensite detwinning line. The parameter h introduces linear kinematic hardening related to the amount of transformation strain, while m and R define the radius of the elastic domain. The role of each material parameters is clarified in Figure 3.16(a). Here, the white area represents the elastic domain for positive transformation strain in the uniaxial stress-temperature diagram (for negative transformation strain, the slope of the lines is $-k$).

As it can be seen, the uniaxial diagram associated to this model is quite different from most phase diagrams (see for example Figure 3.16(b)). As the austenite to twinned martensite transformation is not described, the vertical transformation strip present in most phase diagrams disappears. Moreover, while the hysteresis associated to detwinning and phase transformation (d_d and d_{tr}, respectively) are generally different, in this model they are both defined by the choice of the parameters m and R. Indeed, in different versions of

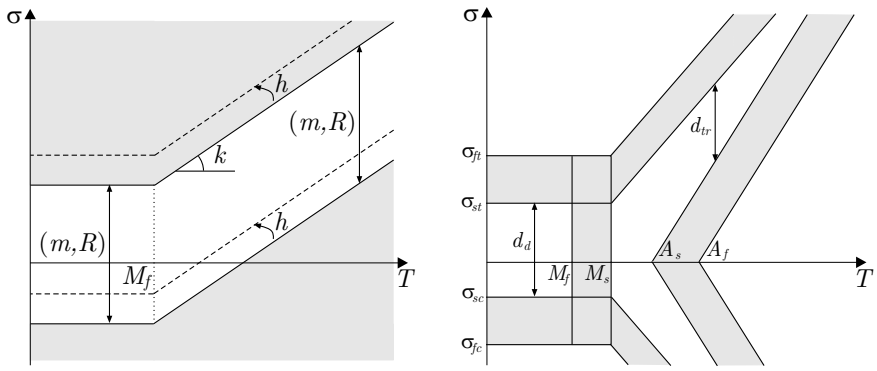

(a) Auricchio and Petrini (2004a) model (b) Typical phase diagram

Figure 3.16: Uniaxial phase diagrams

the model these parameters have been defined either in terms of the tension-compression critical stresses for detwinning, as in Equation (3.169), or the phase transformation hysteresis, as in Equation (3.171). Finally, for temperatures between M_f and pure superelastic behaviour, the critical stress for the reverse transformation (or detwinning) reaches very low compressive values which are not accounted for in any other phase diagram.

3.4 Experimental characterisation and modified phase diagram

Superelasticity and the shape memory effect are only two examples of the variety of responses displayed by shape memory alloys subjected to a general stress-strain-temperature loading path. Most constitutive models present in the literature, including those discussed in the previous section, predict the shape memory alloy behaviour in complex loading based on a phase diagram, which can be experimentally characterised with a relatively small number of simple tests, usually performed in constant stress or constant temperature conditions. A phase diagram which can accurately describe the shape memory alloy behav-

iour in complex loading is particularly crucial when dealing with shape memory alloys embedded in a host structure, whose loading history depends upon the relative stiffness of the shape memory and host structure.

The phase diagram proposed by Brinson (1993) is still the most common in the literature. Recently, however, some attempts have been made to define modified phase diagrams taking into account other features of the shape memory alloy behaviour (He et al., 2006; Popov and Lagoudas, 2007). In particular, two assumptions underlying the Brinson's phase diagram are questioned, namely the existence of a limit stress value for the formation of detwinned martensite and the definition of the reverse martensite to austenite transformation strip.

In the following, the two mentioned issues are discussed based on experiments carried out on untrained Nitinol wires. Though further evidence of the phenomena discussed in the following can be found in recent literature works, such material behaviour is generally not incorporated in constitutive models. The present experimental work is thus intended as a starting point for the development of a new constitutive model incorporating the observed phenomena.

3.4.1 Detwinned martensite formation at low stress levels

Shape memory alloy wires embedded in a composite matrix experience a complex loading history. Indeed, in this case shape recovery is totally or partially hindered by the presence of the matrix. A limit condition which can be used to simulate embedded shape memory alloys is to completely prevent the wires deformation. This condition is usually termed as constrained recovery.

In constrained recovery, the shape memory alloy is deformed at low temperature and then externally constrained. As the temperature increases, the reverse phase transition starts and a recovery stress is developed in the material as it tries to recover its original shape (slope 2-3). During cooling in presence of stress, detwinned martensite is reformed and the recovery stress is totally or partially released (slope 4-5). Figure 3.17 reports two schematic constrained recovery loading paths as depicted in the Brinson's model phase diagram. In Figure 3.17(a), the material is loaded and subjected to a constrained temperature cycle, while in Figure 3.17(b) the material is prestrained and then unloaded prior to the temperature cycle.

The stress developed in constrained recovery is crucial in active composites

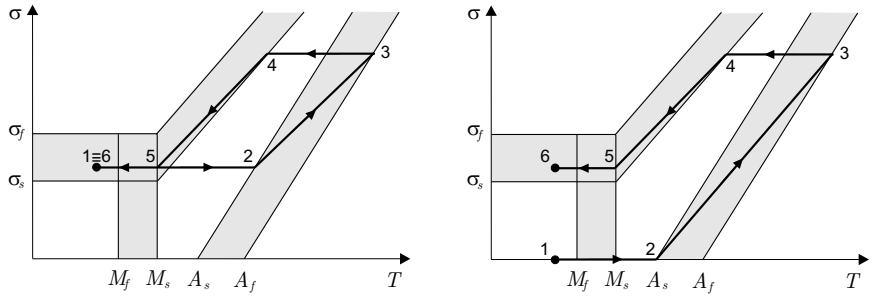

Figure 3.17: Constrained recovery sketch in Brinson's phase diagram

applications, as it is discussed in Chapter 4. The amount of recovery stress developed during cooling and its release during heating are important, for example, in structural shape control. Indeed, if the stress is not completely released, the original structural shape cannot be fully recovered (see Figure 4.3 on the right in Chapter 4).

Some experimental data concerning constrained recovery are available in the literature (Prahlad and Chopra, 2001), however most of them concentrate on the heating branch (Li et al., 2003). In the following, some tests on Nitinol wires in constrained recovery are reported. The tests were carried out at the Center for Intelligent Material Systems and Structures of the Virginia Polytechnic Institute and State University. The results presented here are intended only as preliminary observations on low temperature phenomena in constrained shape memory alloys, while a thorough experimental investigation is, to the author's knowledge, still lacking.

Results regarding prestrained and prestrained-unloaded samples respectively are reported in Figure 3.18. As it can be seen, in both cases the stress was completely released upon cooling. This suggests that in constrained recovery detwinned martensite is formed even at very low stress levels. According to Popov and Lagoudas (2007), the ability to develop detwinned martensite at low stress levels is related to the shape memory alloy training.

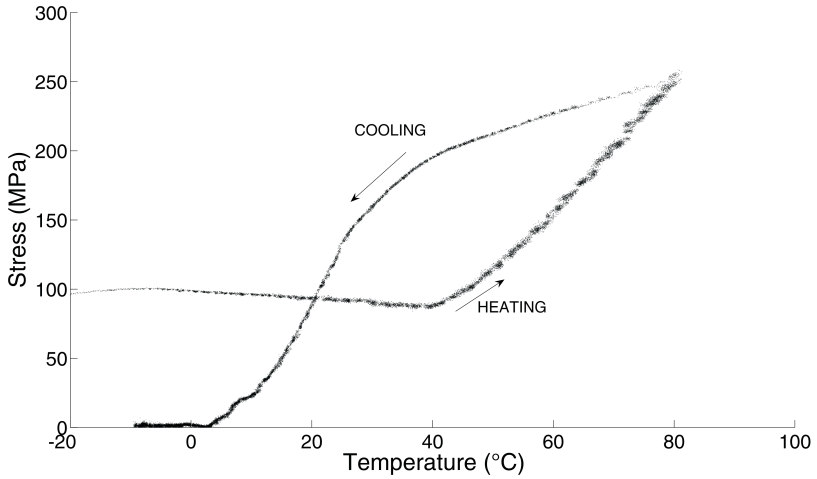

(a)

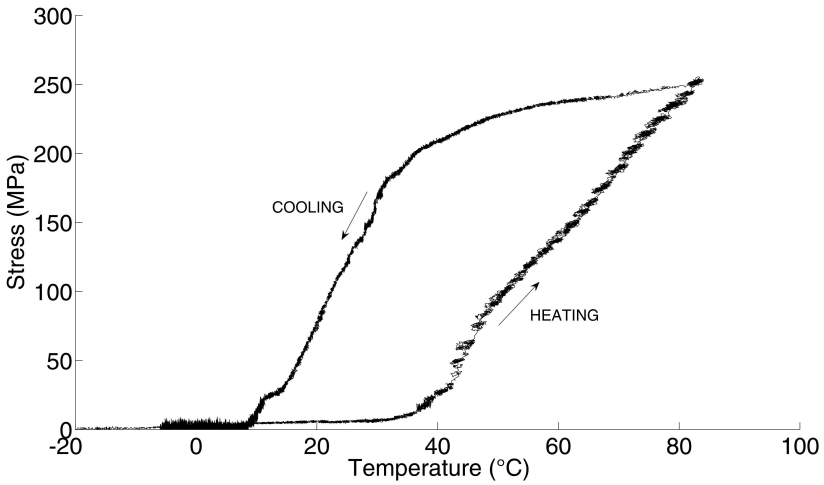

(b)

Figure 3.18: Nitinol wires in constrained recovery

Most constitutive models discussed in the previous section are not able to model complete release of the recovery stress, as most phase diagrams envisage a limit stress below which no further detwinned martensite can be formed. An exception is the model by Popov and Lagoudas (2007), in which the critical stress for detwinned martensite formation can be arbitrarily introduced or removed thanks to the independence of the twinned and detwinned martensite transition zones (see Section 3.3). As one-dimensional models are still very popular in the engineering literature, a simple modification to the Brinson's model allowing to include constrained recovery stress release at low stress levels is here proposed (Daghia et al., 2006).

According to Brinson's model, the residual stress at cooling is always greater than σ_s. Consider Figure 3.17: once the temperature falls below M_s, a further increase in detwinned martensite can only occur if the stress increases; however, due to the constant strain condition, more detwinned martensite would cause the stress to decrease, therefore the only possible equilibrium is at constant stress and constant detwinned martensite. Between M_s and M_f the phase transformation continues, but the martensite developed is twinned and does not contribute to the change in the shape memory alloy stress state.

The required modification can be introduced without changing the shape of the phase diagram, by admitting a certain degree of detwinning in the temperature martensite formed in the presence of stress. This amounts to changing the kinetic laws for the vertical transformation strip. The new kinetic laws must satisfy some requirements:

- detwinned martensite is formed only as a part of the temperature martensite and it is not originated by stress;
- at zero stress there should be no detwinned martensite formed.

Given the listed criteria, the natural way of describing the detwinned martensite increase between M_s and M_f is as a function of the temperature induced martensite and the stress level. The temperature induced martensite is given by Equation (3.25) and it can be expressed as

$$\xi^t = \xi_0^t + f(T)\,. \tag{3.174}$$

Assuming that, depending on the applied stress, a part of the newly formed

Table 3.2: Nitinol material properties

M_f °C	M_s °C	A_s °C	A_f °C
-12	20	28	43

C_A MPa/°C	C_M MPa/°C	σ_s MPa	σ_f MPa	E_M GPa	E_A GPa	Θ MPa/°C	ε_L
6.2	6.2	70	170	11	28	0	0.065

martensite is detwinned, the previous equation can be modified as follows:

$$\xi^d = \xi_0^d + g(\sigma) f(T), \quad \xi^t = \xi_0^t + [1 - g(\sigma)] f(T), \tag{3.175}$$

where $g(\sigma)$ is a function of the applied stress, which needs to be null at $\sigma = 0$ to ensure satisfaction of the second requirement. A simple choice for $g(\sigma)$ can be taken as

$$g(\sigma) = \begin{cases} 1 & \text{if } \sigma_s \leq \sigma \leq \sigma_f \\ \sigma/\sigma_s & \text{if } \sigma < \sigma_s \end{cases}, \tag{3.176}$$

however different functions could be chosen according to the experimental data, introducing or removing the limit stress for detwinned martensite formation.

The original and modified Brinson's models are used to simulate the observed experimental results. The shape memory alloy material parameters used in the simulation are reported in Table 3.2 (notice that a mean elastic modulus was considered for simplicity). The results are reported in Figure 3.19. As it can be seen, the modified Brinson's model is able to capture the constrained recovery stress relaxation below M_s, while the original Brinson's model shows a residual recovery stress which cannot be eliminated by further cooling.

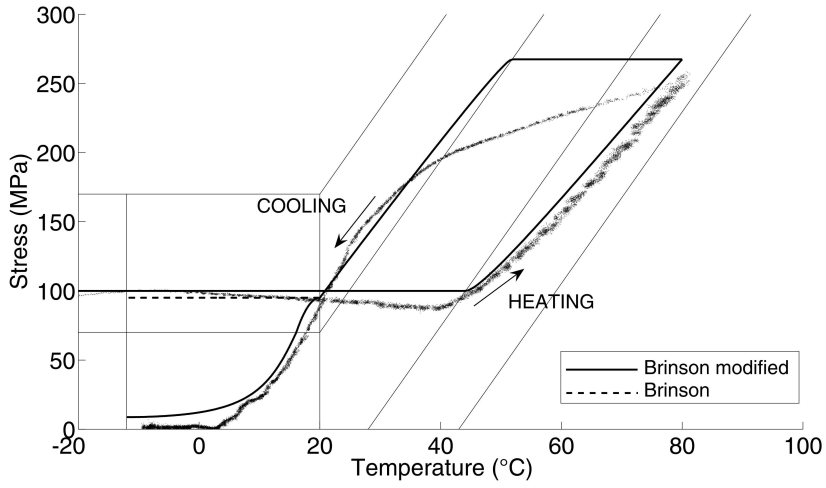

(a)

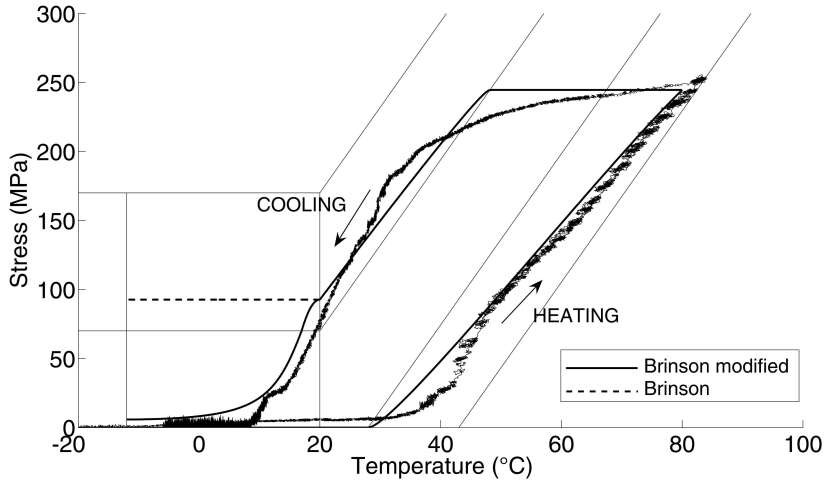

(b)

Figure 3.19: Comparison between original and modified Brinson's models

3.4.2 Influence of the loading path on the reverse phase transition temperatures

Recently, a number of researchers have started to question the assumption on the existence of a single transformation strip for the martensite to austenite phase transition. Indeed, modified phase diagrams have been proposed (He et al., 2006; Popov and Lagoudas, 2007) displaying two separate strips for the twinned and detwinned martensite transitions into austenite. In particular, zero-stress phase transition temperatures for detwinned martensite are generally higher than those for twinned martensite.

The modification to the phase diagram is motivated by calorimetric observations. Popov (2005) reports DSC measurement on various shape memory alloy specimens, both trained and untrained. The wires, initially in twinned martensite state, were mechanically loaded and unloaded at room temperature to achieve complete detwinning, then DSC tests were performed starting with a heating ramp to achieve complete phase transition into austenite. The DSC results consistently showed an increase in the reverse phase transition temperatures during the first heating, in which the detwinned martensite was transformed into austenite. The subsequent cooling and heating cycles, involving only austenite and twinned martensite, were consistent with those observed for the wires which had not been subjected to mechanical loading.

A similar test was carried out within the present experimental campaign, yielding results which were consistent with those reported by Popov (2005). A DSC test was performed on a 0.5 mm diameter shape memory alloy wire which had been mechanically strained to 4% elongation. Details on the wire preparation and the test itself are reported later in this section, while the result of the DSC test is reported in Figure 3.20. Due to the presence of the intermediate austenite to R-phase transition, the first and second cooling cycles were interrupted at 30°C and -20°C, respectively. This allowed to observe the R-phase to austenite transition ($R \rightarrow A$) during the second heating and the twinned martensite to austenite transition ($M^t \rightarrow A$) during the third heating.

As anticipated, these results are consistent with those reported by Popov (2005). In particular, the trough in the black line (first heating, $M^d \rightarrow A$) is significantly shifted to the right, while the cooling curves are completely superimposed. The two separate peaks in cooling represent the $A \rightarrow R$ and $R \rightarrow$

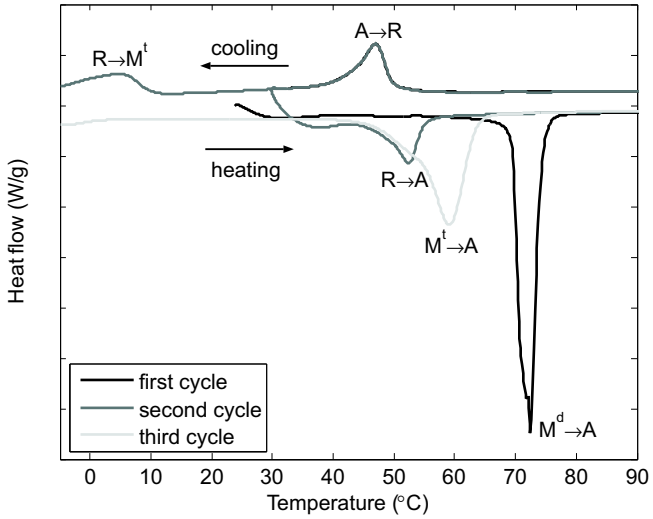

Figure 3.20: DSC for shape memory alloy wire with 4% elongation

M^t transitions, respectively. The $R \rightarrow A$ and $M^t \rightarrow A$ troughs in the second and third heating are consistent with those obtained for the virgin specimen.

Both the results reported by Popov (2005) and the present experiment show a shift in the zero-stress reverse phase transition temperatures related to the different loading history of the material (virgin specimen versus mechanically loaded specimen). The effect of the mechanical loading on the $M \rightarrow A$ transition, however, is temporary as it disappears once the material is heated above the (current) austenite finish temperature during the first DSC heating. The observed phenomenon is thus generally different from the permanent change of the phase transition temperatures and enthalpy of the transformation documented in experimental and modelling studies concerning the effects of training (Auricchio et al., 2003; Miller and Lagoudas, 2000; Wada and Liu, 2005). In order to incorporate the non-uniqueness of zero-stress reverse phase transition temperatures into a modified phase diagram, a thorough experimental investigation is required, including partially detwinned shape memory alloy specimens and a variety of complex stress-temperature loading histories.

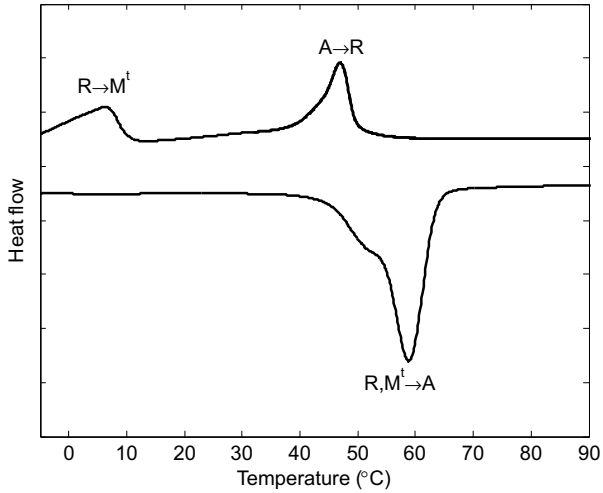

Figure 3.21: DSC test for the virgin specimen

Experimental setup

To further investigate the effect of the loading history on the zero-stress reverse transformation temperatures, DSC measurements were performed on untrained Nitinol wires subjected to different loading histories. The experiments were carried out at the Institute for Composite and Biomedical Materials of the Italian National Research Council (CNR).

Shape memory alloy wire (diameter 0.5 mm) was provided by Memory Metalle GmbH[7]. The virgin material characteristic temperatures were determined via DSC (Figure 3.21). In particular, the formation of R-phase during cooling is noticed.

Prior to testing, the wires were heated to 100°C to remove the effects of packaging and handling. As noticed in the virgin specimen DSC, upon cooling at room temperature the wires are in the R-phase and further cooling is required to obtain a twinned martensite structure. For this reason, all the described experiments were carried out on two different sets of wires, whose initial crystal

[7] www.memory-metalle.de

structure is composed of martensite and R-phase, respectively.

Three different loading histories were considered:

1. mechanical loading to a given elongation at room temperature;
2. thermal cycling at constant stress (restrained recovery);
3. thermal cycling at constant strain (constrained recovery).

The first and third tests were carried out using an Instron 8501 machine with thermal chamber. In test 1, the wire was loaded and unloaded at room temperature, leaving a residual deformation; in test 3, the wire was first loaded at room temperature to a given strain, then heated above the phase transition temperature and cooled to room temperature while keeping the strain constant, finally unloaded at room temperature. In test 2, the constant load was simply applied by hanging a weight to the wire. The wire was heated electrically and allowed to cool to room temperature, then unloaded.

The following DSC test was carried out on material taken from each wire:

- stabilise at 25.00°C;
- heat to 120.00°C at 10.00°C/min;
- cool to 30.00°C at 10.00°C/min;
- heat to 120.00°C at 10.00°C/min;
- cool to −20.00°C at 10.00°C/min;
- heat to 120.00°C at 10.00°C/min.

The behaviour after the first heating was quite repeatable, confirming the temporary effect of the loading history, which is erased with a single heating at zero stress. For this reason, only the first heating is reported in the following DSC graphs, while an example of the complete cycle was reported earlier in this section (Figure 3.20). As the width of the peaks varies considerably in the different tests, the temperature value considered for comparison is the peak temperature.

Test 1: deformation at room temperature

The first set of results concerns wires that have been strained at room temperature before the DSC test. The experiment previously discussed and reported in Figure 3.20 belongs to this group. The first heating curve of the first and second sets of wires (martensite and R-phase) are reported in Figure 3.22(a) and 3.22(b), respectively. Figure 3.23, moreover, reports the strain plotted against the peak temperature values for all considered specimens.

As it can be seen from the graphs, reverse phase transition temperatures increase with increasing strain. The martensite and R-phase wires follow a similar trend, although the peak temperatures for the same strain are generally different in the two cases. This difference is probably related to the different phenomena occurring within the material during mechanical loading ($R \rightarrow M^d$ phase transition versus $M^t \rightarrow M^d$ detwinning). Indeed, at 10% strain both detwinning and phase transition are over, the wires are in detwinned martensite state and their austenite transition temperatures are the same.

On the other hand, the greatest difference between the martensite and R-phase wires can be observed in the 2% strain graphs. For ease of comparison, they are both reported in Figure 3.24. As the $R \rightarrow M^d$ phase transition is not complete at 2% strain, the R-phase graph shows two troughs, denoting the $R \rightarrow A$ (left trough, peak temperature 52.7°C) and the $M \rightarrow A$ (right trough, peak temperature 61.5°C). On the other hand, the martensite graph shows a single trough (peak temperature 66.0°C), not allowing to distinguish between twinned and detwinned martensite.

Mechanical deformation at low temperature induces a stabilisation of the martensite phase, demonstrated by the increase in the reverse phase transition temperatures in the reported tests. In this case, the amount of stabilisation appears to increase as the strain increases. Martensite stabilisation due to cold deformation was previously observed, among others, by Liu and Favier (2000). The interpretation and consequences on the phase diagram modification are discussed later in this section.

Test 2: thermal cycling at constant stress

The second set of experiments is aimed at investigating the effect of temperature on the martensite stabilisation. A thermal cycle is performed on wires subjected

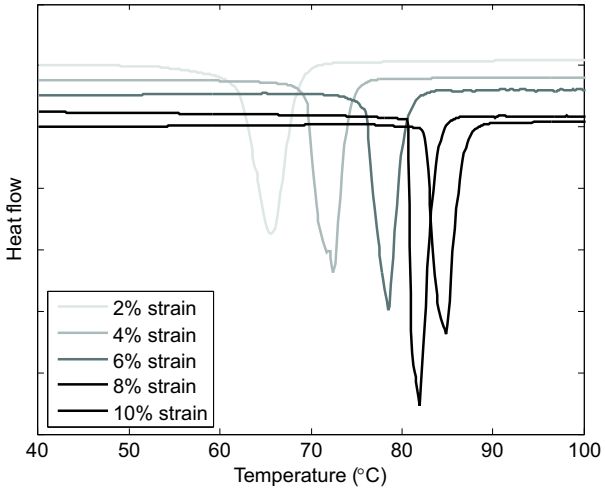

(a) Martensite specimens

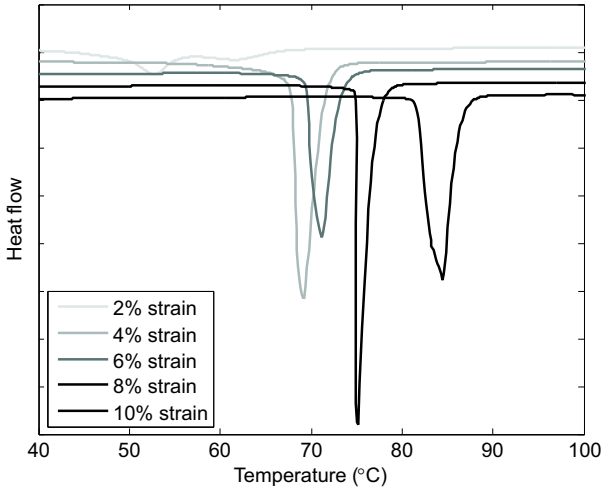

(b) R-phase specimens

Figure 3.22: First heating curve for specimens strained at room temperature

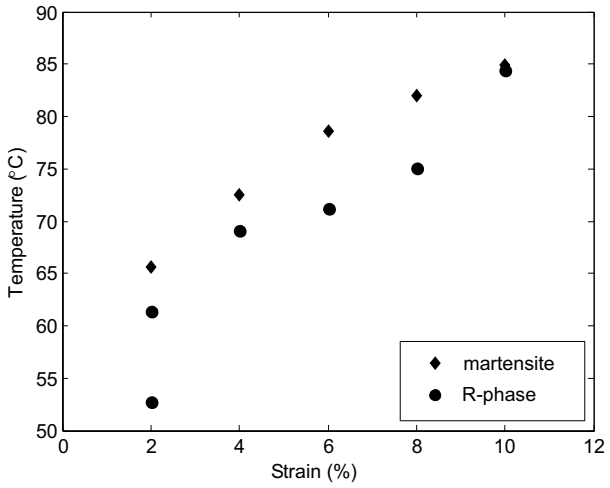

Figure 3.23: Strain versus peak temperature values for test 1

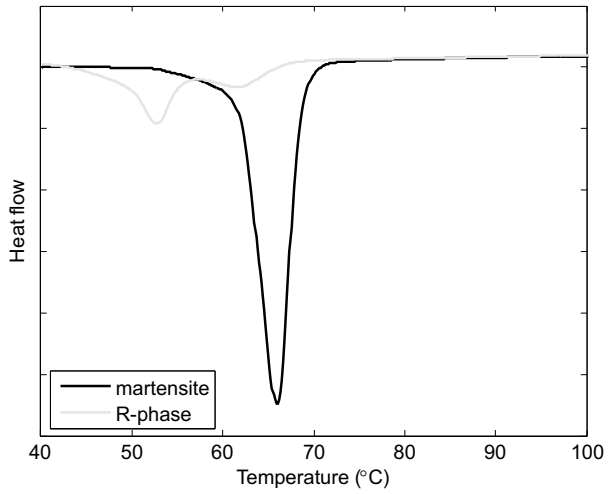

Figure 3.24: First heating curve for specimens strained at room temperature - detail of 2% strain

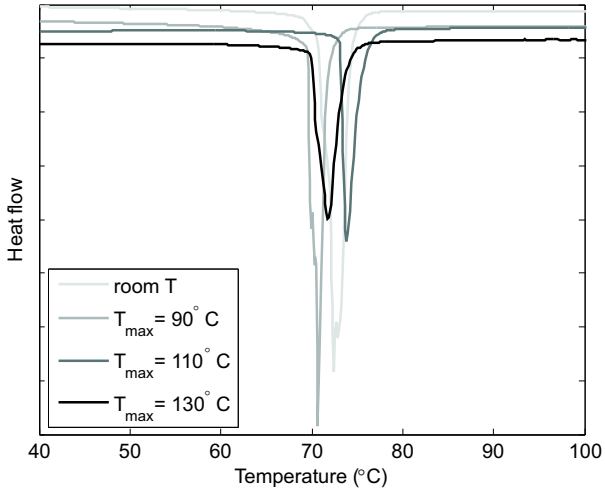

(a) Martensite specimens

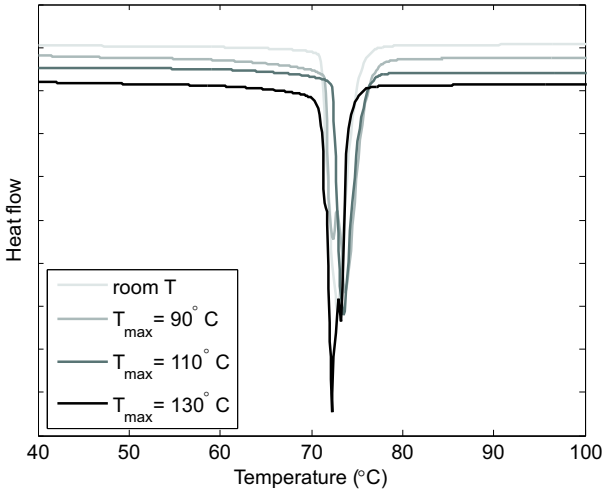

(b) R-phase specimens

Figure 3.25: First heating curve for specimens thermally cycled under 200 MPa constant stress

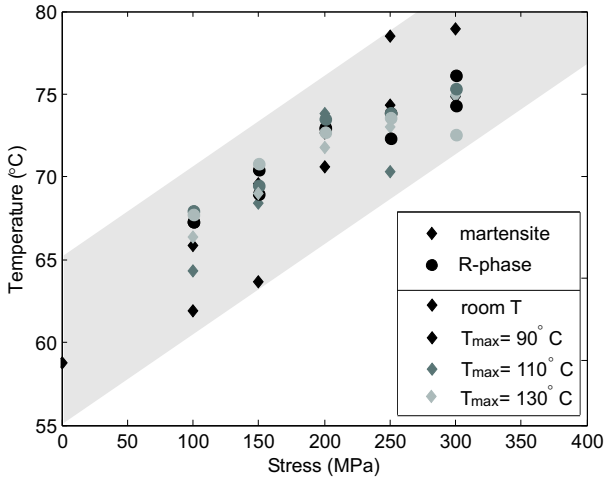

Figure 3.26: Applied stress versus peak temperature values for test 2

to a constant load. During heating, the detwinned martensite initially obtained with the application of the load transforms into austenite and the wire recovers the initial deformation, working against the applied load. During cooling under constant load, austenite transforms back into detwinned martensite because of the temperature change. Upon load removal, therefore, the wire is in a detwinned martensite state and the DSC test allows to measure the zero-stress phase transition temperatures of martensite formed under constant loading.

Four wires were considered for each load value. The first was loaded at room temperature and no thermal cycle was carried out; the second, third and four wires were heated to a maximum temperature of 90°C, 110°C and 130°C, respectively. This amounts to a significant number of tests, thus only some of the DSC results obtained are reported here. In particular, Figures 3.25(a) and 3.25(b) report the results for 200 MPa constant stress and different maximum temperatures for the first and second sets of wires (martensite and R-phase), respectively. It is interesting to notice that the DSC curves are nearly superimposed and they are similar for martensite and R-phase specimens. It should be noted that the peak temperature observed in Figures 3.25(a) and 3.25(b) is

similar to the one observed in test 1 for a 4% strain. These two conditions (200 MPa stress and 4% strain) both correspond to the end of the loading plateau, demonstrating a coherence between the results observed in tests 1 and 2.

To further investigate the effect of the applied stress on the reverse phase transition temperatures, Figure 3.26 reports the applied stress against peak temperature values for all considered specimens. The graph clearly shows that the peak temperature tends to increase with increasing applied stress, regardless of the thermal cycling. The data dispersion could be decreased by performing more controlled experiments, recording also the deformation associated to the thermal cycling.

Test 3: thermal cycling at constant strain

The third set of experiments concerns wires that have been subjected to a constrained recovery cycle prior to DSC testing. As already discussed in Section 3.4.1, heating and cooling at constant strain constitutes a complex loading history for the shape memory alloy wires. Indeed, the two driving forces of the martensitic phase transition, stress and temperature, vary contemporarily during constrained recovery, thus making it difficult to separate their effects. On the other hand, an accurate interpretation of the constrained recovery behaviour of shape memory alloys in terms of phase transition temperatures is crucial when dealing with shape memory alloy hybrid composites, as discussed in Chapter 4.

In order to evaluate the effect of a constrained recovery cycle on the shape memory alloy reverse phase transition temperatures, the DSC measurements obtained in test 3 are compared to those obtained in test 1 at the same level of prestrain. Figures 3.27(a) and 3.27(b) show such comparison for martensite and R-phase wires mechanically strained by 4%. The third heating curve is also reported in the graphs as representative of the virgin specimen behaviour. As it can be seen, the reverse phase transition temperatures for the constrained recovery specimen fall between those for the virgin specimen and those for the specimen strained at room temperature. Based on this observation, a thermal cycle at constant deformation appears to partially remove the martensite stabilisation related to the cold deformation which was observed in test 1.

In relation with the complex loading history given to the wires, the DSC results for test 3 showed some inconsistencies which were not observed in tests 1 and 2. In particular, in some cases DSC measurements carried out on specimens

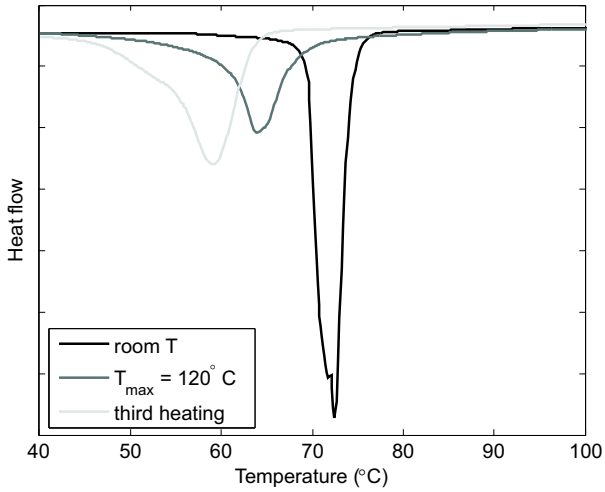

(a) Martensite specimens

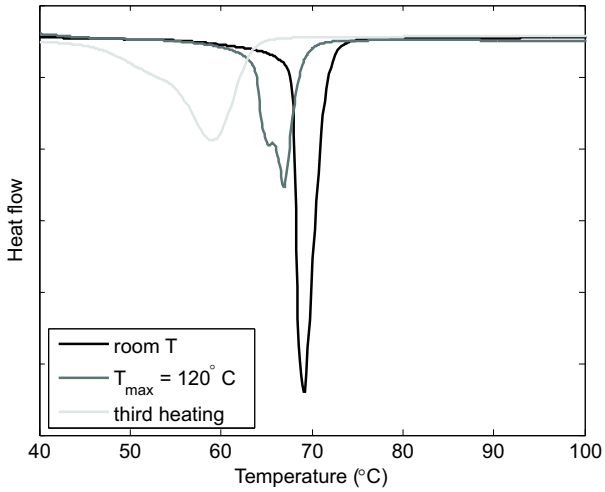

(b) R-phase specimens

Figure 3.27: First heating curve for specimens thermally cycled at 4% constant strain

taken from the same wire yielded different results on the first DSC heating in terms of position and depth of the phase transition peak, thus making it difficult to univocally characterise the wires transition temperatures. A possible interpretation is related to the dominance of local effects due to the absence of global deformation. Indeed, both tests 1 and 2 involved macroscopic deformation of the shape memory alloy wires, thus the phase transition, initially occurring by nucleation in restricted zones of the wires, ended up involving the whole wire. In test 3, on the other hand, no global deformation was allowed because of the constraint, thus local effects tend to be more evident. As the present investigation is aimed at characterising the shape memory alloy behaviour at the macroscale, the significance of local effects could be diminished by evaluating the reverse phase transition temperatures using techniques which involve the whole wire, such as the resistivity measurements investigated by Antonucci et al. (2007).

Further results on the calorimetric characterisation of constrained recovery shape memory alloys can be found in the work by Li et al. (2003), who performed DSC and recovery stress measurements on Nitinol wires which had been mechanically strained and cycled in constrained recovery to different maximum temperatures. Their DSC graphs display two separate peaks during the first heating. The lower temperature peak occurred at temperature similar to those observed for the virgin specimen, while the higher temperature peak occurred at temperatures above those observed for the wire which had been mechanically strained at room temperature. As the maximum temperature reached during constrained recovery increases, the lower peak becomes more evident and the higher peak tends to disappear. Thus, the lower peak appears to be related to the martensite fraction which is involved in the phase transitions occurring during constrained recovery. The higher peak, on the other hand, is related to a residual amount of martensite which formed during the room temperature prestrain prior to the constrained recovery cycle. The occurrence of two different phase transitions at different temperatures is confirmed by recovery stress measurements, showing a two step increase of the recovery stress during the second heating of a constrained recovery wire.

Interpretations and modelling considerations

The present experimental investigation shows that the zero stress reverse phase transition temperatures for untrained shape memory alloys are not constant but

significantly depend upon the loading history of the material. Summarising the results of the three tests:

- in test 1, the reverse phase transition temperatures are shown to increase gradually with increasing strain;
- in test 2, the reverse phase transition temperatures are shown to increase gradually with increasing applied stress, and the thermal cycling at constant applied stress does not seem to significantly affect the observed shift;
- in test 3, the reverse phase transition temperatures are lower than those observed in test 1 for the same strain; moreover, literature results document the presence of two different phase transition peaks, with the lowest peak becoming more evident as the amount of martensite involved in the constrained recovery phase transitions increased.

From the results summarised above, it is clear that the definition of two sets of phase transition temperatures for twinned and detwinned martensite, as proposed by He et al. (2006) and Popov and Lagoudas (2007) in their modified phase diagrams, is not sufficient to account for the extreme variability of the phase transition temperatures. Indeed, the twinned and detwinned martensite fraction cannot be clearly distinguished via DSC measurements of partially detwinned specimens, such as the one reported in 3.24. In that case, the R-phase and detwinned martensite are perfectly distinguishable (light grey line), whereas a single peak is observed for specimen containing partially detwinned martensite (black line).

The change in the reverse phase transition temperatures appears to be continuous and governed by the global deformation in the shape memory alloy. Indeed, the peak temperature shift is clearly observed in both tests 1 and 2, involving formation of detwinned martensite under constant temperature or constant stress conditions. In test 3, involving formation of detwinned martensite under constant strain conditions, the stabilisation effect related to the mechanical straining appears to have been partially removed. The literature results for test 3, displaying two separate peaks in the DSC measurements and a two step actuation in the recovery stress measurements, suggest the presence of two different phase transitions involving the martensite formed during mechanical straining at room temperature and the martensite formed during cooling in constrained recovery, respectively. An increase of the recovery stress was observed

during both phase transitions, thus both martensite fractions are at least partially detwinned. The increase of recovery stress is indeed a global indicator of detwinned martensite phase transition, as such it can be used to characterise the macroscopic behaviour of shape memory alloys in constrained recovery. A similar two step actuation was observed in the experimental testing of a shape memory alloy hybrid composite beam, discussed in Section 4.2.1. In that section, the behaviour of the composite is interpreted in light of the observations discussed here and the proposed interpretation is tested by simulating the composite behaviour and introducing a simple modification to the Brinson's model. The simulation is found to capture the main features of the composite behaviour.

A number of interpretations were suggested for the mechanical stabilisation of martensite related to deformation, based on the development of plastic deformation and internal stresses (see, for example, Liu and Favier, 2000). To the author's knowledge, however, the effects of the different loading histories considered here have not been fully addressed. The present experimental investigation involves mostly macroscopic measurements, thus it is not sufficient to develop and support a complete micromechanical interpretation of the observed phenomena. However, a preliminary explanation is proposed based on the comparison between the different tests. If the formation of detwinned martensite is accompanied by a global deformation of the wire, a more ordered microstructure is obtained, thus a higher temperature is required to achieve the reverse phase transition. Viceversa, detwinning associated to the martensite formed during constrained recovery cooling occurs to accommodate a preexistent wire deformation, thus the resulting microstructure is similar in some sense to the twinned martensite formation under zero load and the reverse phase transition temperatures vary accordingly. In order to further investigate this interpretation, microscopic observations or similar experimental techniques could be employed to observe the microstructures associated to each loading history.

As regards the modified phase diagram, the present results suggest to account for the change in the reverse phase transition temperatures by redefining the parameters A_s and A_f as functions of the material loading history. The definition of such functional relations, requiring the support of further experimental investigation and an accurate micromechanical interpretation, would involve the introduction of new internal variables keeping track of the history in terms of global deformation of the shape memory alloy material.

Compositi attivi con fili a memoria di forma

I compositi combinano materiali diversi per ottenere strutture con proprietà uniche. Grazie al loro comportamento accoppiato, i materiali attivi sono in grado di reagire a cambiamenti ambientali modificando le proprie caratteristiche. L'integrazione di materiali attivi all'interno di compositi permette di creare strutture adattive, in cui le capacità di sensore ed attuatore sono trasferite dal materiale attivo alla struttura stessa.

A partire dai primi anni '90 è stata proposta la realizzazione di strutture composite con integrati elementi a memoria di forma. Come nei compositi tradizionali, la matrice ed il rinforzo possono variare significativamente a seconda dell'applicazione. Nel seguito, l'attenzione viene posta soprattutto su compositi fibro-rinforzati con fili o nastri a memoria di forma integrati.

I materiali a memoria di forma possiedono una significativa capacità di smorzamento, utilizzabile per il controllo passivo delle vibrazioni o l'aumento della resistenza all'impatto. La maggior parte delle applicazioni dei compositi attivi si basa però sul recupero attivo della forma, ottenuto in seguito ad un riscaldamento. In questo caso, elementi a memoria di forma sono predeformati ed inseriti nella struttura in fase martensitica. Al riscaldamento, si attiva la transizione di fase ma il recupero della forma è impedito totalmente o parzialmente da vincoli esterni o dal composito stesso. Gli sforzi che si sviluppano possono essere utilizzati per controllare la rigidezza o la forma della struttura.

Il controllo della rigidezza avviene tramite elementi vincolati esternamente, la cui tensione varia al variare della temperatura. Tale meccanismo permette di influenzare la stabilità, il comportamento dinamico e la risposta all'impatto della struttura. Variando la rigidezza a seconda della necessità è possibile, ad esempio, modificare le frequenze proprie della struttura per allontanare il rischio di risonanza al variare dell'eccitazione esterna. Un'altra applicazione particolarmente promettente è il controllo dell'instabilità termica: in questo caso il riscaldamento costituisce la fonte di instabilità e allo stesso tempo genera sforzi di recupero nei materiali a memoria di forma, che fungono sia da sensori che da attuatori.

Il controllo della forma è una possibilità unica fornita dai materiali attivi. In questo caso, gli elementi a memoria di forma sono vincolati al composito, che impedisce in parte il recupero della forma attivato durante il riscaldamento.

Le tensioni generate negli elementi attivi sono trasferite alla struttura, dando origine ad una deformazione che dipende dalla rigidezza della struttura stessa e dalla temperatura e posizione degli elementi a memoria di forma. Al raffreddamento, la struttura fornisce la forza di ritorno al materiale a memoria di forma e la configurazione originale è totalmente o parzialmente recuperata.

In questo capitolo viene descritto, con un approccio comune, il controllo della forma e della rigidezza. L'attenzione viene concentrata su elementi strutturali tipo piastra, modificando la posizione e il vincolamento degli elementi a memoria di forma per ottenere diverse configurazioni. Nella sezione 4.1 si propone un modello ad elementi finiti per i compositi ibridi, mentre in 4.2 viene presentato uno studio sperimentale di piastre ibride in controllo di forma. Lo scopo è di definire uno strumento semplice e flessibile per la progettazione dei compositi ibridi in grado di prevedere il comportamento strutturale in controllo di forma o di rigidezza. Il modello è validato considerando il controllo della forma perché costituisce la configurazione più sensibile alla scelta dei parametri del modello.

Chapter 4

Active composites with shape memory alloy wires

Composites combine different materials to achieve structures with unique properties. Due to their coupled behaviour, active materials are able to sense changes in the environment and actively respond to them by modifying their properties. Embedding active materials within a composite allows to create adaptive structures, in which the sensing and actuating capabilities are transferred from the active material to the structure itself. Some state of the art examples of active composites are morphing structures, self-healing structures and power harvesting devices.

Since the early 1990s, the concept of embedding shape memory alloy elements in a composite has been investigated for various uses. Composites with embedded shape memory alloys are usually termed as shape memory alloy hybrid composites, or SMAHC. As in traditional composites, both matrix and reinforcement can considerably vary according to the sought application. Metal, polymer and concrete matrix composites with embedded shape memory alloy particles (Lòpez et al., 2007), short fibres (Zhang et al., 2007) or long fibres all fall into the broad definition of SMAHC (Wei et al., 1998). In the following, we concentrate mainly on fibre-reinforced composites with embedded shape memory alloy long wires or ribbons.

Besides displaying an active behaviour related to thermomechanical cou-

pling, shape memory alloys have a significant damping capacity in both superelastic and shape memory range, which can be exploited to enhance the composite's energy dissipation in vibration control (Birman, 2008) or impact resistance (Meo et al., 2005). However, most SMAHC applications make active use of the phase transition which lies behind the shape memory alloy functional properties. The martensite to austenite transition allows to change the SMAHC properties according to two different mechanisms, namely active property tuning and active strain energy tuning.

Active property tuning exploits the different properties, mainly elastic modulus, of the two phases to change the composite stiffness. In this case, no shape recovery or macroscopic deformation is associated to the phase transition. This concept requires a large volume fraction of shape memory alloy material within the composite to achieve a significant stiffness change, as the ratio of the elastic moduli of the two phases is not large (usually $E_A/E_M \simeq 3$ for Nitinol). Active strain energy tuning, on the other hand, makes use of constrained shape recovery to develop large recovery stresses in the shape memory alloy, which influence the overall behaviour of the structure. In this case, shape memory alloy elements are prestrained and embedded in the composite in the martensitic state. Upon heating, the phase transition is triggered but shape recovery is totally or partially hindered either by external constraints or the composite itself. The recovery stresses which develop can be used to control the stiffness or the shape of the structure.

Controlling structural stiffness allows to modify properties such as the buckling load, dynamic behaviour (Ostachowicz et al., 2000) and impact behaviour (Khalili et al., 2007b) of a structure. Indeed, buckling and vibration control applications are among the earliest studies on SMAHC (Baz and Chen, 1993; Baz et al., 1992; Ro and Baz, 1995a,b,c). In stiffness control, shape memory alloy wires are pre-elongated and externally constrained, thus tensile stress is generated during actuation. Due to the external constraints, the stress is not transferred to the composite but the taut wires contribute to increase the overall structural stiffness. Using the terminology introduced by Khalili et al. (2007a), this contribution can be classified as acquired stiffness, as opposed to the essential stiffness of the composite, which is due to the material characteristics only and is not influenced by external events. The shape memory alloy wires can be directly bonded to the composite or set within sleeves, either inside the com-

posite or on its surface. The sleeves, in turn, could be bonded to the composite continuously or at discrete points (Birman, 2007, 2008). The use of sleeves removes a number of technological issues, such as surface adhesion between the shape memory alloy wires and composite, deterioration of the shape memory effect and heating of the polymer matrix.

Notice that taut wires made of traditional materials, such as steel wires, could also be used to increase structural stiffness. However, the advantage of shape memory alloys in this context is two-fold. As the wires recovery stress varies with temperature, the stiffness can be tuned according to need, whereas the increase in stiffness related to traditional reinforcement is fixed. This allows for example to shift the structure's natural frequencies away from resonance as the external excitation changes, while also taking advantage of the additional damping introduced by shape memory alloys elements (Aoki and Shimamoto, 2003; Zhang et al., 2006). The controlled shifting of resonant frequencies is particularly advantageous in the design of rotating machines (see, for example, Żak and Cartmell, 2002, who used shape memory alloy wires to change the stiffness of a rotor bearing). Moreover, in some applications environmental changes could constitute the source of actuation. An example is thermal buckling, where a temperature increase is the source of the instability and at the same time it triggers the shape memory alloy actuation, engendering a stiffness increase only when needed without the aid of external actuation mechanisms. In such cases, shape memory alloy stiffness control could be advantageous with respect to traditional stiffeners (Birman, 1997).

Active shape control of a structure by embedded actuators is a unique possibility offered by active materials. Shape control with embedded shape memory alloys requires transfer of the stress between the wires and the host structure. As such, shape memory alloy wires are usually embedded directly in the composite. Upon actuation, shape recovery of the wires is partially hindered by the composite itself, acting as a constraint. The recovery stress is transferred from the shape memory alloy wires to the host structure, causing a shape change which depends upon the composite stiffness, amount of recovery stress and wire positioning within the composite. During cooling, the original shape is totally or partially recovered as the host structure acts as a bias element to the shape memory alloy wires. With appropriate design of the SMAHC, different shape changes can be achieved. Out-of-plane bending of a plate can be simply obtained

by embedding shape memory alloy wires at a distance from the plate midplane, whereas composite lay-up can be designed to engender coupled bending-torsion with a shape memory alloy bender element (Chandra, 2001). Obviously, the amount of shape change that can be achieved strongly depends upon the stiffness of the host structure and its deformation before fracture. As such, a quite different bending actuation behaviour can be obtained using elastomer (Lind and Doumanidis, 2003), fibre-reinforced polymer (Turner et al., 2006) or concrete (Deng et al., 2006) as host structure.

The compressive recovery stresses that shape memory alloy wires can transmit to the host structure can be used for damage repair. SMAHC patches can be used to reduce stress concentration in the adhesive layer in composite joints (Chen et al., 2007) and to provide closure stress for composite repair (Wang, 2002), whereas in self-healing composites the cracks in the host structure are repaired by the reverse transformation and shape recovery of embedded shape memory alloy wires (Araki et al., 2002; Burton et al., 2006; Li et al., 2007). Recently, this idea has been applied to crack closure in shape memory alloy reinforced concrete beams (Pascale et al., 2008).

In this chapter, stiffness and shape control applications are discussed within a unified framework. The attention is focused on SMAHC plate structures, in which stiffness and shape control can be achieved by changing the boundary conditions and the position of the shape memory alloy wires relative to the plate midplane. In particular, wires embedded at a certain distance from the midplane force the plate to bend. A finite element model for SMAHC is presented in Section 4.1 and an experimental investigation of the bending control of SMAHC plates is carried out in Section 4.2. The aim is to provide a simple and flexible design tool which is able to predict the structural behaviour in both stiffness and shape control. The model validation, however, is carried out by focusing on the shape control configuration, as it is more sensitive to the choice of the model parameters.

4.1 Modelling SMAHC

A number of approaches are described in the previous chapters regarding the modelling of traditional fibre-reinforced composites and shape memory alloy materials. As it should be clear from the discussion, both of them are still open

research problems and even more so is the modelling of hybrid composites incorporating active materials. In this case, indeed, the modelling issues related to the interaction of different materials, typical of composites, are further complicated by the coupling in the active material constitutive laws. On the other hand, a simple and flexible model is required to allow the design and control of a hybrid composite.

As regards SMAHC, a wide variety of modelling approaches can be found in the literature. As embedded shape memory alloys are generally in a nearly constrained recovery configuration, the simplest idea is to model the active material simply as a force acting on the structure (Chaudhry and Rogers, 1991; Sun et al., 2002a,b). The amount of recovery stress can be obtained from constrained recovery experiments on shape memory alloy wires or from simple calculations on basic constitutive models such as Liang and Rogers' or Brinson's. In the stiffness control configuration, externally constrained shape memory alloy wires are sometimes modelled as an equivalent elastic foundation acting on the composite (Birman, 2007, 2008; Epps and Chandra, 1997; Tsai and Chen, 2002), where the elastic foundation stiffness is related to the tension in the shape memory alloy wire. Both these approaches lead to simple models as the complex shape memory alloy constitutive behaviour is only partially taken into account.

As pointed out by Zhang and Zhao (2007a), however, all these approaches amount to neglecting the change in length of the shape memory alloy elements and the interaction between the composite and shape memory alloy deformations. A second approach, allowing to take this interaction into account, is to model the hybrid composite as an equivalent continuum by making use of homogenisation techniques. The simplest homogenisation is analogous to the derivation of equivalent single layer theories, described in Chapter 2, and amounts to assuming perfect bonding and integrating over the beam or plate section (Ghomshei et al., 2001; Turner and Patel, 2007; Zhang and Zhao, 2007b). More complex homogenisation techniques have also been proposed, involving micro-macro analysis (Herzog and Jacquet, 2007; Marfia, 2005).

Homogenisation techniques are an accurate way of modelling the interaction between the different composite constituents, however they have a number of drawbacks if a simple and flexible model for SMAHC design is sought. First of all, the material non linearity of shape memory alloys generates a non linear equivalent continuum, increasing the problem complexity. Furthermore,

depending upon the type of homogenisation, a three-dimensional shape memory alloy material model might be needed. As discussed in Chapter 3, three-dimensional constitutive models for shape memory alloys are still an open problem and require increased computational effort, whereas the shape memory alloy elements usually introduced in SMAHC are generally described well considering a one-dimensional behaviour. Finally, changing SMAHC design parameters such as the number, size or placement of the shape memory alloy reinforcement elements requires to recalculate the homogenised constitutive laws for the composite. Thus, while homogenised SMAHC models can be useful to investigate in detail the behaviour of the hybrid composite, a simpler model is needed for its preliminary design.

A third modelling approach discussed in the literature is to consider the shape memory alloy wires and the host structure as separate elements and model their interaction. This approach has been proposed by a number of researchers (Gao et al., 2006, 2005; Lagoudas and Tadjbakhsh, 1993; Lee and Lee, 2000; Lee et al., 1999) and it is particularly convenient for preliminary design, as it overcomes some of the drawbacks of homogenisation techniques. Indeed, if the shape memory alloy and host structure are described separately, the host structure could be modelled with a linear constitutive law if appropriate. Moreover, depending upon the modelling choices, a one-dimensional constitutive law could be adopted for the shape memory alloy elements and changes in the design parameters previously mentioned could be easily implemented into the model.

A finite element model for the SMAHC plate is developed here, based on the third described approach (Daghia et al., 2007b). The plate is idealised by geometrically non linear two dimensional thin plate elements, while one dimensional truss elements are implemented separately to describe the shape memory alloy wires and then properly connected to the plate nodes. Geometric non linearity is introduced in order to model the effect of embedded shape memory alloy wires on the plate buckling response. By modelling the host structure and the shape memory alloy wires separately, material non linearity affects only the shape memory alloy elements. In addition, the choice of truss elements allows to use a one dimensional shape memory alloy constitutive law. Differently from the recent works by Gao et al. (2006, 2005), the present finite element model is actually two dimensional. Indeed, it does not require any mesh refinement along the plate thickness in order to model shape memory alloy wires embedded

off the plate midplane, so reducing the number of nodal degrees of freedom and improving simplicity and computational efficiency.

The finite element model is described in the following and numerically validated by comparing its predictions to those previously published by Gao et al. (2005). In Section 4.2, on the other hand, experimental work on the shape control configuration is presented and the results obtained are used to further validate the present model. The shape control configuration is chosen because of its greater sensitivity to model parameters.

4.1.1 Finite element formulation

The variational formulation is based on the principle of virtual displacements. The procedure for deriving the non linear equilibrium equations is here described in compact notation, then the terms are specified for the host structure plate element and the shape memory alloy wire element.

Let us consider a virtual displacement field $\delta\mathbf{u}$, obtained as a variation of the real deformed configuration $\mathbf{u}$. The principle of virtual displacements states that

$$\int_{\Omega} \delta\mathbf{e}^{\mathrm{T}}\mathbf{s}\mathrm{d}\Omega - \delta L_{ext} = 0 \qquad (\forall\delta\mathbf{u})\,, \tag{4.1}$$

where $\delta\mathbf{e}$ is the virtual generalised strain vector compatible with the virtual displacements, $\mathbf{s}$ contains the generalised stresses and δL_{ext} is the virtual work of external forces.

The displacement approximation is introduced as follows:

$$\mathbf{u} = \mathbf{U}\mathbf{q}, \tag{4.2}$$

where $\mathbf{q}$ are the nodal displacement parameters and $\mathbf{U}$ is the matrix of the shape functions. Based on this assumption, the virtual displacements and strains can be put in the form

$$\delta\mathbf{u} = \mathbf{U}\delta\mathbf{q}, \qquad \delta\mathbf{e} = \mathbf{B}\delta\mathbf{q}, \tag{4.3}$$

where $\mathbf{B} = \mathbf{B}(\mathbf{q})$ is the strain-displacement matrix, which depends upon the nodal displacement parameters $\mathbf{q}$ due to geometric non linearity.

Substituting in Equation (4.1) yields

$$\delta\mathbf{q}^{\mathrm{T}}\left(\int_{\Omega} \mathbf{B}^{\mathrm{T}}\mathbf{s}\mathrm{d}\Omega - \mathbf{f}_{ext}\right) = 0 \qquad (\forall\delta\mathbf{q})\,, \tag{4.4}$$

being $\mathbf{f}_{ext}$ the external nodal forces vector. Setting the bracketed term equal to zero yields the classical form of the nodal equilibrium equation:

$$\mathbf{R}(\mathbf{q}) = \mathbf{f}_{int}(\mathbf{q}) - \mathbf{f}_{ext} = \mathbf{0}. \tag{4.5}$$

The Newton-Raphson solution of the non linear equilibrium equation requires the computation of the tangent stiffness matrix:

$$\mathbf{K}_T = \frac{\partial \mathbf{R}}{\partial \mathbf{q}} = \int_\Omega \mathbf{B}^{\mathrm{T}} \frac{\partial \mathbf{s}}{\partial \mathbf{q}} \mathrm{d}\Omega + \int_\Omega \frac{\partial \mathbf{B}^{\mathrm{T}}}{\partial \mathbf{q}} \mathbf{s} \mathrm{d}\Omega = \mathbf{K}_{Tm} + \mathbf{K}_{Tg}. \tag{4.6}$$

Here, $\mathbf{K}_{Tm}$ is the material stiffness, while $\mathbf{K}_{Tg}$ is the geometric stiffness. Introducing a general constitutive relation $\mathbf{s} = \mathbf{C}(\mathbf{e})$, the material stiffness matrix becomes

$$\mathbf{K}_{Tm} = \int_\Omega \mathbf{B}^{\mathrm{T}} \frac{\partial \mathbf{C}}{\partial \mathbf{e}} \frac{\partial \mathbf{e}}{\partial \mathbf{q}} \mathrm{d}\Omega = \int_\Omega \mathbf{B}^{\mathrm{T}} \frac{\partial \mathbf{C}}{\partial \mathbf{e}} \mathbf{B} \mathrm{d}\Omega, \tag{4.7}$$

allowing for the presence of material non linearity.

The Newton-Raphson strategy is briefly outlined here. Let $\mathbf{q}_i$ be the solution at the previous load step. A load increment is applied and the residual forces vector is approximated in Taylor series as follows:

$$\mathbf{R}(\mathbf{q}) \simeq \mathbf{R}(\mathbf{q}_i) + \left.\frac{\partial \mathbf{R}}{\partial \mathbf{q}}\right|_{\mathbf{q}_i} (\mathbf{q} - \mathbf{q}_i) = 0. \tag{4.8}$$

An iteration scheme can be established:

$$\mathbf{K}_T^k \Delta \mathbf{q}^k = -\mathbf{R}^k, \tag{4.9}$$

where the superscript k refers to quantities evaluated at the k-th iteration.

4.1.2 Host structure plate element

The host structure finite element is based on the CLPT. The linear continuum model introduced in Chapter 2 is enriched by introducing the non linear Von Kármán strain assumption. The compatibility relations become:

$$\mathbf{e} = \nabla_x^{(s)} \mathbf{u} - z \nabla_x^{(s)} (\nabla_x w) + \frac{1}{2} (\nabla_x w \otimes \nabla_x w) = \boldsymbol{\mu} + z\boldsymbol{\chi} = \boldsymbol{\mu}_l + \boldsymbol{\mu}_{nl} + z\boldsymbol{\chi}. \tag{4.10}$$

The membranal generalised strains are composed of a linear part, depending on the in-plane displacements $\mathbf{u}$, and of a non linear part, depending on the

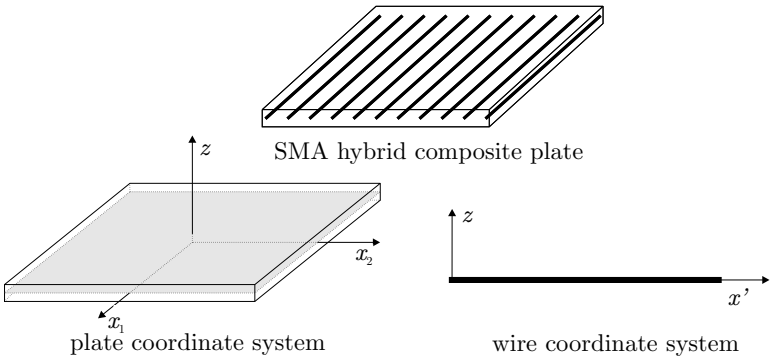

Figure 4.1: SMAHC plate and reference systems

transverse displacement w. Besides the introduced geometric non linearity, the continuum model is analogous to the one previously described and it is not reported here.

A four node finite element is developed by introducing the following displacement field assumptions:

$$\mathbf{u} = \mathbf{U}_u \mathbf{q}_u, \quad w = \mathbf{U}_w^H \mathbf{q}_w, \tag{4.11}$$

where $\mathbf{U}_u$ collects the standard Lagrangian shape functions, while $\mathbf{U}_w^H$ contains Hermite polynomials, ensuring C^1 continuity to the transverse displacement w as required by the CLPT displacement-based finite element formulation. Notice that the vector of nodal w parameters, $\mathbf{q}_w$, contains the nodal displacements w_i and its derivatives, namely $\partial w_i/\partial x_1$, $\partial w_i/\partial x_2$ and $\partial^2 w_i/\partial x_1 \partial x_2$, thus the element has six degrees of freedom per node.

The discretised compatibility equations, Equation (4.10), are written in operator form as follows:

$$\boldsymbol{\mu}_l = \mathbf{D}_m \mathbf{U}_u \mathbf{q}_u, \quad \boldsymbol{\chi} = \mathbf{D}_b \mathbf{U}_w^H \mathbf{q}_w, \quad \boldsymbol{\mu}_{nl} = \frac{1}{2} \mathbf{D}_{mw} \mathbf{D}_{nl} \mathbf{U}_w^H \mathbf{q}_w, \tag{4.12}$$

where

$$\mathbf{D}_m = \begin{bmatrix} \partial/\partial x_1 & 0 \\ 0 & \partial/\partial x_2 \\ \partial/\partial x_2 & \partial/\partial x_1 \end{bmatrix}, \quad \mathbf{D}_b = \begin{bmatrix} -\partial^2/\partial x_1^2 \\ -\partial^2/\partial x_2^2 \\ -2\partial^2/\partial x_1 \partial x_2 \end{bmatrix}, \tag{4.13}$$

$$\mathbf{D}_{mw}=\begin{bmatrix} \left(\partial \mathbf{U}_w^H/\partial x_1\right)\mathbf{q}_w & 0 \\ 0 & \left(\partial \mathbf{U}_w^H/\partial x_2\right)\mathbf{q}_w \\ \left(\partial \mathbf{U}_w^H/\partial x_2\right)\mathbf{q}_w & \left(\partial \mathbf{U}_w^H/\partial x_1\right)\mathbf{q}_w \end{bmatrix}, \quad \mathbf{D}_{nl}=\begin{bmatrix} \partial/\partial x_1 \\ \partial/\partial x_2 \end{bmatrix}. \tag{4.14}$$

Variation of the generalised strains yields:

$$\delta\boldsymbol{\mu}_l = \mathbf{D}_m\mathbf{U}_u\delta\mathbf{q}_u, \tag{4.15}$$

$$\delta\boldsymbol{\chi} = \mathbf{D}_b\mathbf{U}_w^H\delta\mathbf{q}_w, \tag{4.16}$$

$$\delta\boldsymbol{\mu}_{nl} = \mathbf{D}_{mw}\mathbf{D}_{nl}\mathbf{U}_w^H\delta\mathbf{q}_w, \tag{4.17}$$

thus the matrix $\mathbf{B}$ for the host structure finite element is expressed as follows:

$$\mathbf{B}=\begin{bmatrix} \mathbf{D}_m\mathbf{U}_u & \mathbf{D}_{mw}\mathbf{D}_{nl}\mathbf{U}_w^H \\ \mathbf{0} & \mathbf{D}_b\mathbf{U}_w^H \end{bmatrix}, \tag{4.18}$$

where the dependence on the nodal displacement parameters is contained in the matrix $\mathbf{D}_{mw}$.

The host structure constitutive relations are linear:

$$\begin{bmatrix} \mathbf{N} \\ \mathbf{M} \end{bmatrix}=\begin{bmatrix} \mathbf{C}_m & \mathbf{C}_{mb} \\ \mathbf{C}_{mb} & \mathbf{C}_b \end{bmatrix}\begin{bmatrix} \boldsymbol{\mu}-\bar{\boldsymbol{\mu}} \\ \boldsymbol{\chi}-\bar{\boldsymbol{\chi}} \end{bmatrix}, \tag{4.19}$$

where $\bar{\boldsymbol{\mu}}$ and $\bar{\boldsymbol{\chi}}$ are the strains due to thermal loads and the constitutive matrices are defined by Equations (2.20) to (2.22).

4.1.3 Shape memory alloy wire element

The shape memory alloy wires are modelled using non linear truss elements. The local reference system is shown in Figure 4.1. The displacement components in the $\hat{x}$ and z directions are denoted by $\hat{u}$ and w, respectively.

The uniaxial strain is defined as:

$$\varepsilon=\varepsilon_l+\varepsilon_{nl}=\frac{\mathrm{d}\hat{u}}{\mathrm{d}\hat{x}}+\frac{1}{2}\left(\frac{\mathrm{d}w}{\mathrm{d}\hat{x}}\right)^2. \tag{4.20}$$

A two-node finite element is developed by introducing the following displacement field assumptions:

$$\hat{u}=\mathbf{U}_{\hat{u}}\mathbf{q}_{\hat{u}}, \quad w=\mathbf{U}_{\hat{w}}\mathbf{q}_{\hat{w}}, \tag{4.21}$$

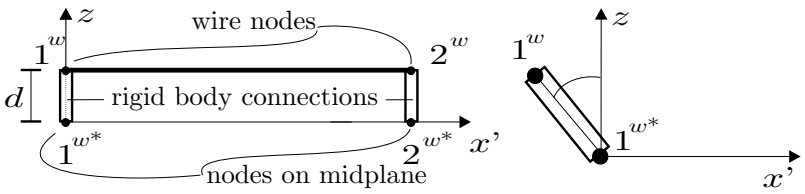

Figure 4.2: Rigid body connections

where $\mathbf{U}_{\hat{u}}$ and $\mathbf{U}_{\hat{w}}$ contain Lagrange shape functions. Note that the nodal parameters $\mathbf{q}_{\hat{u}}$ can be transformed to $\mathbf{q}_u$ by a reference system rotation, and that $\mathbf{q}_{\hat{w}}$ contain only the nodal displacements w_i and not its derivatives.

The discretised compatibility equations read:

$$\varepsilon_l = \frac{\mathrm{d}}{\mathrm{d}\hat{x}}\mathbf{U}_{\hat{u}}\mathbf{q}_{\hat{u}}, \quad \varepsilon_{nl} = \frac{1}{2}\left(\frac{\mathrm{d}}{\mathrm{d}\hat{x}}\mathbf{U}_{\hat{w}}\mathbf{q}_{\hat{w}}\right)^2 \tag{4.22}$$

and their variation yields the matrix $\mathbf{B}$

$$\mathbf{B} = \left[\begin{array}{cc} \frac{\mathrm{d}}{\mathrm{d}\hat{x}}\mathbf{U}_{\hat{u}} & \left(\frac{\mathrm{d}}{\mathrm{d}\hat{x}}\mathbf{U}_{\hat{w}}\mathbf{q}_{\hat{w}}\right)\frac{\mathrm{d}}{\mathrm{d}\hat{x}}\mathbf{U}_{\hat{w}} \end{array}\right]. \tag{4.23}$$

The strain is related to the axial stress through shape memory alloy one dimensional constitutive relations. To this purpose, the model proposed by Brinson (1993) is adopted here because of its simplicity, but at this stage any other shape memory alloy one dimensional constitutive model could be chosen, such as the ones discussed in Chapter 3. Knowing the strain-temperature state of the shape memory alloy element it is possible through the Brinson's model to evaluate the stress. The generalised stress of the one dimensional model is the axial force, computed as the product of the stress and the wire cross-sectional area.

Given the two dimensional nature of the model, assembly requires that all the nodes should belong to the plate midplane. To this purpose, shape memory alloy wires embedded off the plate midplane are connected to plate nodes through rigid body links. The idea is shown in Figure 4.2. The wire nodes, labelled by w and positioned at $z = d$, are projected onto the plate midplane (nodes labelled by w^*) and rigid body connections are introduced. The displacement

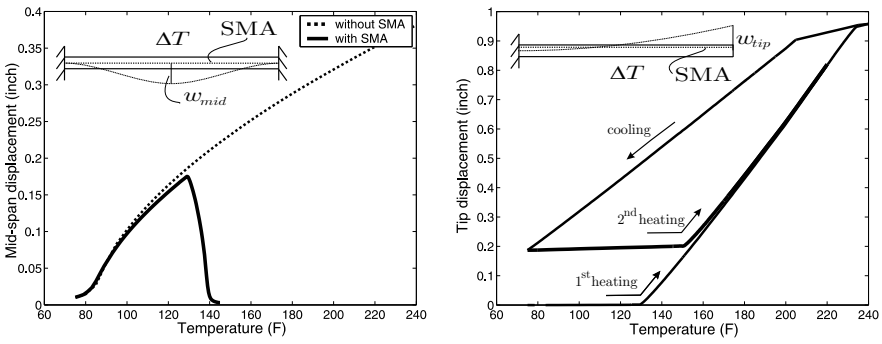

Stiffness control Shape control

Figure 4.3: Numerical validation: stiffness and shape control

parameters $\mathbf{q}$ and the corresponding generalised forces $\mathbf{f}$ are transferred from the w to the w^* nodes before assembly. If d is set to zero the w and w^* nodes coincide, while if the shape memory alloy is embedded off the plate midplane the wire elements contribute to the rotational stiffness of the midplane nodes.

4.1.4 Numerical validation

The model is numerically validated by comparing it with the results previously published by Gao et al. (2005) on a laminated composite plate strip in which shape memory alloy ribbons are replacing part of the laminate layers. The SMAHC was subjected to a thermal load which is uniform along the beam length. By changing the laminate boundary conditions and the position of the shape memory alloy ribbons with respect to the neutral axis, a stiffness and a shape control configurations are obtained.

The results predicted by the present model are shown in Figure 4.3. The temperature is reported in Fahrenheit degrees and the displacement in inches to facilitate comparison with the graphs in Gao et al. (2005). It can be immediately observed that the predictions of the two models are in very good agreement. As already mentioned earlier, however, the present model is simpler and computationally more efficient being fully two dimensional.

Figure 4.3 (left) represents the stiffness control case. The SMAHC is clamped at both ends and the shape memory alloy ribbons are embedded symmetrically with respect to the plate midplane. The temperature is gradually increased from 75 F to 240 F. The mid-span displacement is plotted versus the temperature in two different cases: the dotted line represent the composite without shape memory alloy reinforcement, while the solid line shows the behaviour of the SMAHC. In the first case, thermal buckling occurs because of the thermal load and the displacement increases with temperature. When the shape memory alloy ribbon is present, however, the shape memory alloy actuation causes the mid-span displacement to decrease, thus preventing thermal buckling and controlling the structure's stiffness.

Figure 4.3 (right) represents the shape control case. The SMAHC is in a cantilevered configuration and the shape memory alloy ribbons are embedded at a certain distance from the neutral axis. The temperature is gradually increased from 75 F to 240 F, then gradually decreased to 70 F, then increased again up to 240 F. The plot shows the variation of the tip displacement as the temperature changes. Upon heating above the shape memory alloy transformation temperature, the SMAHC starts to bend and the tip displacement gradually increases. During cooling, the inverse transformation takes place and the tip displacement decreases. A residual displacement is present at the end of the cooling branch as the recovery stress was not completely released.

In the stiffness control configuration, the actuation temperature of the shape memory alloy elements is the main design parameter. Once the ribbons are in tension, the plate quickly reaches the configuration with zero mid-span displacement, a further temperature increase does not cause significant changes in the plate configuration. On the other hand, in shape control the plate configuration continues to change as the temperature increases. The amount of displacement that can be achieved depends upon the geometric and material characteristics of the SMAHC components. Thus, in shape control the correct choice of the model parameters plays a crucial role in the prediction of the SMAHC response.

4.2 Building and testing shape control SMAHC

The present experimental investigation on shape memory alloy hybrid composites focuses on shape control applications. Indeed, the shape control configura-

tion is highly sensitive to the material parameters of both shape memory alloy wires and host structure, thus it requires careful design and provides a more severe test for the model proposed in the previous section. Similarly to the numerical simulation in Figure 4.3, the investigation is centred on the controlled bending of a cantilevered plate by actuation of prestrained shape memory alloy wires embedded at a distance from the plate neutral axis.

The experimental work is divided in two parts. The aim of the first part is to experimentally demonstrate the capability of embedded shape memory alloy wires to influence structural properties. In this preliminary investigation, an SMAHC beam is built by gluing some prestrained shape memory alloy wires on top of a carbon fibre laminate strip. The simple proof-of-concept specimen allows to remove all technological issues related to the hybrid composite manufacturing while still obtaining experimental data to preliminary validate the SMAHC concept and the proposed model. In order to achieve controlled heating and cooling of the shape memory alloy wires, the SMAHC beam is tested in an environmental chamber, recording temperature and displacement data and comparing them to the model predictions.

In the second part of the experimental investigation, hybrid composite making is investigated. Different materials and manufacturing techniques are tested and their advantages and drawbacks are discussed. As a result, an SMAHC plate made of glass fibre and epoxy resin pre-preg with embedded shape memory alloy wires is built and tested. In this case, the shape memory alloy wires are heated via Joule heating, as it would be the case in most applications. Temperature and displacement data are recorded and compared to the model predictions.

4.2.1 SMAHC beam

The experimental work on the SMAHC beam, discussed in this section, was carried out at the Center for Intelligent Material Systems and Structures of the Virginia Polytechnic Institute and State University. The aim is to demonstrate the shape control capability of embedded shape memory alloy wires by a simple experiment. In order to remove all technological difficulties related to the hybrid composite manufacturing, a simple proof-of-concept specimen is built by gluing prestrained shape memory alloy wires on top of a carbon fibre laminated composite plate strip.

Table 4.1: Axial and flexural rigidities of laminate strips

	Axial rigidity kN	Bending rigidity kNmm^2
Direction 1	981	211
Direction 2	1045	224

Material characterisation

The host structure and shape memory alloy wires are tested separately in order to obtain their material properties, which are used later in this section for the numerical simulations.

The host structure is a symmetric cross-ply laminate plate of thickness 1.5875 mm from McMaster-Carr[1]. No data concerning the laminae properties and the lamination scheme was available, therefore only the overall plate properties could be obtained from laminate testing. Plate strips of 203.2×25.4 mm (8×1 in, the same dimensions of the SMAHC beam) were cut in the two principal directions and tensile and bending tests were carried out. Tensile rigidity, relating the axial force to the axial strain, and bending rigidity, relating the bending moment to the curvature, were thus evaluated and they are reported in Table 4.1. The laminate stiffness matrices required by the finite element model (see Equation (4.19)) are reported in Table 4.2. They were obtained by calculating the tensile and flexural rigidities per unit width and assuming a typical Poisson's coefficient $\nu = 0.23$ and an in-plane shear modulus $G_{12} = 6000$ MPa. These two material coefficients are indeed not simply determined via laminate static testing, however this assumption is not expected to significantly modify the beam-like response of the specimen under consideration.

A spool of 0.38 mm diameter Nitinol wire was provided by Fort Wayne Metals Research Products Corp. The material properties of the Nitinol were determined via differential scanning calorimeter (DSC) tests and tensile tests at different temperatures. The zero-stress phase transition temperatures determined via DSC were $M_s = 0^\circ$ C, $M_f = 27^\circ$C, $A_s = 40^\circ$C and $A_f = 55^\circ$C. According to Abel et al. (2004), who discussed various experimental techniques

[1] www.mcmaster.com

Table 4.2: Constitutive matrices for the finite element model, units N and mm

$\mathbf{C}_m$	$\mathbf{C}_{mb}$	$\mathbf{C}_b$
$\begin{bmatrix} 40642 & 9348 & 0 \\ 9348 & 43303 & 0 \\ 0 & 0 & 9500 \end{bmatrix}$	all zero 3×3 matrix	$\begin{bmatrix} 8733 & 1963 & 0 \\ 1963 & 9242 & 0 \\ 0 & 0 & 2000 \end{bmatrix}$

Table 4.3: Nitinol wires: material properties

M_f °C	M_s °C	A_s °C	A_f °C
-10	17	30	45

C_A MPa/°C	C_M MPa/°C	σ_s MPa	σ_f MPa	E_M GPa	E_A GPa	Θ MPa/°C	ε_L
8	8	90	140	7	28	0.55	0.065

to determine the transformation temperatures, the DSC test tends to yield higher values than those observed in the applications. For this reason, in light of the experimental results on the SMAHC beam presented further in this section, lower temperature values were used in the simulation of the composite behaviour. The tensile tests, carried out inside a Tenney vacuum-temperature chamber (model 36ST), were used to characterise the Brinson's model phase diagram (see Figure 3.11(b)). The material properties obtained are reported in Table 4.3. Even though different elastic moduli are reported in Table 4.3 for austenite and martensite, a mean elastic modulus was considered in the finite element model for simplicity. Finally, the value of the material modulus Θ was taken from the technical literature and not measured, since it does not modify significantly the SMAHC response.

Various factors influenced the choice of the adhesive used to bond the shape memory alloy wires to the host structure. Indeed, the adhesive should be compliant in order to modify as little as possible the stiffness properties of the original laminate. Moreover, it should cure at room temperature in order to avoid any

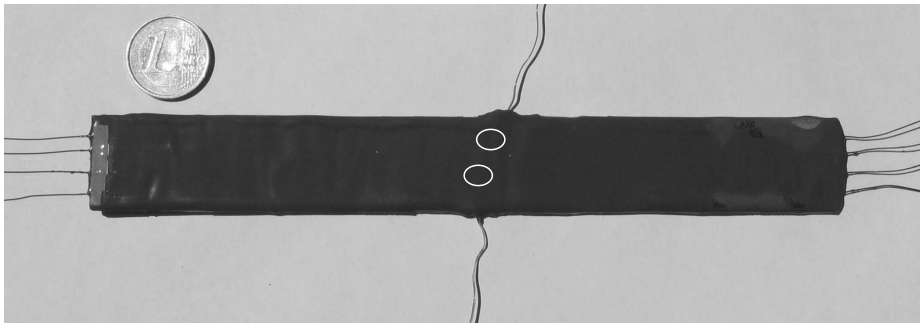

Figure 4.4: SMAHC specimen

actuation of the shape memory alloy wires during the specimen building. This way, the wires do not need to be restrained during adhesive cure. All the stated reasons let to the choice of 3M Scotch-Weld 2216 B/A Epoxy to create the bonding layer.

Specimen preparation

The SMAHC beam preparation requires two steps:

- the shape memory alloy wires are prestrained;
- the shape memory alloy wires are bonded to the host structure.

The Nitinol wires were prestrained by 4% using an Instron 4204 machine. The amount of prestrain influences the amount of recovery stress that can be achieved, thus the behaviour of the SMAHC specimen strongly depends upon the prestrain. For this reason, it is important that all the wires are prestrained by the same amount. In order to eliminate undesired internal stresses, the wires were heated with a Craftsman industrial heat gun before prestraining. Two 550 mm long shape memory alloy wires were prestrained contemporarily to ensure the same amount of deformation; each wire was cut into half to obtain four equally prestrained wires.

The wires were laid equally spaced on the surface of the laminated composite beam. Two Omega type J thermocouples (model 5TC-TT-J-36-36) were

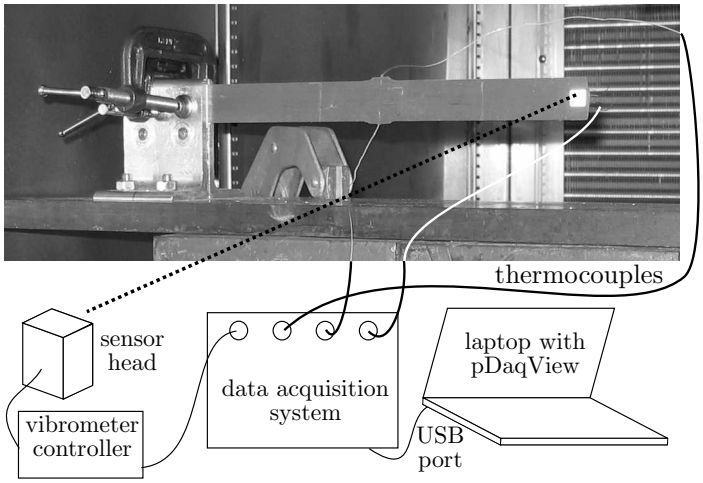

Figure 4.5: Experimental setup for the SMAHC beam

attached to two of the wires at approximately half the beam length with conductive tape. The wires were bonded to the beam using 3M Scotch-Weld 2216 B/A Epoxy adhesive. Two different layers of epoxy were applied, each layer was left to cure 24 hours at room temperature. Figure 4.4 shows a picture of the specimen, the thermocouples' positions are marked with circles. The shape memory alloy wires positioning is a critical phase of the specimen preparation: the shape memory alloy wires must be evenly spaced and laid out symmetrically with respect to the beam axis of symmetry, in order avoid undesired torsional deformation during the actuation. Indeed, some imperfections are inevitably present and a small amount of torsion was observed during the tests.

Experimental setup

The SMAHC was tested in a Tenney vacuum-temperature chamber (model 36ST). Starting from room temperature, the air in the chamber was slowly heated to 125°C and then slowly cooled to 20°C, since a slow temperature change allows to neglect the effects of the loading rate. The sequence was

repeated several times in order to obtain various actuation cycles. In the last actuation, the temperature in the chamber was further increased to 137°C in order to investigate the effect of a change in the actuation conditions. A schematic representation of the experimental setup is reported in Figure 4.5.

In real life applications, shape memory alloy actuators are usually heated via resistive heating. This technique allows quick heating, achieving rapidly the final configuration, while little control is possible on the cooling. For experimental purposes, a relatively slow and controlled heating and cooling was required, thus it was considered best to conduct the experiments in a temperature controlled chamber.

The SMAHC was clamped at one end, leaving a free length of 168 mm. Reflective tape was attached at the free end of the beam and a Polytec laser vibrometer (OFV 303 Sensor head and OFV 3001 Vibrometer controller) was used to measure the tip displacement. Temperature readings were obtained from the two embedded thermocouples and from another thermocouple of the same type, attached to the wire just outside the epoxy layer. The external thermocouple was necessary to capture the temperature gradient generated along the wires: the wire ends, in direct contact with the air inside the chamber, heat up and cool down more quickly than the parts embedded in the epoxy.

The thermocouples and the laser vibrometer were connected to a USB data acquisition system by Omega (model OMB-DAQ-56). The data was recorded on a laptop equipped with the pDaqView software.

Experimental results

The tip displacement is plotted against the external thermocouple reading for different loading cycles. Figure 4.6 depicts the first thermal cycle. The graph starts from point A and follows the direction of the arrows. Upon heating the displacement increases, first slowly due to a different coefficient of thermal expansion between the wires and the laminate, then more quickly as the $M \rightarrow A$ phase transformation starts. At 125°C the tip displacement is 12.4 mm. Upon cooling, the displacement decreases again thanks to the $A \rightarrow M$ phase transformation. However, a residual tip displacement is present when the specimen reaches room temperature.

Figure 4.7 shows again the first actuation (black line) and two representative examples of the following cycles (starting from points B and C, respectively).

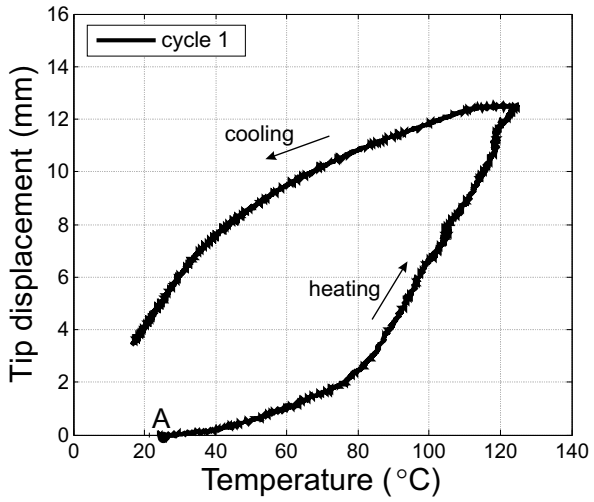

Figure 4.6: SMAHC beam response - cycle 1

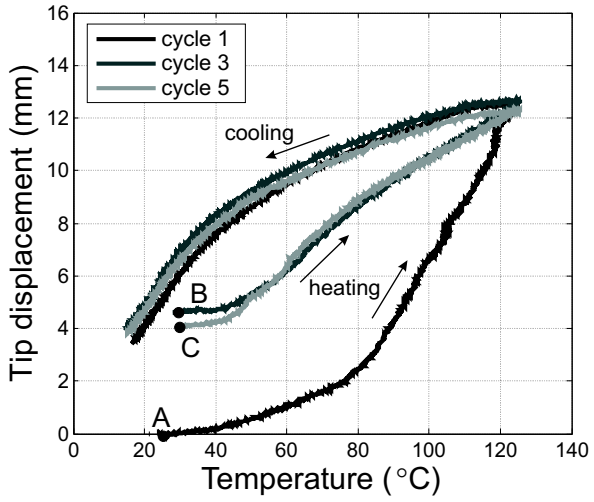

Figure 4.7: SMAHC beam response - cycles 1, 3 and 5

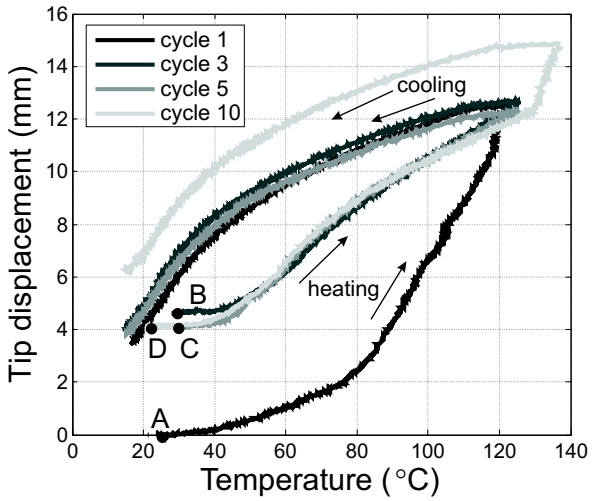

Figure 4.8: SMAHC beam response - cycles 1, 3, 5 and 10

Between the different loading cycles, the environmental chamber was opened in order to check the equipment and the specimen, therefore there is a little temperature gap when data was not recorded. As it can be noted in the graphs, the heating branch of the first cycle is quite different from that of the following cycles, which are stable. In particular, the first actuation occurs at higher temperatures. In order to further investigate this peculiarity, Figure 4.8 reports the previous plots together with the last one, in which the maximum temperature of 137°C was reached (light grey line, starting from point D). Two different steps in the actuation can be observed in the last cycle. The first follows the path of the stabilised cycles, whereas the second, starting at 125°C, continues along the path marked by the first cycle.

Comparison with the model predictions

The experimental behaviour depicted by Figures 4.6 to 4.8 is rather different from the expected response as predicted by models, such as the one discussed in Section 4.1. Indeed, according to Figure 4.3 (right), the heating curves for

the different cycles should overlap and no change in slope is expected during the actuation. However, the different actuation temperatures between the first and subsequent heatings and the change in slope observed in the last cycle could be interpreted in light of the experimental observations on shape memory alloy wires reported in Section 3.4.2.

Let us consider the loading history of the wires in the SMAHC beam. As the wires are prestrained at room temperature, the reverse phase transition temperatures are expected to increase with respect to those of the virgin specimen. During the first heating cycle, the $M \rightarrow A$ transformation occurs and part of the martensite is transformed into austenite. Upon cooling, the $A \rightarrow M$ transformation occurs at nearly constant strain due to the composite beam constraint, thus the newly formed martensite has lower reverse phase transformation temperatures. At this point, two different types of detwinned martensite are present in the wires. The first one, denoted with ξ^{d*}, was formed during the wires prestrain and its phase transition temperatures are denoted with $A_s^* > A_s$ and $A_f^* > A_f$. The second one, denoted with ξ^d, is the martensite formed during cooling at constant strain, its phase transition temperatures are the same as those of the virgin specimen (A_s and A_f). During the first thermal cycle, only ξ^{d*} is present and actuation occurs at temperature A_s^*. In the following cycles, on the other hand, ξ^d is the cause of the first actuation step, starting at temperature A_s. If the temperature is further increased, the transformation of ξ^{d*} starts, explaining the behaviour observed during the last thermal cycle.

The interpretation proposed is tested by simulating the SMAHC beam behaviour using the model discussed in Section 4.1 together with a slightly modified Brinson's constitutive model. The modified model contains two separate internal variables to depict ξ^d and ξ^{d*}, whose kinetic laws are defined in two different phase transition strips. The increase in the reverse phase transition temperatures associated to ξ^{d*} is taken to be 30°C. The modification introduced in the shape memory alloy constitutive law is rather crude and proposed here only as a way to preliminarily test this interpretation of the observed phenomenon. A modified model accounting for the shape memory behaviour for complex loading histories as discussed in Section 3.4.2 is the subject of ongoing research.

The geometrical and mechanical characteristics of the laminate and shape memory alloy wires, discussed earlier in this section, were used as input data.

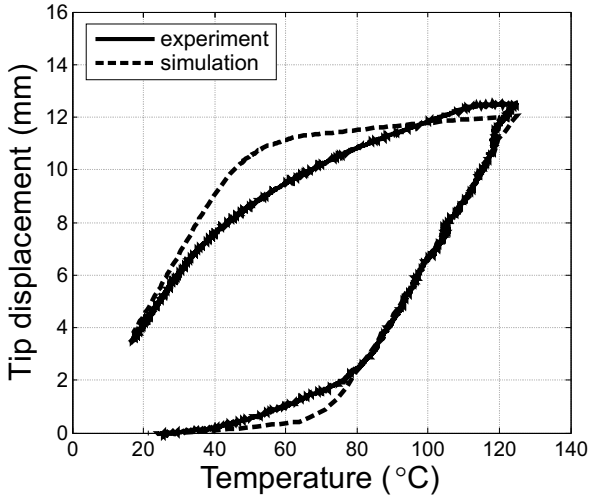

Figure 4.9: Simulation of SMAHC beam response - cycle 1

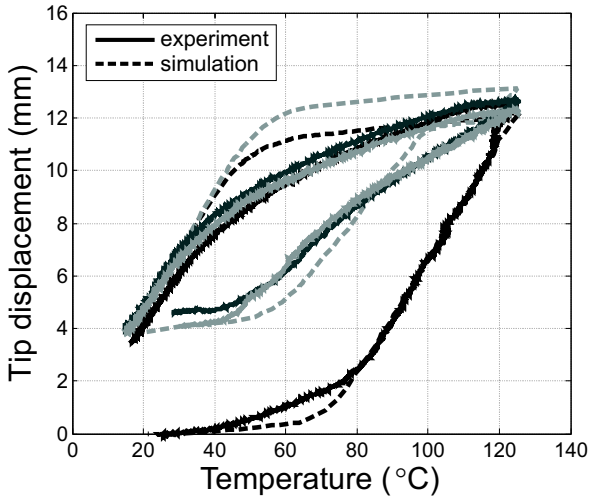

Figure 4.10: Simulation of SMAHC beam response - cycles 1, 3 and 5

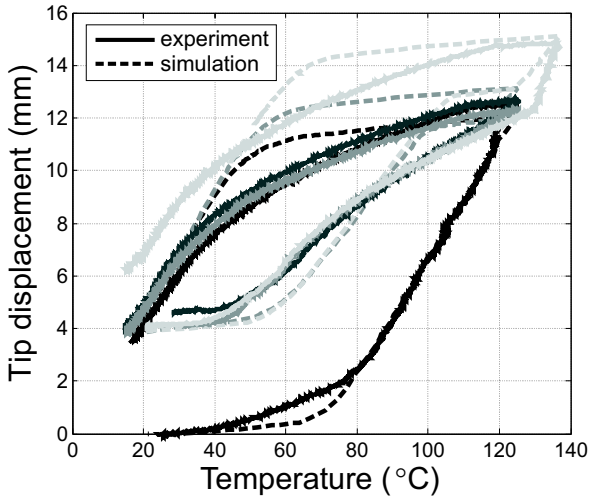

Figure 4.11: Simulation of SMAHC beam response - cycles 1, 3, 5 and 10

The stiffness of the epoxy was neglected since the chosen adhesive is extremely compliant with respect to the composite plate. A mesh of 96×2 thin plate elements was considered. The shape memory alloy wires were modelled using 96 truss elements, the cross-sectional area of each truss element corresponds to the area of all four wires. This FEM model was considered sufficient to capture the beam-like bending behaviour of the SMAHC. Since the FEM structural model requires the temperature of the wire as an input, the readings of thermocouples 1 and 3 were used as input data and a linear temperature gradient was assumed between them.

The SMAHC beam response as predicted by the finite element model is depicted in Figures 4.9 to 4.11. As it can be seen, the model is able to accurately capture the slope of the experimental displacement-temperature graph, while the modified constitutive law for the shape memory alloy wires allows to describe the change in response in the different heating cycles.

4.2.2 SMAHC plate

The second part of the experimental work concerns the manufacturing of a hybrid composite plate. The work was carried out in collaboration with the Institute for Composite and Biomedical Materials of the Italian National Research Council (CNR). Two different manufacturing techniques, namely VARTM and pre-preg lay-up, were investigated.

Initially, VARTM was chosen as a simple and cost-effective technique for SMAHC plate manufacturing. Testing of a VARTM plate, however, revealed some problems which turned out to be related to the manufacturing technique itself. For this reason, a second attempt was made using the pre-preg layup technique. The pre-preg SMAHC plate was tested and its behaviour was compared with the finite element model predictions. The two fabrication techniques are documented in the following, then results concerning the pre-preg SMAHC plate are presented and discussed.

VARTM plate

The VARTM technique consists in impregnating layers of dry fibres by injecting low viscosity resin with the aid of vacuum (see Section 1.3). The described process can be carried out with a variety of resins and fibres. Particularly attractive for the SMAHC manufacturing is the possibility to choose resins whose cure temperature is lower than the shape memory alloy wires actuation temperature, so that the wires do not need to be restrained during composite cure. This is the same concern which governed the choice of the adhesive used for the SMAHC beam in the first part of the experimental investigation.

A spool of 0.5 mm diameter shape memory alloy wire was provided by Memory Metalle GmbH[2]. A bicomponents polyester resin (Arotran Q6530, produced by Ashland) with 1% mekp as the initiator was used. The resin is usually cured in vacuum at a temperature of 60°C for one hour. However, an alternative cure cycle of 50°C for one hour and a half was used in this case in order not to exceed the shape memory alloy wires actuation temperature. The reinforcement is made up of unidirectional glass fibre fabric (weight 600 gr/m^2), produced by Chomarat. Glass fibres are chosen both for their relatively low stiffness as compared to carbon fibres and for the electrical insulation they provide. Indeed,

[2] www.memory-metalle.de

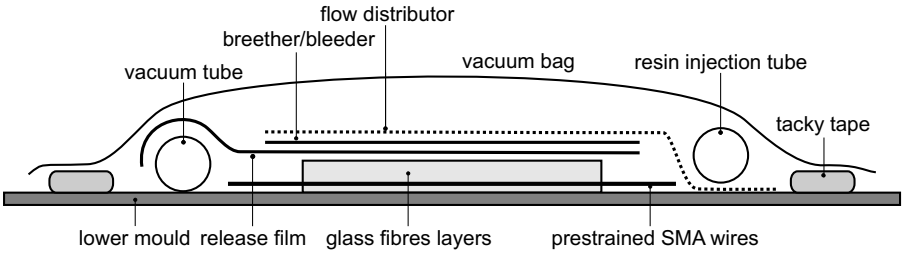

Figure 4.12: VARTM lay-up

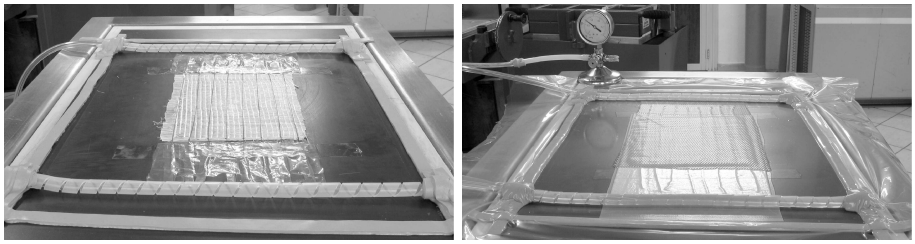

(a) (b)

Figure 4.13: VARTM composite making

carbon fibres conduce electricity, thus Joule heating of the embedded shape memory alloy wires would be difficult to achieve. The laminate is composed of three layers with the fibres perpendicular to the shape memory alloy wires direction. This way, the bending stiffness in the wires direction is minimum and the maximum actuation should be achieved. Eight wires are placed between the first and second fibres layer, thus giving the maximum possible offset from the plate midplane.

The fibre layers and the shape memory alloy wires were placed on top of a heated plate, which had been covered with a release agent to facilitate removal of the composite after cure. On top of the fibre layers, a number of other layers were placed: a release film, which facilitates composite detachment, a

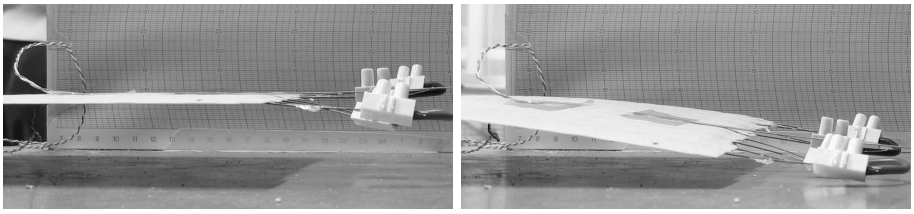

(a) Room temperature (b) 110°C

Figure 4.14: VARTM plate actuation

Compoflex layer used as both breather and bleeder, a flow distributor and finally the vacuum bag. An outline of the final lay-up is shown in Figure 4.12. Figure 4.13 shows two different phases of the VARTM process: in Figure 4.13(a), the first fibres layer and the shape memory alloy wires are placed inside the yellow tacky tape frame and between the air outlet and resin inlet tubes; Figure 4.13(b) shows the whole system after vacuum was pulled.

The SMAHC plate was clamped on one side and actuated using Joule heating. Figure 4.14 shows a picture of the plate at room temperature and during actuation. As it can be seen, significant bending was observed. During cooling, however, the displacement reached during actuation was only partially recovered, and after a few cycles the composite remained in the deformed configuration even at room temperature.

The permanent deformation in the VARTM plate was explained by considering the incomplete resin polymerisation at low temperatures. Indeed, the estimated reticulation of the resin cured at 50°C for 90 minutes is about 0.77. For most applications, this is not an issue as the partially polymerised matrix has already developed the required structural properties. In the SMAHC, however, the uncured fraction of the resin could reach cure temperature during actuation, thus the matrix could complete its cure cycle in the deformed configuration.

In light of the interpretation proposed, the SMAHC manufacturing process needs to be modified. One possibility is to use a resin which completely polymerises at low temperatures, thus significantly limiting the choice of materials for SMAHC making. Alternatively, higher cure temperatures could be applied

provided that the shape memory alloy wires are restrained during the cure cycle. The last approach was chosen in the following. Removing the limitation on the cure temperature allowed a broader choice of manufacturing materials and processes, thus the highly controllable and repeatable pre-preg lay-up process is considered in the following.

Pre-preg lay-up plate

In pre-preg lay-up, fabrics which are already impregnated with semi-solid resin are placed on a lower mould and cured by applying pressure and temperature, usually in autoclave or press. The process is highly controllable and repeatable, allowing to obtain a material with better properties by controlling the amount of resin present in the composite.

As the resin is semi-solid at room temperature, temperatures as high as 120°C are usually required in the cure cycle. During SMAHC cure, therefore, the embedded shape memory alloy wires reach the actuation temperature and need to be prevented from losing their prestrain. A steel frame was build to restrain the shape memory alloy wires during composite making. The frame has an embedded system allowing to prestrain the wires directly before blocking them.

Material characterisation A unidirectional S glass fibre epoxy pre-preg was used for the host structure manufacturing. A plate with five layers placed in the 0° direction and no embedded shape memory alloy wires was made and tested in order to obtain the host structure mechanical properties. The cure cycle used is the same described in the next section for the SMAHC plate. The flexural modulus in the 0° and 90° directions, E_a and E_b, were obtained through mechanical testing, while the Poisson's coefficient ν_{ab} and in-plane shear modulus G_{ab} were assumed. The material properties are reported in Table 4.4.

A spool of 0.5 mm shape memory alloy wire was provided by Saes-Getters[3]. Differently from the shape memory alloy wires used in the experimental work described up to now, these wires were subjected to training by the producers before purchase. Training consists in cyclically loading the shape memory alloy wires multiple times in order to stabilise the material properties. Different

[3] www.saesgetters.com

Table 4.4: Pre-preg glass fibres composite lamina: material properties

E_a GPa	E_b GPa	ν_{ab}	G_{ab} GPa
34.587	7.537	0.3	3

Table 4.5: Trained Nitinol wires: material properties

A_s °C	A_f °C	C_A MPa/°C	E GPa	Θ MPa/°C	ε_L
70	78	5	18	0	0.06

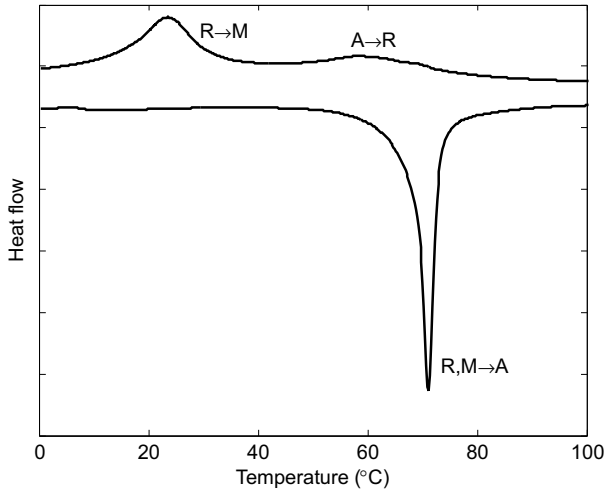

Figure 4.15: DSC measurement on trained wires

training cycles can be designed, involving for example superelastic loading and unloading or heating and cooling under a constant load. In this case, the procedure used for training was not disclosed by the producers. The overall effect of training is to stabilise the material properties of the shape memory alloys and induce a two-way memory effect. The phase transition temperatures for the shape memory alloy wires were obtained via DSC. The calorimetric measurement is reported in Figure 4.15. As it can be seen, austenite to R-phase transition is present during cooling with a very small temperature hysteresis. This feature makes the shape memory alloy wires particularly suitable for actuation by limiting the hysteretic response. The R-phase transition, however, is not described by any of the constitutive models examined in this work. For this reason, the behaviour of the shape memory alloy wires at cooling cannot be described by the numerical simulation reported in the following, which includes only the heating branch. The remaining material properties of the wires which are needed in the simulation of the heating branch were characterised via mechanical testing and are reported in Table 4.5.

Composite design and fabrication The composite lamination scheme is designed to have low stiffness in the direction of the shape memory alloy wires. Indeed, the stacking sequence is (90/90/0/90/90), where the 0° direction coincides with the wires direction. The external layers are all placed at 90°, resulting in a strong bending anisotropy, while the middle lamina with 0° fibres slightly decreases in-plane anisotropy. Ten wires are placed between the first and second layer, thus achieving the maximum possible offset from the plate midplane. The in-plane distance between the wires is 15 mm.

The composite was laid up directly on the steel frame. A release agent was placed on the frame in order to ensure easy detachment of the final composite from the mold. Five layers of pre-preg were cut with dimensions 150×240 mm and laid up on the frame. The shape memory alloy wires were placed between the first and second pre-preg layer. In order to improve adhesion between the shape memory alloy wires and pre-preg layers, the surface of the wires was mechanically treated by abrading it with grit paper (Rossi et al., 2007). The wires were then prestrained by 3.5% and allowed to recover the elastic part of the deformation, resulting in a transformation prestrain of 2.75%. A release film was placed on top of the pre-preg layers, finally the vacuum bag was put

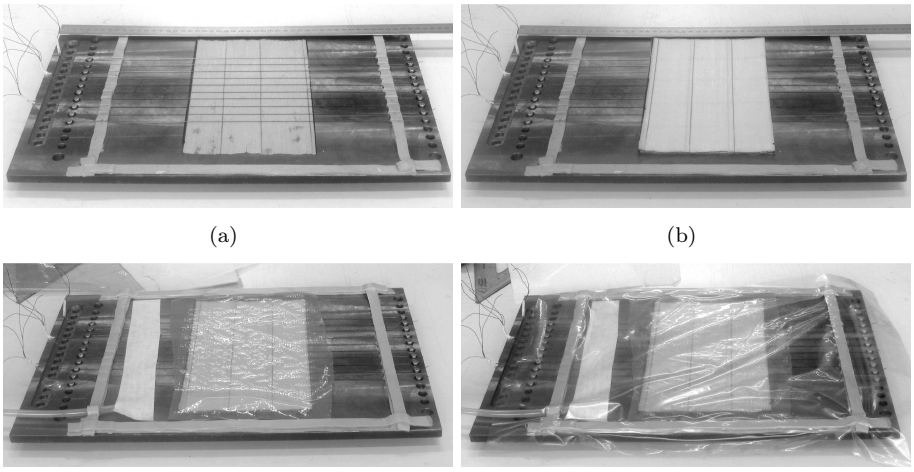

(a) (b)

(c) (d)

Figure 4.16: Pre-preg SMAHC plate making

into place. The various step of composite making are documented in Figure 4.16. Figure 4.16(a) shows the steel frame with the first pre-preg layer, the prestrained shape memory alloy wires and the tacky tape frame necessary to seal the vacuum bag on top of the laminate. Figure 4.16(b) shows the complete composite lay-up, while in Figure 4.16(c) the vacuum tube and the top release film are put into place. Finally, in Figure 4.16(d), the vacuum bag is placed.

The composite was cured with the help of vacuum and a press with controllable plate pressure and temperature. The cure cycle is the following:

- apply vacuum at 0.7 bar for one hour;
- apply a pressure of 3 bar;
- increase the temperature to 128°C at a rate of 2°C/min;
- maintain a constant temperature of 128°C for 90 minutes;
- cool to room temperature at a rate of 2°C/min;
- release the applied pressure.

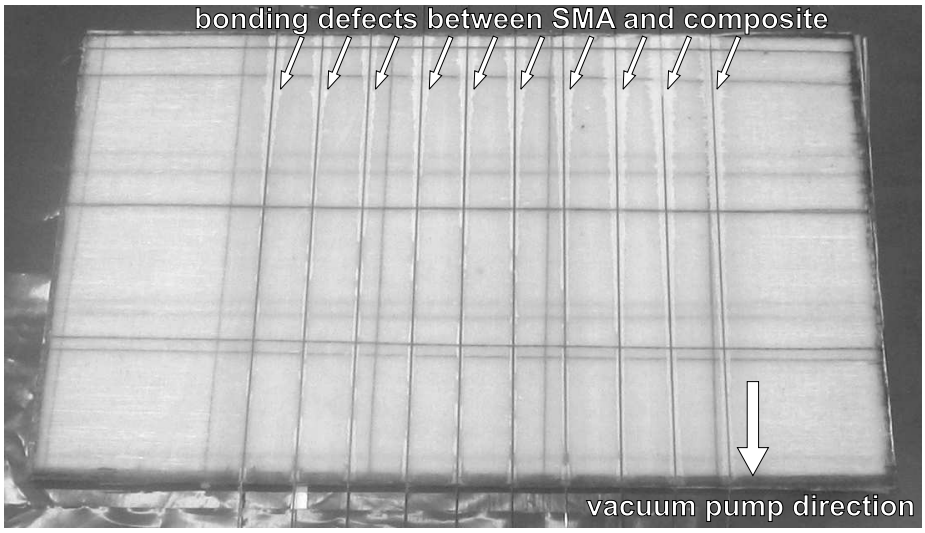

Figure 4.17: Pre-preg SMAHC plate

Figure 4.17 shows a picture of the composite plate as removed from the steel frame. The shape memory alloy wires are perfectly visible under the first glass fibres layer. A visual inspection reveals non perfect bonding between the shape memory alloy wires and the composite layers: the light grey areas around the wires, which are evident in particular in the zones marked by the arrows, denote the presence of some air between the composite layers. Note that the defects are more significant on the side opposite to where the vacuum tube was placed. The presence of bonding defects is mainly related to the size of the wires as compared to the laminae thickness: indeed, 0.5 mm wires were used and the overall laminate thickness is 1.3 mm (mean ply thickness 0.26 mm). The bonding could be improved by using wires with smaller diameter and a less viscous resin which may better penetrate the gaps between the shape memory alloy wires and the composite fibres.

After cure, a 150×150 mm square containing all the shape memory alloy wires was cut from the plate and used for testing. The remaining strips, consisting only of glass fibres composite, were saved in case a calorimetric charac-

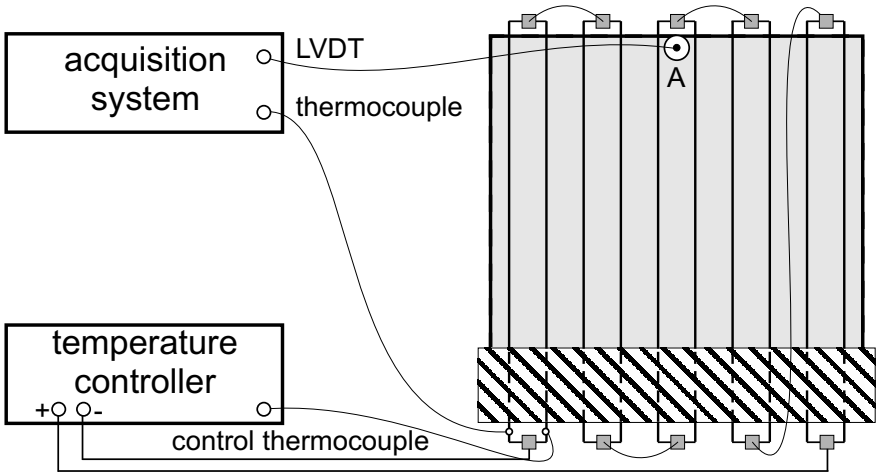

Figure 4.18: Experimental setup for the pre-preg SMAHC plate

terisation of the composite was needed.

Experimental setup The shape memory alloy wires were actuated using Joule heating. An outline of the experimental setup is shown in Figure 4.18. Five couples of wires, each couple connected in parallel, were connected in series and attached to a Eurotherm 2704 temperature controller, using a K type thermocouple as feedback. The plate was clamped on one side, leaving a free length of 125 mm. The displacement of point A in Figure 4.18 was monitored using an LVDT (DFg5 unguided min LVDT, ±5mm stroke). The LVDT and a second K type thermocouple attached to one of the shape memory alloy wires were connected to a DAQ acquisition system, displacement and temperature data were recorded using Labview.

Experimental results Figure 4.19 shows a profile picture of the SMAHC specimen at room temperature and at a temperature of 160°C, where a significant deformation is observed. As it can be seen from the picture, at room temperature the plate is not flat but it shows an initial curvature, mainly related

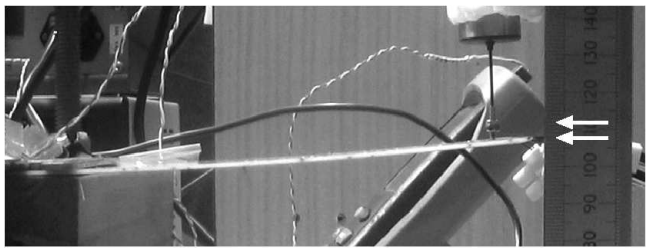

(a) Room temperature

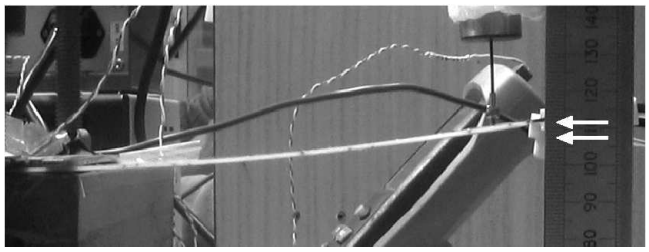

(b) 160°C

Figure 4.19: Pre-preg SMAHC plate actuation

to the presence of an initial stress in the shape memory alloy wires. Indeed, during composite cure at 128°C the shape memory alloy wires developed a recovery stress which was not completely released upon cooling. This is the same phenomenon occurring in the SMAHC beam after the first actuation cycle (see Figure 4.6). In the present case, however, the first actuation of the shape memory alloy wires occurs during composite cure, thus the residual curvature is present right at the beginning of composite testing. The initial displacement of point A with respect to the undeformed flat plate configuration was approximately evaluated to be 3 mm.

Figure 4.20 shows the point A displacement versus temperature graph for a number of loading cycles, reaching different maximum temperatures. Differently from what observed in the SMAHC beam experiment, the actuation is rather repeatable and the hysteresis between the heating and cooling branches is nearly absent. These differences are related partly to the type of shape memory alloy

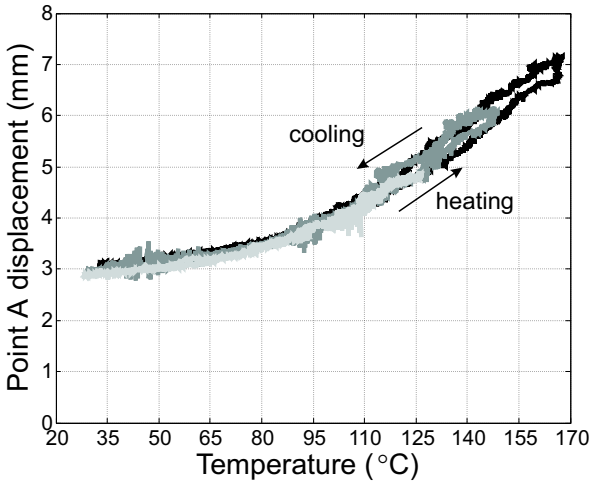

Figure 4.20: Pre-preg SMAHC plate response for different cycles

wires used in the two experiments and partly to the different specimen manufacturing process and experimental setup. Indeed, trained wires tend to have a more stable behaviour than untrained ones, with a smaller hysteresis related to the presence of R-phase. Moreover, the shape memory alloy wires heating occurring during pre-preg SMAHC manufacturing is expected to partially remove the effect of the loading history on the shape memory alloy wires, which constituted the main cause of the different responses observed in the SMAHC beam. Finally, the different experimental setup (Joule heating versus environmental chamber) made it more difficult to achieve controlled shape memory alloys cooling, thus the thermocouple response time may have influenced data acquisition, especially in the cooling branch.

The temperature control and acquisition were indeed a critical point in the experimental design. No thermocouples were embedded in the SMAHC plate in order to prevent the creation of interlaminar defects. For this reason, only the temperature in the external part of the shape memory alloy wires could be recorded, where the significant movements occurring during actuation made it difficult to achieve perfect contact between the thermocouple and wires. Besides

providing useful information for the evaluation of the SMAHC plate response and the validation of the numerical model, good temperature measurements are a crucial feedback for the control system. An idea to improve temperature acquisition for control purposes is to use micrometric thermocouples or optical fibres sensors, which could be directly embedded in the hybrid composite without causing significant interlaminar defects.

Comparison with the model predictions The numerical model discussed in Section 4.1 is used to simulate the behaviour of the SMAHC plate. In Section 4.2.1, a complete simulation was carried out to predict the behaviour of the SMAHC beam during the different loading cycles. In this case, on the other hand, a number of difficulties arise, regarding the definition of the plate geometry and initial conditions and the modelling of the cooling branch.

As already anticipated, the presence of R-phase does not allow to model the shape memory alloy behaviour in cooling. Thus, the numerical simulation is not able to describe a complete actuation cycle and only the heating branch is reported in the following. Due to the actuation occurring during composite cure, the initial conditions of the SMAHC are difficult to evaluate, as is the initial stress in the shape memory alloy wires. On the other hand, a simulation considering different initial stress conditions in the shape memory alloy wires is still expected to capture the slope of the displacement-temperature curve during actuation. For this reason, the simulation was carried out considering an initially flat plate with untensioned shape memory alloy wires. Finally, the composite manufacturing makes it difficult to accurately evaluate the offset of the shape memory alloy wires with respect to the plate midplane, which is a crucial information greatly influencing the predicted plate behaviour. In the following simulation, the offset d was assumed to be $d = h/2 - \phi/2 - h_l = 0.3$ mm, where $h = 1.3$ mm is the plate thickness, $\phi = 0.5$ mm is the wire diameter and the topmost ply thickness was assumed to be $h_l = 0.1$ mm.

The geometrical and mechanical characteristics of the composite material and shape memory alloy wires were used as input data for the simulation. A 20×20 two-dimensional plate elements mesh was considered, with shape memory alloy truss elements connected at the nodes in the appropriate places. The thermocouple reading was used as input data, assuming a uniform temperature along the shape memory alloy wires. As the effects of the loading history

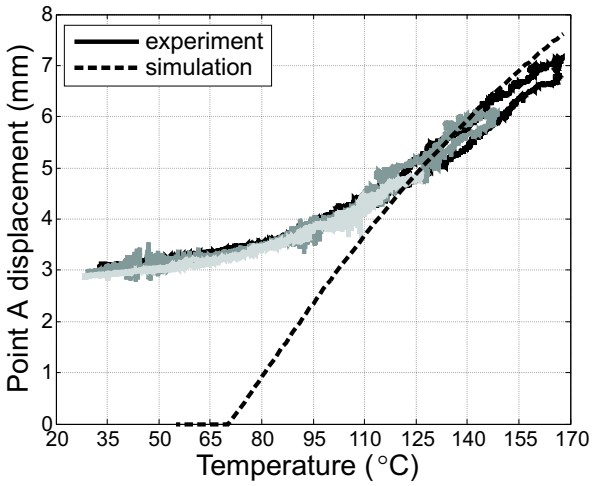

Figure 4.21: Simulation of pre-preg SMAHC plate response

are partially removed by the constrained recovery thermal cycle occurring during pre-preg SMAHC manufacturing, the modification to the Brinson's model discussed in Section 4.2.1 is not considered here.

The SMAHC plate response as predicted by the numerical model is depicted in Figure 4.21. As expected, notwithstanding the different initial conditions, the numerical simulation is able to capture the slope of the displacement-temperature curve in the actuation region.

Conclusions and perspectives

This dissertation discusses a number of issues related to active composites with embedded shape memory alloys. Their different constituents, namely fibre-reinforced composites and shape memory alloy elements, are first examined separately and some original contributions are developed whose validity extends beyond active composites applications. Then, active composites are considered by developing and experimentally validating a simple model to describe both shape and stiffness control configurations.

While the proposed modelling tools are simple and useful for preliminary design and the experimental work demonstrates the feasibility of the shape control concept, a number of problems still need to be faced in order to apply such concept to real structures.

The critical analysis of the shape memory alloy constitutive models has emphasised the need for further research work, related mainly to the three-dimensional behaviour. A particular attention should be paid to the description of complex loading histories, such as those involving a simultaneous change of the stress and temperature conditions. Indeed, the experimental characterisation of Nitinol wires has shown that some traits of the shape memory alloys material behaviour are generally not included in the current constitutive modelling, while the results on the hybrid composite beam have underlined the importance of such traits in the composite modelling. Furthermore, features such as the presence of the R-phase phase transition should not be neglected in the modelling, as they might be significant when dealing with shape memory

alloy actuators.

In order to improve the modelling of both shape memory alloys and their interaction with the host structure, the macroscopic approach adopted for composites and shape memory alloy modelling could be replaced with multiscale techniques, allowing to observe each phenomenon occurring in these complex structures at the appropriate level. This approach should allow to thoroughly describe the active composite behaviour, from the ordinary working conditions all the way to damage and failure mechanisms.

From the technological point of view, the choice of the composite constituents, shape memory materials and manufacturing process should be optimised according to the sought application, addressing the problems which were encountered in the present experimental work, such as the adherence of the shape memory elements to the composite matrix.

Bibliography

Abel, E., Luo, H., Pridham, M., and Slade, A. (2004). Issues concerning the measurement of transformation temperatures of NiTi alloys. *Smart Materials and Structures*, 13:1110–1117.

ADINA (2006). *ADINA 8.4 Theory and Modeling Guide - Volume 1*. ADINA R & D, Inc.

Alfano, G., Auricchio, F., Rosati, L., and Sacco, E. (2001). MITC finite elements for laminated composite plates. *International Journal for Numerical Methods in Engineering*, 50:707–738.

Antonucci, V., Faiella, G., Giordano, M., Mennella, F., and Nicolais, L. (2007). Electrical resistivity study and characterization during NiTi phase transformations. *Thermochimica Acta*, 462:64–69.

Aoki, T. and Shimamoto, A. (2003). Active vibration control of epoxy matrix composite beams with embedded shape memory alloys TiNi fibers. *International Journal of Modern Physics B*, 17:1744–1749.

Araki, S., Ono, H., and Saito, K. (2002). Micromechanical analysis of crack closure mechanism for intelligent materials containing TiNi fibers. *JSME International Journal*, 45(2):208–216.

Araujo, A. L., Mota Soares, C. M., Herskovits, J., and Pedersen, P. (2002). Development of a finite element model for the identification of mechanical and piezoelectric properties through gradient optimization and experimental vibration data. *Composite Structures*, 58:307–318.

Araujo, A. L., Mota Soares, C. M., Moreira di Freitas, M. J., Pedersen, P., and Herskovits, J. (2000). Combined numerical-experimental model for the identification of mechanical properties of laminated structures. *Composite Structures*, 50:363–372.

Auricchio, F., Lovadina, C., and Sacco, E. (2001). Analysis of mixed finite elements for laminated composite plates. *Computer Methods in Applied Mechanics and Engineering*, 190:4767–4783.

Auricchio, F., Marfia, S., and Sacco, E. (2003). Modelling of SMA materials: training and two way memory effects. *Computers and Structures*, 81:2301–2317.

Auricchio, F. and Petrini, L. (2002). Improvements and algorithmical considerations on a recent three-dimensional model describing stress-induced solid phase transformations. *International Journal for Numerical Methods in Engineering*, 55:1255–1248.

Auricchio, F. and Petrini, L. (2004a). A three-dimensional model describing stress-temperature induced solid phase transformations: solution algorithm and boundary value problems. *International Journal for Numerical Methods in Engineering*, 61:807–836.

Auricchio, F. and Petrini, L. (2004b). A three-dimensional model describing stress-temperature induced solid phase transformations: thermomechanical coupling and hybrid composite applications. *International Journal for Numerical Methods in Engineering*, 61:716–737.

Auricchio, F., Reali, A., and Stefanelli, U. (2007). A three-dimensional model describing stress-induced solid phase transformation with permanent inelasticity. *International Journal of Plasticity*, 23:207–226.

Auricchio, F. and Sacco, E. (1997). A one-dimensional model for superelastic shape-memory alloys with different elastic properties between austenite and martensite. *International Journal of Non-Linear Mechanics*, 32(6):1101–1114.

Auricchio, F. and Sacco, E. (1999a). A mixed-enhanced finite-element for the analysis of laminated composite plates. *International Journal for Numerical Methods in Engineering*, 44:1481–1504.

Auricchio, F. and Sacco, E. (1999b). A temperature-dependent beam for shape-memory alloys: constitutive modelling, finite-element implementation and numerical simulations. *Computer Methods in Applied Mechanics and Engineering*, 174:171–190.

Auricchio, F. and Sacco, E. (2001). Thermo-mechanical modelling of a superelastic shape-memory wire under cyclic stretching-bending loadings. *International Journal of Solids and Structures*, 38:6123–6145.

Auricchio, F. and Sacco, E. (2003). Refined first-order shear deformation theory models for composite laminates. *Journal of Applied Mechanics*, 70:381–390.

Auricchio, F., Sacco, E., and Vairo, G. (1999). Partial-mixed formulation and refined models for the analysis of composite laminates within an FSDT. *Composite Structures*, 46:103–113.

Auricchio, F., Sacco, E., and Vairo, G. (2006). A mixed FSDT finite element for monoclinic laminated plates. *Computers and Structures*, 84:624–639.

Auricchio, F. and Taylor, R. L. (1994). A shear deformable plate element with an exact thin limit. *Computer Methods in Applied Mechanics and Engineering*, 118:393–412.

Ayorinde, E. O. and Yu, L. (2005). On the elastic characterization of composite plates with vibration data. *Journal of Sound and Vibration*, 283:243–262.

Bartoli, I., Di Leo, A., and Viola, E. (2003). Parameter estimation of fibre reinforced composite materials using Bayesian sensitivity analysis. In *Proceedings of Composites in Construction International Conference*, pages 595–600.

Bastianini, F., Corradi, M., Borri, A., and di Tommaso, A. (2005). Retrofit and monitoring of an historical building using "Smart" CFRP with embedded fibre optic Brillouin sensors. *Construction and Building Materials*, 19(7):525–535.

Bathe, K.-J. (1996). *Finite Element Procedures*. Prentice-Hall.

Baz, A. and Chen, T. (1993). Performance of nitinol-reinforced drive shafts. In *Smart Structures and Intelligent Systems - SPIE Vol. 1917*, pages 791–808.

Baz, A., Poh, S., Ro, J., Mutua, M., and Gilheany, J. (1992). *Intelligent structural systems*, chapter Active control of nitinol-reinforced composite beam. Kluwer Academic Publishers.

Beck, J. V. and Arnold, K. J. (1977). *Parameter Estimation in Engineering and Science*. John Wiley and Sons, New York.

Benedetti, A., de Miranda, S., and Ubertini, F. (2006). A posteriori error estimation based on the superconvergent Recovery by Compatibility in Patches. *International Journal for Numerical Methods in Engineering*, 67:108–131.

Birman, V. (1997). Theory and comparison of the effect of composite and shape memory alloy stiffeners on stability of composite shells and plates. *International Journal of Mechanical Science*, 39(10):1139–1149.

Birman, V. (2007). Enhancement of stability of composite plates using shape memory alloy supports. *AIAA Journal*, 45:2584–2588.

Birman, V. (2008). Shape memory elastic foundation and supports for passive vibration control of composite plates. *International Journal of Solids and Structures*, 45:320–335.

Bledzki, A. K., Kessler, A., Rikards, R., and Chate, A. (1999). Determination of elastic constants of glass/epoxy unidirectional laminates by the vibration testing of plates. *Composites Science and Technology*, 59(13):2015–2024.

Bo, Z. and Lagoudas, D. C. (1999a). Thermomechanical modeling of polycrystalline SMAs under cyclic loading, Part I: theoretical derivations. *International Journal of Engineering Science*, 37:1089–1140.

Bo, Z. and Lagoudas, D. C. (1999b). Thermomechanical modeling of polycrystalline SMAs under cyclic loading, Part III: evolution of plastic strains and two-way shape memory effect. *International Journal of Engineering Science*, 37:1175–1203.

Bo, Z. and Lagoudas, D. C. (1999c). Thermomechanical modeling of polycrystalline SMAs under cyclic loading, Part IV: modeling of minor hysteresis loops. *International Journal of Engineering Science*, 37:1205–1249.

Bo, Z., Lagoudas, D. C., and Miller, D. A. (1999). Material characterization of SMA actuators under non-proportional thermomechanical loading. *Journal of Engineering Materials and Technology*, 121(1):75–85.

Boyd, J. G. and Lagoudas, D. C. (1996a). A thermodynamical constitutive model for shape memory materials. Part I. the monolithic shape memory alloy. *International Journal of Plasticity*, 12(6):805–842.

Boyd, J. G. and Lagoudas, D. C. (1996b). A thermodynamical constitutive model for shape memory materials. Part II. the SMA composite material. *International Journal of Plasticity*, 12(7):843–873.

Brinson, L. C. (1993). One-dimensional constitutive behavior of shape memory alloys: thermomechanical derivation with non-constant material functions and redefined martensite internal variable. *Journal of Intelligent Material Systems and Structures*, 4:229–242.

Buehler, W. J., Gilfrich, J. V., and Wiley, R. C. (1963). Effect of low-temperature phase changes on the mechanical properties of alloys near composition TiNi. *Journal of Applied Physics*, 34(5):1475–1477.

Buravalla, V. R. and Khandelwal, A. (2007). Differential and integrated form consistency in 1-D phenomenological models for shape memory alloy constitutive behavior. *International Journal of Solids and Structures*, 44:4369–4381.

Burton, D. S., Gao, X., and Brinson, L. C. (2006). Finite element simulation of a self-healing shape memory alloy composite. *Mechanics of Materials*, 38:525–537.

Carrera, E. (2000). A priori vs. a posteriori evaluation of transverse stresses in multilayered orthotropic plates. *Composite Structures*, 48:245–260.

Carrera, E. (2002). Theories and finite elements for multilayered, anisotropic, composite plates and shells. *Archives of Computational Methods in Engineering*, 9:87–140.

Carrera, E. (2007). On the use of transverse shear stress homogeneous and non-homogeneous conditions in third-order orthotropic plate theory. *Composite Structures*, 77:341–352.

Carvelli, V. and Savoia, M. (1997). Assessment of plate theories for multilayered angle-ply plates. *Composite Structures*, 39:197–207.

Casciati, F. and Faravelli, L. (2004). Experimental characterisation of a Cu-based shape memory alloy toward its exploitation in passive control devices. *Journal de Physique IV*, 115:299–306.

Casciati, F., Faravelli, L., and Petrini, L. (1998). Energy dissipation in shape memory alloy devices. *Computer-aided Civil and Infrastructure Engineering*, 13:433–442.

Castellazzi, G., de Miranda, S., and Ubertini, F. (2006). A posteriori error estimation in finite element analysis of plate structures. In *Proceedings of the 7th world Congress in Computational Mechanics - WCCM VII*, Los Angeles, USA.

Cazzani, A., Garusi, E., Tralli, A., and Atluri, S. N. (2005). A four-node hybrid assumed-strain finite element for laminated composite plates. *Computers, Materials & Continua*, 2:22–38.

Cen, S., Long, Y., and Yao, Z. (2002). A new hybrid-enhanced displacement-based element for the analysis of laminated composite plates. *Computers and Structures*, 80:819–833.

Chandra, R. (2001). Active shape control of composite blades using shape memory actuation. *Smart materials and structures*, 10:1018–1024.

Chang, L. C. (1951). Atomic displacements and crystallographic mechanism in diffusionless transformation of gold-cadmium single crystals containing 47.5 atomic percent cadmium. *Acta Crystallographica*, 4:320–324.

Chaudhry, Z. and Rogers, C. A. (1991). Reponse of composite beams to an internal actuator force. In *Proceedings 32nd AIAA/ASME/ASCE/AHS/ASC conference*, pages 186–193.

Chen, J., Wu, X., Li, G., Pang, S.-S., and Taheri, F. (2007). Analysis of an adhesively bonded single-strap joint integrated with shape memory alloy (SMA) reinforced layers. *International Journal of Solids and Structures*, 44:3557–3574.

Coleman, B. D. and Noll, W. (1963). The thermodynamics of elastic materials with heat conduction and viscosity. *Archive for Rational Mechanics and Analysis*, 13:167–178.

Collins, J. D., Hart, G., Hasselman, T. K., and Kennedy, B. (1974). Statistical identification of structures. *AIAA Journal*, 12(2):185–190.

Collins, J. D. and Thomson, W. T. (1969). The eigenvalue problem for structural systems with statistical properties. *AIAA Journal*, 7(4):642–648.

Daghia, F., de Miranda, S., Ubertini, F., and Viola, E. (2007a). Estimation of elastic constants of thick laminated plates within a Bayesian framework. *Composite Structures*, 80:461–473.

Daghia, F., de Miranda, S., Ubertini, F., and Viola, E. (2008). A hybrid stress approach for laminated composite plates within the First-order Shear Deformation Theory. *International Journal of Solids and Structures*, 45:1766–1787.

Daghia, F., Inman, D. J., Ubertini, F., and Viola, E. (2007b). Shape memory alloy hybrid composite plates for shape and stiffness control. *Journal of Intelligent Material Systems and Structures*. In press.

Daghia, F., Viola, E., Seigler, T. M., and Inman, D. J. (2006). Constitutive modeling of SMA in constrained recovery mode. In *Proceedings of ASME International Mechanical Engineering Congress and Exposition*, Chicago, USA. Paper number IMECE206-15616.

de Miranda, S. and Ubertini, F. (2006). A simple hybrid stress element for shear deformable plates. *International Journal for Numerical Methods in Engineering*, 65:808–833.

Deng, Z., Li, Q., and Sun, H. (2006). Behavior of concrete beam with embedded shape memory alloy wires. *Engineering Structures*, 28:1691–1697.

Di Paola, M. and Bilello, C. (2004). An integral equation for damage identification of Euler-Bernoulli beams under static loads. *Journal of Engineering Mechanics*, 58:225–234.

DiCarlo, A., Podio-Guidugli, P., and Williams, W. O. (2001). Shells with thickness distension. *International Journal of Solids and Structures*, 38:1201–1225.

Dolce, M. and Nicoletti, M. (1999). Guidelines for shape memory alloy-based seismic devices. In *Proceedings of MANSIDE project final workshop*, pages II 209–232.

Edwards, K. L. (1998). An overview of the technology of fibre-reinforced plastics for design purposes. *Materials and Design*, 19:1–10.

Epps, J. and Chandra, R. (1997). Shape memory alloy actuation for tuning of composite beams. *Smart Materials and Structures*, 20:251–256.

Epps, J. J. and Chopra, I. (1997). Comparative evaluation of shape memory alloy constitutive models with test data. In *38th AIAA/ASME/ASCE/AHS/ASC Structures, Structural Dynamics and Materials Conference and Adaptive Structures Forum*, Kissimmee, USA.

Fabrizio, M., Grandi, D., and Daghia, F. (2008). A non isothermal Ginzburg-Landau model for martensitic phase transitions in shape memory alloys. In preparation.

Fox, R. L. and Kapoor, M. P. (1968). Rates of change of eigenvalues and eigenvectors. *AIAA Journal*, 6(12):2426–2429.

Fragnito, M. and Vetrella, S. (2002). A space release/deployment system actuated by shape memory wires. *Acta Astronautica*, 51(11):761–770.

Frederiksen, P. S. (1997). Experimental procedure and results for the identification of elastic constants of thick orthotropic plates. *Journal of Composite Materials*, 31(4):360–382.

Frederiksen, P. S. (1998). Parameter uncertainty and design of optimal experiments for the estimation of elastic constants. *International Journal of Solids and Structures*, 35(12):1241–1268.

Gao, X., Burton, D., Turner, T. L., and Brinson, L. C. (2006). Finite element analysis of adaptive-stiffening and shape-control SMA hybrid composites. *Journal of Engineering Materials and Technology*, 128:285–293.

Gao, X., Turner, T. L., Burton, D., and Brinson, L. C. (2005). Finite element analysis of adaptive-stiffening and shape-control SMA hybrid composites. In

Armstrong, W. D., editor, *Smart Structures and Materials 2005: Active Materials: Behavior and Mechanics - SPIE Vol. 5761*, pages 406–416. SPIE.

Ghomshei, M., Khajepour, A., Tabandeh, N., and Behdinan, K. (2001). Finite element modeling of shape memory alloy composite actuators: theory and experiment. *Journal of Intelligent Material Systems and Structures*, 12:761–773.

Ghugal, Y. M. and Shimpi, R. P. (2002). A review of refined shear deformation theories of isotropic and anisotropic laminated plates. *Journal of Reinforced Plastics and Composites*, 21(9):775–813.

Hasselman, T. K. and Hart, G. C. (1972). Modal analysis of random structural systems. *Journal of the Engineering Mechanics Division - ASCE*, 98:561–579.

He, Z., Gall, K. R., and Brinson, L. C. (2006). Use of electrical resistance testing to redefine the transformation kinetics and phase diagram for shape-memory alloys. *Metallurgical and Materials Transactions A*, 37A:579–587.

Herzog, H. and Jacquet, E. (2007). From a shape memory alloys model implementation to a composite behavior. *Computational Materials Science*, 39:365–375.

Hongxing, H., Sol, H., and de Wilde, W. P. (2000). Identification of plate rigidities of a circular plate with cylindrical orthotropy using vibration data. *Computers and Structures*, 77:83–89.

Huang, N. N. (1994). Influence of shear correction factors in the higher order shear deformation laminated shell theory. *International Journal of Solids and Structures*, 31(9):1263–1277.

Hwang, S. F. and Chang, C. S. (2000). Determination of elastic constants of materials via vibration testing. *Composite Structures*, 49:183–190.

ISTECH (2000). *Proceedings of ISTECH project final workshop.*

Janke, L., Czaderski, C., Motavalli, M., and Ruth, J. (2005). Applications of shape memory alloys in civil engineering structures — overview, limits and new ideas. *Materials and Structures*, 38:578–592.

Jenkins, P. P. and Landis, G. A. (1995). A rotating arm using shape-memory alloy. In *NASA. Johnson Space Center, the 29th Aerospace Mechanisms Symposium*, pages 167–171.

Khalili, S. M. R., Shokuhfar, A., and Ashenai Ghasemi, F. (2007a). Effect of smart stiffening procedure on low-velocity impact response of smart structures. *Journal of Material Processing Technology*, 190:142–152.

Khalili, S. M. R., Shokuhfar, A., Malekzadeh, K., and Ashenai Ghasemi, F. (2007b). Low-velocity impact of active thin-walled hybrid composite structures embedded with SMA wires. *Thin-Walled Structures*, 45:799–808.

Kim, J. S. and Cho, M. (2007). Enhanced first-order theory based on mixed formulation and transverse normal effect. *International Journal of Solids and Structures*, 44:1256–1276.

Krevet, B. and Kohl, M. (2003). 3D finite element simulation of a shape memory alloy microgripper. In *Smart Structures and Materials 2003: Active Materials, Behavior and Mechanics. Proceedings of SPIE Vol. 5053*, pages 119–129.

Ladevèze, P., Lubineau, G., and Marsal, D. (2006). Towards a bridge between the micro- and mesomechanics of delamination for laminated composites. *Composites Science and Technology*, 66:698–712.

Lagoudas, D. C. and Bo, Z. (1999). Thermomechanical modeling of polycrystalline SMAs under cyclic loading, Part II: material characterization and experimental results for a stable transformation cycle. *International Journal of Engineering Science*, 37:1141–1173.

Lagoudas, D. C., Bo, Z., and Qidway, M. A. (1996). A unified thermodynamic constitutive model for SMA and finite element analysis of active metal matrix composites. *Mechanics of Advanced Materials and Structures*, 3(2):153–179.

Lagoudas, D. C., Entchev, P. B., Popov, P., Patoor, E., Brinson, L. C., and Gao, X. (2006). Shape memory alloys, Part II: Modeling of polycrystals. *Mechanics of Materials*, 38:430–462.

Lagoudas, D. C. and Tadjbakhsh, I. G. (1993). Deformation of active flexible rods with embedded line actuators. In *Recent developments in stability, vibration, and control of structural systems, AMD - Vol. 167*, pages 89–106.

Lai, T. C. and Ip, K. H. (1996). Parameter estimation of orthotropic plates by Bayesian sensitivity analysis. *Composite Structures*, 34:29–42.

Laitinen, M., Lahtinen, H., and Sjölind, S. G. (1995). Transverse shear correction factors for laminates in cylindrical bending. *Communications in Numerical Methods in Engineering*, 11:41–47.

Lauwagie, T., Sol, H., Roebben, G., Heylen, W., Shi, Y., and Van der Biest, O. (2003). Mixed numerical-experimental identification of elastic properties of orthotropic metal plates. *NDT&E International*, 36:487–495.

Lee, H. J. and Lee, J. J. (2000). A numerical analysis of the buckling and postbuckling behavior of laminated composite shells with embedded shape memory alloy wire actuators. *Smart Materials and Structures*, 9:780–787.

Lee, H. J., Lee, J. J., and Huh, J. S. (1999). A simulation study on the thermal buckling behavior of laminated composite shells with embedded shape memory alloy (SMA) wires. *Composite Structures*, 47:463–469.

Lemaitre, J. and Chaboche, J.-L. (1994). *Mechanics of Solid Materials*. Cambridge University Press.

Lembo, M. and Podio-Guidugli, P. (2007). How to use reactive stresses to improve plate-theory approximations of the stress field in a linearly elastic plate-like body. *International Journal of Solids and Structures*, 44(5):1337–1369.

Lexcellent, C. and Schlömerkemper, A. (2007). Comparison of several models for the determination of the phase transformation yield surface in shape-memory alloys with experimental data. *Acta Materialia*, 55:2995–3006.

Li, H., Liu, Z.-Q., and Ou, J.-P. (2007). Experimental study of a simple reinforced concrete beam temporarily strengthened by SMA wires followed by permanent strengthening with CFRP plates. *Engineering Structures*. In press.

Li, Y., Cui, L. S., Xu, X. B., and Yang, D. Z. (2003). Constrained phase-transformation of a TiNi shape-memory alloy. *Metallurgical and Materials Transactions A*, 34A:219–223.

Liang, C. and Rogers, C. A. (1990). One-dimensional thermomechanical constitutive relations for shape memory materials. *Journal of Intelligent Material Systems and Structures*, 1(2):207–234.

Lind, R. J. and Doumanidis, C. C. (2003). Active deformable sheets: prototype implementation, modeling, and control. *Optical engineering*, 42(2):304–316.

Liu, Y. and Favier, D. (2000). Stabilisation of martensite due to shear deformation via variant reorientation in polycrystalline NiTi. *Acta materialia*, 48:3489–3499.

Lòpez, G. A., Barrado, M., Bocanegra, E. H., San Juan, J. M., and Nò, M. L. (2007). Influence of the matrix and of thermal treatment on the martensitic transformation in metal matrix composites. *Materials Science and Engineering*. In press.

Lubliner, J. and Auricchio, F. (1996). Generalized plasticity and shape-memory alloys. *International Journal of Solids and Structures*, 33(7):991–1003.

Malvern, L. E. (1969). *Introduction to the Mechanics of a Continuous Medium*. Prentice-Hall.

MANSIDE (1999). *Proceedings of MANSIDE project final workshop*.

Marfia, S. (2005). Micro-macro analysis of shape memory alloy composites. *International Journal of Solids and Structures*, 42:3677–3699.

Mazumdar, S. K. (2002). *Composites manufacturing : materials, product, and process engineering*. CRC Press.

Meo, M., Antonucci, E., Duclaux, P., and Giordano, M. (2005). Finite element simulation of low velocity impact on shape memory alloy composite plates. *Composite Structures*, 71:337–342.

Miller, D. A. and Lagoudas, D. C. (2000). Thermomechanical characterization of NiTiCu and NiTi sma actuators: influence of plastic strains. *Smart Materials and Structures*, 9:640–652.

Mohite, P. M. and Upadhyay, C. S. (2002). Local quality of smoothening based a-posteriori error estimators for laminated plates under transverse loading. *Computers and Structures*, 80:1477–1488.

Motahari, S. A. and Ghassemieh, M. (2007). Multilinear one-dimensional shape memory material model for use in structural engineering applications. *Engineering Structures*, 29:904–913.

Noor, A. K., Burton, W. S., and Peters, J. M. (1990). Predictor-corrector procedures for stress and free vibration analysis of multilayered composite plates and shells. *Computer Methods in Applied Mechanics and Engineering*, 82:341–363.

Noor, A. K., Kim, Y. H., and Peters, J. M. (1994). Transverse shear stresses and their sensitivity coefficients in multilayered composite panels. *AIAA Journal*, 32:1259–1269.

Ölander, A. (1932). An electrochemical investigation of solid cadmium-gold alloys. *Journal of the American Chemical Society*, 54:3819–3833.

Ostachowicz, W., Krawczuk, M., and Żak, A. J. (2000). Dynamics and buckling of a multilayer composite plate with embedded SMA wires. *Composite Structures*, 48:163–167.

Otsuka, K. and Wayman, C. (1999). *Shape Memory Materials*. Cambridge University Press.

Park, J. W. and Kim, Y. J. (2003). Local recovery of through-the-thickness stresses in laminated composite plates. *Composite Structures*, 59:291–296.

Pascale, G., Giammarruto, A., and Daghia, F. (2008). In preparation.

Patoor, E., Lagoudas, D. C., Entchev, P. B., Brinson, L. C., and Gao, X. (2006). Shape memory alloys, Part I: General properties and modeling of single crystals. *Mechanics of Materials*, 38:391–429.

Peultier, B., Ben Zineb, T., and Patoor, E. (2007). A simplified micromechanical constitutive law adapted to the design of shape memory applications by finite element methods. *Materials Science and Engineering A*. In press.

Pollard, E. L. and Jenkins, C. H. M. (2005). Shape memory alloy deployment of membrane mirrors for spaceborn telescopes. In *46th AIAA/ASME/ASCE/AHS/ASC Structures, Structural Dynamics & Materials Conference*.

Popov, P. (2005). *Constitutive modelling of shape memory alloys and upscaling of deformable porous media.* PhD thesis, Texas A&M University.

Popov, P. and Lagoudas, D. C. (2007). A 3-D constitutive model for shape memory alloys incorporating pseudoelasticity and detwinning of self-accommodated martensite. *International Journal of Plasticity*, 23(10–11):1679–1720.

Prahlad, H. and Chopra, I. (2001). Comparative evaluation of shape memory alloy constitutive models with experimental data. *Journal of Intelligent Material Systems and Structures*, 12:383–395.

Price, A. D., Jnifere, A., and Naguib, H. E. (2007). Design and control of a shape memory alloy based dexterous robot hand. *Smart Materials and Structures*, 16:1401–1414.

Qidway, M. A. and Lagoudas, D. C. (2000). On thermomechanics and transformation surfaces of polycrystalline NiTi shape memory alloy material. *International Journal of Plasticity*, 16:1309–1343.

Raniecki, B. and Lexcellent, C. (1994). R_L-models of pseudoelasticity and their specification for some shape memory solids. *European Journal of Mechanics A/Solids*, 13(1):21–50.

Reddy, J. N. (1984). A simple higher-order theory for laminated composite plates. *Journal of Applied Mechanics*, 51:745–752.

Reddy, J. N. (1997). *Mechanics of Laminated Composite Plates - Theory and Analysis.* CRC Press, Boca Raton.

Rikards, R., Chate, A., and Gailis, G. (2001). Identification of elastic properties of laminates based on experimental design. *International Journal of Solids and Structures*, 38:5097–5115.

Ro, J. and Baz, A. (1995a). Nitinol-reinforced plates: part I. Thermal characteristics. *Composites Engineering*, 5(1):61–75.

Ro, J. and Baz, A. (1995b). Nitinol-reinforced plates: part II. Static and buckling characteristics. *Composites Engineering*, 5(1):77–90.

Ro, J. and Baz, A. (1995c). Nitinol-reinforced plates: part III. Dynamic characteristics. *Composites Engineering*, 5(1):91–106.

Rolfes, E. and Rohwer, K. (1997). Improved transverse shear stresses in composite finite elements based on first order shear deformation theory. *International Journal for Numerical Methods in Engineering*, 40:51–60.

Rossi, S., Deflorian, F., Pegoretti, A., D'Orazio, D., and Gialanella, S. (2007). Chemical and mechanical treatments to improve the surface properties of shape memory NiTi wires. *Surface & Coatings Technology*. In press.

Sol, H., Hua, H., De Visscher, J., Vantomme, J., and de Wilde, W. P. (1997). A mixed numerical/experimental technique for the nondestructive identification of the stiffness properties of fibre reinforced composite materials. *NDT&E International*, 30(2):85–91.

Soutis, C. (2005). Fibre reinforced composites in aircraft construction. *Progress in Aerospace Sciences*, 41:143–151.

Souza, A. C., Mamiya, E. N., and Zouain, N. (1998). Three-dimensional model for solids undergoing stress-induced phase transformations. *European Journal of Mechanics A/Solids*, 17:789–806.

Stratford, T., Pascale, G., Manfroni, O., and Bonfiglioli, B. (2004). Shear strengthening masonry panels with sheet glass-fiber reinforced polymer. *Journal of Composites for Construction*, 8(5):434–443.

Sun, S., Sun, G., Han, F., and Wu, J. (2002a). Thermoviscoelastic analysis for a polymeric composite plate with embedded shape memory alloy wires. *Composite Structures*, 58:295–302.

Sun, S., Sun, G., and Wu, J. (2002b). Thermo-viscoelastic bending analysis of a shape memory alloy hybrid epoxy beam. *Smart Materials and Structures*, 11:970–975.

Tanaka, K. (1986). A thermomechanical sketch of shape memory effect: one dimensional tensile behavior. *Res Mechanica*, 18:251–263.

Teresi, L. and Tiero, A. (1997). On variational approaches to plate models. *Meccanica*, 32:143–156.

Tsai, X.-Y. and Chen, L.-W. (2002). Dynamic stability of a shape memory alloy wire reinforced composite beam. *Composite Structures*, 56:235–241.

Turner, T. L., Buehrle, R. D., Cano, R. J., and Fleming, G. A. (2006). Modeling, fabrication, and testing of a sma hybrid composite jet engine chevron concept. *Journal of Intelligent Material Systems and Structures*, 17:483–497.

Turner, T. L. and Patel, H. D. (2007). Analysis of SMA hybrid composite structures in MSC.Nastran and ABAQUS. *Journal of Intelligent Material Systems and Structures*, 18:435–447.

Ubertini, F. (2004). Patch recovery based on complementary energy. *International Journal for Numerical Methods in Engineering*, 59:1501–1538.

Vallet, M.-G., Manole, C.-M., Dompierre, J., Dufour, S., and Guibault, F. (2007). Numerical comparison of some hessian recovery techniques. *International Journal for Numerical Methods in Engineering*, 72:987–1007.

Van Humbeeck, J. (2001). Shape memory alloys: a material and a technology. *Advanced Engineering Materials*, 3(11):837–850.

Viola, E., Kay, J. P., and Bartoli, I. (2003). Dynamic identification of elastic constants using finite element method and Ritz approach. In *16th AIMETA Congress of Theoretical and Applied Mechanics*, Ferrara, Italy.

Wada, K. and Liu, Y. (2005). Shape recovery of NiTi shape memory alloy under various pre-strain and constraint conditions. *Smart Materials and Structures*, 14:S273–S286.

Wang, X. (2002). Shape memory alloy volume fraction of pre-stretched shape memory alloy wire-reinforced composites for structural damage repair. *International Journal of Solids and Structures*, 11:590–595.

Wei, Z. G., Sandström, R., and Miyazaki, S. (1998). Shape memory materials and hybrid composites for smart systems: Part II shape-memory hybrid composites. *Journal of Materials Science*, 33:3763–3783.

Yuan, K. Y., Huang, Y. S., and Pian, T. H. H. (1993). New strategy for assumed stresses for 4-node hybrid stress membrane element. *International Journal for Numerical Methods in Engineering*, 36:1747–1763.

Żak, A. J. and Cartmell, M. P. (2002). Dynamics of a rotor system with a smart SMA-embedded sleeve-ring component. Technical Report 4, Department of Mechanical Engineering, University of Glasgow.

Żak, A. J., Cartmell, M. P., Ostachowicz, W. M., and Wiercigroch, M. (2003). One-dimensional shape memory alloy models for use with reinforced composite structures. *Smart Materials and Structures*, 12:338–346.

Zhang, R.-X., Ni, Q.-Q., Masuda, A., Yamamura, T., and Iwamoto, M. (2006). Vibration characteristics of laminated composite plates with embedded shape memory alloys. *Composite Structures*, 74:389–398.

Zhang, R.-X., Ni, Q.-Q., Natsuki, T., and Iwamoto, M. (2007). Mechanical properties of composite filler with SMA particles and short fibers. *Composite Structures*, 79:90–96.

Zhang, Y. and Zhao, Y.-P. (2007a). A discussion on modeling shape memory alloy embedded in a composite laminate as axial force and elastic foundation. *Materials and Design*, 28:1016–1020.

Zhang, Y. and Zhao, Y.-P. (2007b). A study of composite beam with shape memory alloy arbitrarily embedded under thermal and mechanical loadings. *Materials and Design*, 28:1096–1115.

Zhuiykov, S. (2008). Novel sensor-actuator device for early detection of fire. *Sensors and Actuators A*, 141:89–96.

Acknowledgements

I would like to thank Prof. Erasmo Viola for giving me the opportunity of attending the Ph.D. program in Structural Mechanics and for the encouragement and guidance given me throughout these years. I am extremely grateful to Prof. Francesco Ubertini, who taught me many important lessons, both academic and personal.

This work owes to the direct and indirect contribution of my colleagues at DISTART and LAMC, who provided me with advice, support, and most of all friendship. The cover and figures artwork would not have been the same without the help (and patience) of Giovanni Castellazzi.

I would like to thank the research groups at CIMSS, Virginia Tech, USA, and at the CNR Institute for Composite and Biomedical Materials, Portici, for their help in carrying out the experimental part of this work and for allowing me to be one of them for a while. I am particularly grateful to Prof. Daniel J. Inman, who was a wonderful host and guidance during my stay in the USA.

I would like to thank Dr. Elena Trentini, Dr. Antonino Coglitore and Dr. Martino Labanti from ENEA, Faenza, for their help with last minute experimental characterisation. I am grateful to Prof. Ferdinando Auricchio and Prof. Elio Sacco for the valuable discussions on shape memory alloy constitutive models.

I dedicate this work to my parents, Silvia and Claudio, my sister Beatrice and my boyfriend Ludovico, who were always with me from near and from afar and who supported all my crazy ideas.

Finally, I am grateful to my two cats, Alpha and Omega, who are the best way to chill out after a stressful day's work, and to all my friends from Impro', who allowed me to escape from reality once a week and who taught me that improvisation is crucial, in theatre and in real life.

Curriculum Vitæ

Federica Daghia was born in Imola, Italy, on the 12th November 1980. In 1997 she won a two-years scholarship to attend the United World College of the Adriatic in Duino, Italy, and she received the International Baccalaureate (bilingual Italian/English diploma) from the same institution in June 1999. In July 2004, she received the Laurea degree in Civil Engineering (Structures), 100/100 cum laude, from the University of Bologna. From January 2005 to December 2007 she attended the Ph.D. program in Structural Mechanics at the University of Bologna on a full scholarship.

Within the Ph.D. program, she spent eight months as a Visiting Scholar at the Center for Intelligent Material Systems and Structures of the Virginia Polytechnic Institute and State University, USA. Furthermore, she actively collaborated with the CNR Institute for Composite and Biomedical Materials in Portici, Italy, within the context of her doctoral thesis.

Her research interests are in the fields of Computational mechanics and Multiphase materials and structures.

Selected publications

Daghia, F., de Miranda, S., Ubertini, F., and Viola, E. (2008). A hybrid stress approach for laminated composite plates within the First-order Shear Deformation Theory. *International Journal of Solids and Structures*, 45:1766-1787.

Daghia, F., de Miranda, S., Ubertini, F., and Viola, E. (2007). Estimation of Elastic Constants of Thick Laminated Plates within a Bayesian Framework. *Composite Structures*, 80:461-473.

Daghia, F., Inman, D. J., Ubertini, F., and Viola, E. (2007). Shape memory alloy hybrid composite plates for shape and stiffness control. *Journal of Intelligent Material Systems and Structures*. In press.

Daghia, F., Inman, D. J., Ubertini, F., and Viola, E. (2007). Experimental testing of a shape memory alloy hybrid composite plate for active shape control. In: *III ECCOMAS thematic conference on smart structures and materials*, Gdansk, Poland.

Daghia, F., Viola, E., Seigler, T. M., and Inman, D. J. (2006). Constitutive modeling of SMA in constrained recovery mode. In: *Proceedings of ASME International Mechanical Engineering Congress and Exposition*, Chicago, USA. Paper number IMECE2006-15616.

Contact

LAMC – Laboratory of Computational Mechanics
DISTART Department
Alma Mater Studiorum • Università di Bologna
viale Risorgimento 2
40136 Bologna (Italy)
Tel. +39 051 2093373
Fax. +39 051 2093496
Email. `federica.daghia@mail.ing.unibo.it`

This thesis is available in pdf format on the LAMC website:
`www.lamc.ing.unibo.it`